Ore Petrology and Alteration of the West Ansil Volcanic-hosted Massive Sulphide Deposit of the Noranda Mining Camp, Rouyn-Noranda, Québec

A thesis submitted to the

Faculty of Graduate and Postdoctoral Studies

In partial fulfillment of the requirements for the

Master of Science Degree in Earth Sciences

Department of Earth Sciences

Faculty of Science

University of Ottawa

ABSTRACT

The West Ansil deposit, located in 2005, was the first Cu discovery in 25 years in the Noranda Central Camp. It has a combined indicated and inferred resource of ~1.2 Mt. Grades for the indicated resource are 3.4% Cu, 0.4% Zn, 1.4 g/t Au and 9.2 g/t Ag. Locally, gold grades are up to 10 ppm within massive chalcopyrite ore. The bulk of the resource is located in three massive sulphide lenses (Upper, Middle and Lower) that are entirely within the Rusty Ridge Formation but well above the Lewis exhalite. The Lewis exhalite is a key marker horizon at which the nearby Ansil mine occurs (1.58 Mt, 8.03% Cu, 0.09% Zn), about 1.8 km northeast of West Ansil. The overall distribution of massive sulphide ore and stringer zones at West Ansil suggests that a single deposit was dissected by late-stage faulting and diking, producing the separate lenses. The alteration of the Rusty Ridge andesite at West Ansil is consistent with the formation of one main lens where silicification is dominant in the hanging wall and chloritization is dominant in the footwall. A narrow range in Fe-rich chlorite compositions and abundant actinolite and stilpnomelane in the ore also support a single high-temperature mineralizing event or overprint. The mineralization in all three ore lenses consists of massive pyrrhotite + chalcopyrite $\pm$ magnetite. Semi-massive sphalerite is restricted to the upper and lower parts of the Middle lens. Massive magnetite occurs at the center of the Upper and Middle lenses, where it replaces massive pyrrhotite. A hydrothermal origin for the magnetite is strongly suggested by the presence of quartz-magnetite veins in the hanging wall of the Upper lens which indicate introduction of magnetite by hydrothermal fluids after burial of the deposit. The high Cu/Cu+Zn ratio, similar to the Ansil deposit, reflects the high temperature of ore formation, which appears to be a typical feature of deposits in the lowermost stratigraphic units of the Central Camp. A striking feature of West Ansil is the presence of abundant colloform and nodular pyrite

(±marcasite) in the massive sulphides. Late-stage replacement of massive pyrrhotite by colloform pyrite and marcasite, mostly along the upper and lower contacts of the lenses, appears to be a secondary feature caused by supergene alteration of pyrrhotite along fractures in the ore. This is interpreted to be a post-metamorphic (possibly supergene) alteration of pyrrhotite and may be related to shearing at the contacts of the lenses that allowed penetration of groundwater into the massive sulphides.

ACKNOWLEDGEMENTS

I would like to thank the personnel at Xstrata Copper Canada Ltd and Alexis Minerals for providing the geological information such as drill core and Cu-Zn-Ag-Au geochemical data presented in this paper. I am also grateful to the TGI3-Target Geoscience Initiative -3 Abitibi project led by Benoit Dubé from the Geological Survey of Canada for their financial support and scientific contribution. Many thanks to Dr. Mark D. Hannington and Dr. Thomas Monecke for leading me in the right direction with their assistance in the field, as well as for their academic support.

TABLE OF CONTENTS

Cover Page....p. 1

Abstract....p. 2

Acknowledgements....p. 4

Table of Contents....p. 5

List of Tables....p. 8

List of Figures....p. 10

CHAPTER 1. GEOLOGICAL SETTING OF THE WEST ANSIL DEPOSIT....p. 16

1.1 Introduction….....p. 16

1.2 District Geology….....p. 17

1.3 Geology of the West Ansil Deposit….....p. 18

Chapter Tables and Figures....p. 21

CHAPTER 2. WEST ANSIL OREBODY AND MINERALIZATION....p. 28

2.1 Metal Zonation....p. 30

2.2 Principal Ore Types…….....p. 31

Massive Sphalerite-Pyrrhotite....p. 32

Sphalerite Stringer Mineralization....p. 32

Massive Pyrrhotite-Chalcopyrite....p. 33

Massive Chalcopyrite-Pyrrhotite....p. 34

Chalcopyrite Stringer Mineralization....p. 34

Massive Magnetite....p. 35

2.3 Sulphide Mineralogy and Mineral Chemistry....p. 36

Sphalerite....p. 36

Pyrrhotite....p. 37

Chalcopyrite....p. 38

Magnetite....p. 39

Pyrite....p. 40

Galena.....p. 40

Cassiterite.....p. 41

Bi minerals.....p. 41

Co-pentlandite.....p. 41

Cobaltite.....p. 42

Gold.....p. 42

2.4 Ore-related Gangue Minerals.....p. 43

Quartz.....p. 43

Actinolite-Stilpnomelane.....p. 43

Siderite….....p. 43

2.5 Late-stage Colloform Pyrite-Marcasite…….....…….....p. 44

2.6 Trace Element Geochemistry of the Ores…….....……p. 46

Massive Sphalerite…….....…….....p. 46

Sphalerite Stringer Mineralization……..….....……p. 46

Massive Pyrrhotite-Chalcopyrite.....….....p. 46

Massive Chalcopyrite-Pyrrhotite…….....…p. 47

Chalcopyrite Stringer Mineralization……..….....p. 47

Massive Magnetite.....p. 48

Late-stage Colloform Pyrite-Marcasite……..…….....p. 48

Low-temperature versus High-temperature Suites.....p. 48

Low-temperature Suite…….....….....p. 49

High-temperature Suite.....p. 49

2.7 Sulfur Isotopes.....p. 50

Chapter Tables and Figures.....p. 52

CHAPTER 3. ALTERATION OF THE WEST ANSIL DEPOSIT.....p. 92

3.1 Alteration Mineralogy.....p. 92

3.2 Geochemistry of Altered Rusty Ridge Andesite.....p. 93

Major Elements....p. 94

Immobile Elements....p. 95

Mass Changes....p. 96

REE Mobility....p. 97

Trace Element....p. 98

Chapter Tables and Figures....p. 99

CHAPTER 4. DISCUSSION....p. 111

4.1 Evolution of the West Ansil Deposit…….....p. 111

4.2 Origin of the High Cu/Cu+Zn…….....p. 113

4.3 Origin of the Massive Magnetite....p. 115

4.4 Origin of the Quartz-Chlorite-Actinolite-Stilpnomelane Assemblage....p. 120

4.5 Origin of the Pyrite-Marcasite-Hisingerite Alteration....p. 121

4.6 Reconstruction of the West Ansil Lenses....p. 123

Chapter Tables and Figures....p. 124

REFERENCES....p. 131

LIST OF APPENDICES....p. 145

APPENDICES....p. 146

LIST OF TABLES

Table 1.1 Grade and Tonnage for VMS deposits of the Noranda District.

Table 2.1 Characteristics of Principal Ore Types in the West Ansil Deposit.

Table 2.2 Mineralogy of Principal Ore Types in the West Ansil Deposit.

Table 2.3 Composition of Sphalerite in the West Ansil Deposit.

Table 2.4 Electron Microprobe Analyses of Major Ore Minerals and Selected Trace Minerals in the West Ansil Deposit.

Table 2.5. Composition of Magnetite in the West Ansil Deposit.

Table 2.6 Average Chemical Composition of Representative Ore Samples in the West Ansil Deposit.

Table 2.7 Correlation Matrix for Selected Trace Elements in Massive Sulphides of the West Ansil Deposit.

Table 2.8 Sulfur Isotopic Compositions of Mineral Separates from Selected Ore Samples of the West Ansil Deposit.

Table 3.1 Electron Microprobe Analyses of Selected Ore-related Gangue Minerals in the West Ansil Deposit.

Table 3.2 Whole Rock Analyses of the Altered Rusty Ridge Andesite from the West Ansil Deposit.

Table 3.3 Correlation Matrix of Immobile Elements for Mass Balance Calculations.

Table 3.4 Calculated Mass Changes for the Altered Rusty Ridge Andesite from the West Ansil Deposit.

Table 4.1 Summary Characteristics of Noranda Deposits at Different Levels in the Mine Sequence.

LIST OF FIGURES

Figure 1.1 Generalized geological map of the Noranda Camp, showing the regional geology, major structural elements, as well as the distribution of extrusive and intrusive rocks. West Ansil and other VMS deposits of the Mine Sequence are also shown (modified from Monecke et al., 2008).

Figure 1.2 Stratigraphic position of the West Ansil deposit within the reconstructed Noranda cauldron showing the main exhalite horizons, synvolcanic structures, and the significant VMS deposit of the Mine Sequence (modified from Gibson and Galley, 2007).

Figure 1.3 Cu-Zn-Pb ratios of ArcheanVMS Deposits of the Noranda Camp and Phanerozoic Kuroko and Iberian Pyrite Belt Deposits. Data from Shimazaki (1974), Gibson and Watkinson (1990) and Marcoux et al. (1996).

Figure 1.4 Cu/Cu+Zn Ratios for VMS Deposits from the Noranda District.

Figure 1.5 Surface orebody projection of the West Ansil deposit showing the location of drill holes as well as the position of north-south cross sections in Figure 2.2 (modified from Xstrata Copper Canada Ltd, 2005).

Figure 1.6 North-south cross sections (facing west) through the West Ansil deposit showing the position of the Upper, Middle and Lower lenses (modified from Xstrata Copper Canada Ltd, 2005).

Figure 2.1 A three-dimensional view of the West Ansil ore lenses (modified from Xstrata Copper Canada Ltd, 2005).

Figure 2.2 Composite graphic logs of the Upper, Middle and Lower lenses of the West

Ansil deposit showing the dominant massive sulphide ores and stockwork zones, contact relationships, the main mafic volcanic units, and major mafic dikes intruding the lenses.

Figure 2.3 Composite metal zonation of the Upper, Middle and Lower lenses of the West Ansil deposit based on assay data.

Figure 2.4 Inter-element plots for Cu, Zn, Au and Ag in ores of the Upper, Middle and Lower lenses showing a strong Cu-Au association.

Figure 2.5 Photographs of representative drill core samples showing sulphide ore textures in the West Ansil lenses.

Figure 2.6 Photographs of representative drill core samples showing sulphide ore textures and the evolution of the hydrothermal system.

Figure 2.7 Sketches of drill core samples illustrating massive sphalerite-pyrrhotite and sphalerite stringer ore textures in the West Ansil deposit.

Figure 2.8 Sketches of drill core samples illustrating representative massive pyrrhotite chalcopyrite ore textures.

Figure 2.9 Sketches of drill core samples illustrating massive chalcopyrite –pyrrhotite and chalcopyrite stringer ore textures in the West Ansil deposit.

Figure 2.10 Sketches of drill core samples illustrating massive magnetite textures at West Ansil.

Figure 2.11 Locations of samples from the Upper, Middle and Lower lenses of the West Ansil deposit.

Figure 2.12 Reflected light photomicrographs of representative sphalerite ore textures in the Middle lens of the West Ansil deposit.

Figure 2.13 Photomicrographs of representative sphalerite stringer ore and remobilized sphalerite textures in the West Ansil deposit.

Figure 2.14 Range of sphalerite compositions in the West Ansil ores. The range of sphalerite compositions for Corbet from Hannington and Scott (1989) and for Ansil from Galley (1994).

Figure 2.15 A comparison of the average production grade of gold from Archean Cu-Zn deposits in the Noranda district with the average FeS content in associated sphalerite.

Figure 2.16 Reflected light photomicrographs of representative pyrrhotite ore textures in the West Ansil deposit.

Figure 2.17 Reflected light photomicrographs of representative chalcopyrite ore textures in the West Ansil deposit.

Figure 2.18 Photomicrographs of representative chalcopyrite stringer ore textures in the West Ansil deposit.

Figure 2.19 Photomicrographs of representative magnetite ore textures in the West Ansil deposit.

Figure 2.20 Reflected light photomicrographs of primary pyrite in the West Ansil deposit.

Figure 2.21 Reflected light photomicrographs showing the occurrence of galena in the West Ansil deposit.

Figure 2.22 Reflected light photomicrographs of cassiterite in the West Ansil deposit.

Figure 2.23 Reflected light photomicrographs of laitakarite in the West Ansil deposit.

Figure 2.24 Reflected light photomicrographs of Co-pentlandite and cobaltite in the West Ansil deposit.

Figure 2.25 Reflected light photomicrographs of gold in the West Ansil deposit.

Figure 2.26 Photomicrographs of representative ore-related gangue minerals in the West Ansil deposit.

Figure 2.27 Sketches of drill core samples illustrating colloform pyrite-marcasite textures in the West Ansil orebody.

Figure 2.28 Reflected light photomicrographs of representative colloform pyrite marcasite textures in the West Ansil deposit.

Figure 2.29 Inter-element plots of selected trace elements in the ores of the Upper, Middle and Lower lenses of the West Ansil deposit.

Figure 2.30 Sulfur isotope compositions of the West Ansil sulphides. Data for Archean Cu-Zn deposits from Franklin et al. (1981) and for Ansil from Galley (1994).

Figure 3.1 Photomicrographs of representative ore-related gangue minerals in the West Ansil deposit.

Figure 3.2 Chlorite compositions in the Upper, Middle and Lower lenses of the West Ansil deposit compared to other deposits in the Noranda Mining District.

Figure 3.3 Si-Al-(Fe+Mg) ternary plot of alteration mineral compositions and altered

Rusty Ridge andesites from the West Ansil deposit.

Figure 3.4 Plot of Rusty Ridge andesite compositions on a Zr/Ti versus Nb/Y classification diagram from Floyd and Winchester (1978).

Figure 3.5 Immobile element plots of Y versus Zr and TiO_2 versus Zr in altered andesites from the Upper, Middle and Lower lenses.

Figure 3.6 Average absolute mass changes of major elements in the Upper, Middle and Lower lenses in the West Ansil deposit relative to a least-altered Rusty Ridge andesite composition.

Figure 3.7 Chondrite-normalized REE profiles for Rusty Ridge andesite hosting the three lenses in the West Ansil deposit showing the effects of silicification and chloritization.

Figure 4.1 Schematic illustrations of the development of the West Ansil deposit from an early-stage low-temperature hydrothermal system to a later stage high-temperature system.

Figure 4.2 Comparison of the compositions of gold and electrum in Archean and Phanerozoic Cu-Zn deposits.

Figure 4.3 Solubilities of gold and silver with chloride complexes showing the strong Cu-Au association at West Ansil.

Figure 4.4 Temperature versus fo_2 diagram showing the stability fields of py-po-mt in the Fe-S-O system and possible conditions of formation of magnetite in the West Ansil deposit.

Figure 4.5 Quartz solubility diagram showing the possible dumping of silica explaining the white quartz rims on magnetite veinlets .

Figure 4.6 Schematic representation of the possible reconstruction of the West Ansil deposit after the removal of the diorite sill and late faulting.

CHAPTER 1. GEOLOGICAL SETTING OF THE WEST ANSIL DEPOSIT

1.1 INTRODUCTION

The West Ansil deposit is hosted by volcanic rocks of the Blake River Group, one of several Archean volcanic complexes that form the Abitibi greenstone belt of the southern Superior Province (Baragar, 1968; Dimroth et al., 1982; Gélinas et al., 1984; Gélina and Ludden, 1984). The deposit lies conformably in volcanic stratigraphy of the central part of the Central Camp, 6 km north of Rouyn-Noranda (Figure 1.1). The orebody was discovered in 2005 by Xstrata Copper Canada Ltd, and was the first significant new base metal discovery in the Central Camp in 25 years. The deposit occurs at a basalt-andesite contact within the Rusty Ridge Formation and is the only known massive sulphide at this stratigraphic level (Figure 1.2). The original drill targets were characterized by the presence of a significant alteration zone near the intersection of two recognized synvolcanic faults within the Rusty Ridge Formation. Historical drill holes that intersected the alteration did not reach the Lewis exhalite contact, the deep horizon at which the nearby Ansil deposit was found, or the stratigraphic position of the Corbet deposit next to the Flavrian intrusion (Xstrata Copper Canada Ltd, 2005). However, several off-hole geophysical anomalies (borehole EM) were found stratigraphically above the interpreted position of the Lewis contact. These were subsequently targeted for drilling in 2005, and significant Cu-rich stringer mineralization and massive sulphides were intersected in three separate zones. The combined Upper, Middle and Lower lenses of the West Ansil deposit have indicated and inferred resources of ~1.2 Mt with grades for the indicated resource of 3.4% Cu, 0.4% Zn, 1.4 g/t Au and 9.2 g/t Ag (Xstrata Copper Canada Ltd, 2005), typical of Cu-rich Archean Cu-Zn deposits (Figure 1.3; Table 1.1).

Ansil, West Ansil, and the Corbet deposits occur at the base of the Mine Sequence (Cycle 3) of the Central Camp and are characterized by generally higher Cu/Cu+Zn and Au/Ag ratios than the deposits higher in the stratigraphy at the Millenbach and Amulet horizons (Figures 1.3 and 1.4; Table 1.1). Ansil and West Ansil, in particular, differ from the other massive sulphide deposits of the Central Camp (e.g., Riverin and Hodgson, 1980; Cattalani et al., 1990; Riverin et al., 1990) in the following ways: (i) the bulk of the orebodies are dominated by chalcopyrite and pyrrhotite; (ii) massive magnetite forms a significant portion of the deposits; (iii) at West Ansil there is a lack of conspicuous alteration around the Middle lens; (iv) abundant late-stage colloform pyrite±marcasite overprints the massive pyrrhotite. This study documents the evolution of the West Ansil deposit, the main ore types, sulphide mineralogy, and alteration of the deposit, including metal zonation and the mineralogy and geochemistry of altered rocks, and discusses the possible origin of the high Cu/Cu+Zn ratio, the possible link to the abundant magnetite and quartz-chlorite-actinolite-stilpnomelane alteration assemblage, and the unusual late-stage pyrite and marcasite alteration.

1.2 DISTRICT GEOLOGY

The Blake River Group in the Noranda area is 12 to 15 km thick and composed of bimodal mafic and felsic volcanic rocks with rapid facies changes and a marked variation in the thicknesses of individual units (de Rosen Spence, 1976; Gibson and Watkinson, 1990; Riverin et al., 1990). The ore hosting Noranda Volcanic Complex (NVC) has an age of approximately 2.7 Ga, is 35 km in diameter and 7.5 to 9 km thick. It is dominated by the Noranda cauldron and shield volcano (Gibson and Watkinson, 1990) which consists of rhyolitic, andesitic and basaltic flows and minor pyroclastic rocks (Mortensen, 1987; Gibson and Watkinson, 1990). The volcanic rocks have been metamorphosed to the greenschist facies, although some areas include

higher or lower grade rocks. They are divided into 5 cycles, each consisting of an andesitic to basaltic basal unit and mixed rhyolite and andesite upper unit (Gibson and Watkinson, 1990). Cycle 3, also referred to as the Mine Sequence, is host to most of the massive sulphide deposits of the Noranda Central Camp and consists of a bimodal succession of tholeiitic basalt to rhyolite, interpreted to have erupted during periods of cauldron subsidence within the upper central part of the Noranda shield volcano (Gibson and Watkinson, 1990). The Corbet, Ansil and West Ansil deposits are the lowest deposits in the Mine Sequence stratigraphy (Barrett et al., 1991; Barrett et al., 1993a; Galley, 1994) (Figure 1.2). The overall stratigraphic setting has recently been revised by Goutier et al. (2009a, b) based on detailed U-Pb geochronology (e.g., McNicoll et al., 2009), and Goutier et al. (2009a) have assigned the Mine Sequence to the newly defined ~2702-2696.7 Ma Noranda Formation.

1.3 GEOLOGY OF THE WEST ANSIL DEPOSIT

The West Ansil deposit is located at an andesite-basalt contact within the Rusty Ridge Formation, stratigraphically above the Ansil deposit (Figure 1.2). The stratigraphy in the immediate vicinity of the deposit includes the Northwest rhyolite, the Rusty Ridge andesite, the Amulet dacite and the Amulet rhyolite (Figures 1.5 and 1.6). These units generally dip towards the east-northeast, at approximately 30° to 45°. All of the volcanic units have a dominantly tholeiitic affinity (Barrett et al., 1991).

The top of the Northwest rhyolite corresponds to the position of the Lewis exhalite (Figure 1.2), but this horizon has not been observed at West Ansil. At West Ansil the Rusty Ridge Formation, which comprises andesite and basalt, is overlain by and partly intruded by the Amulet dacite and rhyolite. The entire extrusive sequence is underlain by the Flavrian pluton, a composite body of mainly trondhjemitic composition (Goldie, 1978; Gibson and Galley, 2007).

In the deposit, the Rusty Ridge andesite is a dark green massive, pillowed unit, with chloritized and brecciated flow margins. The pillows are metre-sized and locally contain centimetre-scale quartz- and chlorite-filled amygdules, fracture-filling chlorite, and disseminated pyrite and chalcopyrite. The flow breccias have a distinctly chloritized matrix. The overlying Rusty Ridge basalt is also dark green in colour, with massive to brecciated portions. Its upper and lower parts can only be distinguished on the basis of lithogeochemistry (Xstrata Copper Canada Ltd, 2005). However, the brecciated portion is generally located at the top of the unit. The fragments range from 0.2 to 2 cm in size with 2 to 5 vol% chlorite-filled amygdules, and the matrix is chloritized and silicified. The massive portion is generally fine-grained and contains 1 to 2 vol% chlorite-filled amygdules ranging from 1 to 2 mm in size.

The Amulet dacite, which overlies the Rusty Ridge basalt, is pale to medium grey and is characterized by a massive aphanitic texture with rare quartz-filled amygdules and local disseminated pyrrhotite, pyrite and chalcopyrite. It intrudes the Rusty Ridge Formation and generally has brecciated contacts. At West Ansil, the lower contact of the dacite with the Rusty Ridge basalt is discordant confirming its intrusive nature. Above the Rusty Ridge basalt, the Lower Amulet rhyolite (not shown in Figure 1.6) is present where the contact is not cut by the dacite. It is aphyric to granular, pale to medium grey in colour, and contains 2 to 10 vol% quartz- and chlorite-filled amygdules. It is generally massive with flow breccias. The brecciated facies is composed of clasts from 0.5 to 3 cm in size in a chlorite matrix.

The long axis of the West Ansil deposit trends north-south and has a strike length of 200 m, with a thickness of approximately 50 m (Figure 1.5 and 1.6). The Upper lens is located within the upper Rusty Ridge basalt near the contact with the Amulet dacite. The Middle lens occurs in the Rusty Ridge basalt above the andesite. The Lower lens and stockwork zone are

located at the contact between the Rusty Ridge basalt and andesite (Figure 1.6). A large, 60 metre-thick diorite sill separates the Middle lens from the Lower lens at the approximate location of the basalt and andesite contact. Other smaller diorite sills cut through the West Ansil deposit as well as most of the stratigraphy. Subvertical feldspar porphyritic diorite dikes also cut the Middle lens and the Rusty Ridge andesite and basalt. Where they cut the massive sulphides they are associated with local recrystallization of sulphides and quartz-siderite veining.

Table 1.1 Grade and Tonnage for VMS deposits of the Noranda District

VMS Deposit	Mt Ore	Cu (wt%)	Zn (wt%)	Pb (wt%)	Au (g/t)	Ag (g/t)	Cu/Cu+Zn	Au/Ag
Mobrun	1.6	0.8	2.5		2.4	27.4	0.24	0.09
Cycle 4								
Gallen	8.1	0.1	3.4		0.1	2.4	0.02	0.03
Delbridge	0.4	0.6	8.6		2.4	68.6	0.06	0.03
Deldona	0.1	0.3	5.0		4.1	26.0	0.06	0.16
Cycle 3-Mine Sequence								
Norbec	4.5	2.8	4.8		0.9	44.3	0.37	0.02
Vauze	0.4	2.9	0.9		0.7	24.0	0.76	0.03
East Waite	1.5	4.1	3.3		1.8	31.0	0.56	0.06
Old Waite	1.1	4.7	3.0	0.04	1.1	22.0	0.61	0.05
Amulet Lower	4.7	5.1	5.3		1.4	44.1	0.49	0.03
Amulet Upper	0.2	2.4	6.1		2.0	46.0	0.28	0.04
Amulet C	0.6	2.2	8.5		0.6	86.7	0.21	0.01
Amulet F	0.3	3.4	8.6		0.3	46.3	0.28	0.01
Amulet No 11	0.5	3.6	2.4		0.7	22.0	0.60	0.03
Millenbach	3.6	3.5	4.3		1.0	56.2	0.44	0.02
West Ansil	***1.2***	***3.4***	***0.4***		***1.4***	***9.2***	***0.89***	***0.15***
Ansil	***1.6***	***7.2***	***0.9***		***1.6***	***26.5***	***0.88***	***0.06***
Corbet	2.8	2.9	1.6		1.0	21.0	0.64	0.05
Aldermac	2.9	1.5	4.1		0.5	31.2	0.27	0.02

Data for Noranda deposits from Gibson and Watkinson (1990) and Goutier et al. (2009)

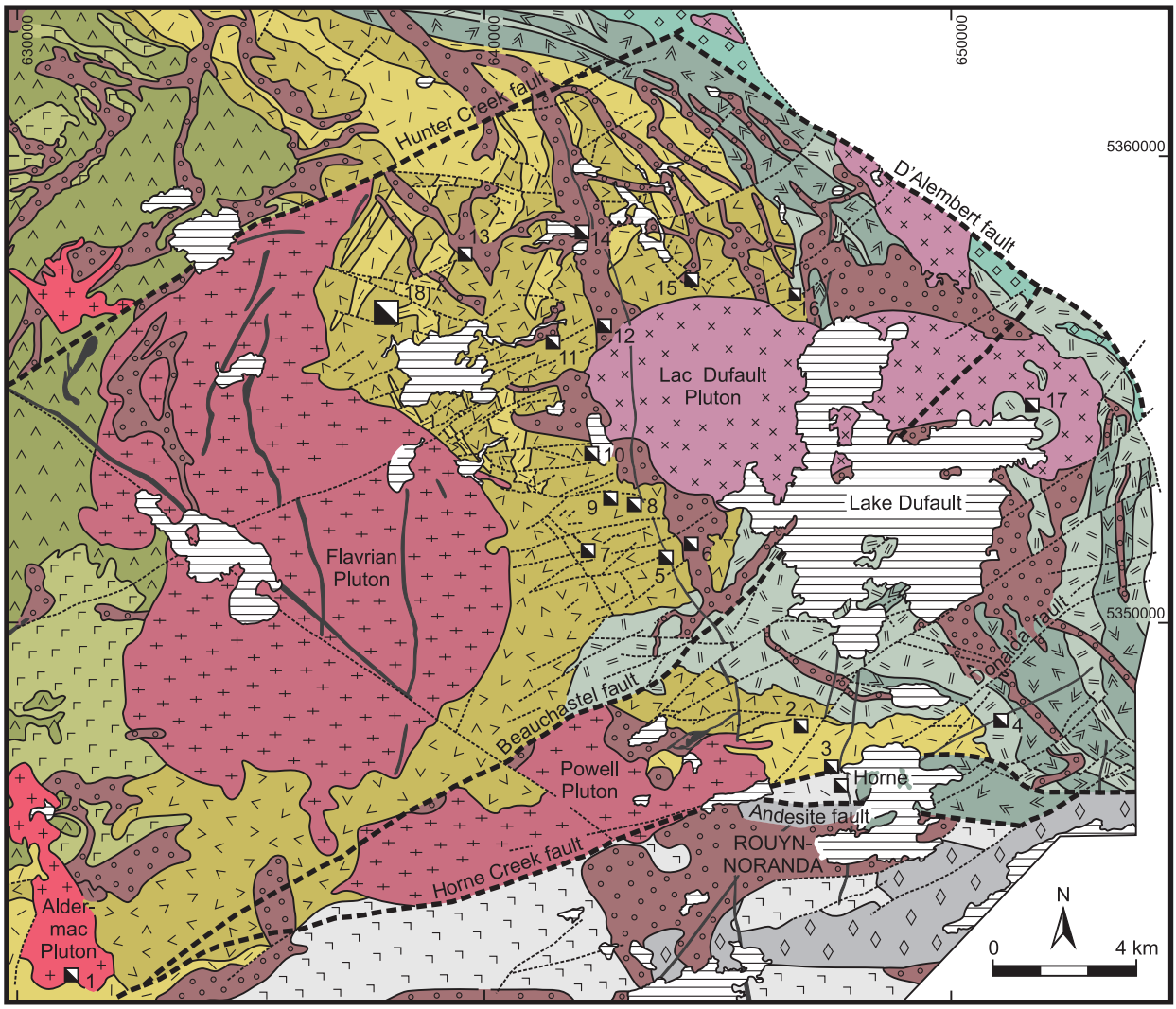

VMS deposits: 1=Aldermac, 2=Joliet, 3=Quemont, 4=Delbridge, 5=D68, 6=Millenbach, 7=Corbet, 8=Amulet A, 9=Amulet C, 10=Amulet F, 11=Old Waite, 12=East Waite, 13=Ansil, 14=Vauze, 15=Norbec, 16=Newbec, 17=Gallen and 18=West Ansil

ARCHEAN EXTRUSIVE ROCKS
Undifferentiated
Rhyolite
Basalt/andesite
Cycle 1+2
Rhyolite
Basalt/andesite
Cycle 3
Rhyolite
Basalt/andesite
Cycle 4
Rhyolite
Basalt/andesite
Cycle 5
Basalt/andesite

ARCHEAN INTRUSIVE ROCKS
Syenite
Granodiorite
Trondhjemite, tonalite
Gabbro, quartz diorite

PROTEROZOIC INTRUSIVE ROCKS
Diabase

Major fault
Minor fault
Deposit

Figure 1.1 Generalized geological map of the Noranda Camp, showing the regional geology, major structural elements, as well as the distribution of extrusive and intrusive rocks. West Ansil and other VMS deposits of the Mine Sequence are also shown (modified after Monecke et al., 2008).

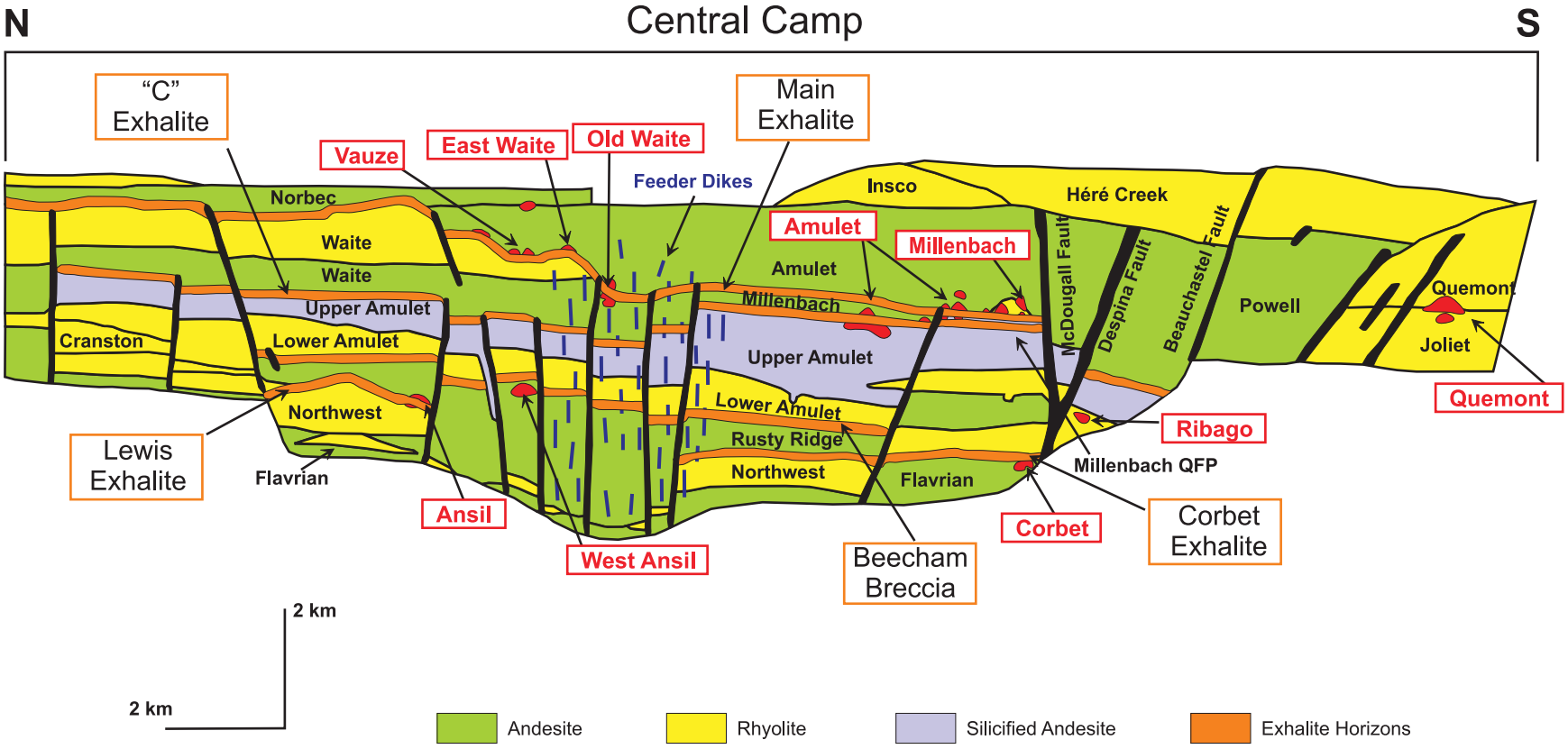

Figure 1.2 Stratigraphic position of the West Ansil deposit within the reconstructed Noranda cauldron showing the main exhalite horizons represented by the orange horizons , synvolcanic structures in black, the Flavrian and Rusty Ridge andesite and Upper Amulet andesite hosting the significant VMS deposits of the Mine Sequence (modified after Gibson, 2007).

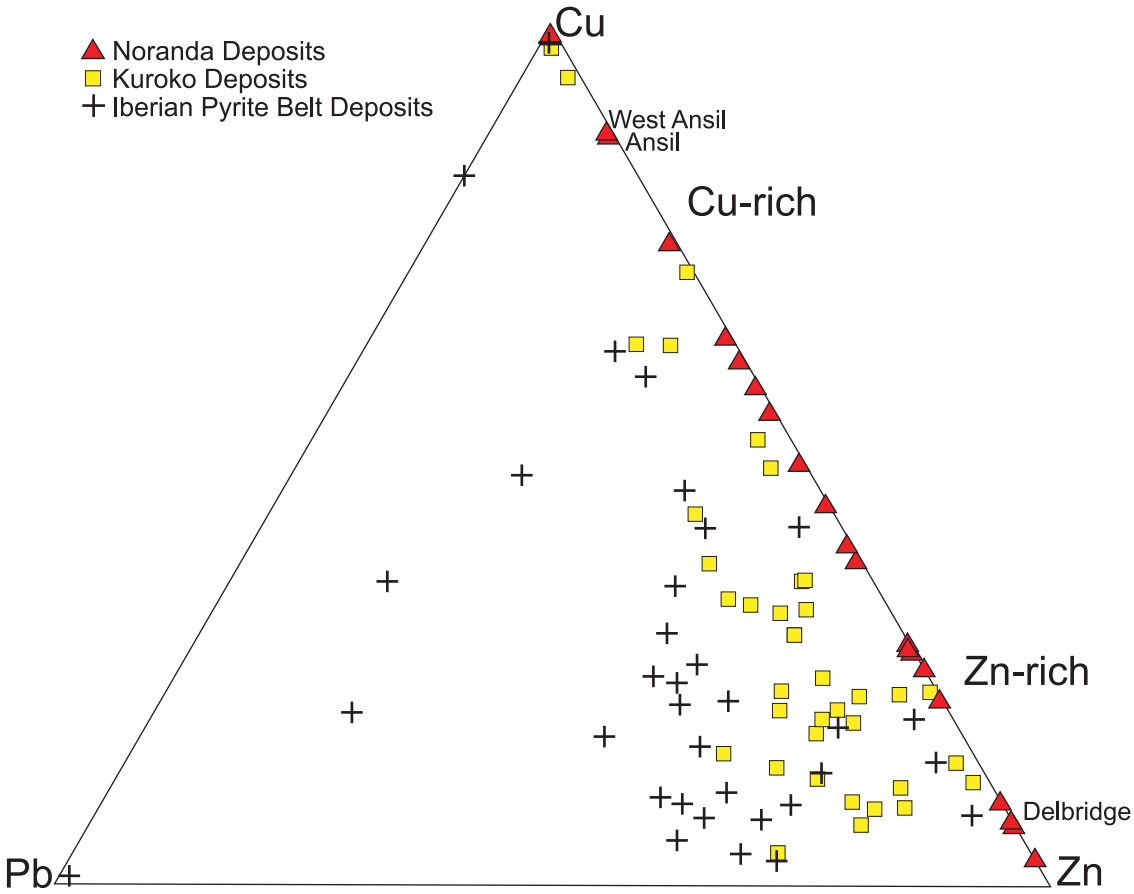

Figure 1.3 Cu-Zn-Pb ratios of Archean deposits from the Noranda camp and Phanerozoic Kuroko and Iberian Pyrite Belt (IPB) deposits. Like Ansil, West Ansil falls in the Cu-rich field and most other Noranda deposits are more Zn-rich and fall in the Zn-Cu field due to their lower Cu/Cu+Zn ratios (e.g. Delbridge). Most Kuroko and IPB contain a higher concentration Pb and are therefore more Zn-Pb-rich. The data for Noranda deposits are summarized in Table 1.1. Data from Shimazaki (1974), Gibson and Watkinson (1990), Marcoux et al. (1996) and Goutier et al. (2009b).

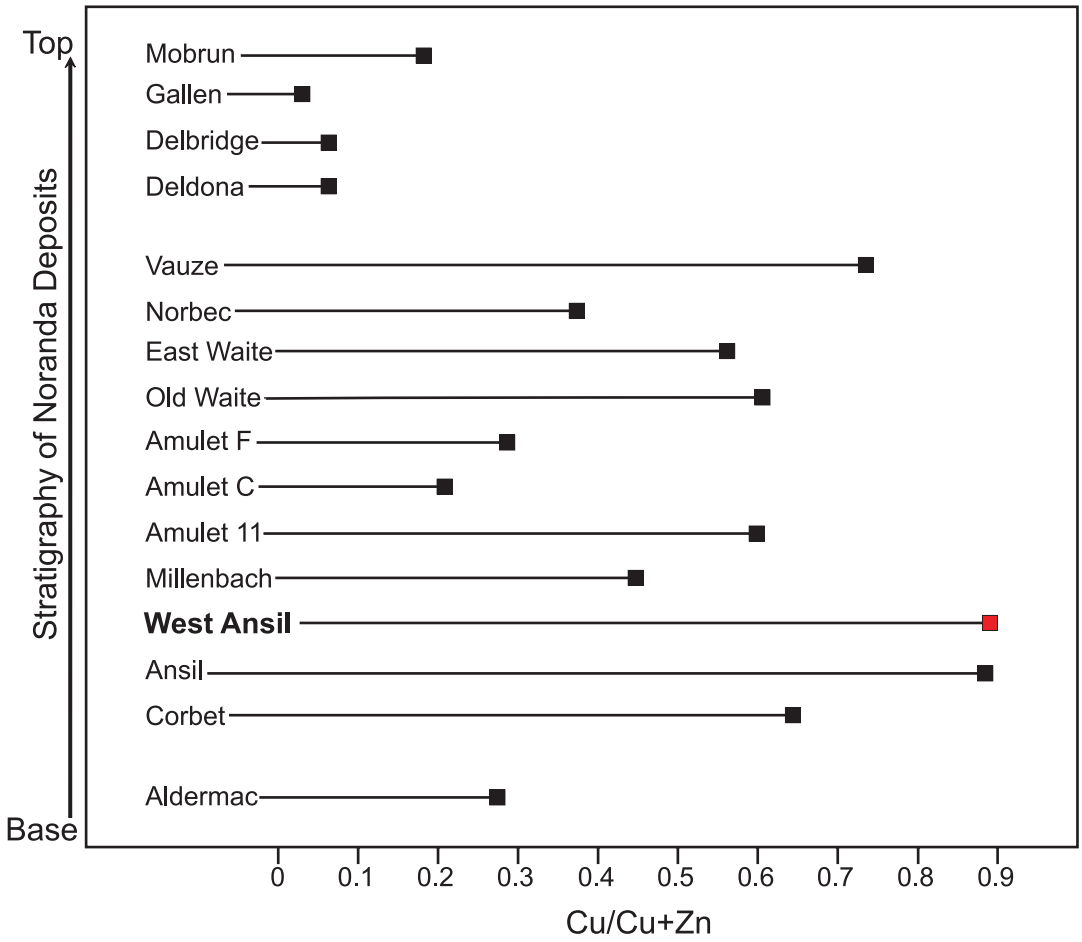

Figure 1.4 Cu/Cu+Zn ratios for selected deposits from the Noranda district showing a relative decrease in values in deposits higher up in stratigraphy. The data are summarized in Table 1.1. Data from Gibson and Watkinson (1990) and Goutier et al. (2009b).

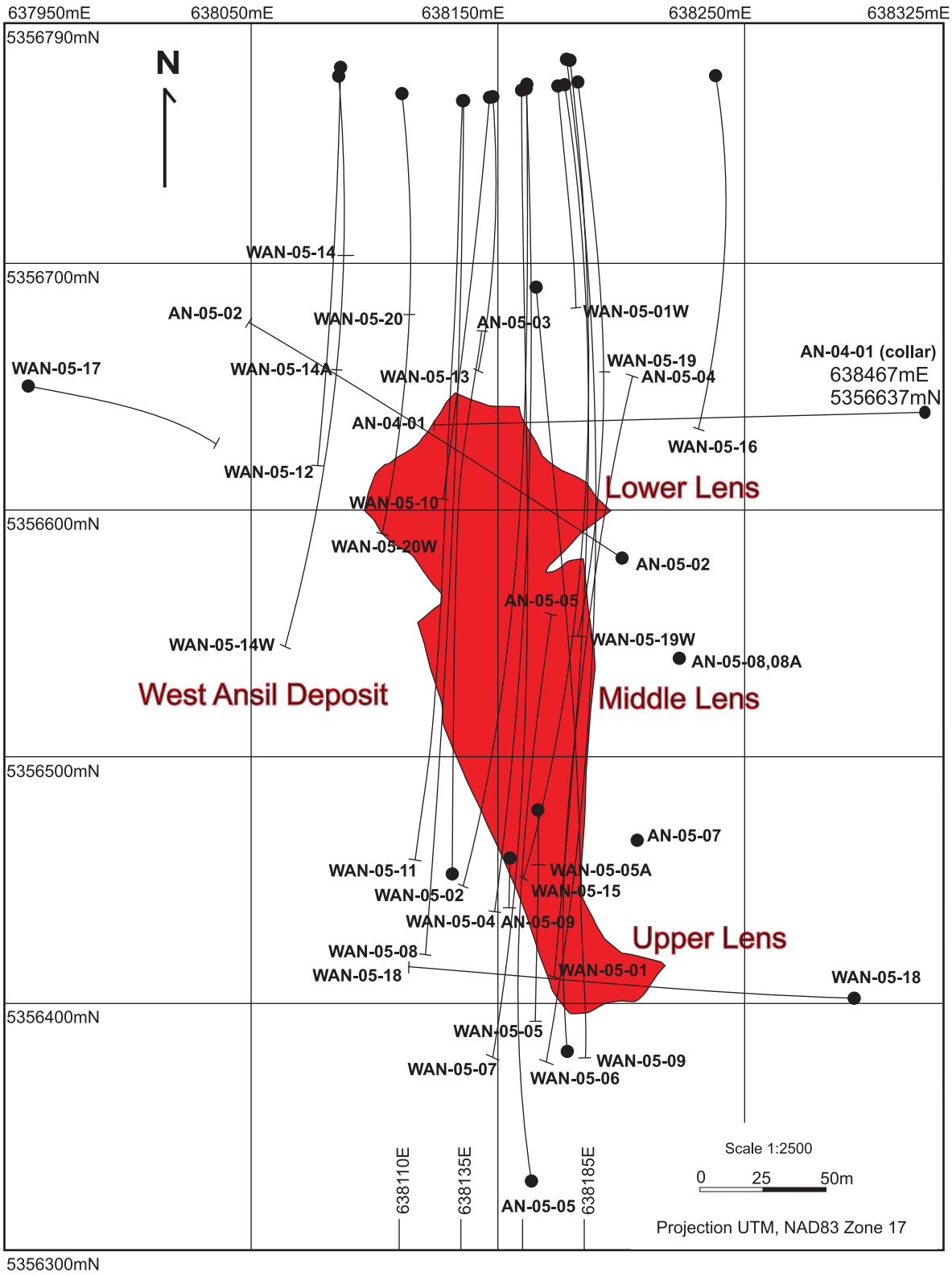

Figure 1.5 Surface orebody projection of the West Ansil deposit showing the location of drill holes as well as the position of north-south cross sections in Figure 1.6 (modified after Xstrata Copper Canada Ltd, 2005).

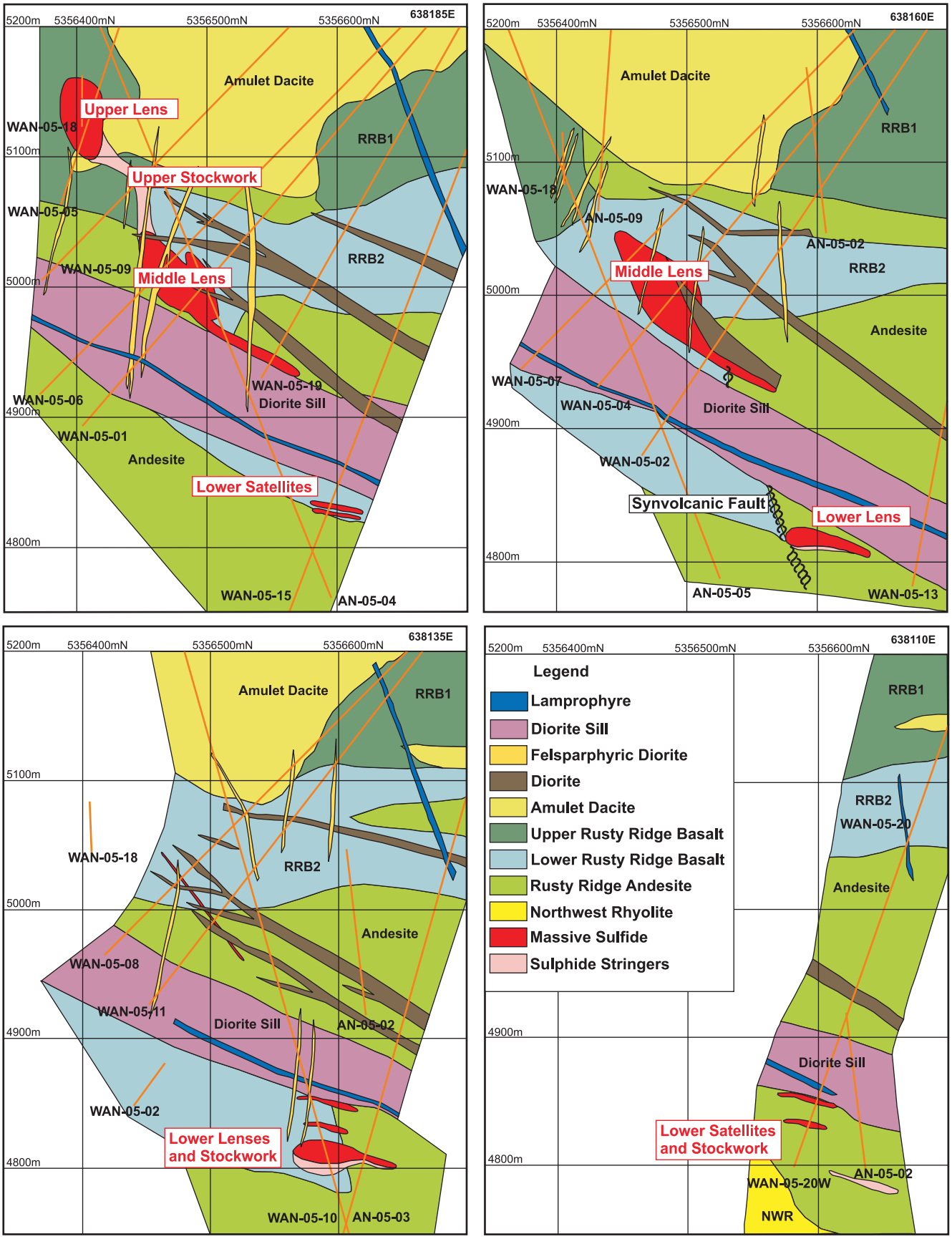

Figure 1.6 North-south cross sections (facing west) through the West Ansil deposit showing the position of the Upper, Middle and Lower lenses. Local stratigraphic units including the Rusty Ridge basalt and andesite, Amulet dacite, as well as diorite sills and subvertical dikes are shown. Logged and sampled drill holes are indicated as orange lines (modified after Xstrata Copper Canada Ltd, 2005).

CHAPTER 2. WEST ANSIL OREBODY AND MINERALIZATION

The Upper lens of the West Ansil deposit is an ovoid body located at a vertical depth of approximately 160 m from surface with a dip extent of roughly 60 m, a maximum thickness of 30 m and a width of 25 m (Figures 1.6 and 2.1). The dominant sulphide is massive pyrrhotite with minor disseminated chalcopyrite and local chalcopyrite veins. Discontinuous zones of massive magnetite up to 1 m thick are present throughout the Upper lens but are more abundant at the top where the thickest intersection of magnetite occurs (6 m; Figure 2.2). A narrow stringer zone extends below the Upper lens has a dip extent of ~ 80 m, a width of 5 to 10 m and a length of 25 m. The stringer mineralization consists of chalcopyrite veins and veinlets with minor magnetite in a strongly chloritized black andesite breccia.

The Middle lens represents the bulk of the West Ansil orebody and is located at a vertical depth of 285 m from surface with a dip extent of 160 m, a width of ~50 m and a thickness of 45 m at its center and 5 to 8 m at its outer edge (Figure 1.6 and 2.1). The lens consists mainly of massive pyrrhotite with minor disseminated chalcopyrite that surrounds a chalcopyrite-rich core. Semi-massive sphalerite also occurs within massive pyrrhotite in the upper western part of the lens (Figure 2.2). Minor massive magnetite is restricted to the lower part. A conspicuous feature of the massive sulphides of the Middle lens is the presence of abundant, partially replaced siliceous and chloritic wallrock fragments. These are interpreted to represent relict clasts of basalt or andesite, possibly along flow contacts, that were infiltrated by the massive sulphides (see massive pyrrhotite-chalcopyrite ore below). Minor network-like stringer mineralization occurs along the lower contact of the massive sulphides, but any obvious pipe-like stockwork zone appears to have been cut out by the diorite sill or was never developed (Figure 1.6 and 2.2). The Middle lens also lacks conspicuous footwall or hanging-wall alteration along most of its

lower and upper contacts. A fault parallel to the lower contact and diorite sill may have removed the immediately adjacent footwall from below the main massive sulphide lens. This fault also appears to offset the Lower lens and stockwork zone from the Middle lens, suggesting that these may have been part of a single lens and stockwork zone, rather than stacked lenses. The structure separating the Middle and Lower lenses may be a reactivated synvolcanic fault.

Two small satellite bodies occur directly below the main diorite sill above the Lower lens. These bodies are subhorizontal and relatively small, with a combined thickness of only 10 m and a width of approximately 25 m. The larger lens is about 20 m thick and 25 m wide and is located at a vertical depth of 485 m below surface. It is relatively flat with a shallow plunge towards the west (Figure 1.6 and 2.1). Massive chalcopyrite mineralization is dominant towards the bottom of this lens and grades into more pyrrhotite-rich massive sulphide with disseminated chalcopyrite at the top.

The Lower stockwork zone is located directly below the Lower massive sulphide lens and has an approximate thickness of 20 m and a width of 25 m (Figure 1.6 and 2.1). The stockwork consists of centimetre-scale chalcopyrite veins as well as network-like veinlets within strongly chloritized and silicified fragmental rocks, including hyaloclastite (Figure 2.2). Sphalerite stringers occur towards the top of the stockwork zone and are cut by the chalcopyrite veins and veinlets.

Conspicuous bands of colloform pyrite-marcasite nodules up to 30 cm thick are present along the upper and lower contacts of the Upper, Middle and Lower lenses (Figure 2.2). These are late-stage, post-metamorphic features and are discussed further at the end of this chapter.

2.1 METAL ZONATION

Ore assays from 1-metre-long core splits were used to construct metal zonation profiles of the Upper, Middle and Lower lenses. Copper, Zn, Au, Ag and Pb concentrations in 16 drill holes from all three lenses were plotted on composite sections in Figure 2.3 and interelement plots of Cu, Zn, Au and Ag are shown in Figure 2.4. Individual metal zonation profiles for each drill hole are in Appendix I to XVI. Metal contents in the West Ansil deposit do not show a consistent stratigraphic zonation of a Cu-rich base to a Zn-rich top, except in the upper part of the Middle Lens. The Upper lens has an ambiguous zonation apparently caused by the late-stage emplacement of massive magnetite (see below). The Lower lens contains a Cu-rich base and is missing a Zn-rich top which further supports the interpretation that it represents a faulted lower portion of the Main lens.

The Upper lens has a Cu-rich core (3-6 wt.% Cu), with up to 8 wt.% Cu in the stockwork zone. High Au (up to 8 ppm) and Ag (up to 15 ppm) also occur in the Cu-rich core, consistent with a strong positive correlation between Cu, Au and, to a lesser extent, Ag throughout the deposit (Figure 2.3 and 2.4). Higher concentrations of Ag (up to 20 ppm) were also found in the Cu-rich stockwork zone. Zn (<0.2 wt.%) and Pb (<0.01 wt.%) grades are very low throughout the Upper lens; however, Zn values up to 1 wt.% are present in the stockwork zone. Neither Au nor Ag show any correlation with Zn. The massive magnetite zone is barren (Figure 2.3 and 2.4).

The Middle lens has a distinctive Zn-rich top (up to 15 wt.% Zn) and Cu-rich core (12-20 wt.% Cu) and a moderately Cu-rich base and stockwork zone (8-12 wt.% Cu). Minor Zn (3-6 wt.% Zn) is also present in the network-like veins at the base of the lens. However, the bulk of

the lens contains less than 2 wt.% Zn. High Au (up to 10 ppm) and Ag (60-150 ppm) are also found in the Cu-rich core and base of the Middle lens, supporting the overall Cu-Au-Ag correlation of the deposit (Figure 2.3 and 2.4). High Pb (~1 wt.%) occurs at the bottom of the lens and can be explained by remobilized quartz-siderite-sphalerite-galena veins; however, most of the lens contains less than 0.2 wt.% Pb. Au, Ag and Pb are poorly correlated with Zn, as in the Upper lens, and the massive magnetite in the Middle lens is barren (Figure 2.3 and 2.4).

The Lower lens and stockwork zone are notably Cu-rich, with up to 12 wt.% Cu in the satellite bodies, 20 wt.% Cu in the core and 12 wt.% Cu in the stringer zone. Au (2-4 ppm) and Ag (15-50 ppm) correlate with the high concentrations of Cu (Figure 2.3 and 2.4). Zn grades (<1 wt.%) are very low throughout the Lower lens, consistent with this being the high-temperature feeder zone of the hydrothermal system. Minor Au, Ag, Pb and Cu in the satellite bodies can be explained by locally remobilized precious metal-bearing galena and chalcopyrite (Figure 2.3).

Although the overall gold content of West Ansil is 1.4 g/t, significantly higher grades are found in Cu-rich parts of the Middle lens. The association with high Cu grades is similar to that observed in other deposits of the Central Camp such as Ansil, Corbet and Millenbach (Knuckey et al., 1982; Barrett et al., 1991; Barrett et al., 1993a).

2.2 PRINCIPAL ORE TYPES

Four main ore types are present in the West Ansil deposit: massive sphalerite-pyrrhotite, massive pyrrhotite-chalcopyrite, massive chalcopyrite-pyrrhotite and chalcopyrite stringer mineralization (Table 2.1). Features of the different ore types are shown in Figures 2.5 to 2.10, and the ore mineralogy is summarized in Table 2.2. The locations of samples collected for this study are given in Figure 2.11 and locations of samples in individual drill holes are in Appendix

XVII to XIX. Detailed descriptions of the mineralogy, mineral chemistry, and trace element geochemistry of the ores are given in the following sections.

Massive sphalerite-pyrrhotite ore

Sphalerite-rich ores are most common in the upper western part of the Middle lens in association with massive pyrrhotite. The sphalerite occurs as millimetre- to centimetre-scale discontinuous to folded bands with over 50 vol% pyrrhotite. Chalcopyrite is also present within the sphalerite bands, replacing both pyrrhotite and sphalerite (Figure 2.5A and Figure 2.7A and B). Contacts between sphalerite and pyrrhotite bands appear gradational, whereas contacts between chalcopyrite and pyrrhotite are sharp. Minor galena, pyrite and cassiterite, and rare cobaltite are disseminated locally in the massive sphalerite-pyrrhotite ore. Sphalerite is also present with pyrrhotite as the matrix between partially replaced siliceous and chloritic wallrock fragments in semi-massive sulphide zones. Chalcopyrite locally replaces the sphalerite-pyrrhotite- rich matrix along the contacts of the siliceous fragments (Figure 2.7C).

Sphalerite stringer mineralization

A network of millimetre- to centimetre-scale sphalerite stringers occurs mostly at the margins of the Lower stockwork zone (below the Lower lens) and locally in the immediate footwall of the Middle lens where it is not cut by diorite (Figure 2.5B). Individual veins of sphalerite are up to several centimetres wide within strongly chloritized hyaloclastite and basalt or andesite breccia. Minor pyrrhotite is also present in the sphalerite stringers and appears to have replaced sphalerite (Figure 2.7D). In the Lower stockwork zone, sphalerite stringers occur outside the chalcopyrite-rich core of the stockwork mineralization but are cut by chalcopyrite-pyrrhotite veinlets.

Massive pyrrhotite-chalcopyrite ore

Massive pyrrhotite-chalcopyrite ore is the most common ore type in all three sulphide lenses. The massive ore contains up to 90 vol% fine-grained pyrrhotite with 1-5 vol% fine-grained disseminated chalcopyrite (Figure 2.5C). Chalcopyrite also occurs as wispy, planar to folded discontinuous bands in pyrrhotite up to several centimetres wide (Figure 2.8A). Contacts between alternating bands of chalcopyrite and pyrrhotite are sharp and smooth to serrate. Massive chalcopyrite is locally concentrated at the upper and lower contacts of the massive sulphide lenses separating the massive pyrrhotite ore from the strongly chloritized basalt and andesite. Minor fine-grained disseminated sphalerite and pyrite are intergrown with pyrrhotite and trace amounts of very fine-grained laitakarite, Co-pentlandite, cobaltite and cassiterite are disseminated locally within the pyrrhotite and chalcopyrite. Annealing of the pyrrhotite and chalcopyrite grains is common and most likely reflects metamorphic or thermal recrystallization.

Rounded millimetre-scale siliceous grains are abundant within the pyrrhotite-rich bands and are interpreted to be relicts of unreplaced siliceous and chloritized wallrock fragments of basalt-andesite breccias and hyaloclastite (Figure 2.6A and B). These "pseudobreccia" zones are present throughout pyrrhotite-chalcopyrite ore and along the footwall and hanging-wall contacts of the sulphide lenses. They consist of angular fragments or clasts of chloritic or siliceous material (partially replaced wall rock) in a matrix of pyrrhotite and chalcopyrite (Figure 2.5D and E, Figure 2.6C, D and E, and Figure 2.8B and C). The less well-defined siliceous clasts, with intense pyrrhotite replacement, locally grade into more angular centimetre-scale chloritized fragments in a fine-grained pyrrhotite $\pm$ chalcopyrite matrix (Figure 2.6C and Figure 2.8B and C). These fragments commonly have alteration rims with projections of pyrrhotite or chalcopyrite into the fragments.

Centimetre-scale colloform pyrite-marcasite nodules also selectively replace the pyrrhotite along upper and lower contacts of the lenses and where late fractures penetrate the massive pyrrhotite (Figure 2.8D, E and F).

Massive chalcopyrite-pyrrhotite ore

Massive chalcopyrite ore occurs in the central part of the Middle lens and dominates the Lower lens. The massive ore contains up to 70 vol% fine-grained anhedral chalcopyrite with 20 vol% disseminated pyrrhotite (Figure 2.5F and Figure 2.9A). Banded ores consist of centimetre-scale continuous to discontinuous bands of chalcopyrite alternating with millimetre-scale bands of pyrrhotite (Figure 2.9B). Locally, chalcopyrite, pyrrhotite and sphalerite are intergrown, with ~50 vol% chalcopyrite, 30 vol% pyrrhotite and 20 vol% sphalerite in some parts of the Middle lens. Widespread pyrrhotite inclusions in the chalcopyrite suggest that the chalcopyrite may have replaced earlier massive pyrrhotite. Partially unreplaced silicified and chloritized remnants of basalt are locally preserved in the massive chalcopyrite as in the pyrrhotite-rich ore (Figures 2.5G and 2.6F). Minor amounts of pyrite and magnetite are also disseminated locally within the massive chalcopyrite-pyrrhotite ore, with trace amounts of very fine-grained laitakarite, Co-pentlandite, cobaltite and cassiterite.

Chalcopyrite stringer mineralization

The chalcopyrite stringer mineralization below the Upper and Lower lenses occurs in two distinct styles: network-like stringers and massive chalcopyrite with minor pyrrhotite veins within strongly chloritized andesite breccias and hyaloclastite. The fine, network-like stringers occupy an extensive zone of microfractures within the chloritic basalt and andesite beneath each of the sulphide lenses, beneath the main stockwork zone of the Lower lens, and also extending a

few metres above the Middle and Lower sulphide lenses (Figure 2.2 and Figure 2.5H). Minor chalcopyrite stringers are also present directly below the Middle sulphide lens but a stockwork zone appears to be missing at this location (Figure 2.2 and Figure 2.5I). Large chalcopyrite veins predominate in the center of the Upper and Lower stockwork zones, where individual veins can be up to 20 centimetres wide, often with cores or rims of pyrrhotite (Figure 2.9C). The more pyrrhotite-rich stringers typically occur in the Upper stockwork zone (below the Upper lens). Both fine network-like stringers and larger veins contain chlorite and quartz which increase in abundance laterally and horizontally away from the core of the main chalcopyrite stockwork zones (Figure 2.9D). Sphalerite is present in minor amounts in the stockwork, intergrown with pyrrhotite and chalcopyrite, as well as trace amounts of laitakarite, Co-pentlandite and cobaltite.

Massive magnetite

Massive magnetite occurs at the top of the Upper lens and as 5 metre-thick pods through the Upper lens and near the bottom of the Middle lens. In the main lenses, the massive magnetite is fine-grained and occurs in centimetre- to metre-scale bands of 60 to 90 vol% magnetite alternating and intergrown with pyrrhotite (Figure 2.5J and Figure 2.10A). Locally, siliceous and chloritic fragments occur in a matrix of magnetite (Figure 2.10B). Quartz, chlorite and actinolite are the dominant gangue minerals intergrown in the massive magnetite zones. Chalcopyrite is abundant as disseminated grains in massive magnetite and especially as millimetre-scale veinlets; the latter appear to have been structurally remobilized into brittle fractures in the massive magnetite and along magnetite-pyrrhotite contacts (Figure 2.5K, Figure 2.6G and Figure 2.10C). Colloform pyrite and marcasite are also commonly present replacing pyrrhotite along the contacts of the massive magnetite (Figures 2.6H and 2.10D).

At the top of the Upper lens the massive magnetite is characterized by re-entrant cusps and centimetre-scale projections of magnetite into the strongly chloritized hanging-wall basalt progressing into disseminated magnetite that extends 15 cm into the basalt above the massive magnetite contact (Figure 2.2). Quartz-chlorite veins and veinlets also extend into the hanging wall and appear to be closely associated with magnetite (Figure 2.5L and M and Figure 2.10E).

2.3 SULPHIDE MINERALOGY AND MINERAL CHEMISTRY

Pyrrhotite, chalcopyrite, sphalerite and magnetite are the principal ore minerals in all three lenses, with trace pyrite, gold, Bi-Pb selenides, cobaltite, Co-pentlandite, galena and cassiterite. Textural relationships among these phases are illustrated in Figures 2.12 to 2.25 and described below. Electron microprobe analyses of selected sulphides and magnetite were carried out on 6 polished specimens and the results are listed in Table 2.3, 2.4 and 2.5. Quantitative analyses were carried out by wavelength dispersive x-ray analysis (WDX) using an automated 4 spectrometer Cameca Camebax MBX electron microprobe in the Earth Sciences Department at Carleton University, Ottawa. The ore minerals were analyzed using 20 kv accelerating voltage, 30 nA beam current with a focused 2 μm diameter beam, and counting times of 10-20 seconds or 40,000 accumulated counts.

Sphalerite

Sphalerite in the massive sphalerite ore is fine- (<100 μm) to medium-grained (<1 mm) and occurs as anhedral masses intergrown with coarse-grained (1-2 mm) granoblastic and annealed pyrrhotite masses (Figure 2.12A). Locally, micrometre-scale sphalerite and pyrrhotite bands alternate with smooth and discontinuous contacts (Figure 2.12B and C). Elsewhere the sphalerite is intergrown with quartz or partly replaces microcsrystalline quartz masses (Figure

2.12D and E). Typical chalcopyrite disease occurs throughout the sphalerite (Figure 2.12F; Barton and Bethke, 1987; Kojima, 1992).

Sphalerite stringers in the Middle lens consist of medium- to coarse-grained anhedral sphalerite with pyrrhotite which appear to have been codeposited in the veins. Sphalerite commonly infills spaces between pyrrhotite grains (Figure 2.13A and B). In the Lower lens, sphalerite stringers contain chalcopyrite with minor pyrrhotite as inclusions (Figure 2.13C). Sphalerite is also locally present in remobilized fracture-controlled veins in chloritic wallrock at the upper and lower contacts of the Middle lens (Figure 2.13D).

Fe contents in sphalerite have a narrow range from 11 mole % FeS in minor sphalerite from the Upper lens to 12.5 % FeS in the Lower lens due to the limited number of analyses (Table 2.3). This narrow range of sphalerite compositions is similar to other Archean Cu-Zn deposits (10-13 mole % FeS: Hannington and Scott, 1989), including other deposits from the Noranda camp such as Ansil and Corbet (Figure 2.14). The high Fe contents and narrow range of sphalerite compositions most likely reflects equilibration with the abundant pyrrhotite > pyrite in the ores. Pyritic deposits higher in the Mine Sequence stratigraphy typically have lower Fe contents in sphalerite, reflecting buffering at a higher fS_2. Hannington and Scott (1989) noted that this relationship also correlated with the gold grades (Figure 2.15). Cadmium contents in sphalerite range from 0.1 to 0.5 wt%. Small amounts of In also occurs in sphalerite at concentrations up to 0.27 wt% (Table 2.3).

Pyrrhotite

Massive and semi-massive pyrrhotite in all three lenses is composed of annealed masses of medium- (0.25-0.5 mm) to coarse-grained (1-2 mm) equigranular pyrrhotite with fine-grained

(<100 μm) chalcopyrite and minor sphalerite infilling between pyrrhotite grains (Figure 2.16A and B). Micrometre-scale pyrrhotite bands with smooth discontinuous contacts alternate with chalcopyrite in the massive ore (Figure 2.16C). Locally, pyrrhotite appears to have replaced minor primary pyrite in massive pyrrhotite ores (Figure 2.16D). The pyrrhotite contains abundant small inclusions of quartz and chlorite-actinolite-rich wallrock fragments (Figure 2.16E and F).

The pyrrhotite usually contains traces of Co (0.1-0.3 wt%), Se (< 0.1%) and Bi (0.1-0.2 wt%), particularly where it is associated with Bi-Pb selenides, Co-pentlandite and cobaltite, and possibly trace amounts of Ni (<0.1 wt%) (Table 2.4).

Chalcopyrite

Chalcopyrite ranges from medium to coarse-grained, anhedral aggregates replacing and infilling grain boundaries of pyrrhotite and, to a lesser extent, sphalerite (Figure 2.17A, B and C). It is also widely disseminated in massive pyrrhotite and sphalerite ore (Figures 2.12E, 2.13B and 2.16A). In semi-massive chalcopyrite ore the chalcopyrite contains abundant rounded siliceous and angular chloritic wallrock fragments (Figure 2.17D and E). Structurally remobilized chalcopyrite commonly penetrates fractures in brittle magnetite aggregates (Figure 2.17F).

Chalcopyrite in stringers is texturally similar to chalcopyrite in the massive ores, reflecting recrystallization and annealing to anhedral grains. Veins and veinlets of chalcopyrite typically contain microcrystalline quartz and/or late siderite (Figure 2.18A and B). Network-like veinlets of chalcopyrite commonly contain chlorite and actinolite (Figure 2.18C and D). Locally, minor sphalerite is present as inclusions in chalcopyrite within veins (Figure 2.18E and F).

Chalcopyrite contains low concentrations of most trace elements, although Se is notably enriched (~0.1 wt%: Table 2.4). It has low As, Co and Bi despite the presence of trace mineral inclusions containing these elements.

Magnetite

In the Upper and Middle lenses the massive magnetite consists of subhedral and euhedral fine- (<100 μm) to medium-grained (<1 mm) aggregates intergrown with fine-grained annealed masses of pyrrhotite along grain boundaries and at triple junctions (Figure 2.19A). It also occurs with microcrystalline quartz and fine-grained actinolite and stilpnomelane needles (Figure 2.19B). Where present, chalcopyrite has been remobilized into brittle fractures in the magnetite (Figure 2.19C).

Magnetite grains are zoned with submicroscopic quartz inclusions as determined during backscattered electron imaging (Figure 2.19D). Zonation is visible as various shades of grey in euhedral and subhedral magnetite grains. The core of the magnetite is mostly irregular in shape. The lightest grey colour in SEM backscattered electron images represents extremely pure magnetite and the darkest grey colour represents the most silica-rich and iron-poor zone in each grain (Figure 2.19D), the darkest grey zone has 1.30 ions Si^{+4} (4.3 wt% SiO_2: Table 2.5). A lighter grey zone has 0.18 Si^{+4} (0.6 wt% SiO_2), extremely pure magnetite has no Si^{+4}, and 23.96 total Fe^{+2} and Fe^{+3} (98.8 wt% FeO: Table 2.5). Locations of analyses are shown in Figure 2.19D. The composition of the magnetite is essentially the same as that previously documented in the Ansil deposit (Westendorp et al., 1991). Westendorp et al. (1991) interpreted the zoning to be due to Si^{+4} replacement of tetrahedral Fe^{+3} in the magnetite lattice. The original magnetite grains are thought to have been altered by a later, siliceous solution leaving an irregularly-shaped

core surrounded by anomalously and variably silica-rich magnetite rims. Continued magnetite crystallization resulted in the precipitation of pure magnetite on the previously altered grain.

Fracture-controlled magnetite is also present along the upper contacts of all three lenses within chlorite-rich wallrock (Figure 2.5L and M and Figure 2.10A). The fine-grained euhedral magnetite forms network-like veinlets, which are rimmed by quartz and fine-grained chlorite (Figure 2.19E). In the Lower lens, late magnetite-siderite-quartz veins cut the top sulphide contact, separating the chloritic wallrock from massive pyrrhotite (Figure 2.19F).

Pyrite

Minor primary pyrite is present within massive pyrrhotite and chalcopyrite in all three lenses and is clearly distinguished from the later pyrite-marcasite nodules (see below). It occurs as fine- to medium-grained subhedral to euhedral crystals as inclusions in pyrrhotite and anhedral chalcopyrite, and it also contains sphalerite inclusions (Figure 2.20A). Larger coarse-grained euhedral pyrite porphyroblasts are also present in sphalerite stringers in chloritic wallrock (Figure 2.20B). At the top of the Middle and Lower lenses, coarse pyrite porphyroblasts appear to have overgrown magnetite (Figure 2.20C).

Galena

Remobilized galena occurs with sphalerite as veins at the top and bottom of the Middle lens, commonly with late siderite (Figure 2.21A and B). These veins cut the sulphide contact and chlorite-rich wallrock and are connected to a larger set of siderite-quartz veins a few centimetres above the contact. In the Lower lens, minor remobilized galena and sphalerite veinlets also occur with siderite and cut the massive pyrrhotite.

Cassiterite

Cassiterite [SnO_2] is present in massive sphalerite as fine (10-20 μm) rounded or subhedral grains intergrown with sphalerite (Figure 2.22A and B). It is less common in sphalerite stringers, massive pyrrhotite or massive chalcopyrite ore, although locally, fine-grained subhedral cassiterite is present in chalcopyrite in massive chalcopyrite ore from the Lower lens (Figure 2.22C).

Bi minerals

A Bi-Pb-Se mineral, laitakarite [$(Bi, Pb)_4(Se, S)_3$], is a common trace mineral in massive pyrrhotite-chalcopyrite, massive chalcopyrite-pyrrhotite and chalcopyrite stringer ores (Figure 2.23A to E). It occurs as fine subhedral to bladed grains intergrown with and disseminated in pyrrhotite and chalcopyrite, commonly with Co-pentlandite and cobaltite. Laitakarite is locally rimmed by clausthalite [PbSe] and bismuth telluride [Bi_2Te_3] and contains native Bi inclusions (Figure 2.23F). Rare bismuthinite [Bi_2S_3] is also present as inclusions in laitakarite and chalcopyrite. The clausthalite rims may account for the Pb in some analyses of laitakarite (Table 2.4). Bismuth telluride rims also may account for the minor Te (up to 8 wt%) in some analyses (Table 2.4). The close association of the Bi and Se minerals with massive chalcopyrite and chalcopyrite stringer mineralization implies that Bi was an important constituent of the highest temperature hydrothermal assemblage.

Co-pentlandite

Small amounts of Co-pentlandite [$(Co, Fe, Ni)_9S_8$] are present as 10-20 μm rounded grains intergrown with and disseminated in pyrrhotite and chalcopyrite, in the massive pyrrhotite-chalcopyrite ore, in massive chalcopyrite-pyrrhotite ore and in chalcopyrite stringer

ores of the Middle and Lower lenses (Figure 2.24A to C). Co-pentlandite and cobaltite typically occur together. Co-pentlandite is the Co analogue of pentlandite, in this case containing only 0.8 wt% Ni (Table 2.4); similar to Co-pentlandite reported from the Vauze mine (Stumpfl and Clark, 1964).

Cobaltite

Trace amounts of cobaltite [(Co,Fe)AsS] typically occur as small (10-20 μm) rounded and euhedral grains intergrown with and disseminated in pyrrhotite and chalcopyrite, in the massive pyrrhotite-chalcopyrite, in massive chalcopyrite-pyrrhotite and in chalcopyrite stringer ores from the Middle and Lower lenses (2.24D to F). Cobaltite contains a minor amount of Se (0.7 wt%) substituting for sulfur (Table 2.4).

Gold

Minor amounts of microscopic gold are present mainly within chalcopyrite in the Middle lens. Very fine rounded gold and anhedral laitakarite grains are disseminated within remobilized chalcopyrite-chlorite veinlets in massive pyrrhotite (Figure 2.25A and B) and in brittle fractures in magnetite where they are infilled by remobilized chalcopyrite (Figure 2.25C). Locally, grains up to 0.5 millimetres in size are present along the contacts (Figure 2.25D).

Silver contents of the gold range between 20 and 23 wt%, and therefore electrum appears to be the dominant gold phase present in the deposit (Table 2.4). The range of gold fineness at West Ansil is 767 to 801, which falls within the range of values in deposits with a strong Cu-Au association, consistent with the most of the gold being introduced with the Cu-rich ore. Westendorp (1992) and Galley (1994) also found that native gold and electrum at Ansil is

strongly associated with Cu-rich ores, although Westendorp (1992) mentions electrum compositions of 50 wt% Au and 50 wt% Ag at Ansil.

2.4 ORE-RELATED GANGUE MINERALS

Quartz

In semi-massive pyrrhotite, chalcopyrite and magnetite, microcrystalline to coarse quartz occurs as minor gangue (Figure 2.26). At the top of the Upper lens, quartz-chlorite-magnetite veins extend above the sulphide contact (Figure 2.5L and M and Figure 2.10A). Microcrystalline quartz is also present with actinolite and stilpnomelane (Figure 2.19F).

Actinolite and stilpnomelane

Fine-to coarse-grained radial aggregates of actinolite and stilpnomelane needles are abundant in the chalcopyrite and chlorite stringers, mostly within chalcopyrite grains and along their boundaries. This texture most likely reflects the growth of silicates while the chalcopyrite was being annealed (Figure 2.26A). Actinolite and stilpnomelane are also present within microcrystalline quartz in massive magnetite (Figure 2.26B). Actinolite is more abundant in the Lower lens and stilpnomelane is more abundant in the Upper lens, associated with magnetite. Both Galley (1994) and Westendorp (1992) also note that actinolite and stilpnomelane are closely associated with magnetite in the Ansil deposit.

Siderite

Minor siderite is present within the altered wallrock, as well as in the stringers and especially late remobilized veins. Disseminated aggregates of very fine- to coarse-grained, anhedral to euhedral siderite occur within the chloritized wallrock as an apparent late overprint. In the Middle lens, siderite is present in remobilized sphalerite and galena veinlets. It also occurs

as coarse euhedral grains with a bladed texture together with remobilized chalcopyrite overgrowing chlorite at the top and bottom of the Middle lens (Figure 2.26C and D). In the Lower lens, siderite is very coarse; subhedral to euhedral grains with a bladed texture occur in veins, surrounding quartz, magnetite, actinolite and stilpnomelane (Figure 2.26E). In the Lower stringer zone, subhedral fine- to coarse-grained siderite is present in the quartz-chalcopyrite veinlets (Figure 2.26F). Locally, fine-grained siderite is also present in late-stage pyrite and marcasite nodules.

2.5 LATE-STAGE COLLOFORM PYRITE-MARCASITE

Distinctive bands or lenses of nodular and colloform pyrite and marcasite occur at the top and bottom contacts of all three sulphide lenses (Figure 2.2 and 2.27). These bands consist of centimetre-sized spheroidal bodies of fine-grained pyrite-marcasite intergrowths (Figure 2.5N), which locally coalesce to form 5 to 40 centimetre-thick porous layers in massive pyrrhotite (Figure 2.5O and P and Figure 2.27B, C and D). The incipient growth of the pyrite nodules appears to begin with clover-leaf shapes formed by the coalescence of small neighbouring clots of pyrite and marcasite; these acted as nuclei for growth of larger nodules (Figure 2.27B). Typically, the pyrite-marcasite growths are centered on fractures in the pyrrhotite, and colloform bands or layers develop parallel to the fractures (Figures 2.5P and 2.27C and D). Contacts between the pyrite-marcasite and massive pyrrhotite are characterized by the presence of "shrinkage cracks" indicating volume loss. Dark brown siliceous material which occupies the shrinkage cracks is hisingerite [$Fe^{+3}_2Si_2O_5(OH)_4 \bullet 2(H_2O)$], an amorphous iron silicate mineral commonly formed as a secondary product of weathering of pyrrhotite-rich ore (Sudo and Nakamura, 1952; Whelan and Goldich, 1961; Murowchick, 1992). It is dark red-brown in colour and occurs locally as centimetre-scale rims around the pyrite-marcasite nodules and also appears

cracked and dessicated. It locally contains inclusions and islands of pyrrhotite, chalcopyrite and sphalerite (Figure 2.28A) and minor fine-grained chlorite, microcrystalline quartz and fine-grained siderite in fractures (Figure 2.28B and C).

The growth of the nodules in the massive pyrrhotite appears to post-dates metamorphism, as the nodules do not show any recrystallized or annealed textures typical of the other sulphides and abundant open spaces between nodules remain empty or have been filled with remobilized sulphides (e.g., Figure 2.27F; galena, sphalerite). Locally, the pyrite and marcasite nodules are replacing pyrrhotite-rich matrix in strongly silicified basalt and andesite breccias where siderite is present within the porous nodules (Figure 2.6I). Recrystallized marcasite is present within late fractures in some colloform bands, possibly indicating late-stage fluid circulation after the growth of the nodules (Figure 2.28E and F).

Internally, the nodules consist of very fine to medium subhedral to euhedral grains (Figure 2.28D, E and F). They range from a few millimetres to centimeters in size. The nodules commonly have a turbid pyrite-rich center (Figure 2.28E) and marcasite rim with many micrometre-scale concentric shrinkage fractures that become gradually less abundant towards the edges. Locally, sphalerite and minor chalcopyrite are present within these fractures (Figure 2.28E). Where the nodules coalesce into bands, the pyrite and marcasite are much less turbid and appear to have been recrystallized (Figure 2.28G). Locally, recrystallized marcasite is present in millimeter-scale fractures that crosscut the nodules (Figure 2.28H and I).

Traces of Co (0.2 wt%), Bi (0.15 wt%) and Se (0.1 wt%) occur in pyrite and marcasite, particularly where laitakarite, Co-pentlandite and cobaltite were present in the original pyrrhotite (Table 2.4).

2.6 TRACE ELEMENT GEOCHEMISTRY OF THE ORES

Table 2.6 lists average chemical analyses of the principal ore types. Data and analytical methods for all 76 ore samples are given in Appendix XX and XXI.

Massive sphalerite-pyrrhotite ore

Massive sphalerite-pyrrhotite ore from the Middle lens contains 100 to 500 ppm Cd, 200 to 300 ppm Sn, 400 to 700 ppm Co, 10 to 50 ppm As and less than 10 ppm Pb (Table 2.6 and Appendix XX). Concentrations of Sn and Cd are typical of Zn-rich ores in other Archean Cu-Zn deposits, but Pb concentrations are unusually low (e.g. Hannington et al, 1999). Cobalt and As concentrations are low compared to the massive pyrrhotite-chalcopyrite and massive chalcopyrite-pyrrhotite ores.

Sphalerite stringer mineralization

Metal concentrations in sphalerite stringers from both the Middle and Lower stockwork zones are very similar. Cadmium ranges from 400 to 700 ppm, Co from 300 to 800 ppm and Hg up to 400 ppb (Table 2.6 and Appendix XX). Sphalerite stringer mineralization contains the highest amount of Hg in the West Ansil deposit. Concentrations of Sn are less than 30 ppm, Pb less than 10 ppm, and Se less than 20 ppm.

Massive pyrrhotite-chalcopyrite ore

Massive pyrrhotite-chalcopyrite ore has relatively low trace metal contents. Selenium concentrations are consistently between 100 and 200 ppm, but Bi is below detection limit (Table 2.6 and Appendix XX). Massive pyrrhotite-chalcopyrite from the Middle and Lower lenses contains high Co, ranging between 1000 to 2000 ppm, and high Se between 100 to 200 ppm. Bismuth concentrations range between 20 and 40 ppm, but some samples contain up to 100 ppm,

reflecting the presence of laitakarite in massive pyrrhotite-chalcopyrite ore (Table 2.6 and Appendix XX). Where remobilized chalcopyrite veinlets occur in the massive pyrrhotite, Au concentrations are up to 27000 ppb; however, background Au in the Middle and Lower lenses ranges from 100 to 500 ppb, and massive pyrrhotite-chalcopyrite ore in the Upper lens contains less than 30 ppb Au. Indium and Pb concentrations are also low in the Middle and Lower lenses.

Massive chalcopyrite-pyrrhotite ore

Trace element concentrations in massive chalcopyrite-pyrrhotite ore in the Middle and Lower lenses are very similar, except for Co. Cobalt contents range from 500 to 1000 ppm in the Middle lens but reach 2000 ppm in the Lower lens, reflecting the abundance of Co-pentlandite. Selenium concentrations are between 500 to 1000 ppm, and Bi concentrations are between 10 to 40 ppm. Locally, Bi reaches 3000 ppm in both lenses reflecting the abundant laitakarite. Massive chalcopyrite-pyrrhotite ore contains the highest amount of As, typically from 10 to 30 ppm, with maximum concentrations up to 200 ppm reflecting the abundance of cobaltite (Table 2.6 and Appendix XX). Indium contents are also high, ranging from 20 to 80 ppm. Gold concentrations are between 300 and 500 ppb. Similar to the other ore types, massive chalcopyrite-pyrrhotite contains less than 10 ppm Pb.

Chalcopyrite stringer mineralization

Chalcopyrite stringers from the Upper and Lower lenses have similar trace metal concentrations: 300 to 800 ppm Co, 300 to 700 ppm Se, 10 to 40 ppm Bi and 10 to 40 ppm In. Concentrations of As are less than 10 ppm and Au less than 100 ppb (Table 2.6 and Appendix XX). In the Upper lens, Ni contents are up to 150 ppm and may reflect the presence of trace amounts of Co-pentlandite. Somewhat lower metal contents in the chalcopyrite stringer

mineralization than in other ores can be explained by the greater abundance of gangue minerals in the samples analyzed.

Massive magnetite

Massive magnetite is almost barren of trace metals, containing very low concentrations of most elements. Cobalt concentrations are less than 400 ppm, Se less than 100 ppm, Bi less than 10 ppm and In less than 5 ppm (Table 2.6 and Appendix XX). Where concentrations of these elements are higher, it reflects the abundance of sulphide inclusions in magnetite or remobilized sulphides in late brittle fractures in magnetite.

Late-stage colloform pyrite-marcasite

Colloform pyrite and marcasite in the Middle and Lower lenses contain between 700 to 2000 ppm Co, 100 to 500 ppm Se, 10 to 20 ppm Bi and less than 10 ppm In. The nodules only contain those elements that are typically found in pyrite (e.g, Co, Ni, Se) or those elements that were introduced after formation of the nodules (e.g., Pb, Tl). Molybdenum contents are locally high in colloform pyrite and marcasite from the Upper lens, reaching up to 180 ppm, which reflects the presence of trace molybdenite in a few samples. The high Pb, Tl and Mo are notably different than in the other sulphides and likely reflect the chemistry of late fluids that formed the nodules.

Low-temperature versus high-temperature suites

Trace elements in the West Ansil ores can be grouped into two main suites: Cd, Sn, $\pm$Hg, $\pm$Sb, $\pm$Ag associated with Zn-rich ores and Se, Bi, Co, In, $\pm$As and $\pm$Au associated with Cu-rich ores. The different trace elements are strongly partitioned into Zn-rich and Cu-rich parts of all three lenses, although this is most obvious in the Middle and Lower lenses. The Upper lens

shows the least enrichment in trace elements most likely because of the abundance of late magnetite. Interelement plots of selected trace elements are shown in Figure 2.29 and a correlation matrix identifying the two main groups of elements is given in Table 2.7.

Low-temperature suite (Zn, Cd, Sn, ±Pb ±Hg, ±Sb and ±Ag): The enrichment of a consistent suite of trace elements in the Zn-rich ores of the Middle lens is typical of polymetallic sulphides in other volcanic-hosted massive sulphide deposits that are interpreted to have formed at low temperatures (e.g., Tanimura et al., 1983). The positive correlation of Sn and Cd with Zn in the Zn-rich ores of the Middle lens and sphalerite stringers is similar to that observed in other Archean Cu-Zn deposits (e.g., Hannington et al., 1999: Table 2.7 and Figure 2.29). The sphalerite stringers of the Middle and Lower lenses are also enriched in Hg compared to the rest of the deposit, explaining the strong Hg and Cd correlation (Table 2.7). Since Ag concentrations in electrum cannot account for all the Ag in the deposit, the remaining Ag is interpreted to be in galena and there is a strong correlation between Ag and Pb. However, a strong correlation is also observed with As, Ni and Sb. No minerals containing these elements have been observed, and Sb concentrations are mostly below 1 ppm throughout the deposit. This suggests the presence of an unidentified trace mineral, most likely with remobilized galena. Uranium also appears to correlate with Pb, Ni and As, but most samples contain only 0.1 ppm U and others do not exceed 1 ppm (Table 2.7).

High-temperature suite (Cu, Co, Se, In, Bi, ±As and ±Au): High concentrations of Co, Se, In, Bi, As and Au in the massive chalcopyrite and chalcopyrite stringer ores are similar to those observed in the highest temperature assemblages of other volcanogenic massive sulphide deposits (Lambert and Sato, 1974; Nishiyama, 1974; Smith and Huston, 1992; Marcoux et al.,

1996; Leistel et al., 1998; Hannington et al., 1999). Selenium shows the strongest correlation with Cu, and this association suggests that Se concentrations in the ore fluids were strongly temperature dependent (Table 2.7 and Figure 2.29). Se is present as a trace element substituting for sulfur in the principal Fe and Cu sulphides; however, discrete selenide minerals (e.g., laitakarite and clausthalite) are also present in the Cu-rich ores. Notable enrichments of Bi occur in the same samples, and the Cu-rich ores contain bismuthinite as well as laitakarite. Strong correlations between Cu and In are also evident in both the Middle and Lower lenses, however a discrete In mineral was not observed (Table 2.6 and 2.7 and Figure 2.29). It was most likely introduced at high temperatures during the emplacement of the massive chalcopyrite, but may also have been introduced in sphalerite together with chalcopyrite disease (up to 40 ppm In). Co concentrations are highest (up to 2450 ppm) in the Cu-rich ores, which reflects the presence of Co-pentlandite and cobaltite in massive chalcopyrite. The cobaltite also accounts for most of the As in the deposit. Gold is present in massive chalcopyrite and in remobilized chalcopyrite veins and is moderately to strongly correlated with Cu, Se, Bi and In (Table 2.7). Values up to 27000 ppb are observed in remobilized chalcopyrite veins. The strong Cu-Au-Bi-In association observed in thin section has been widely interpreted as evidence of direct magmatic contribution of metals to the ore-forming hydrothermal fluids in other volcanogenic massive sulphide deposits (Leistel et al., 1998; Hannington et al., 1999; Dubé et al., 2007; Mercier-Langevin et al., 2007).

2.7 SULFUR ISOTOPES

The sulfur isotope compositions of sulphides were determined in 10 samples using the elemental analyzers (EA) combustion and continuous flow IRMS (Isotope Ratios Mass Spectrometry) in the G.G. Hatch Laboratory at the University of Ottawa. The data are given in Table 2.8 and Figure 2.30. Sulphide minerals were weighed into tin capsules with an equal

amount of tungstic oxide. Calibrated internal standards are prepared with every batch of samples for normalization of the data. The prepared capsules were loaded into the carousel of the AS128 autosampler of the EA1110. The samples were flash combusted at 1800°C with the addition of oxygen. Ultra-pure helium is used to carry the resulting SO_2, and water is cleaned out of the system by magnesium perchlorate traps. The SO_2 is separated for analysis by a GC column (EA1110). The SO_2 gas was analyzed in the Thermo Finnigan DeltaPlus IRMS with an analytical precision of $\pm$0.2 per mil.

The West Ansil sulphides have $\delta^{34}S$ values ranging from 0.9 to 2.6 per mil, similar to those of the Ansil deposit (Barrett et al., 1991) and other Archean volcanogenic massive sulphides (e.g. Franklin et al., 1981). The analyzed sphalerite has a slightly higher $\delta^{34}S$ value than chalcopyrite and pyrrhotite, which are indistinguishable (Table 2.8 and Figure 2.30). However, no significant differences could be determined between the ore types or stratigraphically within individual ore lenses (e.g., Zn-rich ores vs. Cu-rich ores, including the Lower lens) further supporting the interpretation that the deposit formed as a single ore lens.

Because the pyrite-marcasite nodules appear to be a late, post-metamorphic overprint, a number of samples were analyzed to determine if they originated from a separate source of sulfur. However, it appears that the nodules grew from sulfur derived from the original pyrrhotite.

Table 2.1 Characteristics of Principal Ore Types of the West Ansil Deposit

Ore Type	Description
Massive sphalerite-pyrrhotite	Massive banded sphalerite with 50 vol% pyrrhotite and minor disseminated chalcopyrite; also sphalerite-pyrrhotite-rich matrix in pseudobreccia replacing chloritized and siliceous wallrock fragments
Sphalerite stringers	Sphalerite veins and network stringers with pyrrhotite in the Middle lens and chalcopyrite in the Lower lens within chloritized hyaloclastite and basalt-andesite breccia
Massive pyrrhotite-chalcopyrite	Massive and banded pyrrhotite with 5 vol% disseminated chalcopyrite; also pyrrhotite-rich matrix in pseudobreccia replacing chloritized and siliceous wallrock fragments
Massive chalcopyrite-pyrrhotite	Massive and banded chalcopyrite with 20 vol% disseminated pyrrhotite; also chalcopyrite-rich matrix in pseudobreccia replacing chloritized and siliceous wallrock fragments
Chalcopyrite stringers	Chalcopyrite veins and network stringers, with local pyrrhotite and sphalerite within chloritized hyaloclastite and basalt-andesite breccia
Massive magnetite	Massive magnetite bands with 60-90 vol% magnetite alternating with pyrrhotite, locally abundant disseminated chalcopyrite and chalcopyrite within brittle magnetite fractures; also magnetite matrix in pseudobreccia replacing siliceous and chlorite-actinolite-rich wallrock fragments
Colloform pyrite-marcasite	Nodular, spheroidal and colloform bands of pyrite-marcasite replacing pyrrrhotite along sulphide contacts, pyrrhotite-magnetite contacts and within microfractures of massive pyrrhotite; marcasite within fractures in pyrrhotite closely spatially associated with pyrite nodules

Table 2.2 Mineralogy of Principal Ore Types in the West Ansil Deposit

Massive sphalerite-pyrrhotite	Sphalerite stringers	Massive pyrrhotite-chalcopyrite	Massive chalcopyrite-pyrrhotite	Chalcopyrite stringers	Massive Magnetite	Colloform pyrite-marcasite
Sphalerite pyrrhotite chalcopyrite +/-pyrite +/-galena +/-cassiterite +/-cobaltite	Sphalerite pyrrhotite chalcopyrite +/-pyrite +/-galena	Pyrrhotite chalcopyrite sphalerite magnetite pyrite-marcasite +/-pyrite +/-laitakarite +/-Co-pentlandite +/-cobaltite +/-native Bi +/-clausthalite +/- bismuthinite +/- bismuth telluride +/-gold +/-galena +/-cassiterite	Chalcopyrite pyrrhotite sphalerite magnetite +/-pyrite +/-pyrite-marcasite +/-laitakarite +/-Co-pentlandite +/-cobaltite +/-native Bi +/-clausthalite +/-bismuthinite +/-bismuth telluride +/-gold +/-cassiterite	Chalcopyrite pyrrhotite sphalerite +/-pyrite +/-pyrite-marcasite +/-laitakarite +/-Co-pentlandite +/-cobaltite	Magnetite pyrrhotite chalcopyrite +/-pyrite +/-pyrite-marcasite	Pyrite marcasite pyrrhotite chalcopyrite +/-sphalerite +/-magnetite +/-galena
Associated gangue minerals:						
Chlorite quartz actinolite stilpnomelane	Chlorite quartz actinolite stilpnomelane siderite	Chlorite quartz actinolite stilpnomelane hisingerite +/-siderite	Quartz actinolite chlorite stilpnomelane +/-hisingerite	Quartz actinolite chlorite stilpnomelane siderite	Quartz actinolite chlorite stilpnomelane +/-siderite	Quartz hisingerite siderite chlorite +/-actinolite +/-stilpnomelane

Minerals are listed in approximate order of abundance (±indicates minerals present in only a few samples)

Table 2.3 Compositions of Sphalerite in the West Ansil Deposit

West Ansil																			
Sample	Lens	Mole % FeS	Cu	Zn	Fe	S	Au	Ag	Se	Bi	In	Co	Ni	Sn	As	Cd	Te	Hg	Total
WAN089	Upper	11.17	0.08	59.79	6.42	32.43	0.04	<0.01	0.04	0.12	0.07	0.07	<0.01	0.03	0.03	0.47	0.02	0.07	99.67
WAN043	Middle	11.18	0.26	59.36	6.38	32.19	0.07	<0.01	0.08	0.04	0.27	0.10	<0.01	<0.01	<0.01	0.32	0.01	<0.01	99.07
WAN092	Lower	11.77	0.17	59.10	6.74	32.58	0.01	0.05	0.11	<0.01	0.04	0.34	<0.01	<0.01	<0.01	0.21	0.04	0.06	99.44
WAN092	Lower	12.41	0.19	58.59	7.09	32.75	0.07	<0.01	0.07	0.01	0.08	0.24	0.02	<0.01	<0.01	0.08	<0.01	0.08	99.28

Samples were analyzed by a four spectrometer Cameca Camebax MBX electron microprobe by wavelength dispersive X-ray analysis in the Earth Sciences Department at Carleton University, Ottawa, Ontario

Table 2.4 Electron Microprobe Analyses (wt%) of Major Ore Minerals and Selected Trace Minerals in the West Ansil Deposit

Sample	Lens	Ore Type	Mineral		Cu	Zn	Pb	Fe	S	Au	Ag	Se	Bi	In	Co	Ni	Sn	As	Cd	Te	Hg
WAN089	Upper	Massive pyrrhotite	pyrrhotite		0.10	0.06	<0.01	60.6	39.2	<0.01	<0.01	0.01	0.20	<0.01	0.12	<0.01	<0.01	<0.01	<0.01	0.01	0.04
WAN004	Middle	Massive chalcopyrite	pyrrhotite		0.04	0.02	<0.01	60.5	39.4	<0.01	<0.01	0.02	0.07	<0.01	0.13	<0.01	0.11	<0.01	0.03	0.02	<0.01
WAN043		Massive pyrrhotite	pyrrhotite	$Fe_{(1-x)}S$	0.04	<0.01	<0.01	61.5	38.7	<0.01	<0.01	0.10	0.11	<0.01	0.16	0.03	<0.01	<0.01	<0.01	0.04	<0.01
WAN092	Lower	Massive chalcopyrite	pyrrhotite		<0.01	<0.01	<0.01	60.3	39.4	0.05	0.09	0.05	0.12	<0.01	0.27	0.01	0.03	0.02	<0.01	0.01	<0.01
WAN122		Colloform pyrite	pyrrhotite		<0.01	0.01	<0.01	60.9	39.6	<0.01	<0.01	<0.01	0.11	<0.01	0.12	0.03	<0.01	<0.01	0.01	<0.01	<0.01
Pyrrhotite Average					0.03	0.02	<0.01	60.7	39.3	0.01	0.02	0.04	0.12	<0.01	0.16	0.01	0.03	<0.01	0.01	0.02	0.01
WAN089	Upper	Massive pyrrhotite	chalcopyrite		34.3	0.01	<0.01	31.0	34.4	<0.01	<0.01	0.03	0.11	<0.01	0.01	<0.01	<0.01	<0.01	0.02	0.01	<0.01
WAN043	Middle	Massive pyrrhotite	chalcopyrite	$CuFeS_2$	34.4	0.00	<0.01	30.8	34.4	0.05	0.02	0.12	0.16	0.02	0.06	<0.01	0.03	<0.01	0.01	<0.01	0.01
WAN092	Lower	Massive chalcopyrite	chalcopyrite		34.6	0.05	<0.01	30.9	34.3	<0.01	<0.01	0.11	0.08	0.02	0.06	0.01	<0.01	<0.01	<0.01	0.01	<0.01
Chalcopyrite Average					34.4	0.02	<0.01	30.9	34.4	0.02	0.01	0.09	0.11	0.01	0.04	0.00	0.01	<0.01	0.01	0.01	<0.01
WAN089	Upper	Massive pyrrhotite	pyrite/marcasite		0.10	0.01	<0.01	47.9	52.5	<0.01	<0.01	<0.01	0.06	0.03	0.09	0.03	0.06	<0.01	<0.01	<0.01	<0.01
WAN089		Massive pyrrhotite	pyrite/marcasite		0.03	<0.01	<0.01	48.0	52.9	<0.01	0.06	<0.01	0.14	<0.01	0.17	<0.01	<0.01	<0.01	<0.01	0.02	0.05
WAN089		Massive pyrrhotite	pyrite/marcasite		0.08	<0.01	<0.01	48.2	52.4	0.05	<0.01	0.02	0.11	<0.01	0.13	<0.01	<0.01	<0.01	<0.01	<0.01	<0.01
WAN043	Middle	Massive pyrrhotite	pyrite/marcasite		0.15	<0.01	<0.01	47.3	53.2	<0.01	0.02	0.10	0.03	<0.01	0.21	<0.01	<0.01	<0.01	0.04	<0.01	<0.01
WAN043		Massive pyrrhotite	pyrite/marcasite	FeS_2	0.18	0.03	<0.01	47.8	53.1	<0.01	0.02	0.10	0.15	<0.01	0.21	0.03	<0.01	0.05	0.08	<0.01	<0.01
WAN122	Lower	Colloform pyrite	pyrite/marcasite		0.03	0.01	<0.01	48.7	53.6	<0.01	<0.01	0.03	0.10	0.01	0.04	0.06	0.01	<0.01	<0.01	<0.01	<0.01
WAN122		Colloform pyrite	pyrite/marcasite		<0.01	0.02	<0.01	48.6	53.5	<0.01	0.11	<0.01	0.07	<0.01	0.09	0.03	0.02	<0.01	<0.01	0.01	0.01
WAN122		Colloform pyrite	pyrite/marcasite		<0.01	<0.01	<0.01	47.6	54.1	0.03	<0.01	<0.01	0.05	<0.01	0.13	0.04	<0.01	<0.01	<0.01	0.01	0.03
Pyrite Average					0.07	0.01	<0.01	48.0	53.2	0.01	0.03	0.03	0.09	<0.01	0.13	0.02	0.01	0.01	0.02	<0.01	0.01
WAN004	Middle	Massive chalcopyrite	laitakarite		<0.01	0.04	1.15	<0.01	1.96	<0.01	0.04	19.0	77.3	<0.01	0.01	0.03	<0.01	<0.01	<0.01	0.19	<0.01
WAN004		Massive chalcopyrite	laitakarite		0.19	0.04	1.10	0.18	2.20	0.03	0.07	17.7	78.8	<0.01	0.05	0.03	<0.01	<0.01	<0.01	0.07	<0.01
*WAN006		Massive pyrrhotite	laitakarite		0.43	<0.01	0.14	0.32	0.63	0.04	<0.01	11.5	79.2	<0.01	0.01	<0.01	<0.01	<0.01	0.03	8.67	0.07
WAN043		Massive pyrrhotite	laitakarite	$(Bi, Pb)_4(Se,S)_3$	0.16	0.03	3.50	0.20	1.19	<0.01	<0.01	20.6	74.8	<0.01	0.02	<0.01	0.04	<0.01	<0.01	0.15	<0.01
WAN043		Massive pyrrhotite	laitakarite		0.18	<0.01	3.46	1.32	1.06	0.18	<0.01	19.9	74.8	<0.01	<0.01	0.05	<0.01	<0.01	<0.01	0.27	0.08
WAN043		Massive pyrrhotite	laitakarite		0.14	<0.01	3.70	0.65	1.23	<0.01	<0.01	20.3	74.9	<0.01	<0.01	0.03	0.01	<0.01	<0.01	0.26	0.02
Laitakarite Average					0.18	0.02	2.17	0.44	1.38	0.04	0.02	18.2	76.7	0	0.01	0.02	0.01	0	0.01	1.60	0.03
WAN092	Lower	Massive chalcopyrite	Co-pentlandite	$(Co, Fe, Ni)_9S_8$	0.58	0.13	<0.01	4.23	32.9	<0.01	0.03	0.06	0.10	<0.01	62.3	0.81	0.07	<0.01	0.03	<0.01	<0.01
WAN004	Middle	Massive chalcopyrite	cobaltite	(Co, Fe)AsS	0.56	<0.01	<0.01	3.35	21.4	0.01	<0.01	0.73	0.05	<0.01	33.0	0.02	0.06	40.2	<0.01	<0.01	0.01
WAN006	Middle	Massive pyrrhotite	gold (electrum)	(Au,Ag)	0.07	<0.01	<0.01	0.19	0.33	76.8	23.3	0.03	0.26	<0.01	0.05	0.02	0.03	0.00	0.31	0.07	<0.01
WAN006		Massive pyrrhotite	gold (electrum)		0.07	<0.01	<0.01	0.21	0.16	79.8	19.5	0.05	<0.01	<0.01	0.04	0	0	0.03	0.21	0.04	0.17

Samples were analyzed by a four spectrometer Cameca Camebax MBX electron microprobe by wavelength dispersive X-ray analysis in the Earth Sciences Department at Carleton University, Ottawa, Ontario; *Contamination from Bi-telluride rim on grain

Table 2.5 Microprobe analyses of a zoned magnetite grain for sample WAN071 (3 analyses based on 32 oxygens) from the Upper Lens of the West Ansil deposit

	Analysis 1		Analysis 2		Analysis 3	
	Cations	(Oxide wt%)	Cations	(Oxide wt%)	Cations	(Oxide wt%)
Si	0	0.0	0.181	0.6	1.298	4.3
Fe	23.959	98.8	23.696	93.7	21.522	92.6
Al	0.030	0.1	0.090	0.3	0.129	0.4
Ca	0.014	0.0	0.000	0.0	0.196	0.6
Mg	0	0.0	0.015	0.0	0.253	0.6
Mn	0	0.0	0.011	0.0	0	0.0
Total	24.003	98.9	23.9934	94.6	23.399	98.7

Samples were analyzed on a four spectrometer Cameca Camebax MBX electron microprobe by wavelength dispersive x-ray analysis using the silicate routine in the Earth Sciences Department at Carleton University, Ottawa, Ontario; Locations of analyses are shown in Figure 2.18D

Table 2.6 Average Chemical Compositions of Representative Ore Samples for the West Ansil Deposit

		Massive sphalerite	Sphalerite stringers		Massive pyrrhotite			Massive chalcopyrite		Chalcopyrite stringers		Massive magnetite		Colloform pyrite-marcasite		
		Middle	Middle	Lower	Upper	Middle	Lower	Middle	Lower	Upper	Lower	Upper	Middle	Upper	Middle	Lower
	n	4	2	1	4	9	7	5	2	4	6	8	7	3	9	1
Fe	(wt%)	35.7	24.7	18.3	50.2	51.8	48.0	34.6	44.9	30.9	25.2	52.8	48.0	42.4	43.8	40.9
Cu		5.5	0.1	1.1	4.9	1.9	2.6	13.8	12.2	11.3	14.2	1.1	6.2	5.4	3.5	0.9
Zn		13.8	15.4	11.9	0.04	0.27	0.55	0.24	0.16	0.08	0.17	0.02	0.05	0.03	0.22	0.02
S		32.8	18.5	7.2	33.7	35.0	31.3	28.1	33.4	20.2	17.6	13.0	16.4	36.4	30.3	39.5
Pb	(ppm)	7	8	11	15	17	1600	29	10	49	26	13	18	64	384	766
Sn		162	2.2	0.3	0.3	1.4	4.1	18.9	10.3	1.2	5.4	1.8	7.1	2.3	3.4	0.3
Cd		342	293	725	2	8	31	8	4	6	14	1	2	3	8	1
Ag		22	3	3	9	3	6	16	3	21	10	3	8	9	9	3
Hg	(ppb)	19	310	260	7	4	5	9	15	14	4	4	12	10	16	3
Ni	(ppm)	5	18	5	5	8	9	14	12	76	11	11	7	5	27	20
Tl		0.05	0.05	0.05	0.51	0.08	0.07	0.05	0.10	0.30	0.10	0.14	0.18	3.33	1.36	9.80
As		15.1	7.5	0.3	2.2	0.3	30.7	34.4	68.5	3.0	12.3	0.3	4.4	0.3	1.1	0.3
Sb		0.65	1.28	0.05	0.29	0.08	0.05	0.33	0.05	0.36	0.26	0.18	0.26	0.05	0.29	0.90
Au	(ppb)	672	168	314	60	1692	540	5766	416	61	63	362	4638	97	79	1
In	(ppm)	20.5	15	1.9	0.5	3.0	2.8	36.7	22.9	5.5	17.6	1.1	9.7	5.7	10.5	0.9
Co		574	466	358	650	984	1041	552	1767	590	325	419	538	740	1049	1220
Se		65	10	121	114	162	219	694	552	252	384	68	243	276	292	244
Bi		7	9.5	6	1.5	24.6	17.1	644	15.3	13.3	4.4	6.3	26.4	4.7	76.8	12
Mo		0.5	11.8	2.0	10.4	4.2	1.3	1.9	0.7	2.8	1.3	17.7	98.4	141.3	2.4	0.5
Te		3	3	3	3	3	3	4	3	9	6	3	4	3	4	3
W		1.13	11.4	1.10	0.35	1.51	1.66	2.46	1.38	1.04	6.71	11.2	0.81	2.37	1.67	0.35
V		2.50	54.5	184	5.38	5.44	18.9	2.50	4.75	106	63.4	56.5	8.43	7.50	9.85	2.50
U		0.05	0.08	0.10	0.05	0.05	0.05	0.05	0.05	0.09	0.06	0.23	0.05	0.05	0.21	0.05
Ga		53	25	34	1	6	6	4	5	30	25	23	20	1	13	2
Ge		11.6	3.5	1.2	0.7	0.7	0.7	0.5	0.4	0.8	0.7	3.2	4.3	0.8	0.9	0.4
SiO_2	(wt%)	10.4	15.6	30.2	8.1	8.4	13.3	21.9	5.9	22.3	25.9	11.0	12.4	10.8	15.2	13.9
Al_2O_3		0.05	5.25	10.18	0.37	0.38	0.89	0.06	0.24	5.57	5.12	2.49	0.74	0.21	0.59	0.19
Na_2O		0.007	0.007	0.013	0.057	0.009	0.007	0.007	0.009	0.012	0.047	0.031	0.074	0.020	0.015	0.013
K_2O		0.06	0.06	0.06	0.11	0.06	0.06	0.06	0.06	0.06	0.10	0.09	0.10	0.06	0.06	0.06
MgO		0.74	5.37	5.39	0.95	0.27	0.75	0.13	0.21	3.28	3.47	2.15	0.90	1.17	0.57	1.29
CaO		0.05	2.73	0.59	0.39	0.07	0.07	0.02	0.03	0.21	1.23	0.26	0.78	0.13	0.07	0.41
P_2O_5		0.048	0.113	0.108	0.104	0.023	0.035	0.106	0.09	0.114	0.165	0.034	0.088	0.057	0.039	0.021
TiO_2		0.01	0.40	0.67	0.02	0.04	0.09	0.01	0.028	0.49	0.38	0.32	0.04	0.01	0.06	0.01
CO_2		0.04	6.60	0.04	0.01	0.03	0.09	0.04	0.052	0.01	1.22	0.08	0.62	0.09	0.33	0.58
Mn	(ppm)	194	2315	1500	654	104	131	96	111	700	754	1268	474	239	237	99
B		5.0	5.0	5.0	11.3	5.0	5.0	5.0	5.0	6.3	5.0	11.9	5.0	6.7	17.2	5.0
Th		0.05	0.33	0.70	0.14	0.09	0.19	0.27	0.05	0.50	0.38	0.51	0.16	0.05	0.13	0.05
Rb		0.20	0.65	3.00	2.70	0.27	0.37	0.20	0.70	0.53	4.48	3.54	2.76	0.73	0.75	0.20
Sr		2.38	38.50	6.00	18.25	2.06	3.93	1.80	2.25	6.75	7.50	5.13	8.71	13.67	5.65	11.00
Cs		0.05	0.23	1.10	0.58	0.06	0.05	0.05	0.08	0.15	0.22	0.38	0.23	0.18	0.07	0.05
Ba		1.50	1.50	1.50	2.38	1.50	1.86	1.50	1.50	1.50	7.60	3.88	3.00	1.50	2.89	1.50
Br		0.25	0.25	0.25	0.96	0.25	0.92	0.54	0.25	0.25	0.96	1.14	0.25	1.53	1.76	3.80
Hf		0.50	0.50	2.00	0.50	0.50	0.57	0.50	0.50	1.38	1.60	1.00	0.50	0.50	0.50	0.50
Ir		2.50	2.50	2.50	2.50	2.50	2.50	2.50	2.50	2.50	2.50	2.50	2.50	2.50	2.50	2.50
Sc		0.14	8.35	18.9	1.00	0.72	2.03	0.11	0.68	11.3	10.0	6.01	1.52	0.80	2.91	0.50
Li		1.50	2.75	1.50	1.50	1.50	1.50	1.50	1.50	1.50	1.80	1.50	1.50	5.33	1.50	6.00
Be		1.50	1.50	1.50	1.50	1.50	1.50	1.50	1.50	1.50	1.50	1.50	1.50	1.50	1.50	1.50
Y		0.11	10.3	20.8	4.88	0.94	4.51	0.33	1.45	21.5	14.1	6.60	7.57	13.13	7.71	6.30
Nb		1.20	2.00	3.50	1.20	1.20	1.20	1.20	1.20	2.15	1.92	1.89	1.20	1.20	1.20	1.20
Ta		0.10	0.10	0.30	0.10	0.10	0.10	0.10	0.10	0.10	0.10	0.10	0.10	0.10	0.10	0.10
ΣREE		1.5	35.4	50.1	16.5	5.0	15.5	3.7	23.4	102.3	48.9	34.7	26.5	29.1	15.4	23.2

Ore types are listed in Table 2.1 and described in the text; *n* = number of samples analyzed; Samples were analyzed by a combination of ICP-MS and INAA at Activation Laboratories, Ancaster, Ontario; Hg analyzed by FIMS and CO_2 by infrared absorption

Table 2.7 Pearson Correlation Matrix for Selected Trace Elements in Massive Sulphide Ore from the West Ansil Deposit

	Zn	Sn	Cd	Pb	Hg	Ag	Ni	Tl	As	Sb	U	V	W	Fe	Cu	Se	Au	Bi	Co	In	Mo	Te
Zn	1																					
Sn	0.69	1																				
Cd	0.89	0.57	1																			
Pb	0.02	-0.05	0.14	1																		
Hg	0.58	0.02	0.56	0.03	1																	
Ag	0.11	0.13	0.13	0.66	0.06	1																
Ni	-0.04	-0.05	0.02	0.62	0.08	0.78	1															
Tl	-0.09	-0.07	-0.06	0.29	0.03	0.46	0.30	1														
As	0.05	0.11	0.03	0.24	0.04	0.39	0.37	0.07	1													
Sb	0.03	0.01	0.08	0.67	0.12	0.80	0.92	0.35	0.42	1												
U	-0.02	-0.05	0.05	0.57	0.07	0.66	0.81	0.26	0.33	0.87	1											
V	0.06	-0.10	0.17	-0.08	0.17	-0.09	0.02	-0.11	-0.10	-0.03	0.14	1										
W	0.01	-0.05	-0.04	-0.07	0.14	-0.08	-0.06	-0.08	-0.02	-0.03	0.08	-0.03	1									
Fe	-0.26	-0.10	-0.28	0.04	-0.30	-0.15	-0.13	-0.01	-0.04	-0.08	-0.03	-0.34	-0.03	1								
Cu	-0.12	0.06	-0.14	-0.09	-0.12	0.23	0.01	-0.10	0.17	-0.03	-0.09	-0.10	0.01	-0.33	1							
Se	-0.25	-0.07	-0.22	-0.01	-0.09	0.13	0.01	0.13	0.26	0.01	-0.07	-0.22	-0.09	0.01	0.60	1						
Au	0.11	0.11	0.14	0.28	-0.01	0.13	0.05	-0.06	0.07	0.11	0.24	-0.17	-0.12	0.07	0.40	0.08	1					
Bi	-0.04	0.04	-0.04	-0.02	-0.03	0.05	-0.04	-0.04	0.35	0.00	-0.03	-0.07	-0.05	0.04	0.27	0.60	0.30	1				
Co	-0.11	-0.05	-0.10	0.16	-0.05	0.13	0.16	0.34	0.04	0.12	0.00	-0.32	-0.24	0.32	-0.05	0.42	0.11	-0.01	1			
In	0.14	0.13	0.10	-0.02	0.03	0.10	0.02	-0.09	0.28	0.06	-0.01	-0.14	0.00	-0.10	0.49	0.75	0.28	0.62	0.12	1		
Mo	-0.08	-0.07	-0.08	0.09	0.03	0.17	0.13	0.40	0.00	0.17	0.17	-0.08	0.02	0.06	-0.02	-0.01	-0.05	-0.05	-0.03	-0.09	1	
Te	-0.08	-0.04	-0.07	-0.04	-0.03	0.23	0.09	-0.03	0.03	-0.03	-0.06	-0.01	-0.05	-0.29	0.46	0.23	-0.09	0.16	-0.19	0.10	-0.08	1

Correlations are based on 76 samples; coefficients greater than 0.14 are significant at the 95% confidence level

Table 2.8 Sulfur Isotopic Compositions of Mineral Separates from Selected Ore Samples of the West Ansil Deposit

Sample no.	Lens	Mineral	Ore Type	$\delta^{34}S$
WAN018	Middle	Sphalerite	Massive sphalerite-pyrrhotite	2.56
WAN133	Lower	Sphalerite	Sphalerite-chalcopyrite stringers	2.36
WAN077	Upper	Pyrrhotite	Massive pyrrhotite-chalcopyrite	1.03
WAN130	Lower	Pyrrhotite	Massive pyrrhotite-chalcopyrite	1.78
WAN075	Upper	Chalcopyrite	Chalcopyrite stringer	1.56
WAN004	Middle	Chalcopyrite	Massive chalcopyrite	1.27
WAN092	Lower	Chalcopyrite	Massive chalcopyrite	1.66
WAN088	Upper	Pyrite-marcasite	Colloform pyrite-marcasite	1.83
WAN088(Dupl)	Upper	Pyrite-marcasite	Colloform pyrite-marcasite	1.36
WAN061	Middle	Pyrite-marcasite	Colloform pyrite-marcasite	0.85
WAN122	Lower	Pyrite-marcasite	Colloform pyrite-marcasite	1.72
Ansil Ore Deposit				
AN-75-1197m		Pyrrhotite	Massive pyrrhotite-chalcopyrite	0.9
		Chalcopyrite	Massive pyrrhotite-chalcopyrite	1.1
AN-80-1380m		Chalcopyrite	Massive pyrrhotite-chalcopyrite	0.7
AN-70A-1372m		Chalcopyrite	Massive pyrrhotite-chalcopyrite	0.7
AN-75-1211m		Chalcopyrite	Massive pyrrhotite-chalcopyrite	1.4
AN-75-1222m		Chalcopyrite	Massive pyrrhotite-chalcopyrite	1.7

Mineral separates were analyzed using EA combustion and continuous flow IRMS at the G.G. Hatch Isotope Laboratories at the University of Ottawa, Ontario; Data for Ansil from Barrett et al. (1991)

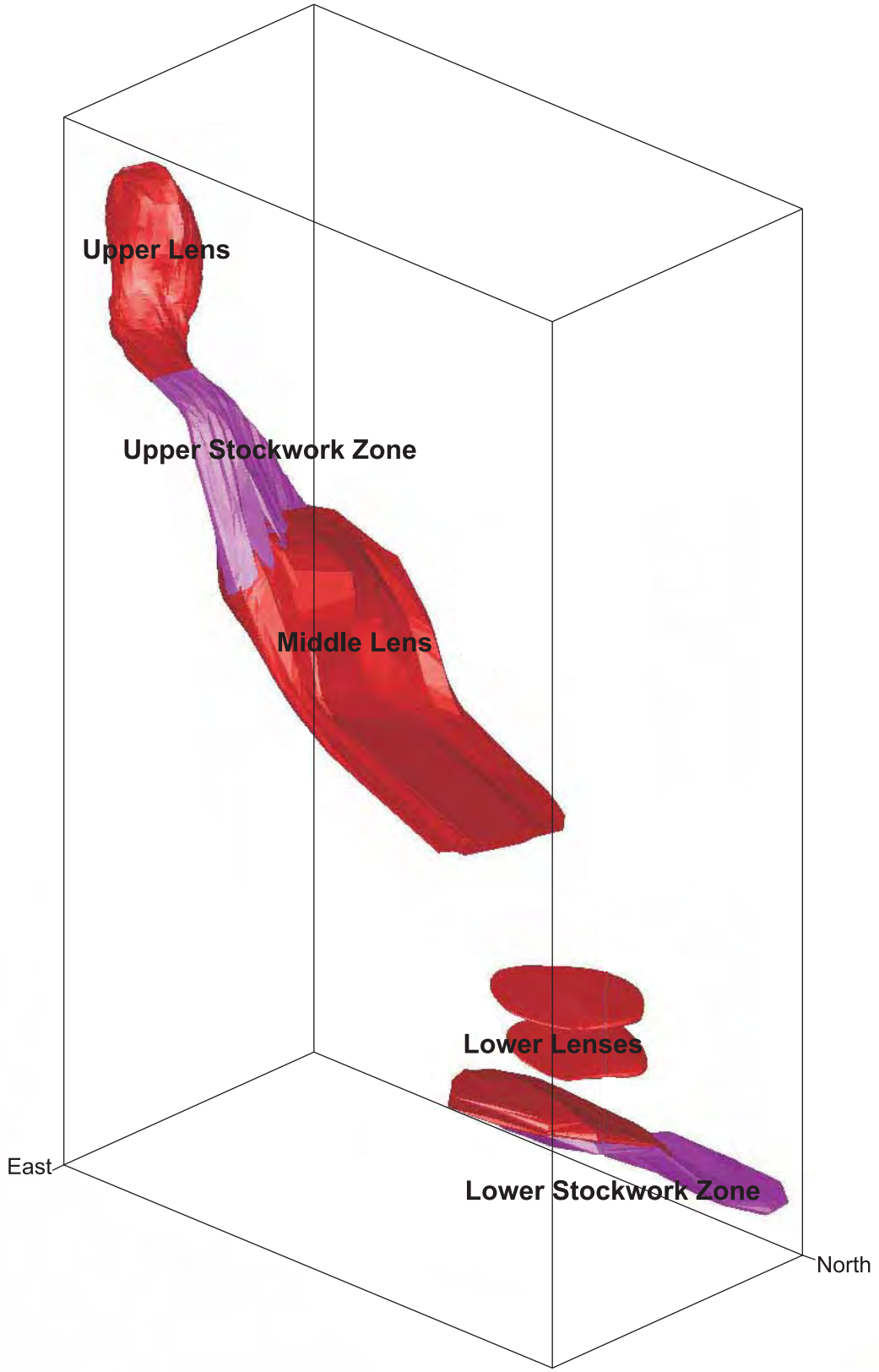

Figure 2.1 A three dimensional view of the West Ansil deposit showing the relative thickness and depth of the Upper, Middle and Lower lenses and their approximate dip extent (modified after Xstrata Copper Canada Ltd, 2005).

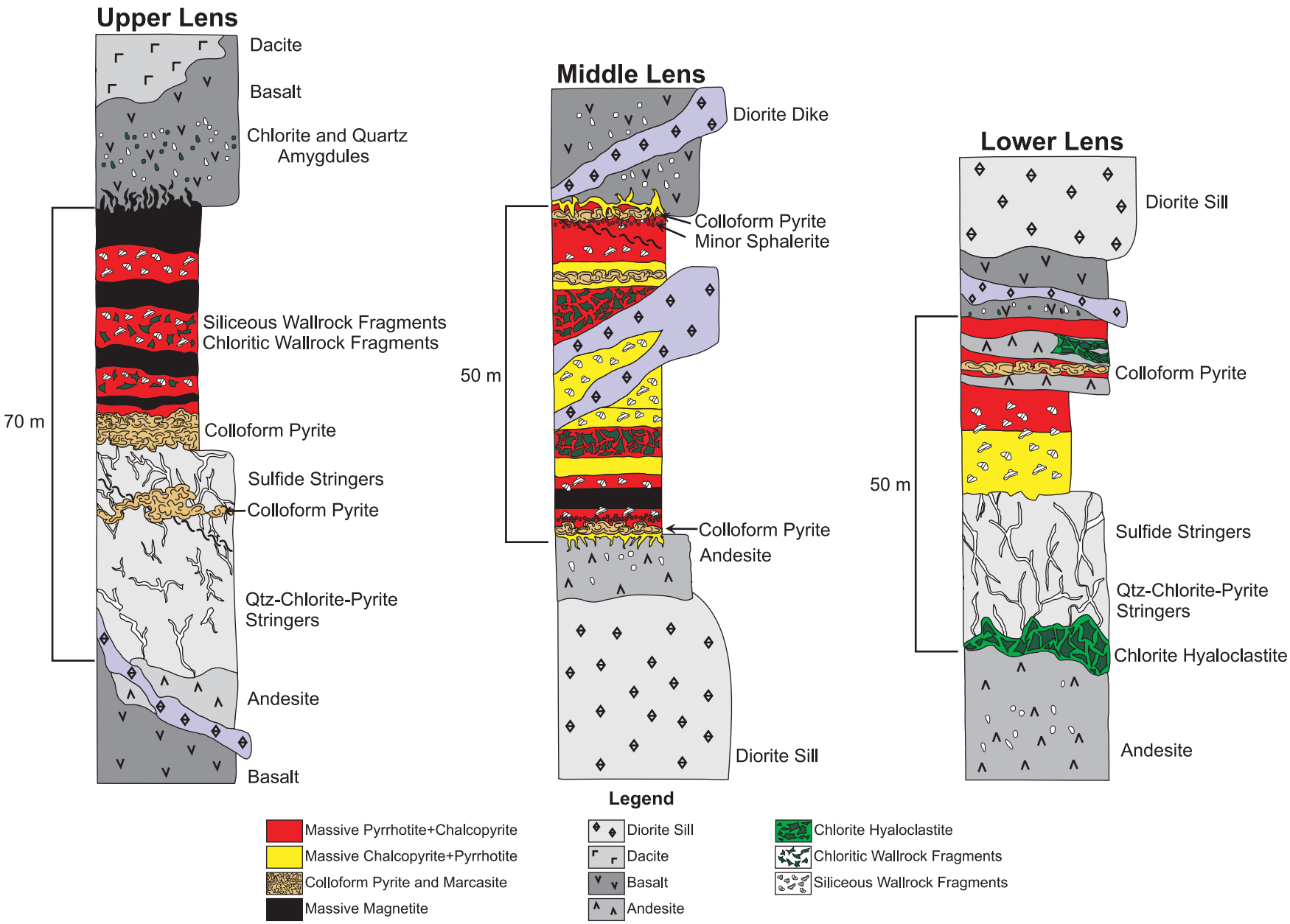

Figure 2.2 Composite graphic logs of the Upper, Middle and Lower lenses of the West Ansil deposit showing the dominant massive sulphide ores and stockwork zones, contact relationships, the main mafic volcanic units, and major mafic dikes intruding the lenses. Note that the scale is intended to show the thickness of the mineralized zones but not of the units in the lenses.

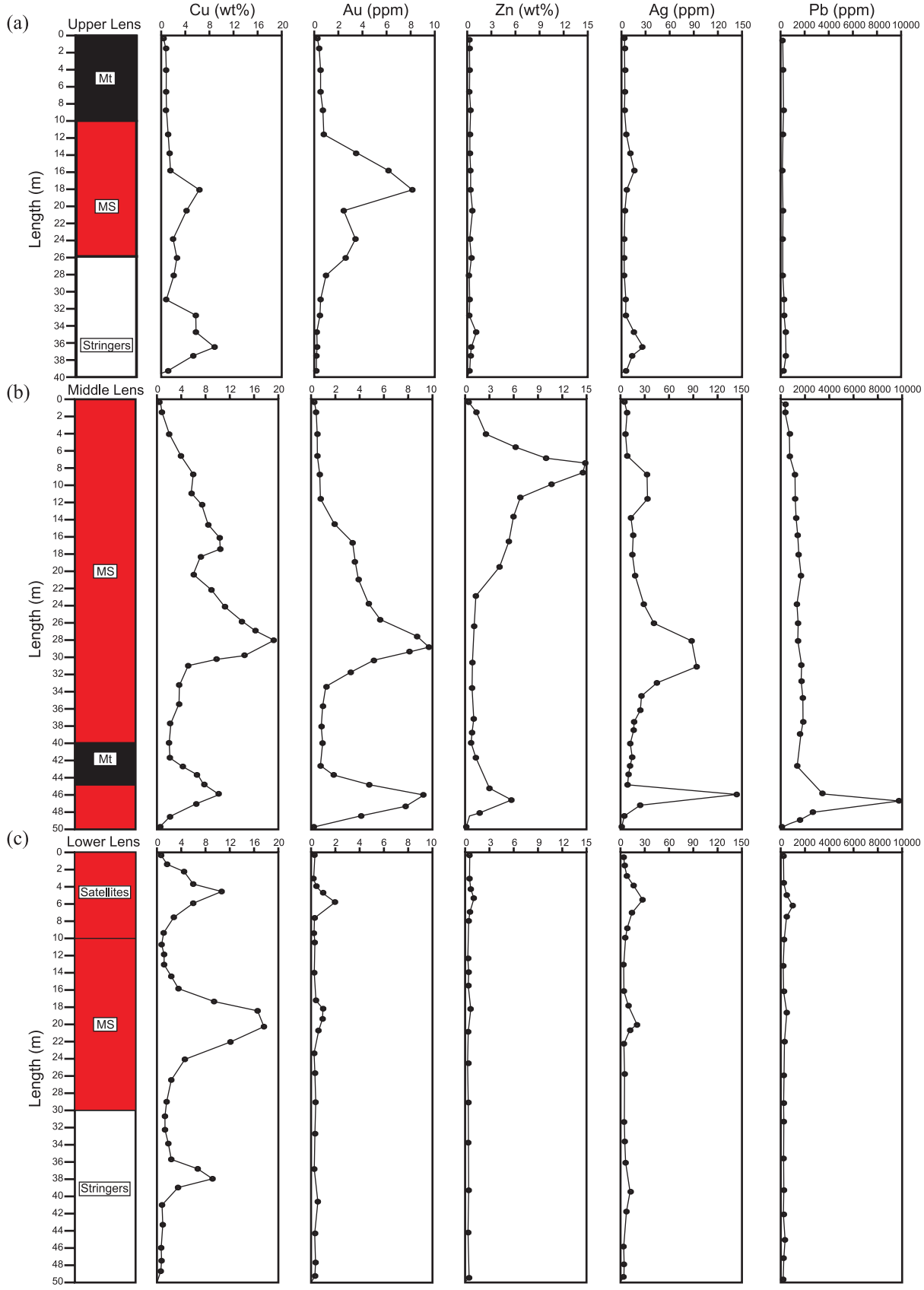

Figure 2.3 a) Composite metal zonation of the Upper lens based on assay data from WAN-05-05, WAN-05-09 and WAN-05-18. Cu, Au and Ag show a positive correlation in the center of the lens and the stockwork zone. Zn and Pb concentrations are uniformly low. b) Composite metal zonation profiles of the Middle lens based on assay data from AN-05-04, WAN-05-01, WAN-05-02, WAN-05-04, WAN-05-06, WAN-05-07 and WAN-05-19W. The Middle lens has a Zn-rich top and a Cu-rich core and stringer zone. Again, a positive correlation between Cu, Au and Ag is apparent in the central part of the lens and stringer zone. The high Pb, Zn, Ag and Au values at the bottom of the lens are due to remobilized galena veins at the basal contact. c) Composite metal zonation of the Lower lens and stockwork zone based on assay data from AN-05-02, AN-05-03, WAN-05-10, WAN-05-12, WAN-05-15 and WAN-05-20W, including a satellite zone. Zn and Pb values are low, and Cu, Au and Ag are positively correlated. MS = Massive Sulphide, Mt = Magnetite.

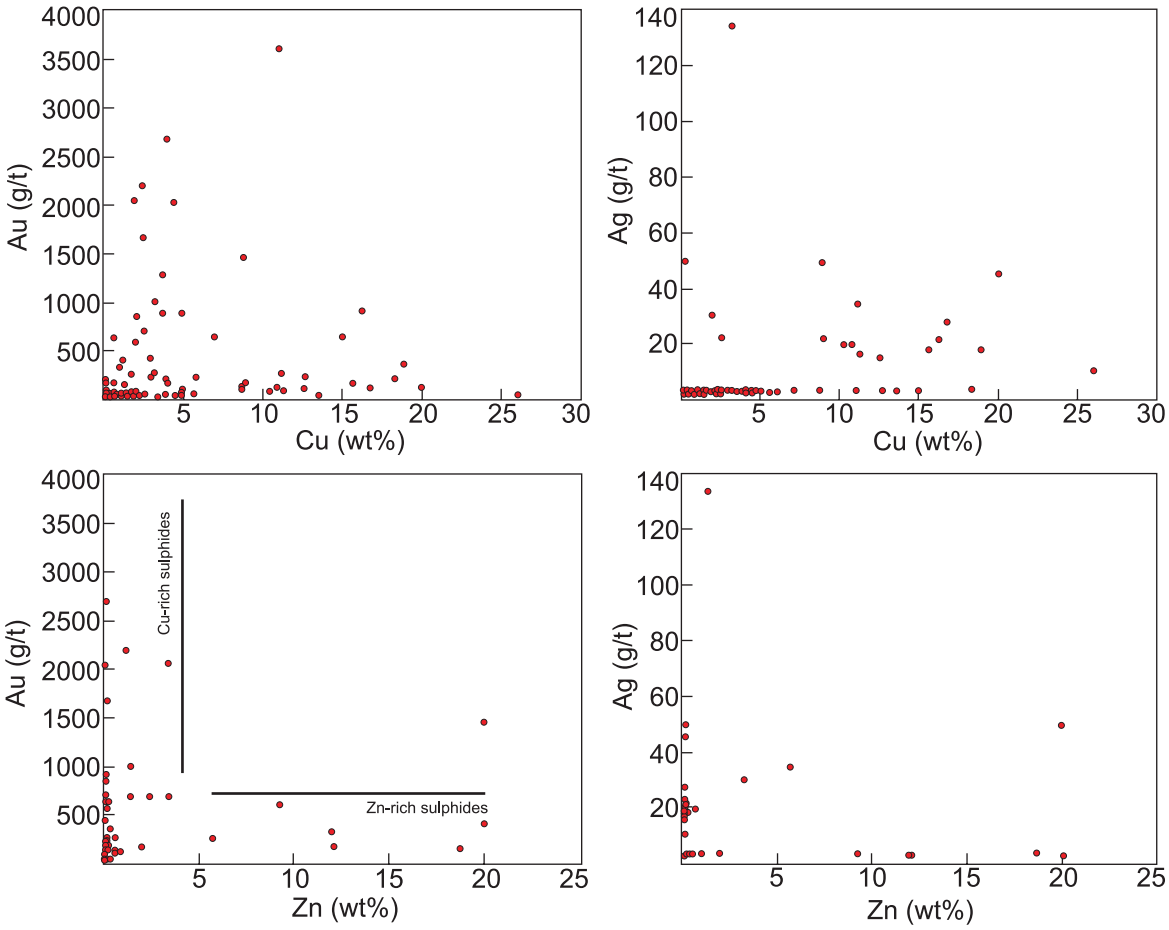

Figure 2.4 Interelement plots for Cu, Zn, Au and Ag in ores from the Upper, Middle and Lower lenses showing a strong Cu-Au association and no Zn-Au association. A minor Cu-Ag is also observed reflecting the higher temperature assemblage of Cu-Au-Ag.

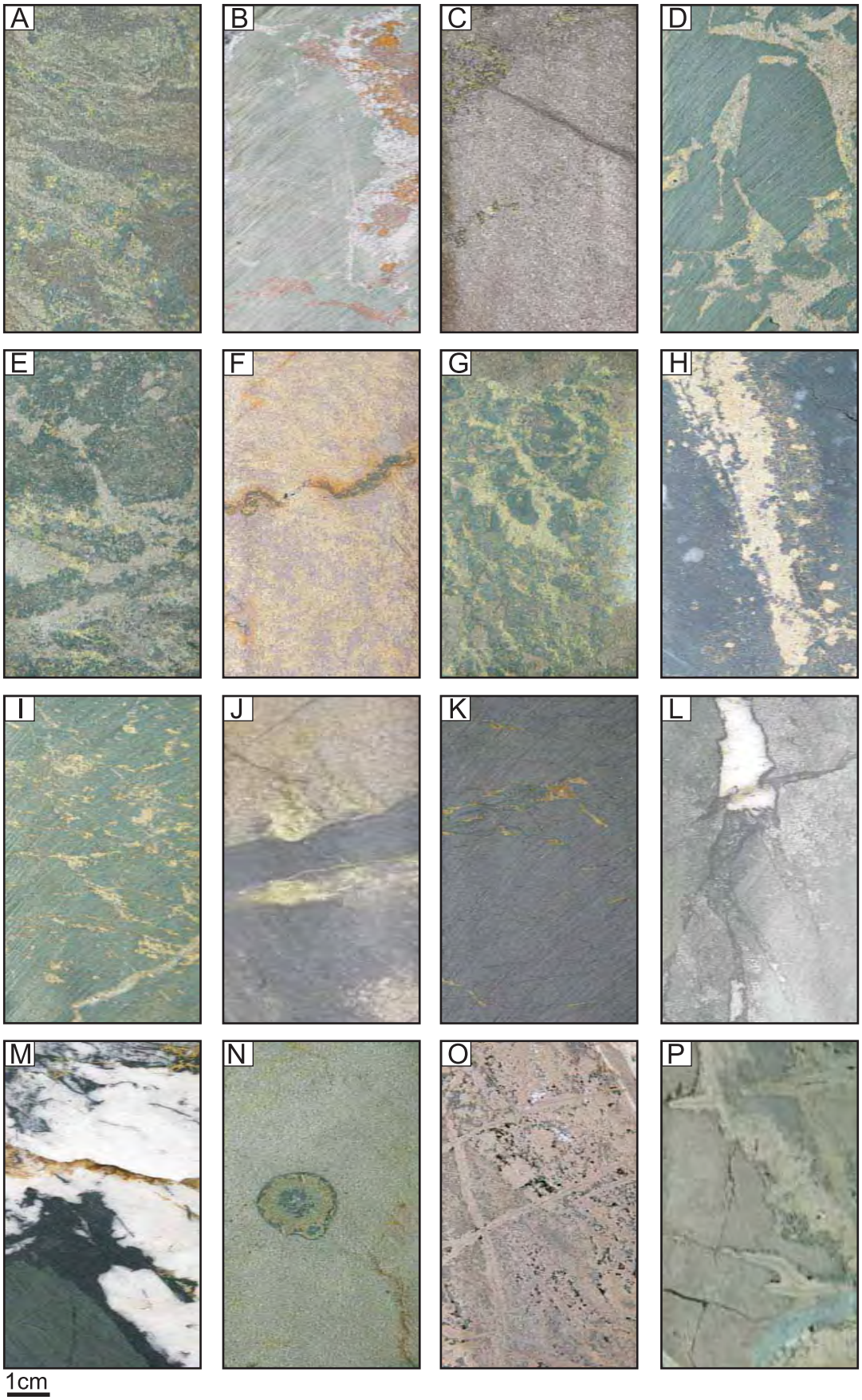

Figure 2.5 Representative photographs of drill core samples showing sulphide ore textures in the West Ansil lenses.

Figure 2.5 Representative photographs of drill core samples showing sulphide ore textures in the West Ansil lenses. A) Massive sphalerite-pyrrhotite in the Middle lens showing semi-continuous sphalerite-rich bands. Rounded microcristalline quartz fragments are also present and rimmed with chalcopyrite; WAN032. B) Sphalerite-chalcopyrite stringer in silicified-chloritized basalt from the Lower stockwork zone; WAN133. C) Massive pyrrhotite ore from the Upper lens with disseminated chalcopyrite; WAN077. D) Strongly chloritized basalt breccia in a pyrrhotite-rich matrix from the Middle lens; WAN008. E) Silicified basalt pseudobreccia, almost completely replaced by massive pyrrhotite ± chalcopyrite from the Middle lens; WAN028. F) Massive chalcopyrite ± pyrrhotite ore Middle lens; WAN004. G) Partially replaced siliceous fragments in a chalcopyrite ± pyrrhotite matrix from the Middle lens; WAN036. H) Chalcopyrite-quartz stringer in chloritized basalt from the Lower lens with quartz- and chalcopyrite-filled amygdules; WAN099. I) Chalcopyrite stringer in silicified-chloritized basalt from the Middle lens; WAN012. J) Magnetite bands in massive pyrrhotite ± chalcopyrite from the Upper lens; WAN078. K) Massive magnetite with remobilized chalcopyrite veinlets from the Upper lens; WAN078. L) Fracture-controlled magnetite, chlorite and quartz in basalt at the top of the Upper lens; WAN084. M) Fracture-controlled magnetite-quartz-chlorite veins within basalt along the top contact of the Upper lens; from drill hole WAN-05-05, no sample. N) Isolated secondary pyrite-marcasite nodule in massive pyrrhotite from the Middle lens; WAN002. O) Porous massive colloform pyrite-marcasite from the Middle lens; WAN070. P) Fracture-controlled recrystallized marcasite in colloform pyrite replacing massive pyrrhotite from the Middle lens; WAN042.

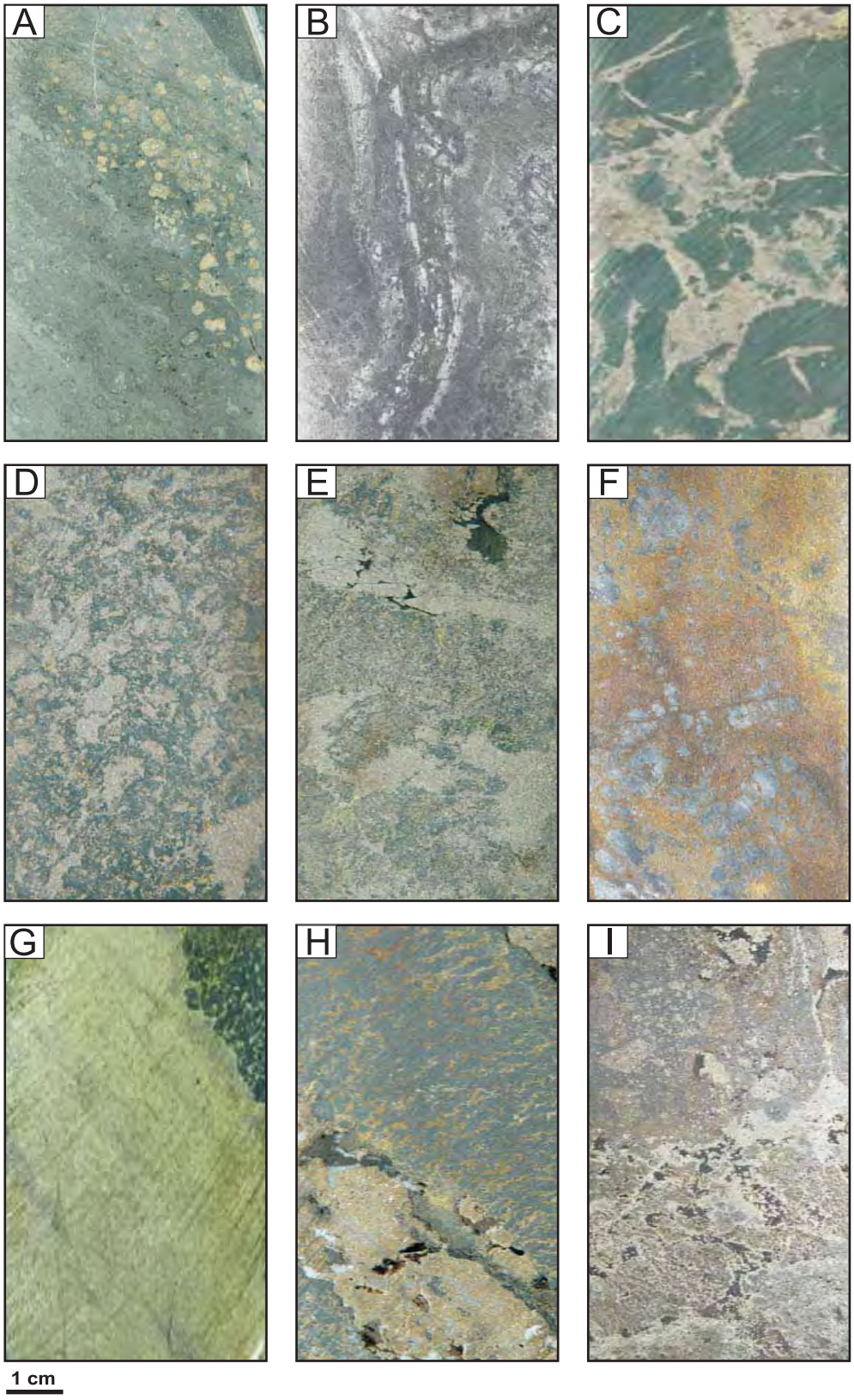

Figure 2.6 Representative photographs of drill core samples showing sulphide ore textures in the West Ansil lenses and the evolution of the hydrothermal system.

Figure 2.6 Representative photographs of drill core samples showing sulphide ore textures in the West Ansil lenses and evolution of the hydrothermal system. A) Andesite hyaloclastite at the bottom contact of the Middle lens; WAN044. B) Chlorite-quartz stringer from the Lower lens; WAN097. C) Strongly chloritized basalt breccia in a pyrrhotite-rich matrix from the Middle lens; WAN008. D) Partially pyrrhotite-replaced silicified and chloritized basalt breccia from the Middle lens ; WAN031. E) Silicified-chloritized basalt breccia completely replaced by massive pyrrhotite-chalcopyrite; from drill hole WAN-05-07, no sample. F) Massive chalcopyrite-pyrrhotite ore with partially replaced siliceous fragments; WAN091. G) Contact between massive chalcopyrite-pyrrhotite and massive magnetite in the Middle lens; from drill hole WAN-05-19W, no sample. H) Massive magnetite in pyrrhotite-chalcopyrite with fracture-controlled colloform pyrite and marcasite replacing pyrrhotite; WAN010. I) Colloform pyrite-marcasite replacing the pyrrhotite-rich matrix of a strongly silicified basalt breccia with late siderite in the porous nodules; WAN027.

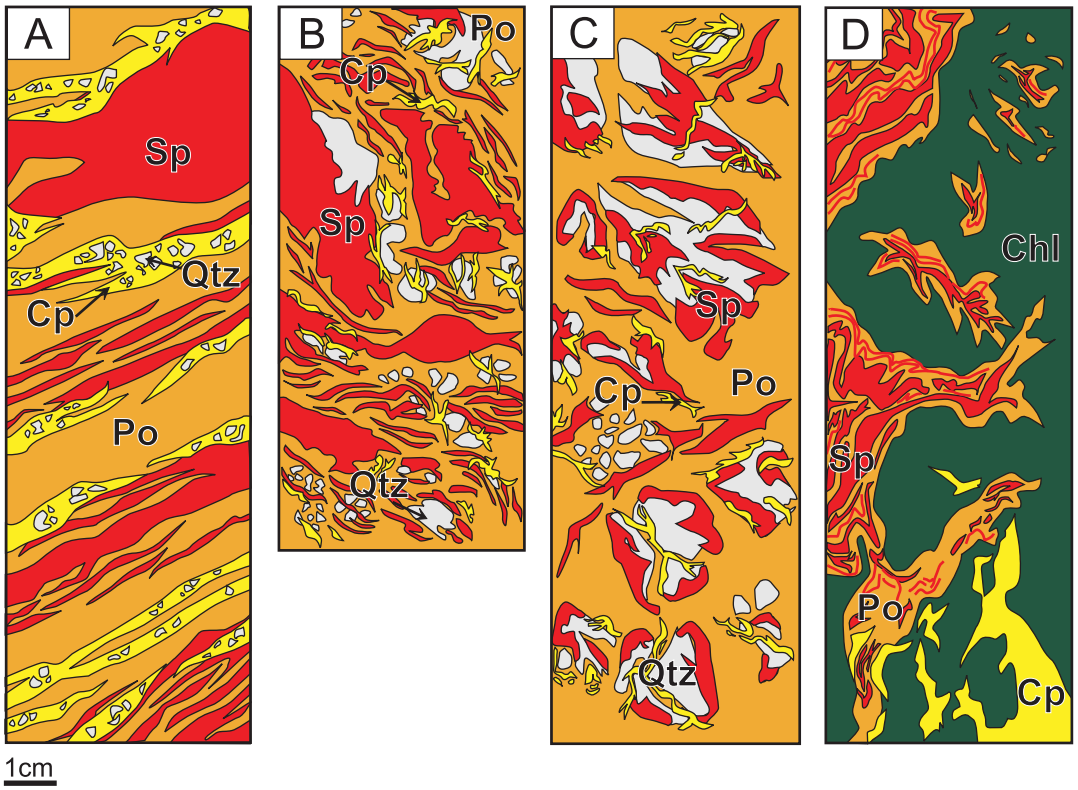

Figure 2.7 Sketches of drill core samples illustrating massive sphalerite-pyrrhotite and sphalerite stringer ore textures in the West Ansil deposit. A) Banded pyrrhotite-sphalerite ± chalcopyrite ore from the Middle lens showing discontinuous millimetre- to centimeter-scale pyrrhotite- and sphalerite-rich bands. Rounded siliceous fragments are present only in the chalcopyrite bands. Contacts between pyrrhotite and chalcopyrite are sharp, whereas contacts between pyrrhotite and sphalerite are more gradational; WAN020. B) Massive pyrrhotite-sphalerite with lesser chalcopyrite in the Middle lens showing millimetre- to centimeter-scale semi-continuous sphalerite-rich bands. Contacts between the pyrrhotite and sphalerite bands are smooth and sharp to gradational. Rounded microcristalline quartz fragments are also present and appear to be the product of strong silicification. Remobilized chalcopyrite is replacing the fragments along their boundaries; WAN034. C) Completely silicified basalt-andesite breccia from the Middle lens with abundant pyrrhotite -sphalerite forming a continuous matrix between angular and partially replaced fragments of microcristalline quartz. Sphalerite and remobilized chalcopyrite are replacing the fragments along their boundaries; WAN032. D) Sphalerite-pyrrhotite stringers at the base of the Middle Lens. The stringers have a rim of pyrrhotite, which may reflect replacement of early sphalerite stringers in a thermally intensifying system; WAN018.

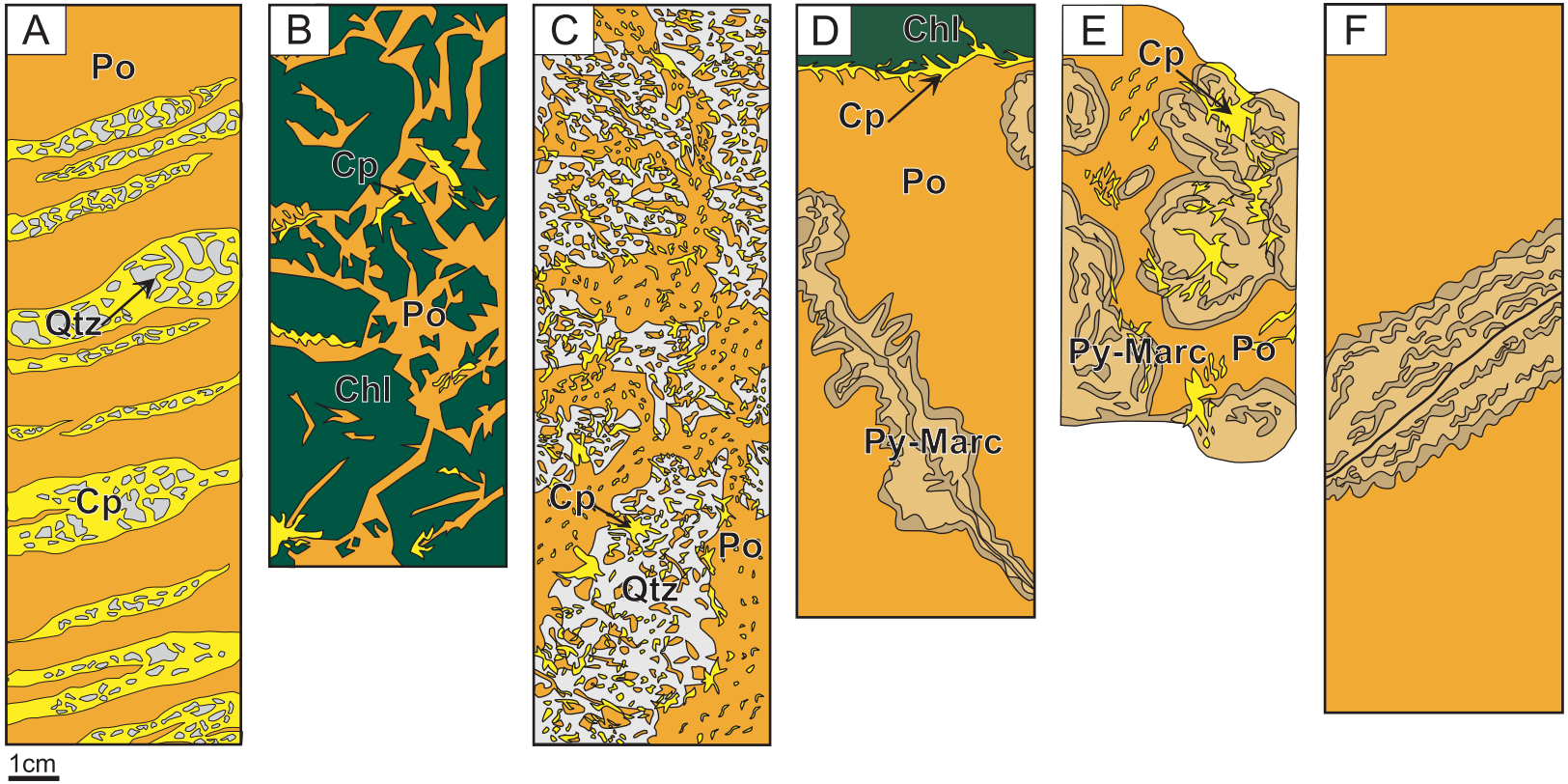

Figure 2.8 Sketches of drill core samples illustrating representative massive pyrrhotite-chalcopyrite ore textures. A) Banded pyrrhotite-chalcopyrite ore from the Middle lens showing discontinuous centimeter-scale chalcopyrite-rich bands containing rounded, partly replaced siliceous wall-rock fragments. Contacts between pyrrhotite and chalcopyrite are sharp and smooth to serrate; WAN019. B) Chlorite-rich basalt breccia from the Middle lens with abundant pyrrhotite in the matrix between angular and partially replaced fragments of black choritized basalt. The pyrrhotite matrix also contains minor disseminated chalcopyrite and remobilized chalcopyrite along the boundaries of chlorite fragments; WAN008. C) Intensely silicified basalt and andesite pseudobreccia from the Middle lens with abundant pyrrhotite and lesser chalcopyrite in the matrix between large centimeter-scale angular and almost completely replaced siliceous clasts. The quartz-rich fragments appear to be the product of very strong silicification of basalt. Both pyrrhotite and chalcopyrite invade the fragments; WAN035. D) Massive sulphide at the top of the Middle lens with remobilized chalcopyrite separating the chloritized hanging-wall basalt from the massive pyrrhotite. Remobilized chalcopyrite-rich stringers extend into both the sulphides and the wall rock. The massive pyrrhotite is also partly replaced by centimeter-scale colloform pyrite-marcasite nodules and veins centered on late fractures; No sample. E) Colloform pyrite-marcasite in massive pyrrhotite from the Middle lens. The large centimeter-scale pyrite-marcarite nodules contain unreplaced pyrrhotite and late-stage remobilized chalcopyrite in shrinkage cracks; WAN007. F) Massive pyrrhotite from the Upper lens with a centimeter-scale colloform pyrite-marcasite band occurring within a microfracture; No sample.

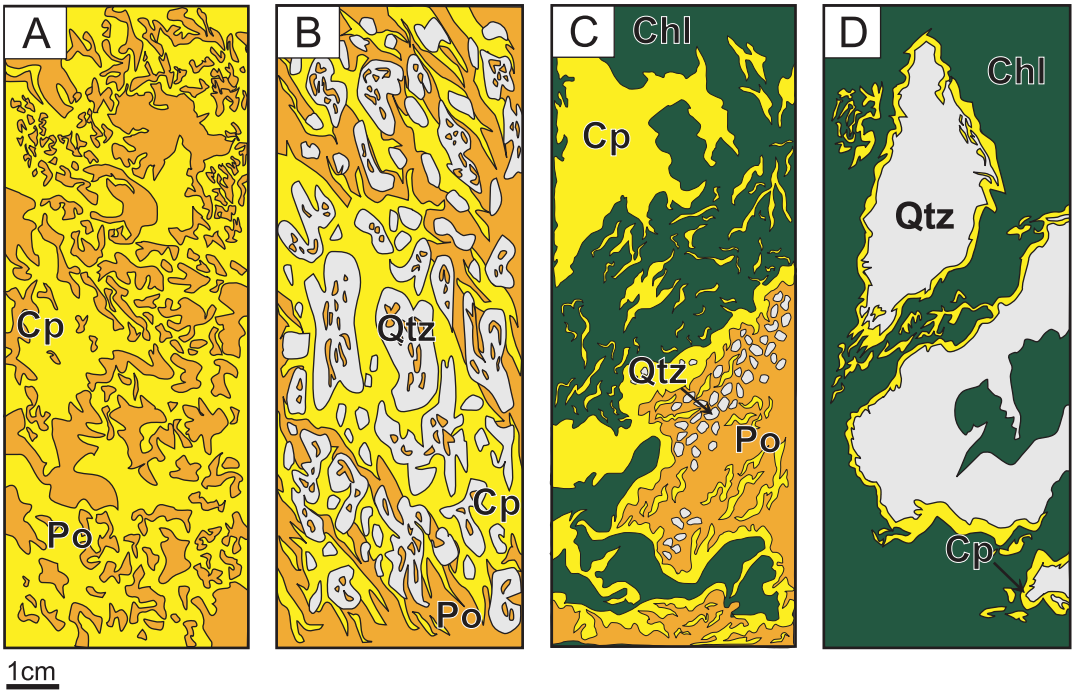

Figure 2.9 Sketches of drill core samples illustrating massive chalcopyrite -pyrrhotite and chalcopyrite stringer ore textures in the West Ansil deposit. A) Massive chalcopyrite-pyrrhotite from the Middle lens. Fine-grained granoblastic pyrrhotite is infilled and being replaced by anhedral chalcopyrite; WAN004. B) Discontinuous chalcopyrite-rich bands from the Middle lens alternating with bands of pyrrhotite. Partly replaced siliceous material is present within the bands and is interpreted to represent unreplaced fragments of silicified wall rock; WAN036. C) Chalcopyrite-pyrrhotite stringer mineralization from the Upper stockwork zone. Large centimeter-scale chalcopyrite network-like veins occur within a strongly chloritized basalt-andesite and appear to have replaced pyrrhotite. Smaller millimetre-scale chalcopyrite veinlets appear to have been locally remobilized into late fractures; WAN079. D) Chlorite and chalcopyrite stringer mineralization in the Lower stockwork zone. Centimeter-scale chlorite-actinolite network-like veins occur within a strongly silicified and chloritized basalt-andesite breccia. Chalcopyrite rims the siliceous fragments and occur as minor micro-veinlets in the more massive chlorite-actinolite; WAN095.

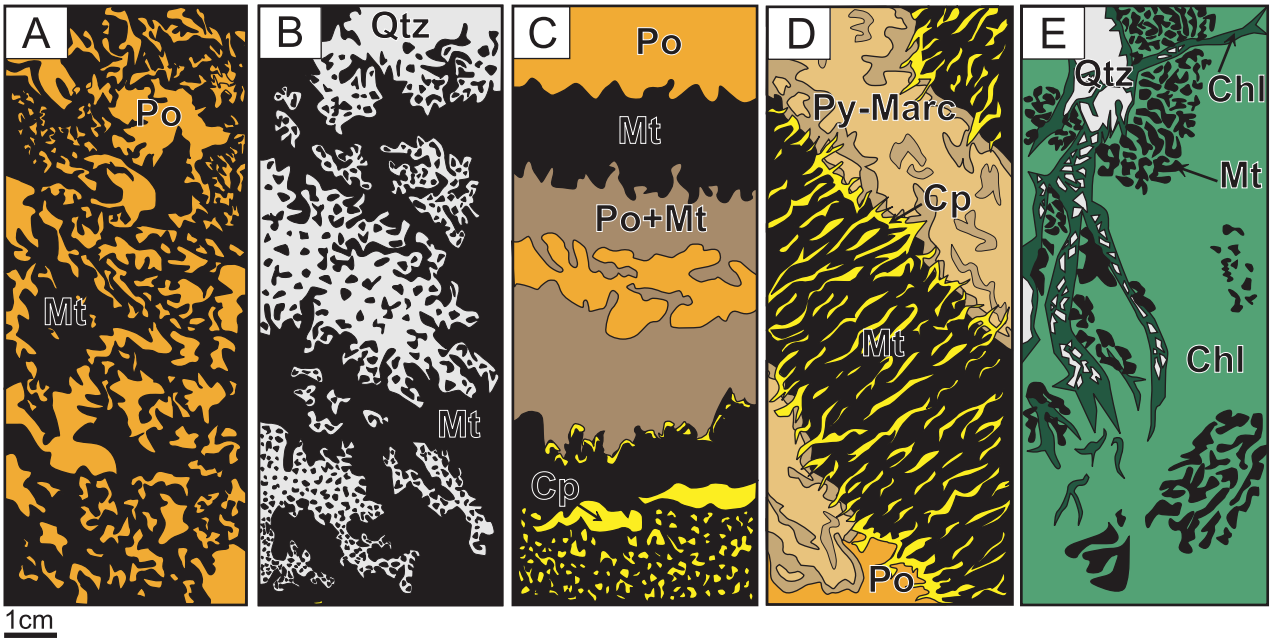

Figure 2.10 Sketches of drill core samples illustrating massive magnetite textures at West Ansil. A) Massive magnetite replacing pyrrhotite from the Upper lens. The massive magnetite contains abundant pyrrhotite inclusions which suggest later introduction of magnetite; WAN086. B) Massive magnetite from the Upper lens replacing strongly silicified basalt fragments and forming a continuous matrix in the pseudobreccia. Minor chlorite and actinolite are also overprinted by magnetite; WAN072. C) Massive magnetite and pyrrhotite from the Upper lens. Massive magnetite generally forms re-entrant cusps into the pyrrhotite. Alternating centimeter-scale bands of pyrrhotite show evidence of extensive remobilization. The magnetite also contains an abundance of disseminated and veinlet chalcopyrite introduced during late remobilization of sulphides into fractures developed in the more brittle magnetite; WAN073. A chalcopyrite-rich rim occurs at the contact between magnetite and pyrrhotite. D) Massive magnetite band from the Middle Lens. The magnetite band appears to crosscut the more massive pyrrhotite. Remobilized chalcopyrite veinlets are present throughout the magnetite in late brittle fractures and along the contact with pyrrhotite. Colloform pyrite-marcasite along the pyrrhotite-magnetite contact locally replaces pyrrhotite but not magnetite; WAN010. E) A magnetite-quartz-chlorite vein cutting basalt at the top of the Upper lens, 10 centimeters from the massive magnetite contact; WAN084.

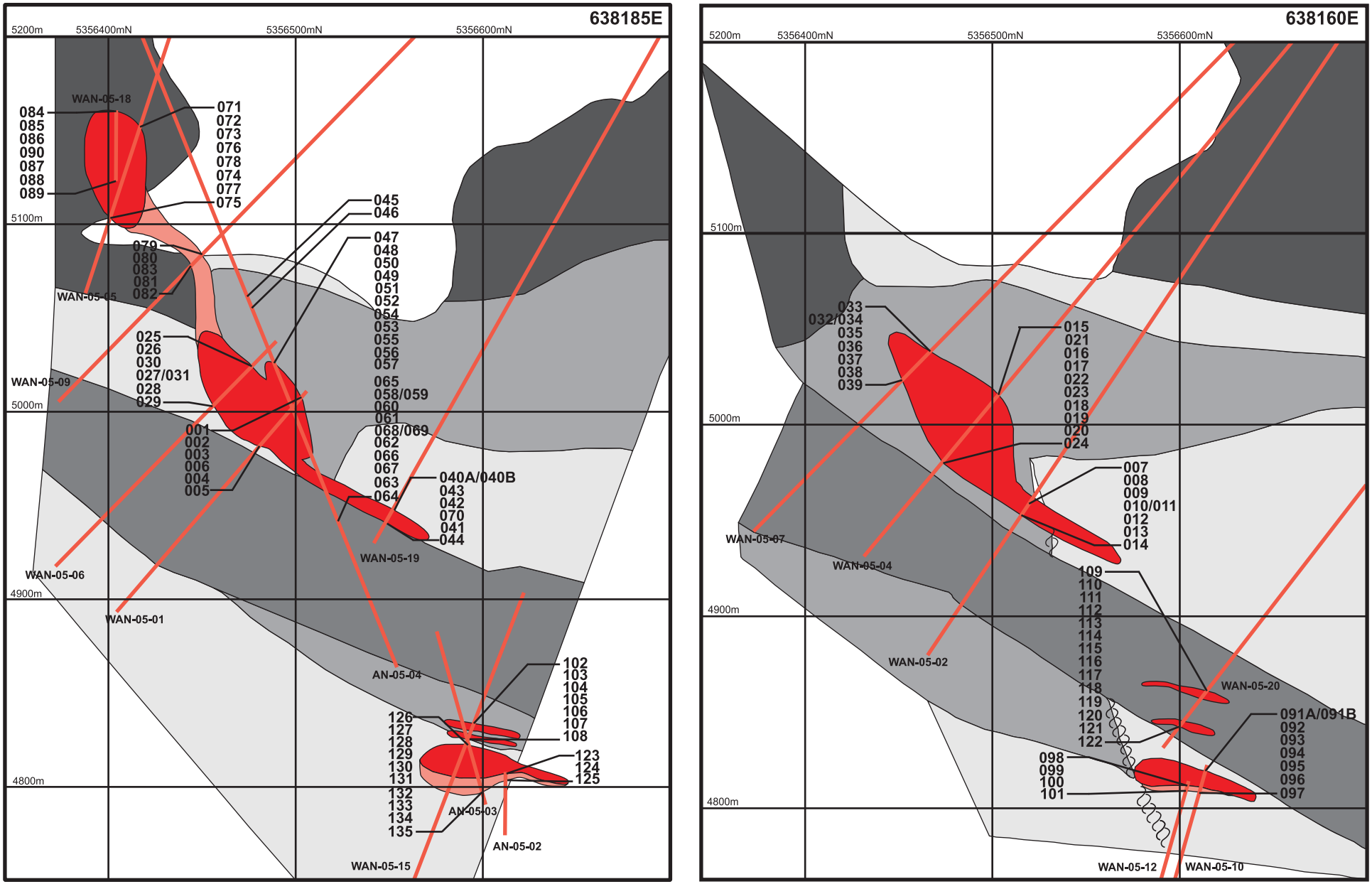

Figure 2.11 Vertical north-south cross-sections showing sample locations on drill holes (red lines) in the Upper, Middle and Lower lenses of the West Ansil deposit (modified after Xstrata Copper Canada Ltd, 2005).

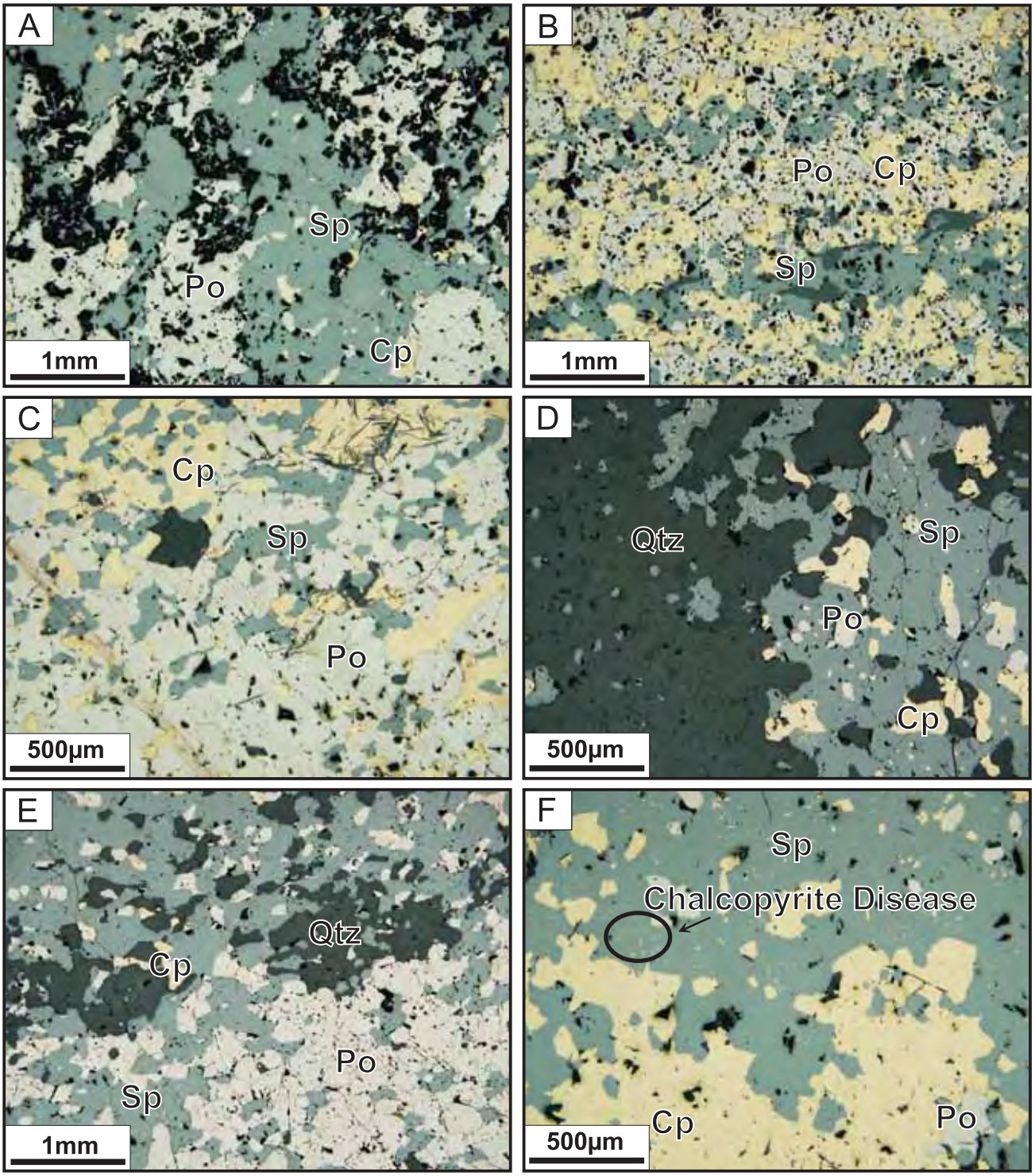

Figure 2.12 Reflected light photomicrographs of representative sphalerite ore textures in the Middle lens of the West Ansil deposit. A) Massive anhedral sphalerite intergrown with pyrrhotite and minor chalcopyrite along grain boundaries; WAN021. B) Alternating bands of sphalerite and pyrrhotite with chalcopyrite infilling along smooth discontinuous contacts; WAN020. C) Sphalerite and pyrrhotite bands at higher magnification; chalcopyrite is abundant along contacts and grain boundaries; WAN019. D) Semi-massive sphalerite intergrown with quartz and containing abundant anhedral inclusions of pyrrhotite and chalcopyrite; WAN032. E) Semi-massive sphalerite and pyrrhotite with quartz; minor chalcopyrite is present along grain boundaries; WAN034. F) Massive sphalerite intergrown with anhedral chalcopyrite. Typical "chalcopyrite disease" occurs in the sphalerite; WAN015.

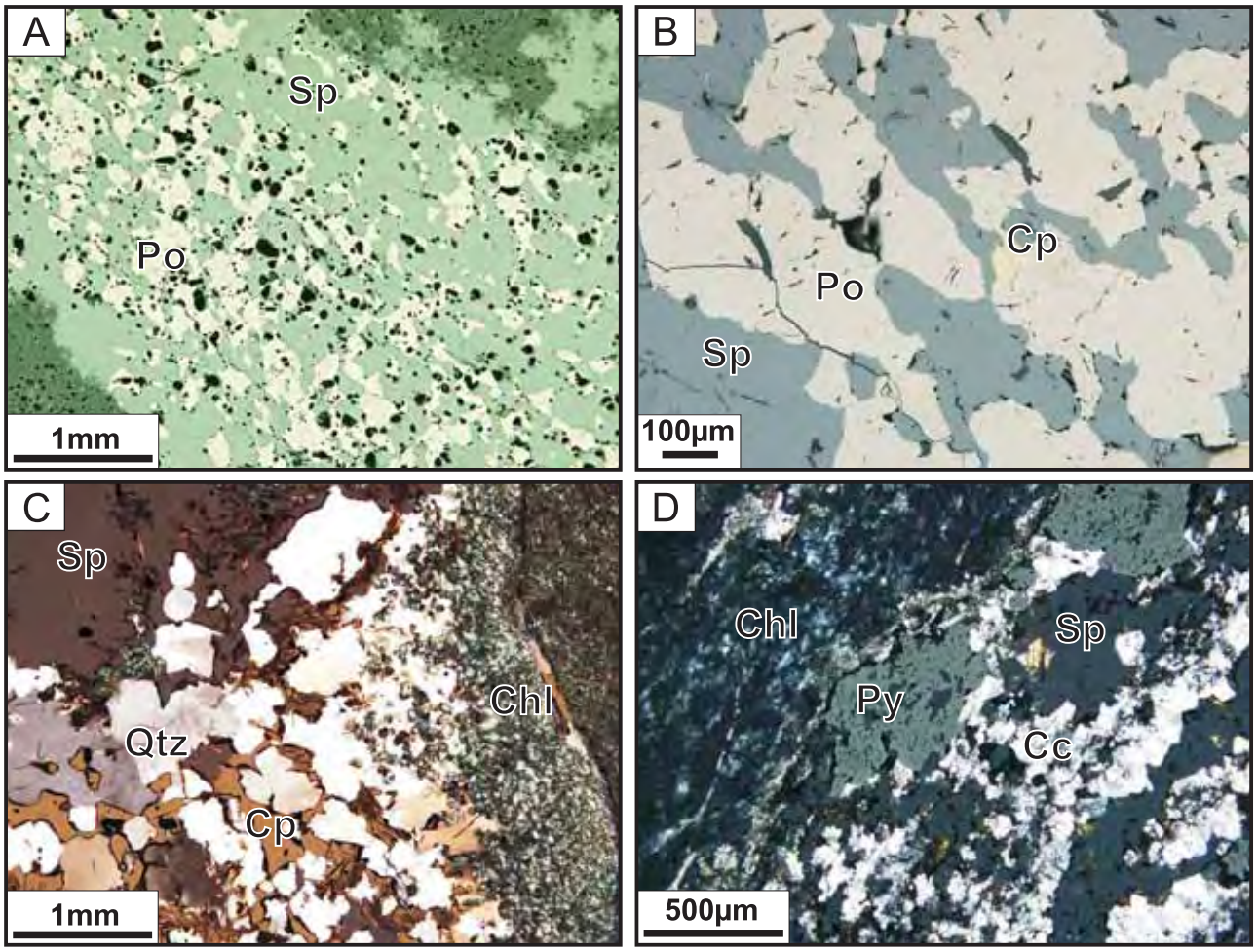

Figure 2.13 Photomicrographs of representative sphalerite stringer ore and remobilized sphalerite textures in the West Ansil deposit. A) Sphalerite and pyrrhotite stringer in the Middle lens within a chlorite and actinolite matrix. Reflected light; WAN018. B) Typical fine-grained anhedral chalcopyrite, pyrrhotite and sphalerite in a stringer of the Middle lens. Reflected light; WAN018. C) Chalcopyrite and sphalerite in quartz cross-cutting chloritic wallrock. Fine chlorite is abundant in the vein adjacent to the wallrock fragment. Reflected and transmitted crossed polarized light; WAN133. D) Fine-grained sphalerite and siderite in a late vein from the bottom of the Middle lens. Coarse euhedral pyrite grains are also present and intergrown with sphalerite. Reflected and transmitted crossed polarized light; WAN013.

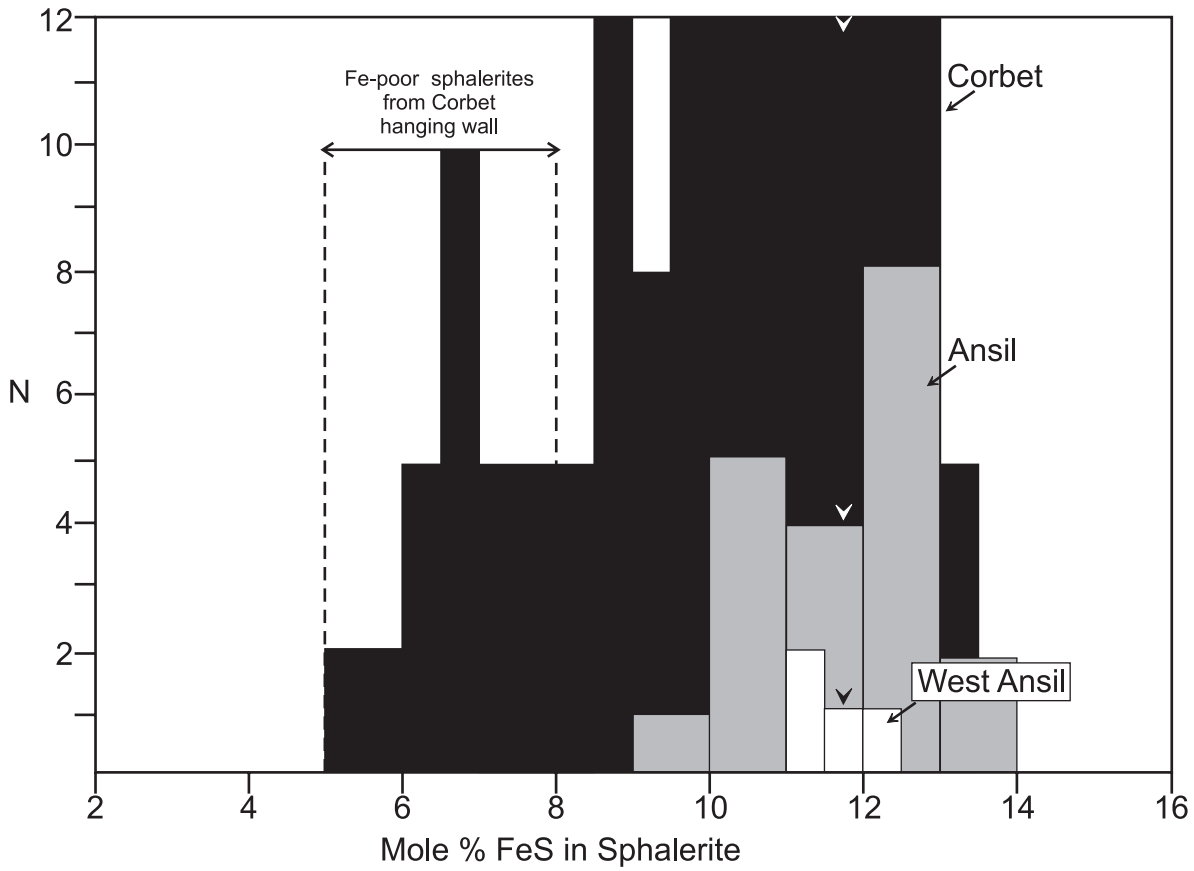

Figure 2.14 Range of sphalerite compositions in the West Ansil ores based on data from 3 samples (4 analyses). The sphalerite has a very narrow range and falls within the composition of sphalerites from Ansil and Corbet. Arrows indicate the average values. The ranges of sphalerite compositions for Corbet are from Hannington and Scott (1989) and for Ansil from Galley (1994).

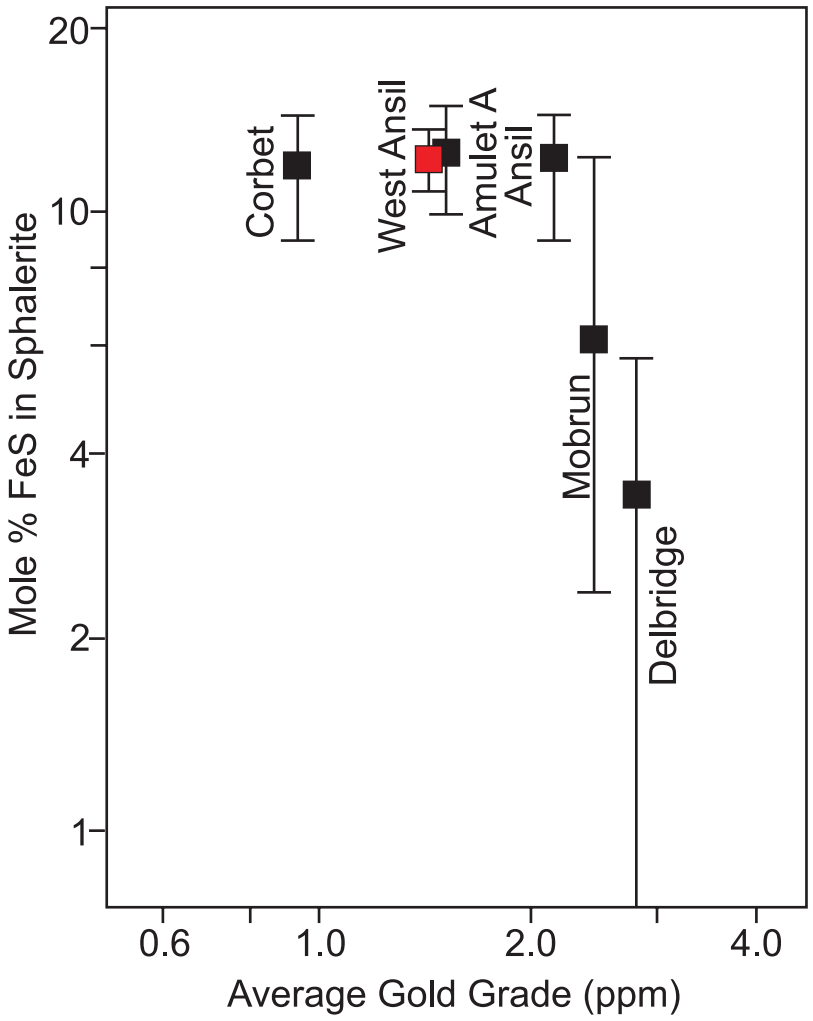

Figure 2.15 A comparison of the average production grade of gold from Archean Cu-Zn deposits in the Noranda district with the average FeS content in associated sphalerite. The data show a higher FeS concentration in deposits lower in stratigraphy versus a lower FeS content in younger deposits of the Noranda district. Data for average mole % FeS from Hannington and Scott (1989) and Galley (1994), and data for average gold production grades from Gibson and Watkinson (1990) and Goutier et al. (2009b).

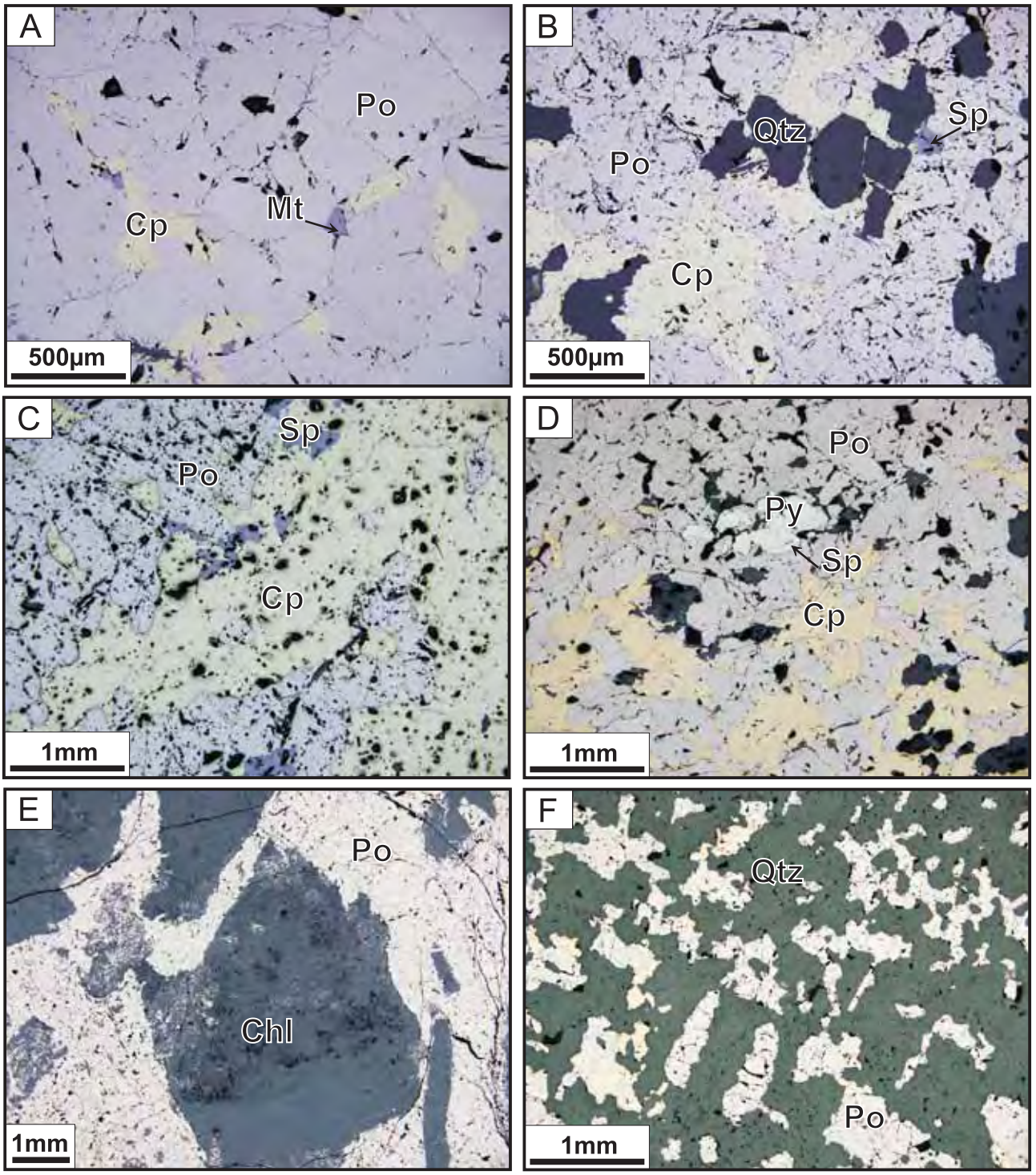

Figure 2.16 Reflected light photomicrographs of representative pyrrhotite ore textures in the West Ansil deposit. A) Massive annealed pyrrhotite from the Upper lens with chalcopyrite infilling grain boundaries and euhedral magnetite within triple junctions of grains; WAN077. B) Massive annealed pyrrhotite from the Lower lens with infilling chalcopyrite and minor sphalerite; WAN114. C) Pyrrhotite- and chalcopyrite-rich alternating bands from the Middle lens showing a smooth contact between bands, with remobilized sphalerite along the contacts; WAN003. D) Massive pyrrhotite and chalcopyrite from the Lower lens replacing primary pyrite containing sphalerite inclusions; WAN103. E) Semi-massive pitted pyrrhotite from the Middle lens partially replacing chloritized wallrock fragments; WAN065. F) Semi-massive pyrrhotite from the Middle lens intergrown with relict quartz; WAN048.

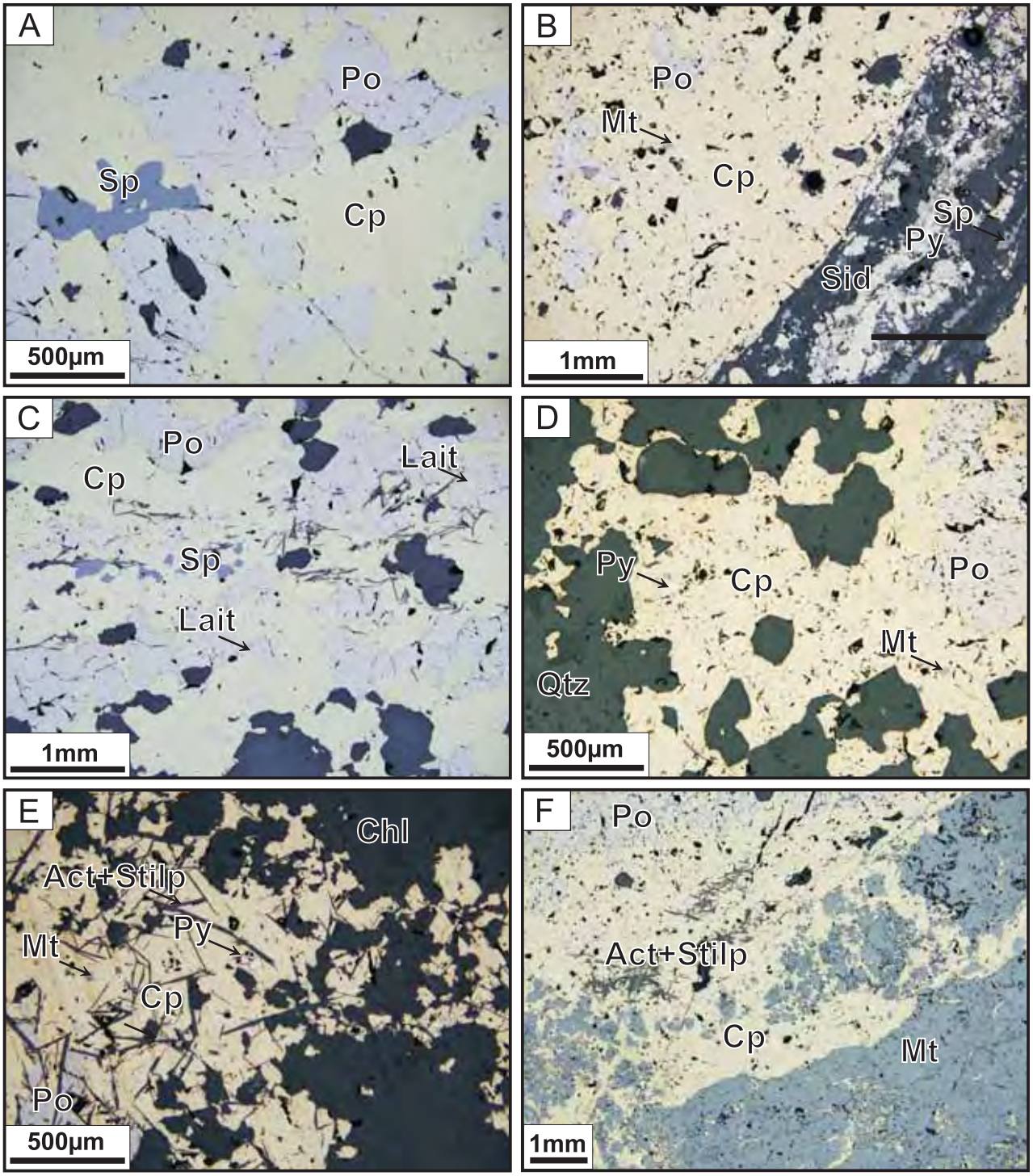

Figure 2.17 Reflected light photomicrographs of representative chalcopyrite ore textures in the West Ansil deposit. A) Massive anhedral chalcopyrite from the Lower lens with inclusions of pyrrhotite with minor sphalerite along grain boundaries; WAN104. B) Massive anhedral chalcopyrite from the Middle lens with inclusions of pyrrhotite and sphalerite in the chalcopyrite. Pyrite, sphalerite and siderite occur along a microfracture; WAN051. C) Massive chalcopyrite from the Lower lens intergrown with pyrrhotite. Minor laitakarite inclusions are present within both pyrrhotite and chalcopyrite; WAN092. D) Semi-massive chalcopyrite from the Middle lens with inclusions of anhedral quartz and pyrrhotite grains, and minor euhedral magnetite along grain boundaries and triple junction. Minor euhedral pyrite is also present; WAN036. E) Semi-massive chalcopyrite from the Lower lens infilling chlorite- and actinolite-rich wallrock fragments. Minor recrystallized fine-grained pyrite and magnetite occur along grain boundaries. Abundant euhedral needles of actinolite and stilpnomelane occur in the massive chalcopyrite; WAN091B. F) Coarse-grained magnetite grain intergrown with massive chalcopyrite from the Lower lens, with minor pyrrhotite and actinolite and stilpnomelane needles in the chalcopyrite; WAN093.

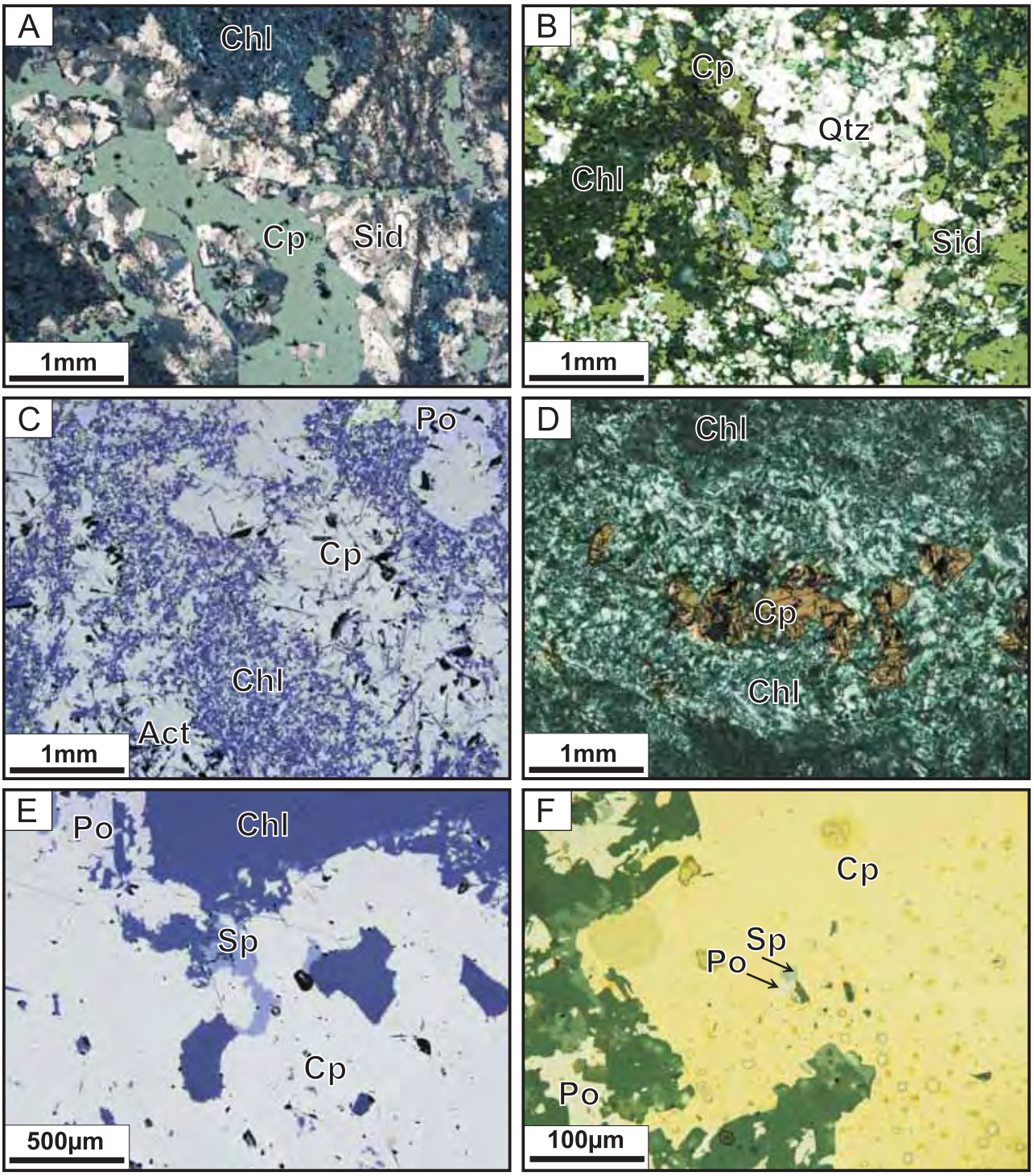

Figure 2.18 Photomicrographs of representative chalcopyrite stringer ore textures in the West Ansil deposit. A) Chalcopyrite from network-like veinlets within chloritic wallrock from the Middle lens. Siderite is interpreted to be late. Reflected and transmitted crossed polarized light; WAN012. B) Chalcopyrite with fine-grained quartz and late siderite stringers from the Lower lens with chloritized wallrock fragments. Reflected and transmitted crossed polarized light; WAN125. C) Chalcopyrite, pyrrhotite and chlorite network-like veinlets from the Lower lens within chlorite-rich wallrock. Abundant actinolite and stilpnomelane needles occur in the chalcopyrite and chloritized wallrock fragments. Reflected and transmitted crossed polarized; WAN111. D) Chalcopyrite and chlorite stringer within chlorite-rich wallrock from the Lower lens. Actinolite and stilpnomelane needles are mostly intergrown with chalcopyrite. Reflected and transmitted crossed polarized; WAN129. E) Minor andedral sphalerite within chalcopyrite stringer from the Lower lens. Reflected light; WAN129. F) Pyrrhotite and sphalerite inclusions within anhedral chalcopyrite grains in the Lower stringer zone. Reflected light; WAN111.

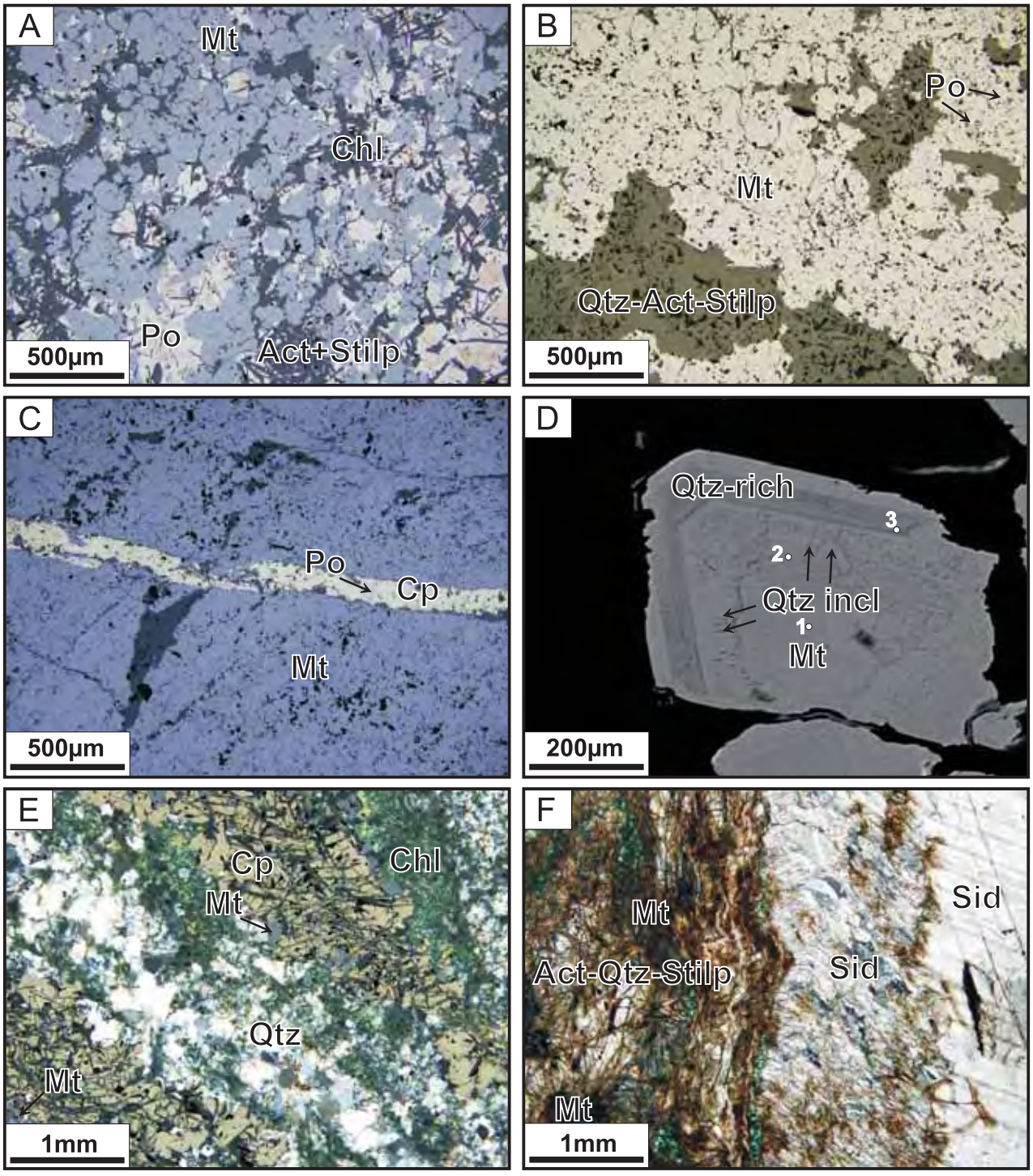

Figure 2.19 Photomicrographs of representative magnetite ore textures in the West Ansil deposit. A) Aggregates of subhedral to euhedral magnetite from the Middle lens intergrown with pyrrhotite along grain boundaries and with minor chlorite, actinolite and stilpnomelane. Reflected light; WAN066. B) Compact massive magnetite from the Upper lens with minor pyrrhotite inclusions, and quartz, actinolite and stilpnomelane. Reflected light; WAN072. C) Veinlets of chalcopyrite with minor pyrrhotite occupying a brittle fracture of massive magnetite from the Upper lens. Reflected light; WAN060. D) Large euhedral magnetite grain (light grey) zoned with submicroscopic quartz inclusions (dark grey) from the Upper lens. 1, 2 and 3 represent the location of electron microprobe analysis (Backscattered Electron Image); WAN071. E) Quartz-magnetite vein from the Lower lens intergrown with chalcopyrite and chlorite. Actinolite and stilpnomelane are present in the chalcopyrite. Reflected and transmitted crossed polarized; WAN127. F) A late-stage magnetite-quartz-siderite vein from the Lower lens. Fine-grained magnetite is intergrown with quartz, actinolite and stilpnomelane, and surrounded by coarse sideraite grains. Reflected and transmitted crossed polarized; WAN116.

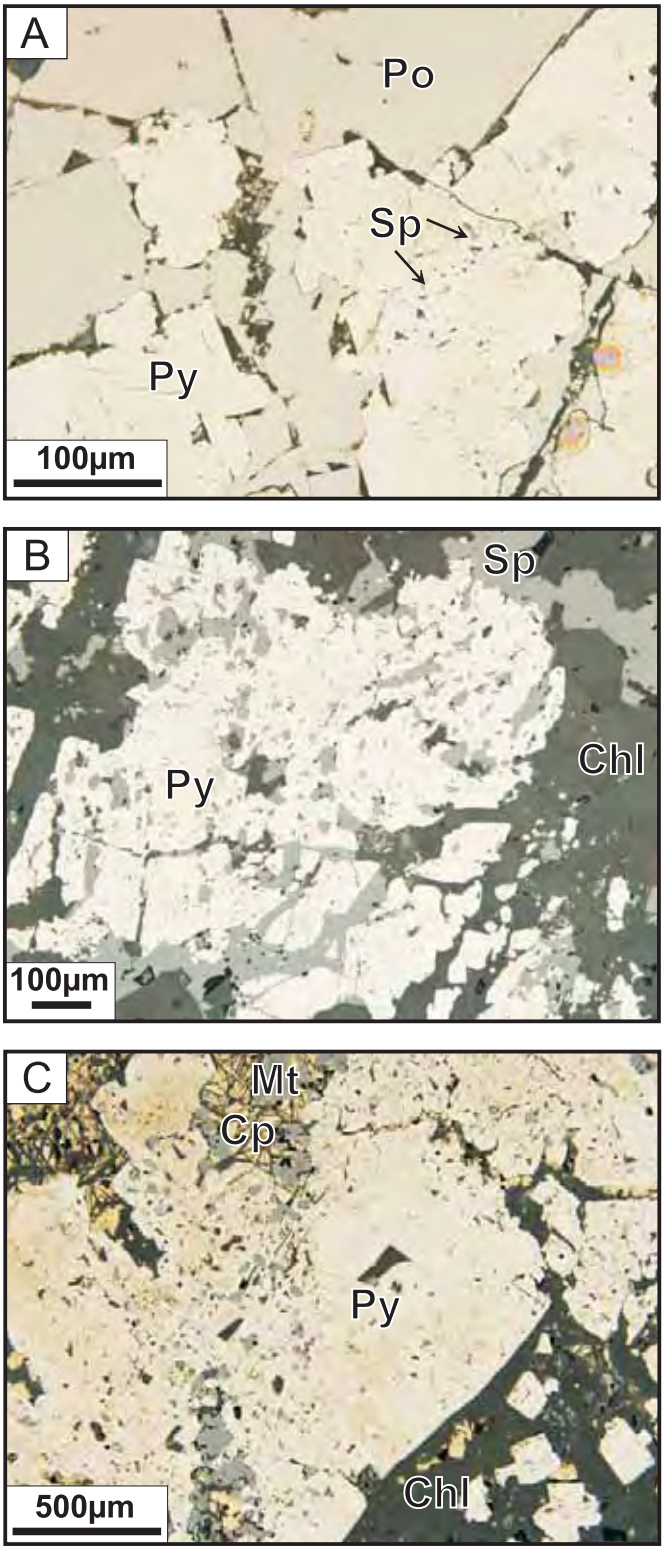

Figure 2.20 Reflected light photomicrographs of primary pyrite in the West Ansil deposit. A) Blocky medium-grained primary pyrite with sphalerite inclusion in massive pyrrhotite from the Lower lens; WAN104. B) Coarse euhedral pyrite porphyroblast intergrown with remobilized sphalerite and late siderite in chloritic wallrock along the bottom contact of the Middle lens; WAN013. C) Coarse euhedral pyrite porphyroblast displaying a poikiloblastic texture intergrown with fracture-controlled magnetite, along the upper contact of the Lower lens; WAN127.

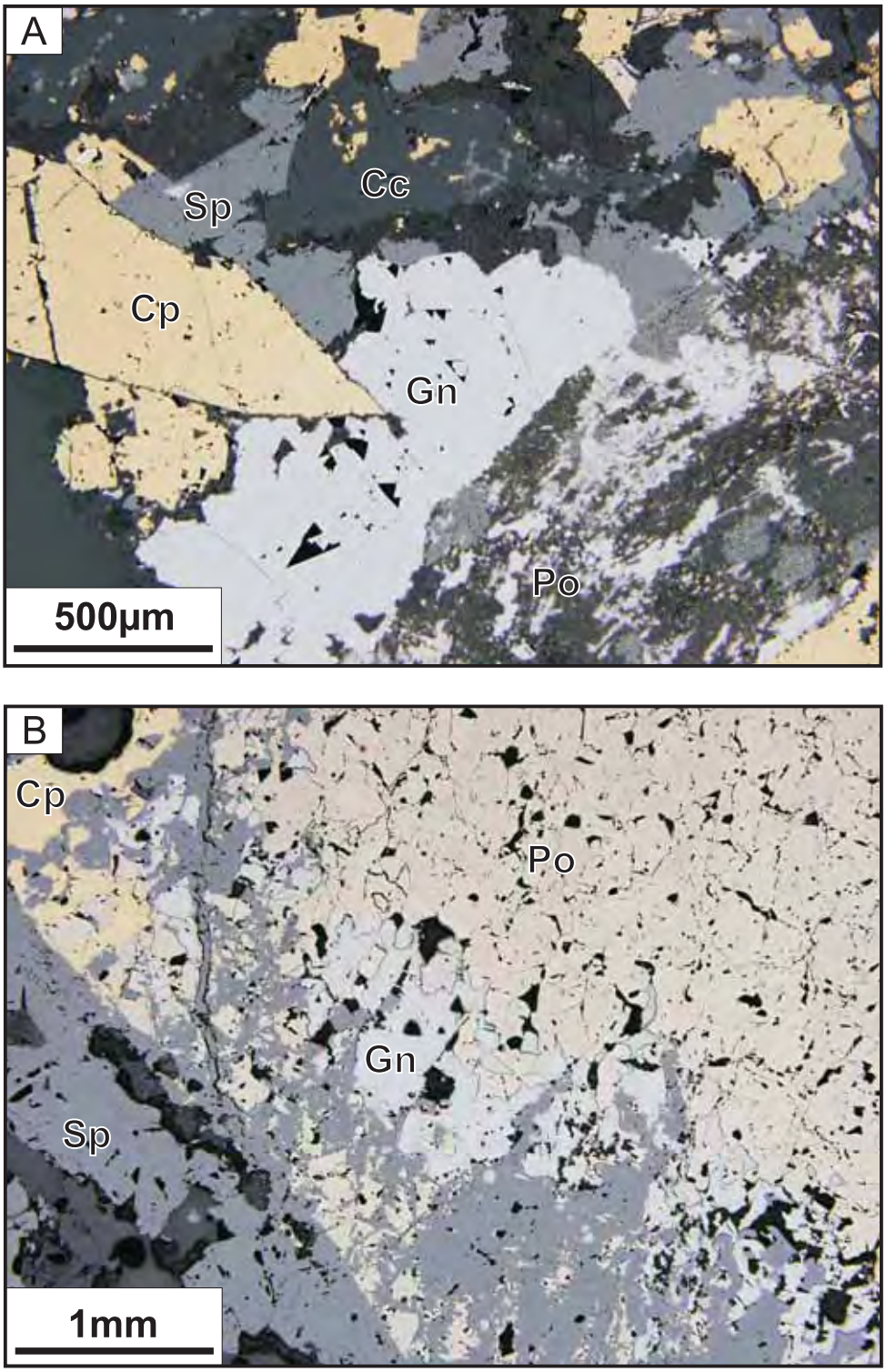

Figure 2.21 Reflected light photomicrographs of the occurrence of galena in the West Ansil deposit. A) Remobilized galena, sphalerite and chalcopyrite in a quartz-siderite veinlet within chloritic wallrock at the upper contact of the Middle lens; WAN040A. B) Remobilized galena and sphalerite within massive pyrrhotite from the Lower lens with minor chalcopyrite in contact with a late siderite vein; WAN121.

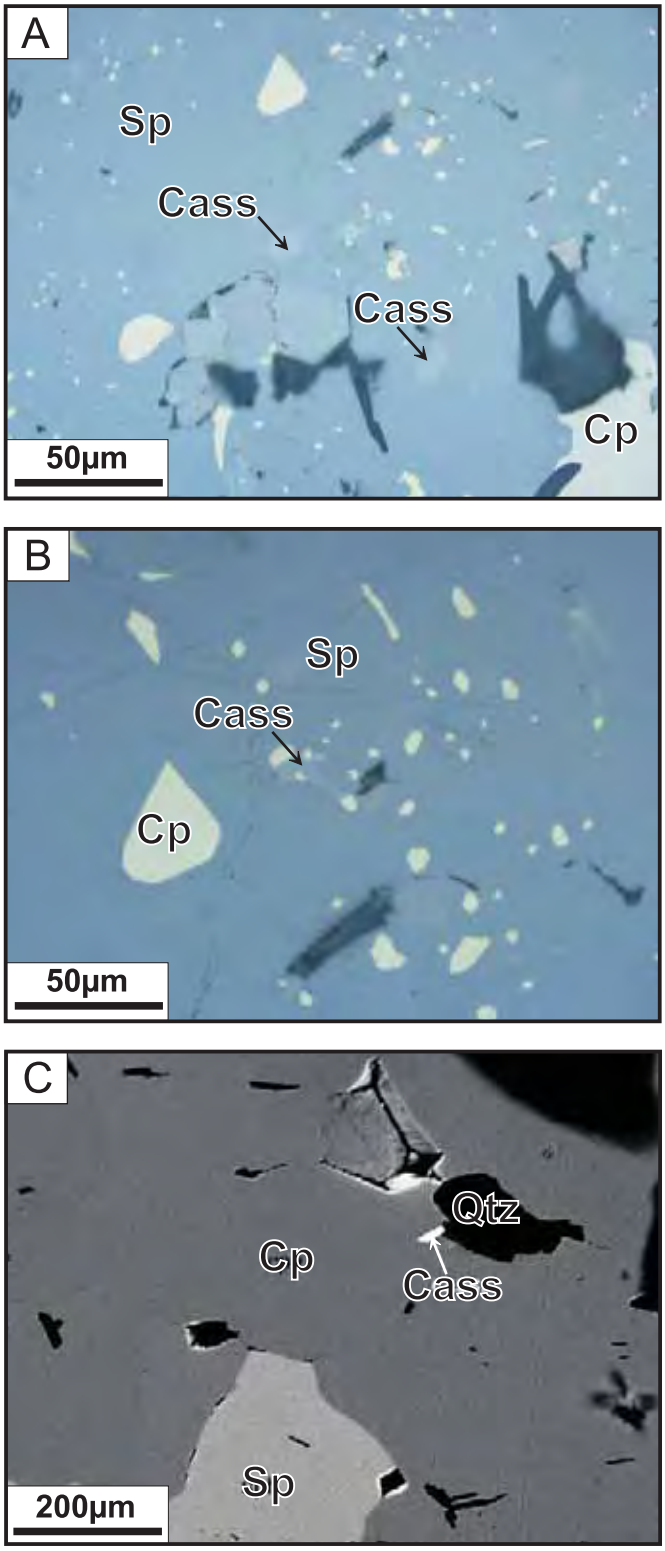

Figure 2.22 Reflected light photomicrographs of the occurrence of cassiterite in the West Ansil deposit. A) Rounded fine grains of cassiterite disseminated with chalcopyrite in massive sphalerite from the Middle lens; WAN015. B) Fine grain of cassiterite with disseminated chalcopyrite in massive sphalerite from the Middle lens; WAN021. C) Fine subhedral cassiterite grain (white) along a quartz grain within massive chalcopyrite from the Lower lens (backscattered electron image); WAN092.

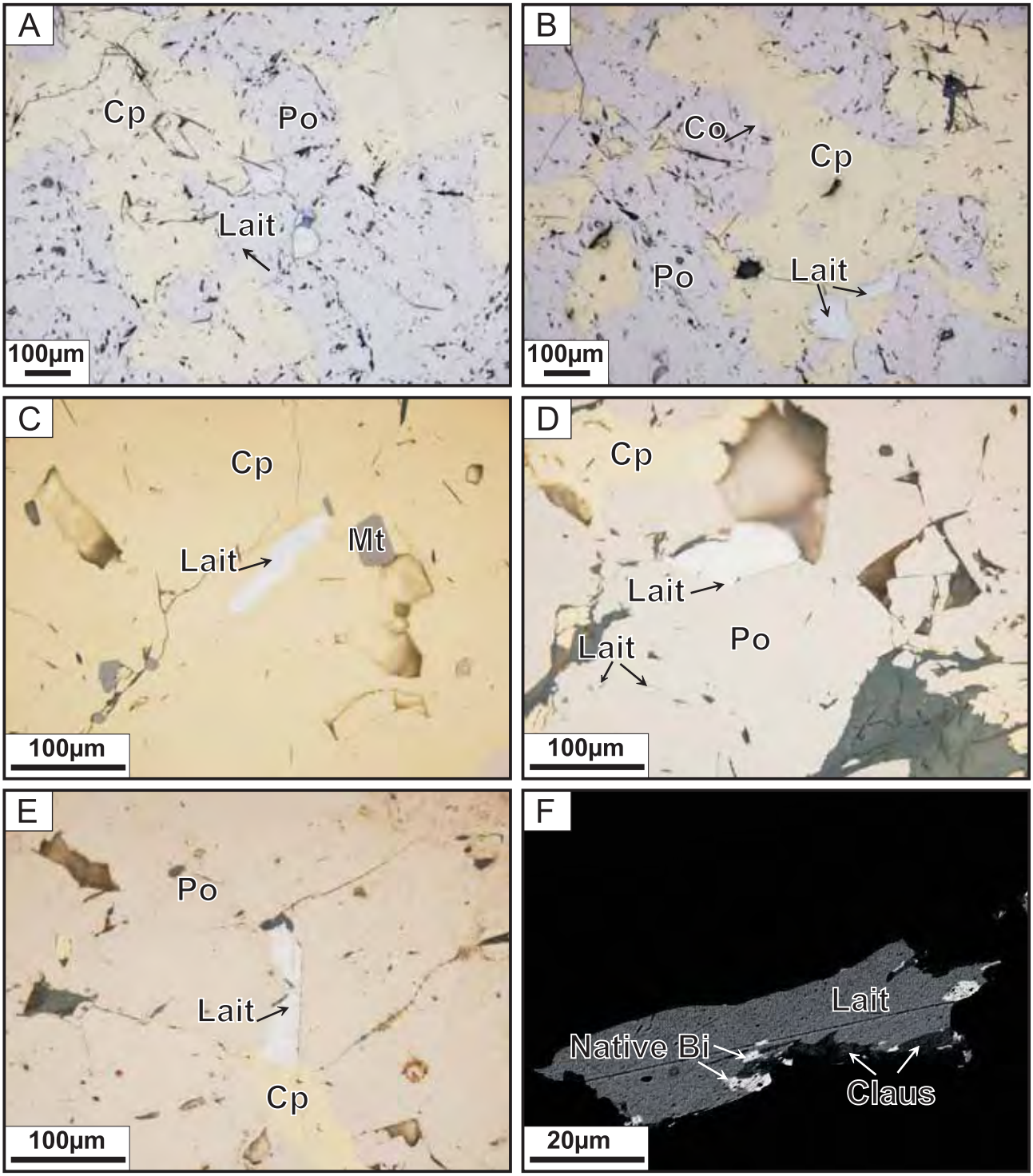

Figure 2.23 Reflected light photomicrographs of the occurrence of laitakarite in the West Ansil deposit. A) Large grains of subhedral laitakarite disseminated within pyrrhotite and chalcopyrite grains in massive chalcopyrite ore from the Middle lens; WAN004. B) Large subhedral laitakarite grains within chalcopyrite and fine-grained cobaltite replacing pyrrhotite in massive chalcopyrite ore from the Middle lens; WAN052. C) Bladed fine-grained laitakarite in massive chalcopyrite ore from the Lower lens; WAN092. D) Disseminated fine-grained subhedral laitakarite grains and bladed laitakarite in massive pyrrhotite ore from the Middle lens; WAN043. E) Bladed laitakarite in pyrrhotite from the chalcopyrite stringer ore of the Lower stockwork zone; WAN125. F) Inclusions of native Bi (white) in a laitakarite (grey) grain rimmed with clausthalite (dark grey) in massive pyrrhotite ore from the Middle lens (backscattered electron image); WAN043.

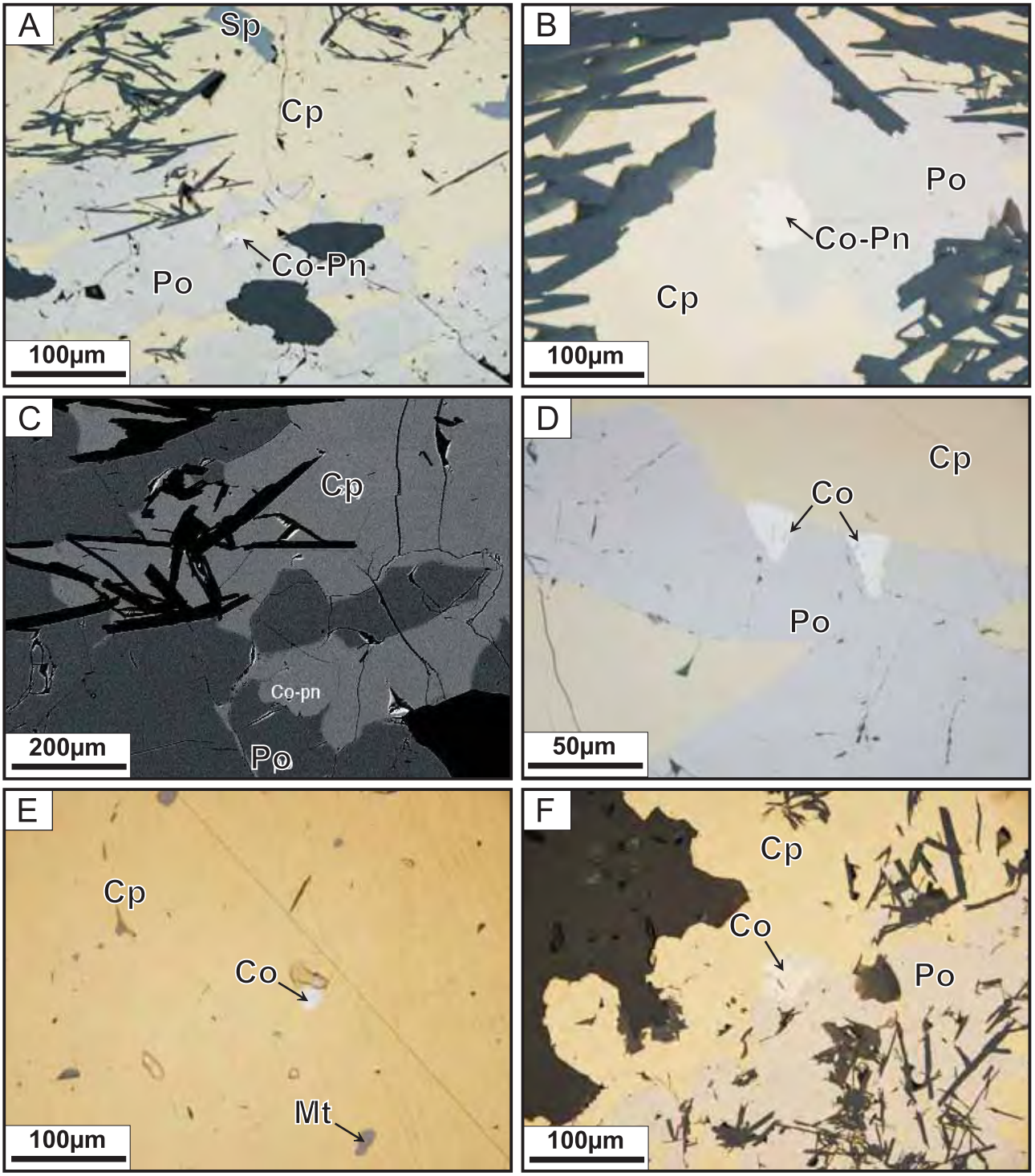

Figure 2.24 Reflected light photomicrographs of the occurrence of Co-pentlandite and cobaltite in the West Ansil deposit. A) Rounded fine-grained Co-pentlandite replacing pyrrhotite within massive chalcopyrite from the Lower lens; WAN092. B) Large rounded Co-pentlandite grain replacing pyrrhotite in chalcopyrite stringer ore from the Lower stockwork zone; WAN101. C) Co-pentlandite (light grey) disseminated within pyrrhotite (dark grey) in massive chalcopyrite (light grey, similar to Co-pentlandite) from the Lower lens (backscattered electron image); WAN092. D) Disseminated subhedral and fine-grained cobaltite in pyrrhotite from the massive chalcopyrite ore of the Middle lens; WAN004. E) Fine-grained rounded subhedral cobaltite in massive chalcopyrite ore from the Middle lens; WAN052. F) Large euhedral aggregate of cobaltite grains replacing pyrrhotite in chalcopyrite stringer ore from the Lower stockwork zone; WAN095.

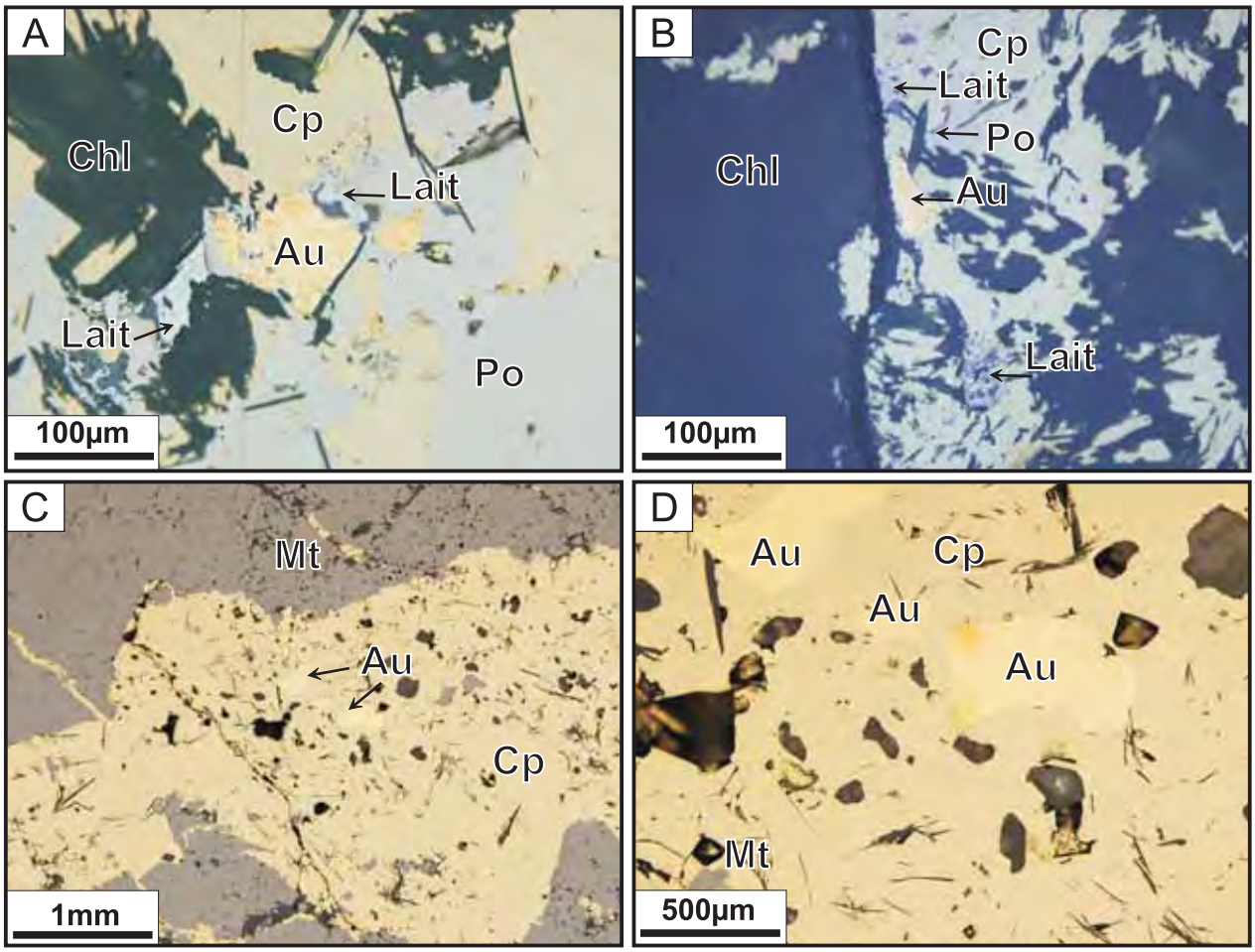

Figure 2.25 Reflected light photomicrographs of the occurrence of gold in the West Ansil deposit. A) Anhedral grains of gold and laitakarite as inclusions in remobilized chalcopyrite in a chlorite veinlet cutting massive pyrrhotite from the Middle lens; WAN006. B) Very fine-grained gold and laitakarite in a remobilized chalcopyrite veinlet; WAN006. C) Rounded and fine gold grains in remobilized chalcopyrite along a magnetite-pyrrhotite contact from the Middle lens; WAN062. D) Close up of E, rounded gold grains up to 0.5mm in size within remobilized chalcopyrite. Note that the gold grains are variably cut and truncated against actinolite needles in the chalcopyrite; WAN062.

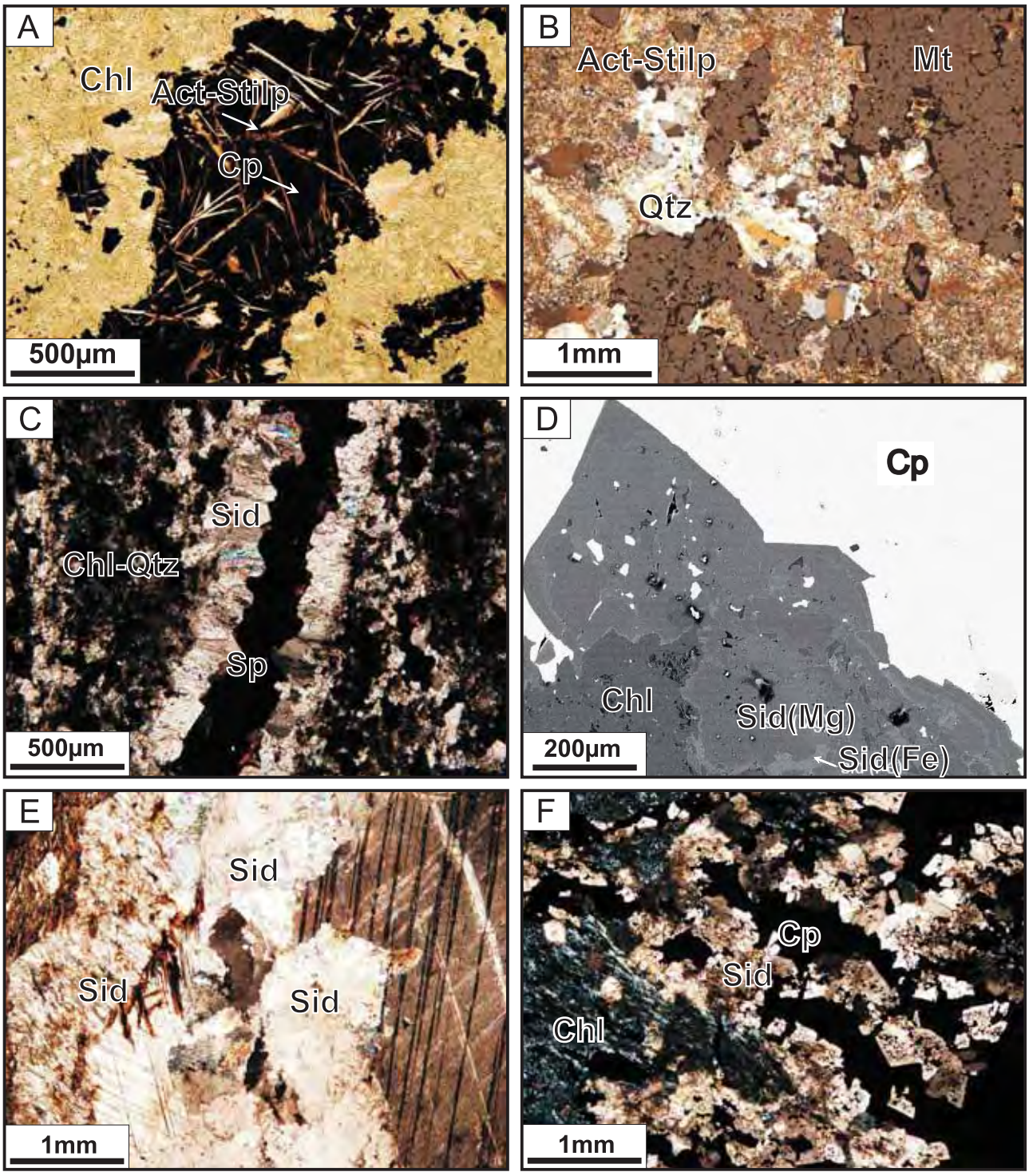

Figure 2.26 Photomicrographs of representative ore-related gangue minerals in the West Ansil deposit. A) Actinolite and stilpnomelane needles intergrown with chalcopyrite in chlorite-rich wallrock from the Middle lens. Transmitted plane polarization light used for photomicrograph; WAN039. B) Fine-grained actinolite and stilpnomelane needles intergrown with quartz in massive magnetite from the Upper lens. Reflected and transmitted crossed polarization used for photomicrograph; WAN072. C) Euhedral siderite lining a remobilized sphalerite veinlet within chloritized wallrock along the bottom contact of the Middle lens. Transmitted crossed polarization light used for photomicrograph; WAN013. D) Late siderite overgrowing chlorite in a remobilized chalcopyrite vein. The siderite is Fe-rich at the contact with chlorite (Backscattered Electron Image); WAN012. E) Coarse siderite vein occurring with magnetite and actinolite in the Lower lens. Transmitted crossed polarization light used for photomicrograph; WAN116. F) Coarse subhedral siderite and chalcopyrite veins within chlorite-rich wallrock from the Middle Lens. Transmitted crossed polarization light used for photomicrograph; WAN102.

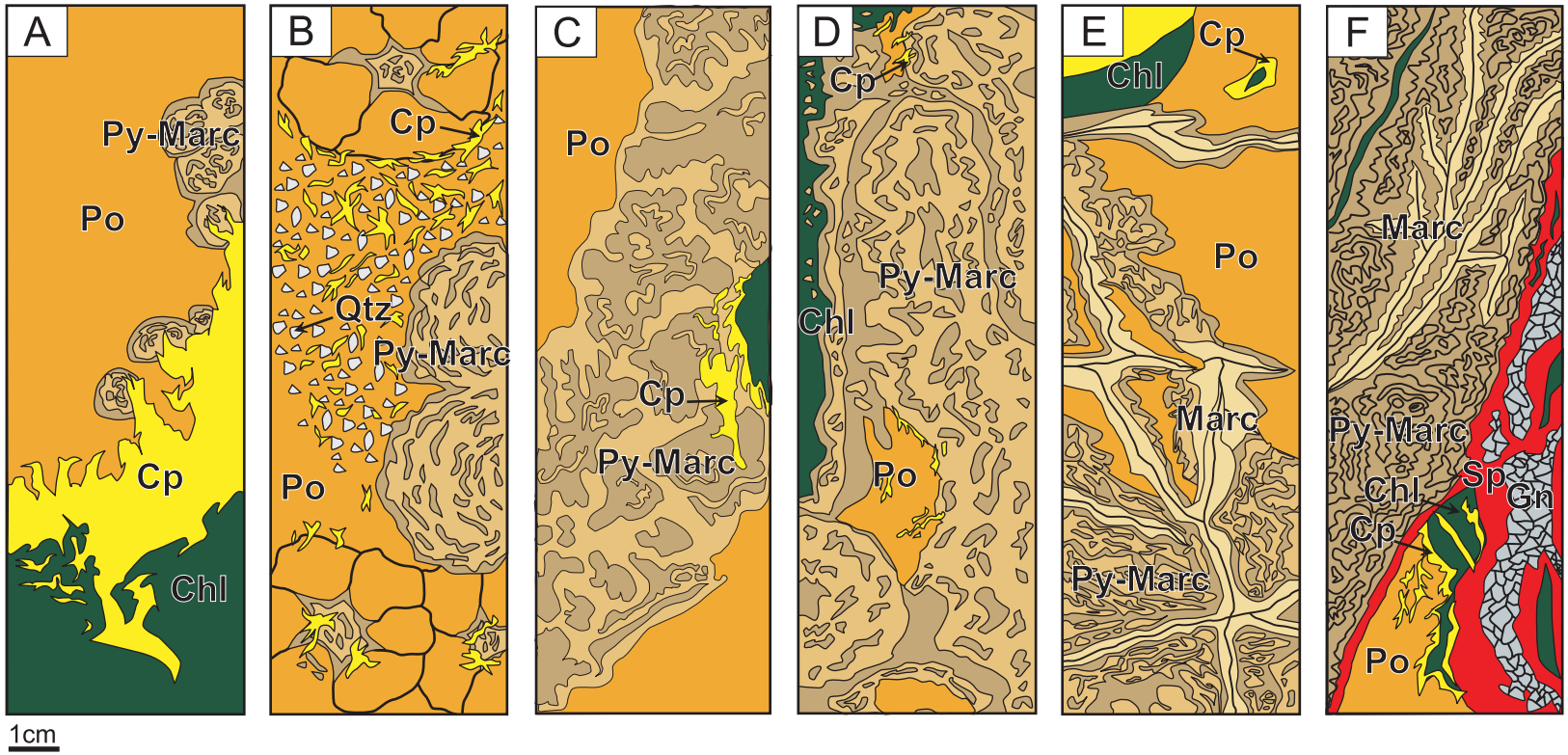

Figure 2.27 Sketches of drill core samples illustrating colloform pyrite-marcasite textures in the West Ansil orebody. A) Massive sulphide at the bottom of the Middle lens with remobilized chalcopyrite separating the chloritized footwall basalt from the massive pyrrhotite. Remobilized chalcopyrite-rich stringers extend into both the sulphides and wall rock. Colloform centimetre-scale pyrite-marcasite nodules selectively replace the fine-grained pyrrhotite along the lower sulphide contact; WAN029. B) Colloform pyrite-marcasite replacing massive pyrrhotite in the Middle lens. Fracture-controlled centimeter-scale pyrite-marcasite nodules and spheroids are centered on late fractures and invade the massive pyrrhotite. Remobilized chalcopyrite also occurs in the late fractures. The radial pattern of some fractures reflect volume loss during replacement of pyrrhotite by pyrite and marcasite; WAN026. C) Colloform pyrite-marcasite band in massive pyrrhotite from the Upper lens where late-stage pyrite-marcasite is selectively replacing pyrrhotite along a fracture; No sample. D) Massive colloform pyrite-marcasite along the bottom contact of the Middle Lens. Nodular pyrite and marcasite form spheroidal bodies have packed together to form a centimeter-scale colloform band replacing pyrrhotite; No sample. E) Colloform pyrite-marcasite in massive pyrrhotite in the Middle lens. Replacement of pyrrhotite by centimetre-scale spheroidal bodies of pyrite-marcasite occurs along and between late fractures. Recrystallized pyrite is present within the fractures and remobilized sphalerite fills; WAN042. F) Colloform pyrite-marcasite centimeter-scale band along the upper contact of the Middle Lens formed from nodular fine-grained pyrite and marcasite. Recrystallized millimetre-scale marcasite veinlets are also present within fractures and are closely spatially associated to pyrite nodules a few centimeters above. A large centimetre-scale remobilized sphalerite-galena vein is also present along the upper contact; WAN016.

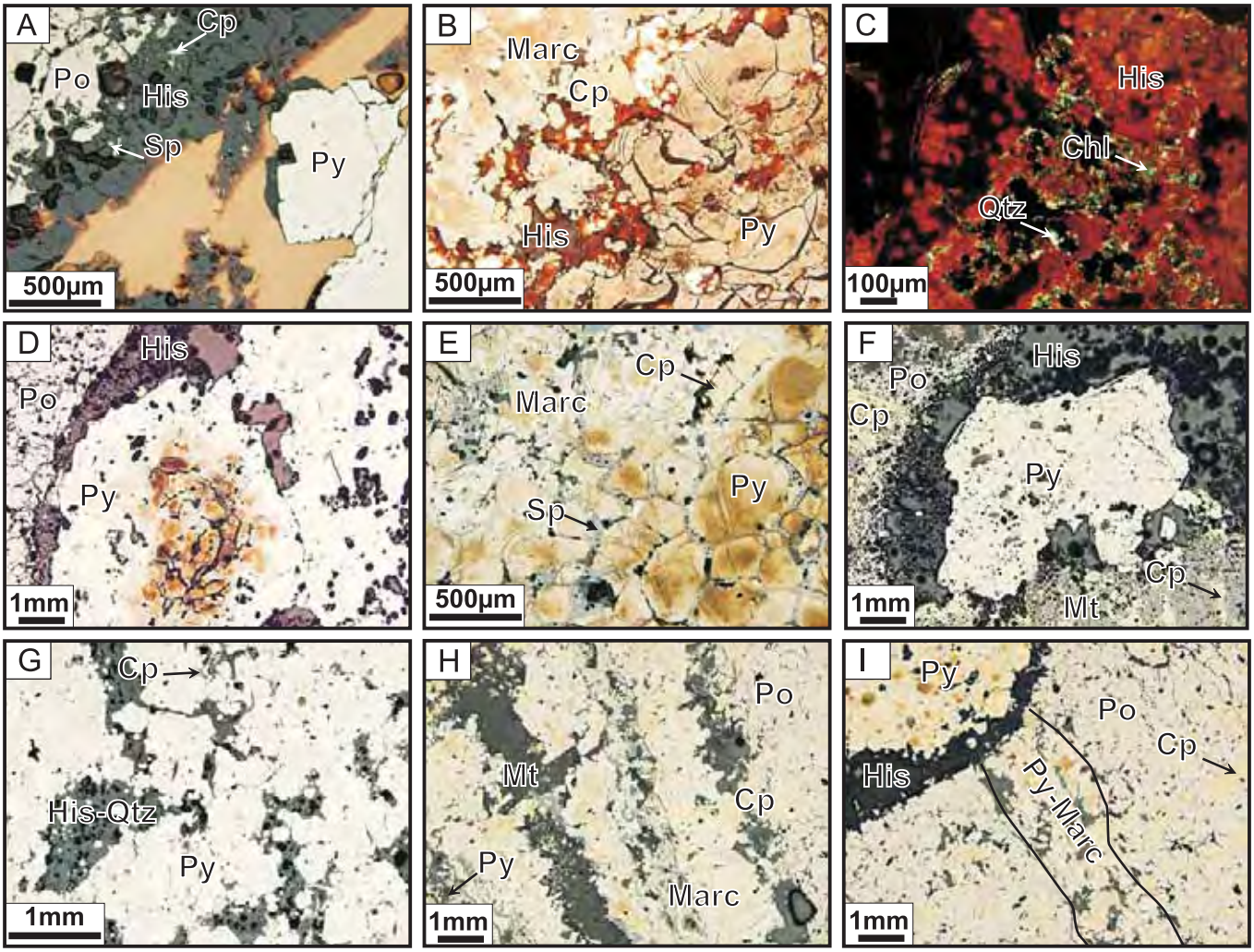

Figure 2.28 Reflected light photomicrographs of representative colloform pyrite-marcasite textures in the West Ansil deposit. A) Amorphous hisingerite displaying shrinkage cracks from the replacement of pyrrhotite by colloform pyrite and marcasite in the Middle lens. Angular fragments of Cp, Sp and Po are present in hisingerite. Reflected and transmitted plane polarization used for photomicrograph; WAN002. B) Fractured pyrite nodule from the Lower lens with a marcasite-rich rim and a pyrite-rich center. Hisingerite occurs within the shrinkage cracks with minor chalcopyrite; WAN122. C) Hisingerite with fine-grained chlorite occurring between pyrrhotite and pyrite nodules in the Lower lens. Transmitted crossed polarization light used for photomicrograph; WAN122. D) Pyrite nodule in massive pyrrhotite from the Middle lens. Concentric fractures occur in the turbid center of the nodule. Hisingerite is present between pyrrhotite and pyrite; WAN002. E) Colloform and nodular pyrite in the Middle lens with marcasite-rich rims and pyrite-rich cores. Sphalerite occurs within the concentric fractures, and with minor chalcopyrite; WAN016. F) Colloform pyrite along a pyrrhotite and magnetite contact from the Middle lens with hisingerite and remobilized chalcopyrite; WAN010. G) Massive colloform pyrite from the Middle lens consisting of subhedral to euhedral fine pyrite grains. Minor hisingerite and microcrystalline quartz are present along grain boundaries together with remobilized chalcopyrite; WAN070. H) Medium- to coarse-grained euhedral marcasite with minor magnetite in a fracture within massive pyrrhotite from the Middle lens. The marcasite is closely spatially associated with pyrite nodules a few centimetres above; WAN049. I) Pyrite nodule at the contact with massive pyrrhotite, cut by a pyrite-marcasite vein in the Lower lens; WAN106.

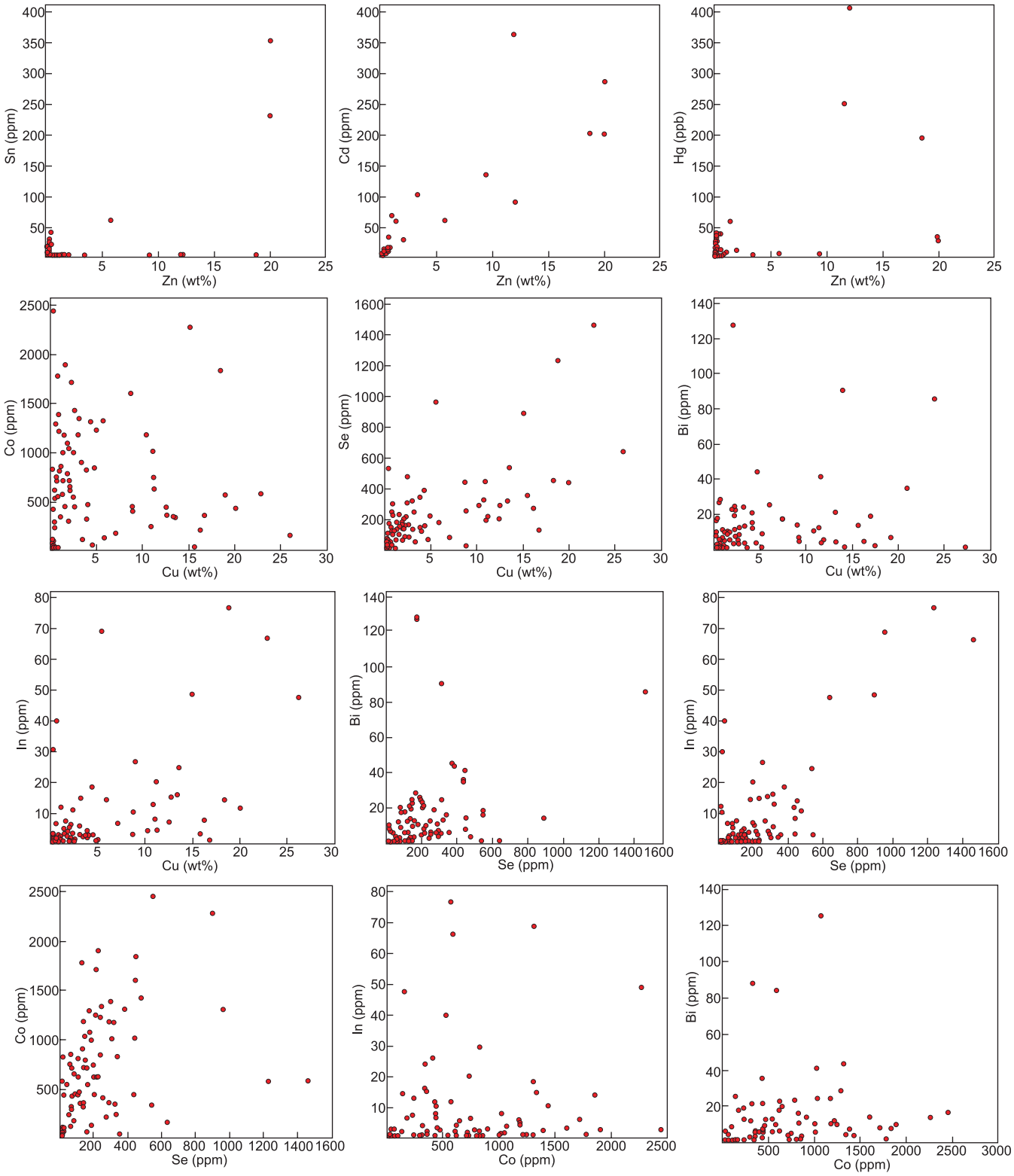

Figure 2.29 Interelement plots of selected trace elements in the ores in the Upper, Middle and Lower lenses of the West Ansil deposit (n = 76). A correlation is observed between Zn and the lower-temperature suite of trace elements Sn, Cd and Hg, whereas Cu is apparently correlated with the higher-temperature suite of trace elements Co, Se, Bi and In.

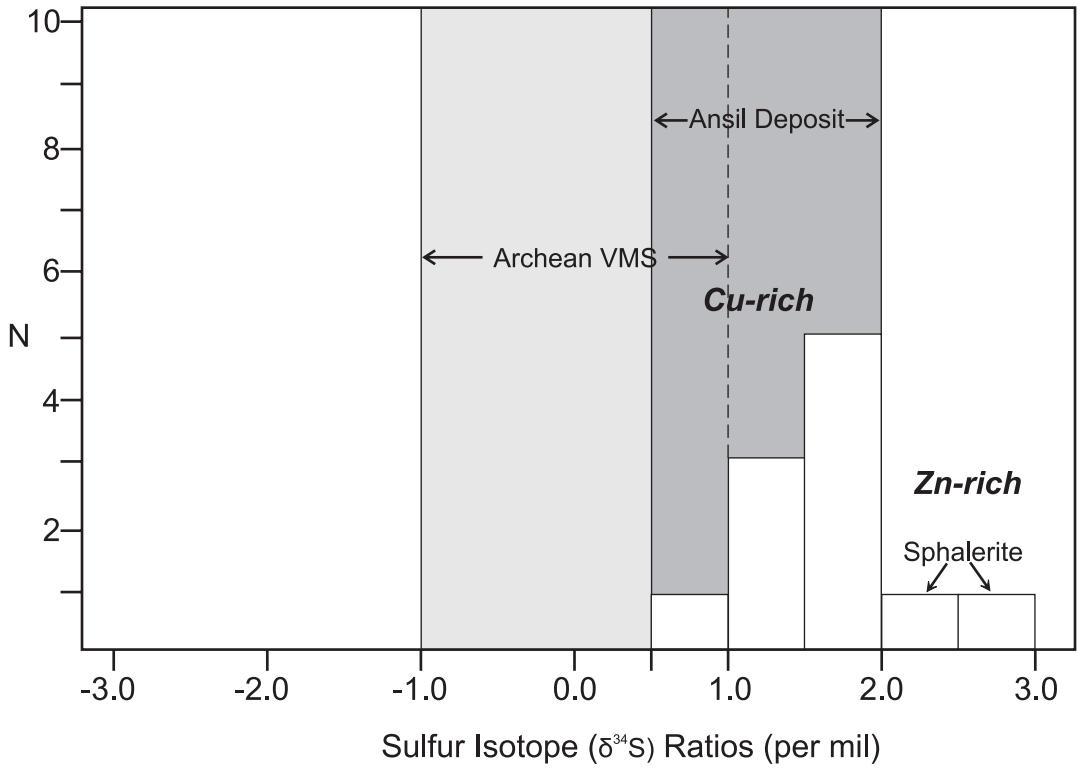

Figure 2.30 Sulfur isotope composition of the West Ansil sulphides. A distribution of $\delta^{34}S$ values from mineral separates of sphalerite, pyrrhotite, chalcopyrite and colloform pyrite-marcasite. Sphalerite is slightly heavier than the other sulphides, and late colloform pyrite-marcasite is indistinguishable from earlier pyrrhotite and chalcopyrite. This suggests that the colloform pyrite-marcasite derived its sulfur from the original pyrrhotite. Data for Archean Cu-Zn deposits from Franklin et al. (1981) and for Ansil from Galley (1994).

CHAPTER 3. ALTERATION OF THE RUSTY RIDGE ANDESITE

3.1 ALTERATION MINERALOGY

The principal alteration minerals in the Rusty Ridge andesite are quartz, chlorite, actinolite and stilpnomelane. Textural relationships among these phases are illustrated in Figures 3.1. The alteration of the host rocks is dominated by quartz and chlorite. Two generations of chlorite are evident: chloritization of wall rock and chlorite in stringers. The earlier stage pervasively replaces the wall rock and occurs as radial, very fine- to medium-grained chlorite displaying a green-blue birefringence (Figure 3.1A and B). Disseminated ilmenite, rutile and titanite are present throughout the chloritized wallrock and occur as clusters of very fine euhedral grains. Locally, minor very fine-grained siderite is disseminated through the rock with ilmenite (Figure 3.1A and B). Fracture-controlled chlorite occurs in the stringer zones as fine- to coarse-grained radial aggregates with a greenish blue to purple birefringence in the Lower and Middle lenses, to berlin blue birefringence towards the Upper lens (Figure 3.1C). It forms network-like veinlets which crosscut the chloritized wall rock. Fine- to medium-grained chlorite associated with chalcopyrite is also present in the stringer zones (Figure 3.1D).

Two generations of quartz are also present: silicification of wall rock and quartz stringers. Two types of quartz stringers are recognized: microcrystalline quartz and chlorite in network-like stringers (Figure 3.1E) and quartz and chalcopyrite veinlets (Figure 3.1F). Quartz replaces the wall rock adjacent to quartz-chlorite stringers (Figure 3.1G). Locally, millimetre-sized quartz-filled amygdules are also present in the altered wall rock of the Lower stringer zone. The quartz-filled amygdules also locally contain minor chalcopyrite (Figure 3.1H).

Very fine- to medium-grained intergrown actinolite and stilpnomelane needles, commonly in a radial pattern, are disseminated throughout the chloritized wall rock (Figure 3.1I

and J). Actinolite is more abundant in the Lower lens and stilpnomelane is more abundant in the Upper lens.

Electron microprobe analyses of silicates and oxides were carried out in 6 polished specimens and chemical compositions for the principal alteration minerals are listed in Table 3.1. The silicates and oxides were analyzed using 20 kV accelerating voltage, 20 nA beam current, and a focused 2 μm diameter beam. Counting times were 10-20 seconds or 40,000 accumulated counts. Chlorite has a narrow range of Fe/Fe+Mg ratios (0.59 to 0.72) in the Upper, Middle and Lower lenses, with a slight Fe enrichment in the Upper lens (Table 3.1). Compositions range from Fe-rich pycnochlorite in the Lower lens and stockwork, to ripidolite in the Middle lens and brunsvigite in the Upper lens (Figure 3.2). The chlorite compositions are very similar to those from the Ansil and Corbet deposits (Table 3.1), where the majority of Fe-rich chlorites are in altered mafic rocks below the ore lenses (Barrett et al., 1991 and Barrett et al., 1993a). Deposits that are higher in stratigraphy appear to have chlorites with variable compositions, spanning a range from low to high Fe contents (clinochlore to ripidolite).

3.2 GEOCHEMISTRY OF THE RUSTY RIDGE ANDESITE

Chemical analyses of 8 samples from the Upper, Middle and Lower lenses of the altered Rusty Ridge andesite are given in Table 3.2, including major, trace and rare earth element geochemical data. These samples were collected immediately above or below massive sulphide contacts and in the Upper and Lower stockwork zones, and were analyzed at Geoscience Laboratories (GeoLabs, Ontario Geological Survey) in Sudbury, Ontario. The analytical methods are described in Appendix XXI.

Major Elements

The Rusty Ridge andesite in the Upper, Middle and Lower lenses is low in Na_2O, K_2O and P_2O_5 and enriched in SiO_2, Fe_2O_3, Al_2O_3 and MgO, reflecting the abundance of hydrothermal minerals such as chlorite, quartz, actinolite and stilpnomelane (Table 3.2). Na_2O is virtually stripped from the rocks in the immediate footwall and hanging wall of the massive sulphides. K_2O concentrations are mostly low (<0.5 wt%) which reflects the absence of sericite in most samples. CaO is also low (<1 wt%); however concentrations increase in the Middle lens (2-4 wt%) due to siderite introduced by late faulting and the intrusion of the large diorite sill directly below the Middle lens (Figure 1.6). SiO_2 concentrations are variable (40-70 wt%) and consistent in all three lenses; however, a slight increase is observed in the immediate footwall and hanging wall of the Middle and Lower lenses reflecting the abundance of quartz. Fe_2O_3 concentrations are also high (~30 wt%) in both the Upper and Middle lenses but decrease towards the Lower lens (10-15 wt%). Al_2O_3 and MgO concentrations are similar in all three lenses, ranging from 7 to 15 wt% Al_2O_3 and 3 to 8 wt% MgO. Al_2O_3 concentrations are slightly higher in the Upper and Middle lenses (up to 18 wt%) than the Lower lens (< 14 wt%). The composition of the strongly chloritized andesite can be superimposed on an anhydrous Si-Al-(Fe+Mg) tetrahedron (Figure 3.3). Tielines between the coexisting minerals on Figure 3.6 outline the fields of the alteration minerals discussed above. The least-altered sample from Ansil plots between the quartz + chlorite and quartz + chlorite $\pm$ sericite field. Most altered samples from West Ansil plot in the quartz + chlorite + magnetite + actinolite + stilpnomelane, consistent with the observed mineralogy field.

Immobile Elements

Most studies of altered volcanic rocks in VMS systems indicate that the high-field-strength elements (HFSE), Ti, Zr, Nb and Y, are relatively immobile during hydrothermal alteration (MacLean and Kranidiotis, 1987; MacLean and Barrett, 1993; Skirrow and Franklin, 1994). Although the absolute concentrations are affected by net mass changes in the system, the inter-element ratios of immobile elements remain the same. Other elements that have been shown to remain essentially immobile during alteration include Al, heavy REE (Lu, Yb), Hf, and Ta (MacLean and Kranidiotis, 1987; MacLean and Barrett, 1993; Gifkins et al., 2005). For samples collected from the Rusty Ridge andesite, the elements Zr, Y, Nb, Hf, Ta, Ti, Al, Th, Yb, and Lu were all tested for immobility, using the methods of MacLean and Kranidiotis (1987).

Zr, Y, and Nb are generally incompatible and their ratios vary according to magmatic affinity (MacLean and Barrett, 1993; Gifkins et al., 2005). Samples of the Rusty Ridge andesite at West Ansil mostly lie within the andesite and andesite/basalt fields of Floyd and Winchester's (1978) discrimination diagram (Figure 3.4). Samples from different magmatic suites produce separate linear trends on incompatible-incompatible element plots (Figure 3.5). At West Ansil, the majority of collected samples fall within the tholeiitic range of a Y-Zr plot (Figure 3.5a), typical of nearly all rocks in the Noranda Camp (Barrett et al., 1991; Barrett et al., 1993a). A few samples that fall outside this range were collected in the Upper and Lower chalcopyrite-chlorite-rich stockwork zones. On such diagrams, net mass changes caused by alteration occur along separate alteration lines for each chemically distinct rock unit (MacLean and Barrett, 1993; Barrett et al., 1993b). On a TiO_2-Zr plot, the altered andesites form an array or alteration line that plots through the origin toward a least-altered precursor (Figure 3.5b). Most samples in all

three lenses experienced mass gain when compared to a least-altered Rusty Ridge andesite from Ansil, previously identified by Barrett et al. (1991).

Mass Changes

Mass changes during alteration are proportional to the concentration of the immobile elements in the fresh precursor relative to the altered sample (MacLean and Kranidiotis, 1987). Therefore, mass changes for each mobile element can be calculated from the relative increase in the concentration or dilution of an immobile component. The absolute mass change of a component "a" is calculated using the following formula:

$$\Delta^a = [Z^o / Z^a \cdot C^a] - C^o$$

where Δ^a is the absolute mass change of "a" expressed in g/100 g, C^a is the wt % proportion of "a" in the altered rock, C^o is the wt % in the precursor rock, Z^a is the proportion of the immobile element in the altered rock, and Z^o is the proportion of the immobile element in the precursor rock (MacLean and Kranidiotis, 1987; MacLean and Barrett, 1993; Gifkins et al., 2005). Niobium from the least-altered Rusty Ridge andesite from the Ansil deposit was chosen as the immobile monitor for mass balance calculations in the West Ansil altered samples because it showed the most uniform behaviour of the possible immobile elements in the range of least-altered precursors and because of its strong correlation with other typical immobile incompatible elements (Table 3.3). Since no least-altered samples were available at West Ansil, an average value of 10 ppm Nb was used from the least-altered Rusty Ridge andesite at Ansil (Barrett et al., 1991; Table 3.2).

Calculated mass changes for mobile elements in the altered andesite hosting the Upper, Middle and Lower lenses are given in Table 3.4, and average mass changes of major elements in

the West Ansil deposit are shown in Figure 3.6. Mass gains are dominated by addition of SiO_2, Fe_2O_3, MgO and S (Figure 3.6). Major additions of SiO_2 in the andesite hosting all three lenses reflect silicification throughout the West Ansil deposit. The largest additions occur at the base of the Middle lens and Lower lens. Major additions of Fe_2O_3 are observed in the Middle, Upper and Lower lenses. Andesite hosting the Upper lens appears to have gained more Fe_2O_3 than the Lower lens, consistent with the overall increase in the Fe content of the deposit in the Lower lens. Additions of MgO and Al_2O_3 are related to chloritization of the footwall and hanging wall rocks in the West Ansil deposit. Minor MnO and TiO_2 additions occur in almost all samples from all three lenses. A minor addition of CaO and CO_2 is observed in andesite hosting the Middle lens (Figure 3.3 and Table 3.3) which appears to be related to the addition of late siderite. Andesite hosting all three lenses shows similar mass losses in Na_2O and, to a lesser extent, K_2O and P_2O_5.

Rare Earth Element Mobility

Chondrite-normalized rare earth element data for West Ansil are presented in Figure 3.7. Values for C1 carbonaceous chondrites from McDonough and Sun (1995) used to normalize the data are given in Table 3.2. Rare earth elements (except Eu) are typically incompatible during igneous fractionation and only the heavy REE (HREE; Lu and Yb) are essentially immobile during hydrothermal alteration (MacLean and Barrett, 1993; Gifkins et al., 2005). The concentrations of the light REE (LREE; particularly La) are variable, which suggests some degree of mobility. Incremental decreases in mobility from the light to the heavy REE typically result in sloping chondrite-normalized REE profiles (MacLean and Barrett, 1993; Gifkins et al., 2005). As a result, a fan-shaped array of REE profiles is common in proximal altered zones associated with VMS deposits (MacLean and Barrett, 1993).

The Rusty Ridge andesite at West Ansil shows both depletions and slight enrichments in LREE and all have distinct negative Eu anomalies (Figure 3.7a). To compare altered samples with least-altered rocks of the Rusty Ridge andesite, the data of Barrett et al. (1991) from the Ansil deposit were plotted together with data from West Ansil (Figure 3.7a). Mass changes associated with alteration affect the proportions of the REE and produce significant vertical shifts of the profiles. REE profiles for altered andesite hosting the Upper and Middle lenses are shifted downwards as a result of mass gains due to alteration, in particular the strong silicification in both lenses. REE profiles for altered andesite hosting the Lower lens display an upward shift which indicates a net mass loss, consistent with chloritization of the Lower lens and stockwork zone (Figure 3.7b).

Trace Elements

The Rusty Ridge andesite at West Ansil is enriched in Zn, Cu, Co, V, Ga $\pm$ Ni compared to least-altered andesite. Zn concentrations are mostly between 100 and 200 ppm, Co concentrations are 50 to 100 ppm, V concentrations are 150 to 200 ppm, Ga concentrations are 30 to 50 ppm and Ni concentrations are 10 to 20 ppm (Table 3.2). Concentrations of Cu vary from 30 ppm up to 3000 ppm, but most samples contain more than 100 ppm. Values above 2000 ppm Cu can be explained by the presence of chalcopyrite stringers in the altered wall rock. Concentrations of Zn (~100 ppm) reflect the presence of trace sphalerite in the wall rock. High concentrations of Co and Ni may reflect the presence of pyrrhotite which is enriched in these elements. The high V in altered andesite from West Ansil compared to typical tholeiitic basalt (e.g., Taylor et al., 1969) may reflect high V in chlorite or Fe-oxides. This is supported by the high Al_2O_3 and MgO in the most V-rich ore samples (Table 2.6). Moderate concentrations of Ga may reflect the substitution of Ga for Al in chlorite or Ga for Zn in sphalerite.

Table 3.1 Microprobe Analyses of Selected Alteration Minerals from the Rusty Ridge Andesite in the West Ansil Deposit

Mineral	Chlorite (based on 28 oxygens)					Actinolite (based on 23 oxygens)		Stilpnomelane (based on 20 oxygens)	
	Upper Lens WAN071	Middle Lens WAN012	Lower Lens WAN102	Ansil RRA Average (n=11)	Corbet FA Average (n=6)	Lower Lens WAN102	Ansil NWR Average (n=5)	Upper Lens WAN072	Ansil NWR Average (n=3)
(wt%)									
SiO_2	26.83	25.54	26.24	25.1	25.2	53.31	40.59	51.83	47.36
Al_2O_3	17.34	19.71	18.44	19.2	21.6	1.53	1.51	0.69	2.02
FeO	37.14	33.14	31.42	38.0	30.3	17.30	38.85	33.23	38.77
MgO	7.96	10.30	12.12	6.58	10.9	12.25	2.34	5.68	2.31
Na_2O	<0.01	0.004	0.01	0.01	0.04	0.20	<0.01	0.04	<0.01
K_2O	<0.01	0.01	0.07	0.01	0.03	0.06	<0.01	0.63	1.06
TiO_2	0.05	0.07	0.05	0.05	0.05	0.04	<0.01	0.03	<0.01
CaO	0.02	0.01	0.01	<0.01	0.08	11.9	10.01	<0.01	3.99
MnO	0.27	0.06	0.18	0.29	0.36	0.44	0.61	0.58	0.28
BaO	<0.01	<0.01	<0.01	<0.01	<0.01	<0.01	<0.01	<0.01	<0.01
NiO	<0.01	<0.01	<0.01	<0.01	<0.01	<0.01	<0.01	<0.01	<0.01
V_2O_3	0.04	0.02	0.07	<0.01	<0.01	0.03	<0.01	<0.01	<0.01
Cl	0.02	0.01	0.03	<0.01	<0.01	0.01	<0.01	0.04	0.19
F	<0.01	0.09	0.03	<0.01	<0.01	0.15	<0.01	0.05	<0.01
Total	89.65	88.96	88.66	89.2	88.6	97.17	93.89	92.81	95.98
Si	5.89	5.53	5.66	5.56	5.35	7.87	6.87	7.29	8.00
*Al	4.48	5.03	4.68	5.03	5.47	0.27	0.30	0.11	0.43
Fe	6.81	6.00	5.66	7.08	5.54	2.14	5.13	3.91	5.52
Mg	2.60	3.32	3.90	2.19	3.50	2.70	0.57	1.19	0.82
Mn	0.05	0.01	0.03	0.06	0.07	0.05	0.09	0.07	0.04
Na	0	0.002	0.00	0	0	0.06	0	0.01	0
K	0	0.003	0.02	0	0	0.01	0	0.11	0.28
Ti	0.01	0.01	0.01	0	0	0.004	0	0.000	0
Ca	0.004	0.003	0.00	0	0	1.88	1.88	0	0.04
V	0.009	0.004	0.02	0	0	0.004	0	0	0
Cl	0.007	0.004	0.01	0	0	0.002	0.04	0.01	0.08
F	0	0.06	0.02	0	0	0.07	0	0.02	0
Total	19.86	19.98	20.01	19.9	19.9	15.06	14.89	12.73	15.21
Fe/Fe+Mg (cations)	0.72	0.64	0.59	0.76	0.61	0.44	0.90	0.77	0.87

Samples were analyzed on a four spectrometer Cameca Camebax MBX electron microprobe by wavelength dispersive x-ray analysis in the Earth Sciences Department at Carleton University, Ottawa, Ontario; Data for Ansil from Barrett et al. (1991) and Galley et al. (2000) and for Corbet from Barrett et al. (1993a); RRA (Rusty Ridge Andesite), NWR (Northwest Rhyolite), FA (Flavrian Andesite); *Al^{IV} and Al^{VI} were calculated for West Ansil chlorites: WAN071 (2.11, 2.375), WAN012 (2.46, 2.57) and WAN102 (2.34, 2.36).

Table 3.2 Whole Rock Analyses of the Rusty Ridge Andesite from the West Ansil Deposit

		WAN082	WAN039	WAN044	WAN045	WAN097	WAN098	WAN128	WAN135	Average Least-altered	
		Upper	Middle			Lower				RRA Ansil *(n=24)*	FA Corbet *(n=15)*
SiO_2	(wt%)	39.58	25.73	48.91	43.39	60.57	56.38	30.63	72.00	57.72	46.23
Al_2O_3		13.02	15.66	18.89	1.57	9.06	11.37	14.30	6.99	15.54	16.13
Fe_2O_3		29.39	38.50	14.24	36.31	16.97	16.04	37.54	12.10	12.18	17.54
MgO		7.55	9.02	4.63	5.02	5.99	8.33	5.31	3.52	4.79	8.44
TiO_2		1.20	1.63	0.82	0.06	0.62	0.81	1.39	0.55	1.39	1.19
MnO		0.20	0.26	0.12	0.17	0.16	0.15	0.26	0.13	0.26	0.19
CaO		0.85	0.07	2.52	3.97	0.75	0.65	1.88	0.19	5.30	2.41
Na_2O		0.01	0.01	0.20	0.01	0.01	0.40	0.01	0.01	3.67	1.21
K_2O		0.02	0.09	3.38	0.22	0.04	0.24	0.58	0.10	0.18	0.18
P_2O_5		0.09	0.03	0.22	0.01	0.04	0.05	0.09	0.02	0.19	0.13
LOI		6.73	7.90	6.49	5.08	5.85	6.14	7.43	3.50	n/a	5.69
Total		98.6	98.9	100.4	95.8	100.0	100.6	99.4	99.0	n/a	105.35
CO_2		0.28	0.23	2.09	0.42	0.73	0.31	0.83	0.25	n/a	0.61
S		0.76	0.33	0.01	7.47	0.02	0.01	0.93	0.02	n/a	0.60
Rb	(ppm)	0.78	5.95	29.2	5.64	1.94	2.37	46.7	2.52	4.00	5.93
Ba		3.40	8.80	339	8.00	12.0	22.0	63.7	34.7	n/a	n/a
Sr		5.10	4.70	21.9	23.0	5.40	10.10	12.0	2.80	112	60.73
Zr		98.0	133	83.0	15.0	70.0	93.0	163	72.0	152	140.87
Y		98.4	32.3	11.8	8.83	32.9	25.0	42.4	22.6	37	30.67
Nb		5.33	7.22	5.16	0.39	4.85	4.67	8.43	3.49	10	7.07
Zn		157	216	108	53	102	143	170	42	127	n/a
Sn		1.14	0.67	1.76	1.84	0.58	1.29	1.01	0.54	n/a	n/a
Cd		0.27	0.27	0.03	0.43	0.09	0.02	0.16	0.01	1	n/a
Pb		1.40	2.50	1.00	42.0	0.60	0.30	2.10	0.70	13	n/a
Ni		24.6	13.2	25.9	196.9	20.5	15.2	3.2	11.6	7	n/a
Tl		0.02	0.06	0.27	1.09	0.01	0.01	0.52	0.01	n/a	n/a
W		5.04	1.51	0.60	1.25	27.78	16.38	0.93	5.35	1	n/a
Cu		2900	2593	31.1	2900	178	40.9	2521	205	3825	n/a
Co		82.0	75.6	31.9	187	60.2	55.6	151	34.4	46	n/a
Bi		0.18	0.08	0.08	1.29	0.27	0.08	5.33	0.26	2	n/a
In		0.10	0.17	0.20	1.90	0.09	0.15	0.54	0.07	n/a	n/a
Sb		0.07	0.11	0.10	0.41	0.04	0.02	0.10	0.04	<1	n/a
Mo		23.4	1.40	0.36	0.62	4.89	0.81	2.56	1.85	14	n/a
U		0.64	0.40	0.31	0.05	0.30	0.12	0.38	0.18	<1	n/a
V		226	326	166	19	164	165	174	131	2	n/a
Hf		2.70	3.72	2.04	0.38	1.81	2.42	4.23	1.85	3	n/a
Ta		0.34	0.48	0.33	0.03	0.33	0.34	0.54	0.23	<1	n/a
Th		1.17	1.50	0.99	0.09	0.72	0.72	1.37	0.62	1	n/a
Ga		58.0	58.0	17.6	9.56	52.0	32.7	58.0	23.8	n/a	n/a
Cs		0.47	1.18	0.90	0.82	0.49	0.52	2.78	0.23	<1	n/a
Sc		23.3	36.1	16.1	2.20	19.3	24.2	28.9	16.1	5	n/a
Li		1.30	0.70	9.20	10.40	3.40	18.8	4.20	13.9	n/a	n/a
Be		0.23	0.45	0.66	1.37	0.34	0.49	0.35	0.26	n/a	n/a
C1 chondrites											
La 0.24	(ppm)	130.85	14.41	5.28	3.14	52.38	5.92	15.17	14.92	12.10	10.15
Ce 0.61		273.91	33.31	12.62	6.14	113.89	14.10	35.05	32.05	29.83	26.15
Pr 0.09		35.71	4.67	1.68	0.77	14.81	2.13	5.03	4.24	n/a	n/a
Nd 0.46		146.48	20.75	7.45	3.16	61.35	10.41	22.63	18.17	20.33	14.75
Sm 0.15		35.20	4.99	1.86	0.88	13.46	3.13	6.17	4.52	4.77	4.975
Eu 0.06		1.11	0.31	0.42	0.16	1.14	0.74	0.92	0.51	1.40	1.4
Gd 0.20		31.37	4.76	1.93	1.11	11.34	3.84	7.35	4.78	n/a	n/a
Tb 0.04		4.14	0.80	0.33	0.21	1.44	0.66	1.20	0.72	0.89	1
Dy 0.25		22.45	5.51	2.10	1.59	7.21	4.40	7.78	4.36	n/a	n/a
Ho 0.05		4.00	1.22	0.45	0.33	1.25	0.92	1.59	0.85	1.31	1.6
Er 0.16		10.12	3.81	1.37	0.99	3.19	2.78	4.63	2.39	n/a	n/a
Tm 0.02		1.31	0.62	0.21	0.14	0.43	0.42	0.68	0.34	n/a	0.275
Yb 0.16		7.55	4.47	1.43	0.89	2.71	2.69	4.49	2.12	3.58	4.225
Lu 0.02		0.99	0.75	0.22	0.12	0.40	0.39	0.68	0.32	0.53	0.6825

Samples were analyzed at Geoscience Laboratories, Ontario Geological Survey, Sudbury, Ontario; Major oxides analyzed by XRF, minor and trace elements analyzed by ICP-MS, S and CO_2 analyzed by infrared absorption; REE data have not been normalized; Values for C1 carbonaceous chondrites from McDonough and Sun (1995); Trace elements for Ansil are not from least-altered RRA (Rusty Ridge Andesite) but from average *(n=5)* NWR (Northwest Rhyolite); FA (Flavrian Andesite); Data for Ansil from Barrett et al. (1991) and Galley et al. (2000) and data for Corbet from Barrett et al. (1993a)

Table 3.3 Pearson Correlation Matrix of Immobile Elements for Mass Balance Calculations

	Al_2O_3	TiO_2	Yb	Lu	Zr	Y	Nb	Ta	Th	Hf
Al_2O_3	1									
TiO_2	0.68	1								
Yb	0.35	0.73	1							
Lu	0.41	0.82	0.89	1						
Zr	0.74	0.83	0.56	0.65	1					
Y	0.21	0.51	0.95	0.89	0.34	1				
Nb	0.81	0.86	0.56	0.65	0.97	0.36	1			
Ta	-0.30	-0.28	-0.25	-0.32	-0.44	-0.07	-0.37	1		
Th	-0.12	0.06	-0.05	-0.05	-0.38	0.02	-0.23	0.71	1	
Hf	0.03	0.30	0.02	0.07	-0.09	-0.02	0.02	0.57	0.91	1

Correlations are based on 9 samples; coefficients greater than 0.14 are significant at the 95% confidence level

Table 3.4 Calculated Mass Changes (g/100g) for Altered Rusty Ridge Andesite from the West Ansil deposit

Sample no.	Lens	SiO_2	TiO_2	Al_2O_3	Fe_2O_3	MnO	MgO	CaO	Na_2O	K_2O	P_2O_5	S	CO_2
WAN082	Upper	16.58	0.86	8.90	42.99	0.12	9.38	-3.70	-3.66	-0.14	-0.02	1.42	0.30
WAN039	Middle	-22.06	0.87	6.16	41.17	0.10	7.71	-5.20	-3.66	-0.06	-0.15	0.45	0.09
WAN044		36.99	0.20	21.04	15.40	-0.03	4.18	-0.42	-3.28	6.37	0.24	0.01	3.82
WAN045		1061	0.16	24.92	923.64	4.12	124.59	97.02	-3.41	5.49	-0.06	192.52	10.59
WAN097	Lower	67.09	-0.11	3.13	22.79	0.07	7.55	-3.75	-3.66	-0.10	-0.11	0.03	1.27
WAN098		63.14	0.35	8.83	22.20	0.06	13.07	-3.91	-2.81	0.33	-0.08	0.01	0.43
WAN128		-21.37	0.26	1.43	32.37	0.05	1.51	-3.07	-3.66	0.51	-0.08	1.09	0.75
WAN135		148.52	0.19	4.48	22.48	0.11	5.29	-4.76	-3.66	0.11	-0.13	0.05	0.49

Nb used as the immobile monitor component for mass balance calculations

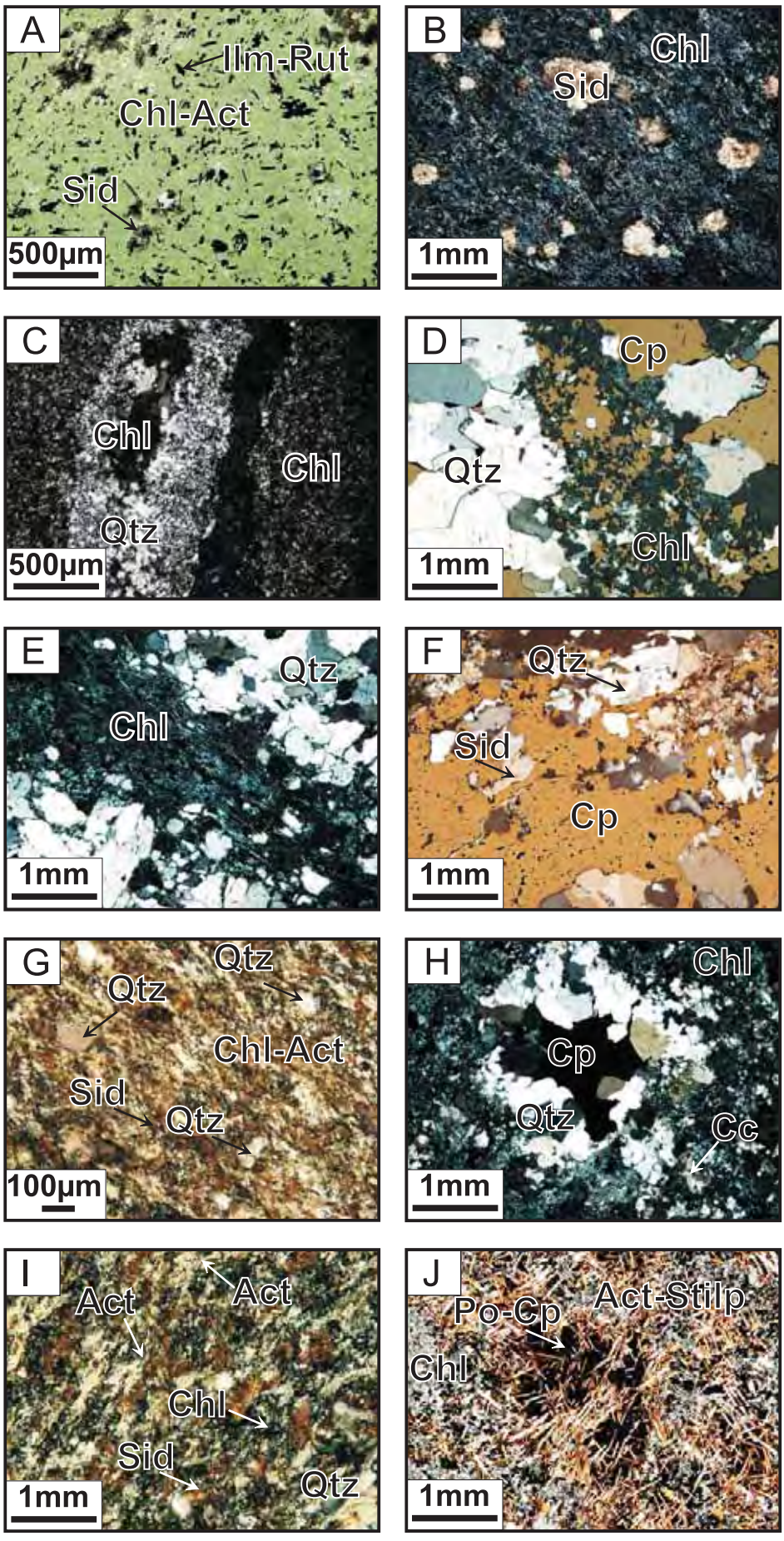

Figure 3.1 Photomicrographs of representative alteration minerals in the West Ansil deposit.

Figure 3.1 Photomicrographs of representative alteration minerals in the West Ansil deposit. A) Fine-grained chlorite and actinolite altered wallrock from the Lower lens with disseminated fine-grained euhedral illmenite and rutile with minor subhedral siderite. Transmitted plane polarized light; WAN129. B) Chloritic wallrock with late disseminated subhedral medium-grained siderite from the Middle lens. Transmitted crossed polarized light; WAN012. C) Fine-grained chlorite and quartz in a veinlet within chlorite-rich wallrock from the Lower stringer zone. Transmitted crossed polarized light; WAN135. D) Chlorite and chalcopyrite veinlet cutting an earlier chlorite and quartz stringer from the Lower zone. Reflected and transmitted crossed polarized light; WAN099. E) Quartz-chlorite stringer from the Lower stockwork zone. Transmitted crossed polarized light; WAN109. F) Chalcopyrite stringer from the Lower stockwork zone with quartz and late siderite. Reflected and transmitted crossed polarized light; WAN124. G) Fine-grained quartz aggregates in a chlorite- and actinolite-rich wallrock from the Lower lens with disseminated siderite. Transmitted crossed polarized light; WAN115. H) Quartz-filled amygdule containing chalcopyrite in chloritic wallrock with minor siderite from the Lower stringer zone. Transmitted crossed polarized light; WAN099. I) Very fine actinolite needles in chlorite-rich wallrock with quartz and siderite from the Lower lens. Transmitted crossed polarized light; WAN115. J) Randomly oriented medium-grained actinolite and stilpnomelane needles intergrown with fine-grained chlorite, pyrrhotite and chalcopyrite from the Lower lens a few centimetres above the upper sulphide contact. Transmitted crossed polarized light; WAN091A.

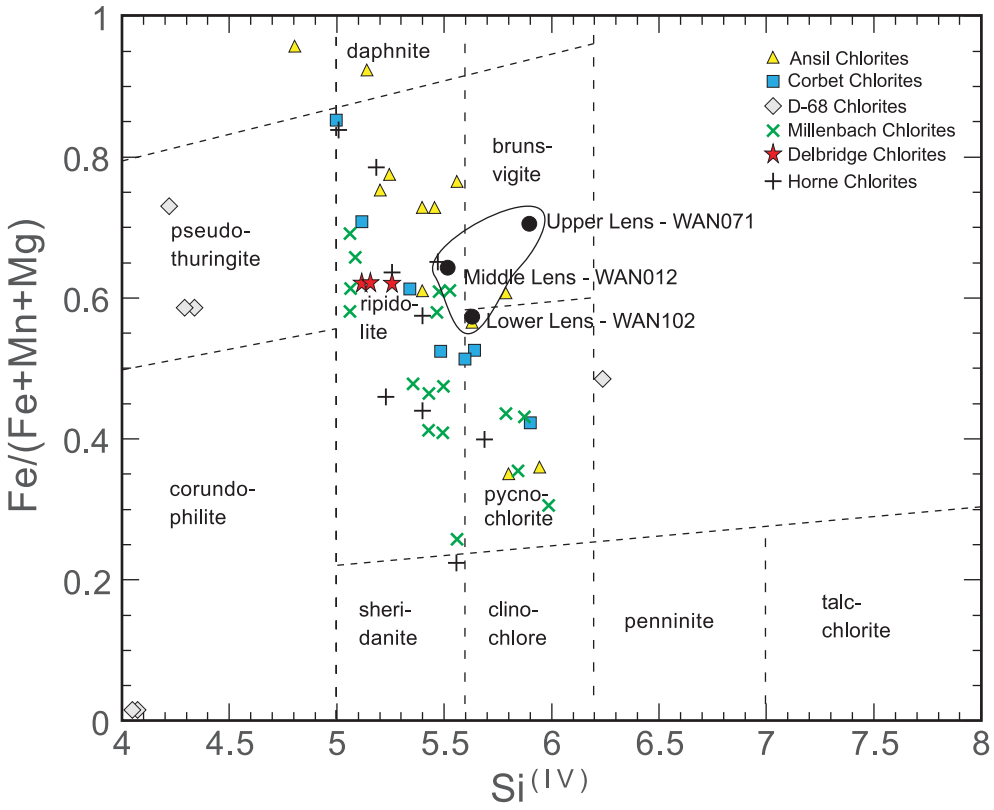

Figure 3.2 Composition of West Ansil chlorites in the Upper, Middle and Lower lenses. All three lenses contain Fe-rich chlorite; however, the Upper and Middle lenses are more Fe-rich. Chlorite from Ansil and West Ansil is generally more Fe-rich than chlorite from Millenbach and other deposits higher in the stratigraphy of the Central Mining Camp. The classification scheme is that of Hey (1954). Data for Ansil from Barrett et al. (1991) and Galley et al. (2000), for Corbet from Barrett et al. (1993a), for D-68 from Ikingura et al. (1989), for Millenbach from Kalogeropoulos and Scott (1988), for Delbridge from Barrett et al. (1993b), and for Horne from MacLean and Hoy (1991).

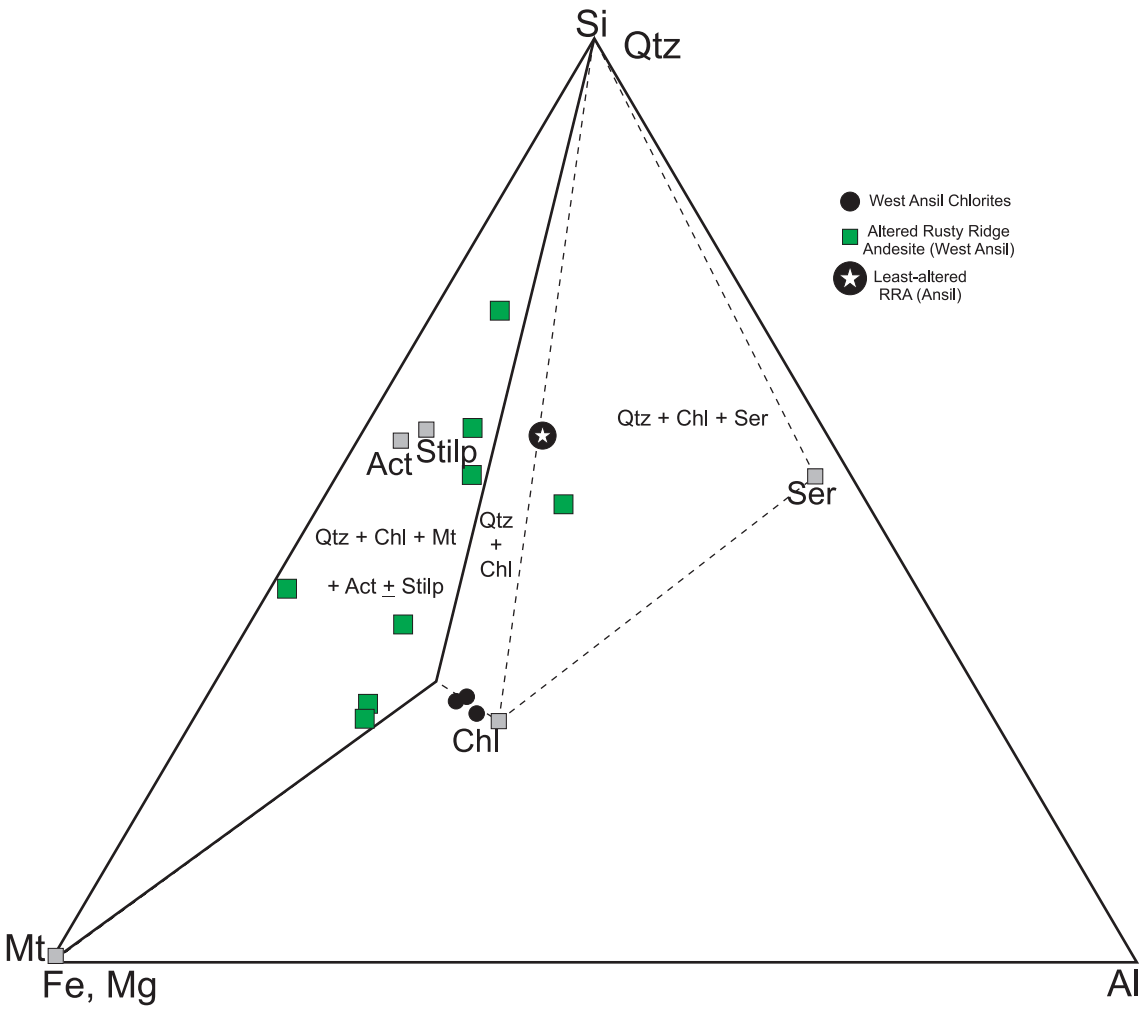

Figure 3.3 Si-Al-Fe-Mg plot for chlorites and altered Rusty Ridge andesites from the Upper, Middle and Lower lenses of the West Ansil deposit, and fields of stable assemblages. The altered rocks from West Ansil plot in the quartz-chlorite-magnetite-stilpnomelane-actinolite field. Modified after MacLean and Kranidiotis (1987).

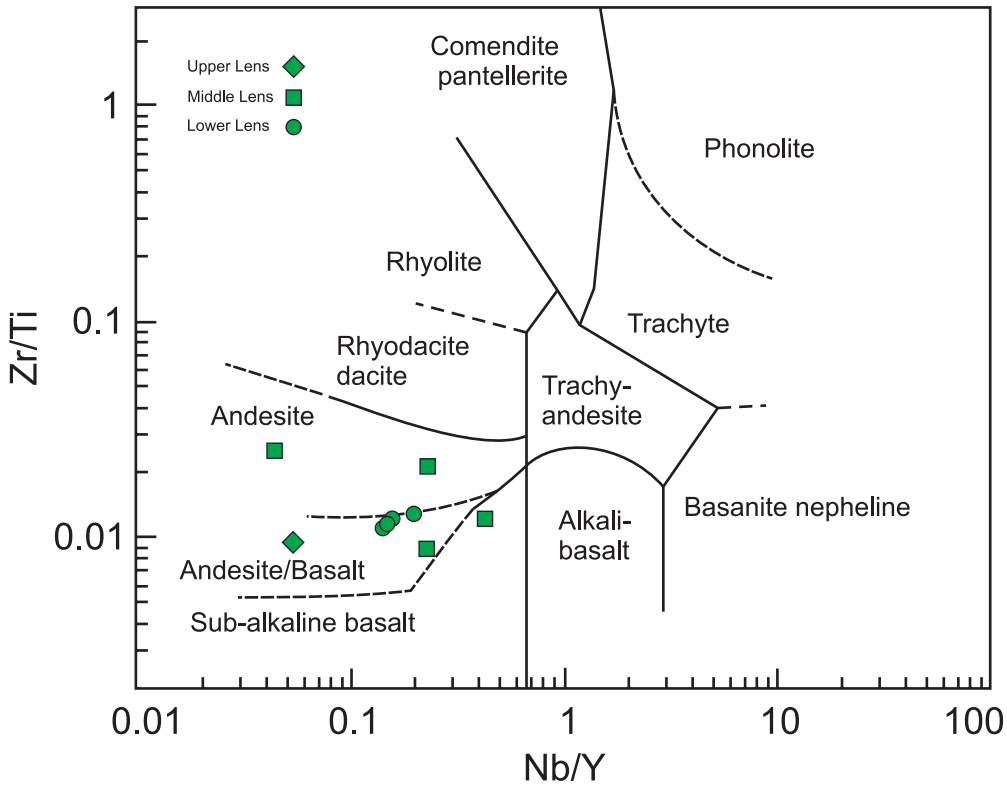

Figure 3.4 Discrimination diagram of Nb/Y versus Zr/Ti classifying Rusty Ridge mafic volcanic rocks as andesite and andesite/basalt (Modified after Floyd and Winchester, 1978).

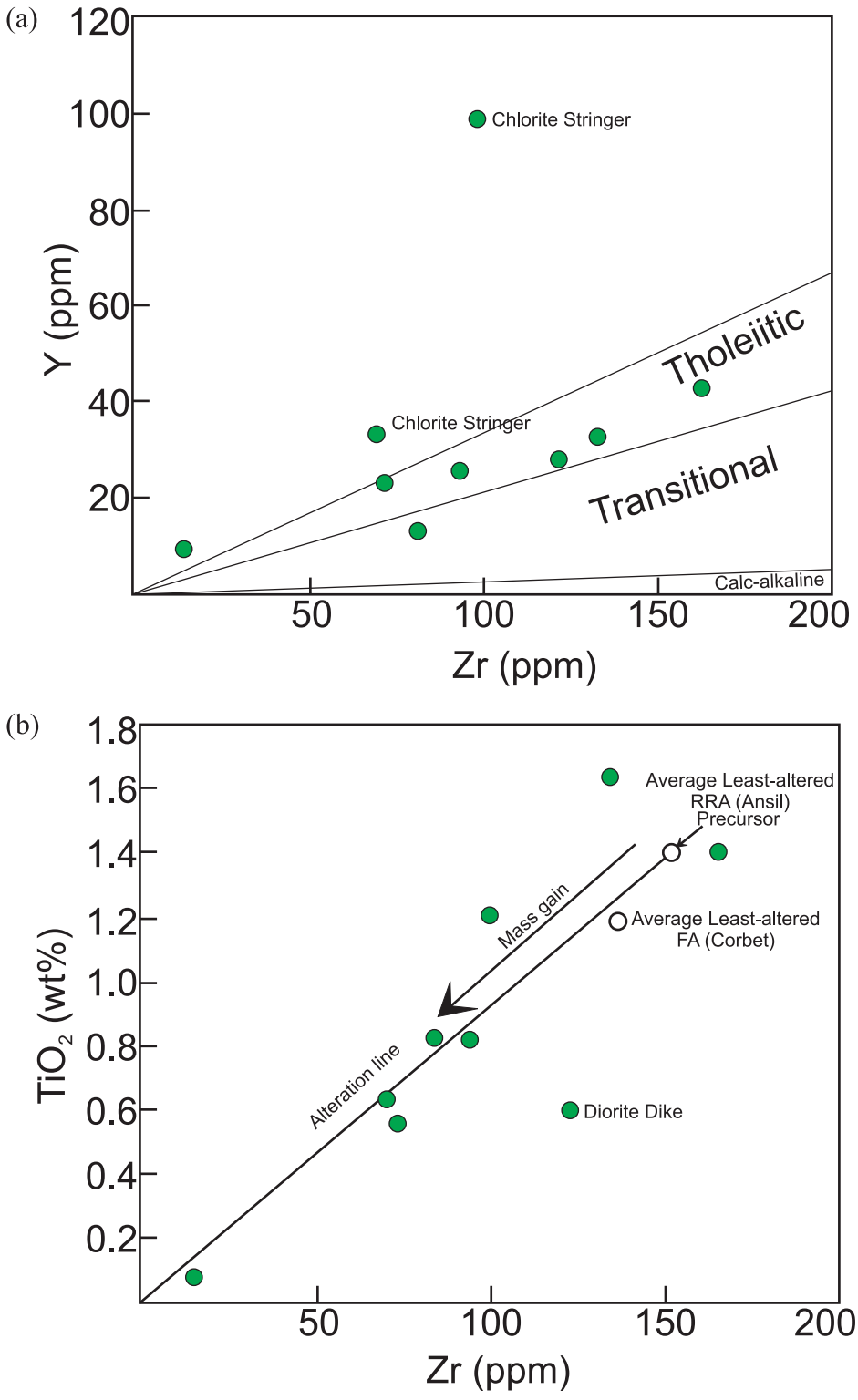

Figure 3.5 a) Immobile element plot of Y versus Zr where the data show the Rusty Ridge andesites from the Upper, Middle and Lower lenses of the West Ansil deposit lie within the tholeiitic composition range. A few samples are outside the tholeiitic range and they occur in the strongly chloritized Lower stockwork zone. b) Immobile element plot of TiO_2 versus Zr for altered andesites from West Ansil where the data show that compared to the least-altered precursors from the Ansil and Corbet deposits, the andesites have been subjected to an obvious mass gain for almost all samples. One sample appears outside the alteration line and it is interpreted to be collected from one of the many subvertical feldspar porphyritic diorite dykes cutting through the ore lenses. Data for Ansil from Barrett et al. (1991) and for Corbet from Barrett et al. (1993a).

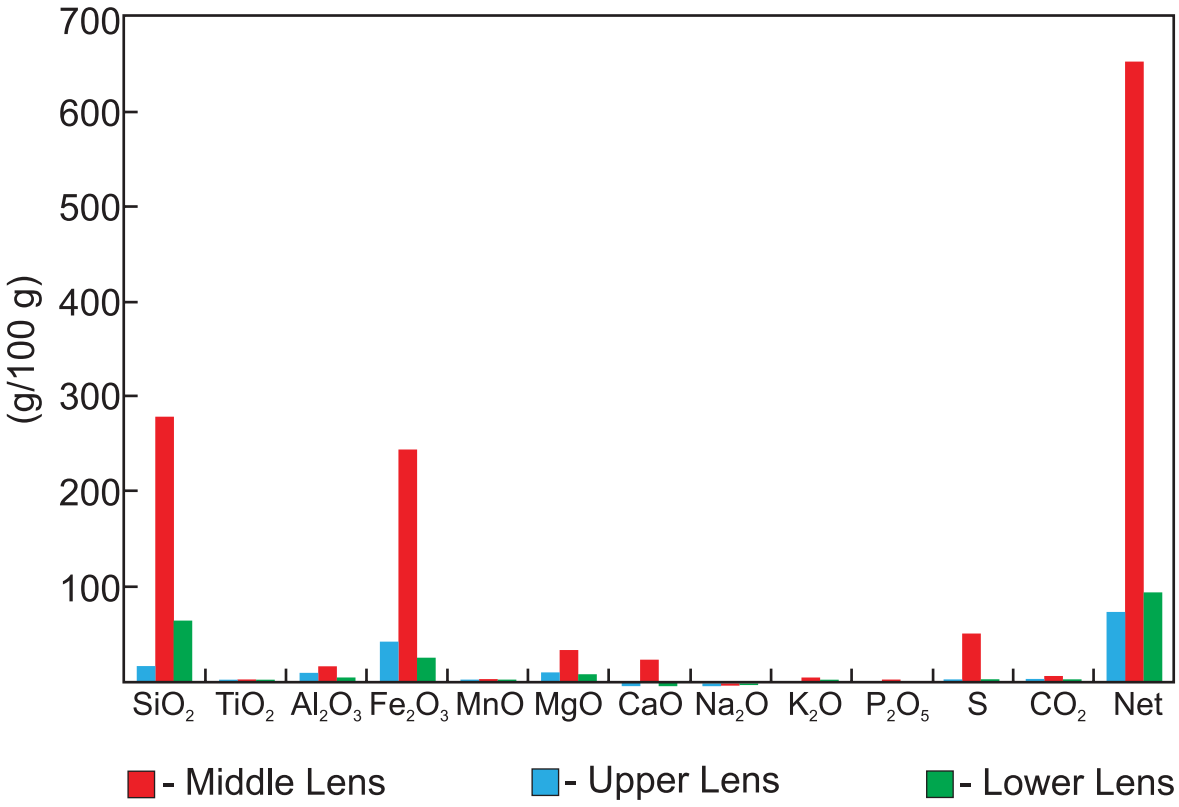

Figure 3.6 Bar graph showing the average estimated absolute mass changes of major elements in the Upper, Middle and Lower lenses of the West Ansil deposit. The data show the largest additions of most elements but especially SiO_2 and Fe_2O_3 in the Middle lens. Depletions in Na_2O and K_2O are observed in all three lenses due to alteration by chlorite and quartz.

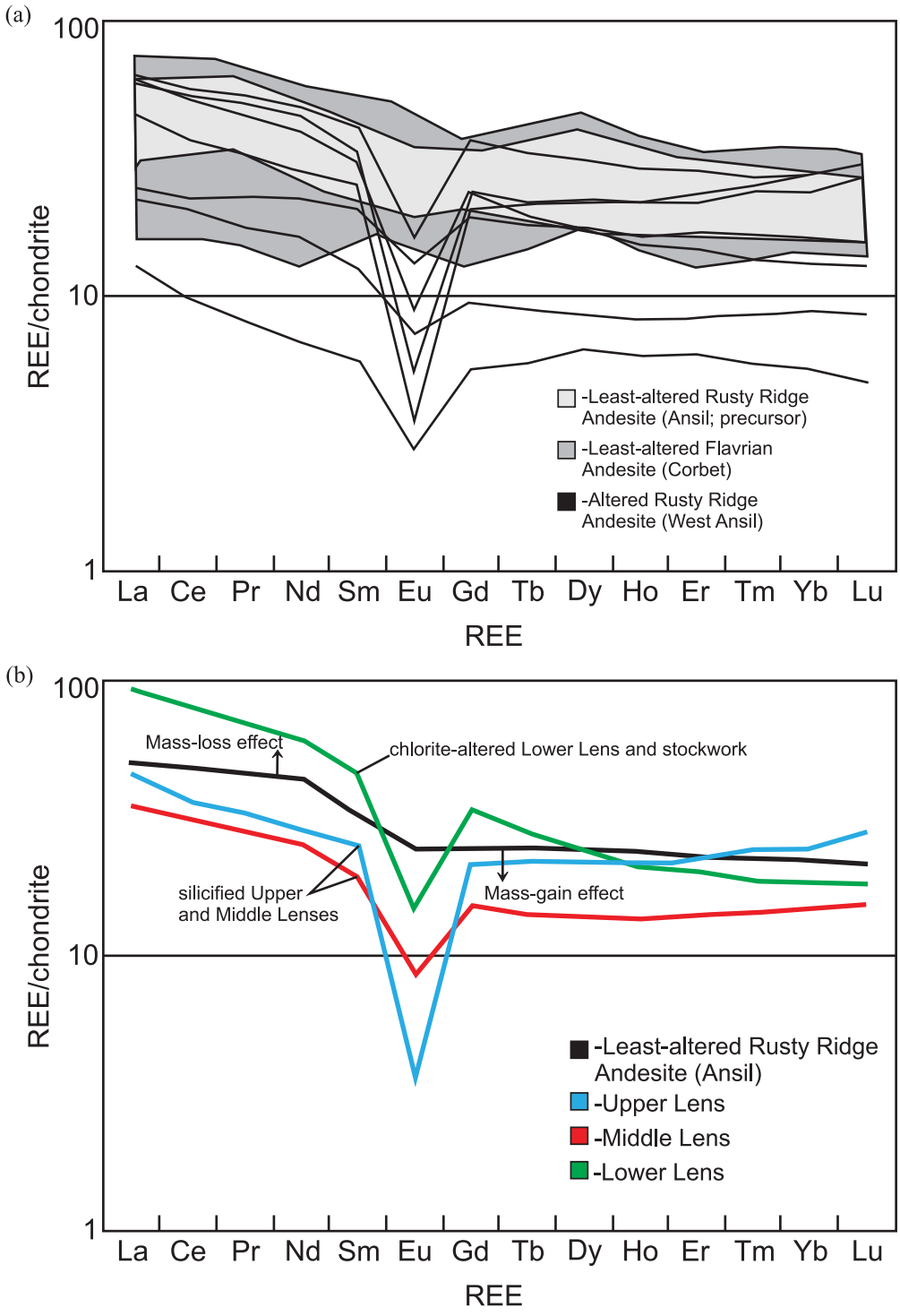

Figure 3.7 Chondrite-normalized REE profiles for the three lenses in the West Ansil deposit. a) Compared to least-altered Ansil Rusty Ridge andesites and Corbet Flavrian andesites, the Rusty Ridge andesites at West Ansil show both depletions and slight enrichments in LREE and all have distinct negative Eu anomalies. b) The average of representative samples from the Upper, Middle and Lower lenses with respect to the averaged precursor from the least-altered Rusty Ridge andesite at Ansil. The downward shifts in REE patterns in Upper and Middle lenses are mainly due to silicification and the upward shift in REE reflects the mass loss in the Lower lens due to chloritization. Data for Ansil from Barrett et al. (1991) and for Corbet from Barrett et al. (1993a).

CHAPTER 4. DISCUSSION

4.1 EVOLUTION OF THE WEST ANSIL DEPOSIT

The overall distribution of massive sulphide ore and stringer zones at West Ansil suggests the dissection of a single deposit by late-stage faulting followed by the intrusion of a large diorite sill. The presence of a subvertical synvolcanic fault controlling high-temperature stockwork mineralization is suggested by displacement in the volcanic stratigraphy near the Upper and Lower lenses (Figure 1.6). However, a stockwork zone beneath the larger Middle lens appears to be missing and likely was removed by the massive diorite sill. The Main lens and Lower stockwork zones are therefore interpreted to be part of a single deposit. However, the presence of a continuous stockwork zone between the Upper lens and Main lens, and the presence of the Amulet dacite in some holes that intersect the footwall of the Upper lens, suggest that it may be part of a stacked system perched above the Main lens.

Alteration zonation (i.e., silicification in the hanging wall and dominantly chloritization in the footwall) also suggest an intact hydrothermal system including the Main and Lower lenses rather than stacked lenses. The coherent Cu-to-Zn metal zonation in the Middle lens suggests that it is intact except for the absence of the stockwork zone. The lack of Zn or Pb enrichment in the Upper lens is consistent with it being a separate lens rather than a faulted portion of the Main lens.

Two stages of mineralization are recognized at West Ansil: 1) an early stage of sphalerite-pyrrhotite with lesser pyrite mineralization and associated chlorite-quartz alteration, and 2) a later stage of pyrrhotite-chalcopyrite mineralization with magnetite replacement. Figure 4.1 illustrates the inferred stages of development of the West Ansil hydrothermal system: 1) construction of a “low-temperature” subseafloor sphalerite-pyrrhotite vent complex, above a

sphalerite-pyrrhotite stockwork, 2) development of higher-temperature chalcopyrite stringer networks due to capping by Rusty Ridge basalt, 3) emplacement of massive magnetite along a replacement front at the base of the massive sulphide lens, 4) alteration of massive pyrrhotite by penetration of groundwater along sheared contacts and late fractures.

The deposit is interpreted to have formed mainly in the subseafloor and continued through the emplacement of the Rusty Ridge andesite. Abundant relicts of chloritized and silicified wall rock in the massive sulphides (pseudobreccia) are interpreted to be partly replaced andesite breccia and hyaloclastite. In some sections, there are no obvious subvertical feeders immediately below massive sulphide parts of the lenses, but semi-conformable zones of disseminated sulphides and magnetite are present with semi-massive sulphide infilling chlorite-altered hyaloclastite. This suggests that mineralizing fluids may have moved in part laterally through the Rusty Ridge unit, probably through zones of high porosity such as breccia and hyaloclastite (see also Barrett et al., 1991). In the early stages of mineralization, construction of a low-temperature partly subseafloor sphalerite-pyrrhotite vent complex occurred above a sphalerite-pyrrhotite stockwork (Figure 4.1). Remnants of the early-stage mineralization (massive banded sphalerite-pyrrhotite and sphalerite-pyrrhotite-cemented pseudobreccia) occur at the western top of the Middle lens. Remnants of sphalerite-pyrrrhotite-rich stringer mineralization also occur locally within strongly chloritized and silicified andesite below the Middle lens and at the margins of the Lower stockwork zone.

The second stage of mineralization involved the development of a pyrrhotite-chalcopyrite vein system below the Lower lens, where the most intense chloritization of the basalt and andesite occurs (Figure 4.1). On-lapping of the Rusty Ridge basalt allowed an increase in temperature creating an impermeable cap rock that promoted the replacement of pyrrhotite by

chalcopyrite. A Cu-rich stockwork grades upward into pyrrhotite-chalcopyrite-rich massive sulphide. Higher temperatures allowed the enrichment of Cu, Se, Co, Bi, In and Au in the sulphides and the chloritization in the footwall of the Rusty Ridge andesite (Figure 4.1b). A similar pattern is observed in the separate Upper lens. The Middle lens lacks this conspicuous transition, which was most likely removed by the diorite sill that separates the Middle lens from the Lower lens. However, the Middle and Lower lenses both contain a chalcopyrite-rich core which likely formed at peak temperatures in the hydrothermal system (e.g., Barrett et al., 1991). Eventually, increasing temperatures allowed replacement of pyrrhotite by magnetite and remobilization of Cu.

The alteration is notably Fe-rich throughout the deposit. The abundant Fe-rich chlorite reflects the high-temperature of the hydrothermal upflow and possibly a late-stage overprint of Ca-Fe-rich fluids similar to those that affected the nearby Ansil deposit (Galley et al., 1995). The narrow range of Fe/Fe+Mg ratios (0.59-0.72) of chlorite from all three lenses also suggests one single high-temperature mineralizing event or overprint during the formation of the West Ansil deposit. A variety of chlorite geothermometers for Al-saturated conditions (i.e., in the presence of other aluminous minerals) all indicate temperatures of at least ~300°C for chlorites of this composition (de Caritat et al., 1993) consistent with the high temperature of alteration inferred for West Ansil.

4.2 ORIGIN OF THE HIGH Cu/Cu+Zn

The high Cu/Cu+Zn ratios of the Ansil and West Ansil deposits compared to deposits higher in the Mine Sequence most likely reflects their high temperature of formation. Galley et al. (1995) pointed out that the Ansil deposit formed under nearly 500 m of contemporaneous lava, which greatly increased the temperature of the hydrothermal system late in its evolution,

resulting not only in the replacement of pyrrhotite by magnetite (see below) but also significant upgrading of Cu compared to typical Noranda Cu-Zn deposits. They concluded that Zn was also remobilized out of the deposit, contributing to the overall low Zn grades. The lower Cu/Cu+Zn ratios of the deposits higher in the Mine Sequence may indicate lower overall temperatures of formation and possibly shallower water depths (Table 4.1). Deposits deeper in the Mine Sequence may have formed during the earliest stages of rifting, possibly at a time of higher heat flow. Ansil and West Ansil are also closely spatially associated with the Old Waite Paleofissure, which is thought to have been the locus of rifting and magmatic activity within the Noranda cauldron (Gibson, 1990).

Deposits like Ansil and West Ansil are characterized by po>py, locally abundant magnetite, and a strong Cu-Au association (Table 4.1). The majority of the sulphides exhibit textures typical of recrystallization at high temperature (e.g., annealing textures, triple junction contacts, abundant chalcopyrite disease in sphalerite, remobilization of chalcopyrite into brittle magnetite fractures) (Craig and Vaughan, 1981; Barton and Bethke, 1987; Kojima, 1992). In general, gold fineness in the Noranda district also appears to correlate with Cu/Cu+Zn ratios. This is consistent with the observations of Huston et al. (1992), who noted the high fineness of gold associated with high-temperature Cu-rich ores in other deposits (Figure 4.2). This can be explained by the precipitation of gold from chloride complexes at high temperature while Ag remains in solution down to low temperatures (Figure 4.3). The association of Cu, Au, Bi and Se in the high-temperature ores also may be related to direct magmatic contributions to the hydrothermal fluids. A Au-Bi association in Cu-rich ores may reflect the well-known scavenging of Au by Bi at high temperatures (e.g., Ciobanu et al., 2006; Tooth et al., 2008).

4.3 ORIGIN OF THE MASSIVE MAGNETITE

Massive magnetite found in the Upper and Middle lenses appears to have formed as a replacement of pyrrhotite-rich ore. Magnetite generally forms re-entrant cusps into the massive pyrrhotite and appears to have advanced into or replaced the massive sulphides, as observed at Ansil (Riverin et al., 1990; Westendorp et al., 1991; Westendorp, 1992). However, magnetite feeders have not been observed directly below the massive magnetite. Because of its brittle nature the massive magnetite is commonly veined by remobilized chalcopyrite. Trace elements in the massive pyrrhotite-chalcopyrite ore appear to have been "cleaned out" during replacement by magnetite, and the magnetite is essentially free of trace elements. Magnetite is not found as inclusions in any of the major sulphides, but open spaces in magnetite commonly contain unreplaced or structurally mobilized pyrrhotite or chalcopyrite. In thin section, contacts between magnetite and pyrrhotite are typically sharp, with magnetite penetrating into the massive sulphides. The majority of the sulphides exhibit textures typical of recrystallization at high temperature (e.g., annealing textures, triple junction contacts, abundant chalcopyrite disease in sphalerite, remobilization of chalcopyrite into brittle magnetite fractures). These observations are all consistent with the late emplacement of the magnetite.

Magnetite is a common, but typically minor, component of VMS deposits. It is locally abundant in the deposits of the Matagami camp (e.g., Orchan) and in other Archean Cu-Zn deposits (e.g., Gossan Hill, WA). A variety of models have been proposed for the formation of magnetite: from late-stage H_2S-poor fluids (Sharpe and Gemmell, 2002); as a result of increasing fo_2 during mixing with seawater (Large, 1977; Barrett et al., 1991); or from thermal metamorphism or late-stage Ca-Fe-rich magmatic hydrothermal fluids (e.g., Galley et al., 1995). In some of the Noranda deposits, magnetite has formed where the massive sulphides are cut by

late diorite dikes or sills (e.g., Vauze deposit: Spence, 1975). In nearly all cases, magnetite is interpreted to have formed during a late-stage of replacement of pre-existing massive sulphides.

At Ansil, Westendorp (1991, 1992), Cattalani et al. (1990, 1993) and Galley et al. (1995, 2000) interpreted the magnetite replacement to have formed when rising hot (350°C) fluids were able to mix with cooler, less acidic, and more oxidized seawater along the footwall and hanging-wall contacts of the massive sulphide lenses, although Westendorp (1992) acknowledges that the formation of magnetite can also be a product of temperature increase at constant fS_2, fO_2 and pH. In either case, the replacement of the massive pyrrhotite-chalcopyrite ore by magnetite was interpreted as a late-stage, high-temperature process, possibly caused by the burial of the active hydrothermal system by Rusty Ridge andesite. The magnetite at West Ansil did not form as a result of contact metamorphism, as suggested at the Vauze deposit (Spence, 1975), as there is no magnetite associated with the diorite sill. Rather, a hydrothermal origin for the magnetite is strongly suggested by the quartz-magnetite veins in the hanging wall of the Upper lens which indicate introduction of magnetite by hydrothermal fluids after burial of the deposit (Figure 2.5L and M and Figure 2.10A).

Notable enrichment of Cu occurs at the margins of the massive magnetite, most likely related to mobilization of Cu to the outer margins of the magnetite zone during replacement of the massive sulphides, although the present distribution of chalcopyrite is also related to structural remobilization into late brittle fractures at the margins of the massive magnetite zones. The magnetite itself is free of most trace elements that were originally enriched in the massive pyrrhotite-chalcopyrite ore (especially Co, As and Ni). These were presumably occluded during crystallization of the magnetite. The high Si content of the magnetite, noted in electron backscatter images, is similar to that observed at Ansil and may be a consequence of the

replacement of preexisting quartz gangue in the massive pyrrhotite ore, although Westendorp et al. (1991) interpreted this to reflect reaction with a Si-rich fluid.

Extensive overprinting and replacement reactions were noted in the Ansil deposit as a result of burial of the massive sulphides by 500 m of massive lavas of the Rusty Ridge andesite (e.g., Galley et al., 1995). These reactions were driven by the development of steep, post-burial thermal and chemical gradients in the hydrothermal system. The replacement reactions mainly follow the temperature dependent stabilities of the ore minerals, including in the Fe-S-O system. Fluids that originate near the pyrite-pyrrhotite buffer in the Fe-S-O system will begin to form magnetite at high temperatures at a constant H_2S. At the same time, Cu (and Zn) will be mobilized out of the magnetite zone in a high-temperature zone-refining process as observed at West Ansil.

Volume-for-volume replacement of pyrrhotite by magnetite, as suggested in this study, can only proceed if the reaction results in a negative change in molar volume (e.g., Seward and Barnes, 1997). For the reaction,

$$3FeS + 1/2O_2 + 3H_2O \rightarrow Fe_3O_4 + 3H_2S \quad \text{(reaction 1)}$$

$$\Delta V = 14.8 \text{ cm}^3\text{/mol (magnetite)} - 3\text{x}18.5 \text{ cm}^3\text{/mol (pyrrhotite)} = -40.7 \text{ cm}^3\text{/mol}$$

Thus, there is a large negative change in molar volume allowing for the observed replacement and accounting for the abundant open spaces in magnetite that are filled by quartz, chlorite and remobilized sulphides.

Barrett et al. (1991) appealed to a similar reaction to account for magnetite replacement of massive pyrrhotite+chalcopyrite ore in the Ansil deposit, but concluded that oxidative

dissolution of chalcopyrite was interpreted as the main cause of the high Cu grades (up to 23 wt.% Cu) along the magnetite-pyrrhotite replacement front. This is similar to the interpretation of Westendorp et al. (1991) and Cattalani et al. (1990, 1993) noted above (i.e., an increase in fo_2 caused by late-stage incursion of seawater into the hydrothermal system). However, it is unclear whether mixing with seawater in a reduced Archean ocean would have resulted in a significant change in fo_2 at the high temperatures of magnetite formation and it is clear that chalcopyrite can be dissolved without inceasing fo_2 (Figure 4.4). Thus, the presence or absence of magnetite may or may not provide meaningful information about the redox state of the fluid (e.g., Ohmoto, 2003). Others have interpreted the formation of magnetite in VMS as a result of late-stage, sulfur-poor fluids (e.g., Sharpe and Gemmell, 2002), but the likely increase in temperature during magnetite formation at West Ansil is not consistent with a decrease in H_2S. There is little evidence for cooling of the hydrothermal system by mixing with seawater at this stage (e.g., chalcopyrite is remobilized rather than deposited), and all evidence points to the formation of the magnetite when the deposit was already buried by flows of the Rusty Ridge Andesite and therefore less likely to have been infiltrated by cold seawater.

Preliminary fluid inclusion data on the early-stage mineralization at Ansil indicated a formation temperature of 250-270°C (Galley et al., 1995). But temperatures increased dramatically when the system was buried by the Rusty Ridge Andesite, and the higher temperatures associated with burial of a still active hydrothermal system led to the formation of a "skarn" assemblage (see below). The resulting calc-silicate minerals were interpreted to have formed at temperatures of at least 350-400°C (Galley et al., 1995; Galley et al., 2000). Weierhauser (2005) reported homogenization temperatures for fluid inclusions in quartz from the

Ansil deposit up to 390°C. Similar temperatures are suggested here for the formation of massive magnetite at West Ansil.

The quartz-magnetite veins in the hanging wall of the Upper lens are associated with distinctly Fe-rich chlorite, which typically is formed at high temperatures as noted above. The high temperatures are also consistent with the abundance of ferroactinolite in the ore-related gangue as observed elsewhere in the Noranda Camp (see below). Oxygen isotope data for quartz-magnetite pairs from other deposits in the Noranda camp have indicated equilibrium temperatures of about 345 +/- 20°C for this assemblage (e.g., Cattalani et al., 1993; MacLean and Hoy, 1991; Hoy, 1993). These high temperatures suggest that the white quartz rims on the magnetite veinlets may be a result of dumping of silica as the fluids exceeded the solubility maximum of quartz at about 400°C (Figure 4.5).

The unique skarn-like calc-silicate assemblage documented by Galley et al. (1995, 2000) at the Ansil deposit includes andradite, hedenbergite, ferroactinolite, and ilvaite, which formed during magnetite emplacement. The Ca-Fe fluids were interpreted to have been sourced from the trondhjemitic phases of the nearby Flavrian intrusion. The skarn minerals are overprinted by a retrograde assemblage of ferroactinolite, quartz, stilpnomelane and Fe-carbonate, similar to that observed at West Ansil, but garnet is still abundant in the rocks. Although it cannot be ruled out that similar Ca-Fe fluids may have been responsible for the formation of the massive magnetite at West Ansil, there appears to be no evidence for a similar skarn assemblage.

4.4 ORIGIN OF THE QUARTZ-CHLORITE-ACTINOLITE-STILPNOMELANE ASSEMBLAGE

The dominant alteration at West Ansil is quartz-chlorite-stilpnomelane-actinolite±siderite. This contrasts with the typical quartz-muscovite-chlorite assemblage that dominates most other deposits of the Noranda camp, except the nearby Ansil deposit. The bulk rock composition reflects the Fe-rich nature of the alteration and plots within the quartz + chlorite + magnetite + actinolite + stilpnomelane field (Figure 3.3). The alteration was caused by coincident silicification and addition of Fe+Mg and leaching of Na, Ca and K. The formation of Fe-rich chlorite in the footwall was apparently contemporaneous with intense silicification in the host rocks of the Main lens and hanging wall. The abundant actinolite is similar to that observed in the highest-temperature alteration zones of other Noranda deposits, where it overprints Fe-rich chlorite (Hannington et al., 2003).

Stilpnomelane is a Fe-rich phyllosilicate that is commonly associated with metamorphosed iron-rich sediments and metamorphosed iron ores and develops in preference to biotite where the rocks have a high Fe content. It is abundant in a number of Archean Cu-Zn deposits that contain significant magnetite (e.g., Ansil: Westendorp, 1992 and Galley, 1994; Vauze: Spence, 1975; Orchan: Large, 1977). The stability field of stilpnomelane occurs at high temperatures for most bulk rock compositions and further suggests that the alteration and mineralization at West Ansil formed at a very high temperature (Miyano and Klein, 1989; Elmer et al., 2008). It is clear that both actinolite and stilpnomelane were recrystallized during remobilization of chalcopyrite, as they commonly form coarse, randomly oriented needles in the enclosing chalcopyrite. However, it is unlikely that regional metamorphism could have accounted for this assemblage, as these minerals are not present in the adjacent wall rock.

4.5 ORIGIN OF THE PYRITE-MARCASITE-HISINGERITE ALTERATION

The colloform pyrite textures in the massive pyrrhotite ore at West Ansil were originally considered to be a primary feature of the ore but are now recognized as a post-metamorphic replacement of pyrrhotite, most likely related to supergene alteration along structures that reach the surface. Shearing and faulting at the contacts of the massive sulphide lenses at West Ansil may have allowed meteoric water to penetrate into the ore zone to alter the pyrrhotite. The observed nodular and spheroidal pyrite and marcasite closely resemble supergene alteration of massive pyrrhotite in pyrrhotite-rich NiS deposits in other Archean greenstone belts (e.g., Butt and Nickel, 1981). The replacement of massive pyrrhotite by pyrite and marcasite leads to a significant volume reduction, which likely accounts for conspicuous "shrinkage cracks" associated with the replacement (Fleet, 1978). The amorphous iron oxide, hisingerite, present in these cracks is also a product of sulphide weathering (Murowchick, 1992).

This feature is rare in other deposits of the Noranda Central Camp but has been described at the New Insco deposit north of Noranda (Larson, 1983). Petrographic observations show that the colloform pyrite-marcasite nodules formed after the deformation, since no fabric or recrystallization textures were observed, and therefore they were not part of the original hydrothermal system. Most pyrite nodules also overgrow actinolite and stilpnomelane needles supporting a late origin. Sulfur isotope data for the pyrite and marcasite are indistinguishable from other sulphides suggesting that the sulfur was derived from the pre-existing pyrrhotite with no fractionation during the alteration process. The low trace element contents of the pyrite-marcasite nodules (e.g., Zn, Pb, Cd, Hg) compared to the Main lens and the presence of other trace elements that are not found in the unaltered massive sulphides (e.g., Tl) are consistent with the interpreted post-metamorphic origin of the colloform pyrite.

The replacement of pyrrhotite by pyrite and marcasite is accompanied by a significant reduction in modal volume (Fleet, 1978; Murowchick, 1992), and the porous nature of the pyrite-marcasite nodules suggests that Fe was removed as part of the volume loss. Murowchick (1992) showed that pyrite or marcasite formed by wholesale replacement of pyrrhotite exhibits up to 30 modal% pore space, with gaps between the pyrite and parent pyrrhotite commonly filled with by-product siderite, magnetite or other Fe-bearing phases. The change in partial molar volumes of the products is:

$$2FeS \rightarrow FeS_2 + Fe^{+3}$$

$$\Delta V = 23.9 \text{ cm}^3\text{/mol (pyrite)} - 2\text{x}18.5 \text{ cm}^3\text{/mol (pyrrhotite)} = -13.1 \text{ cm}^3\text{/mol}$$

(from molar volume data compiled by Seward and Barnes, 1997).

Hisingerite is a common secondary mineral formed from weathering or late-stage deuteric alteration of iron-bearing silicates or sulphides (Sudo and Nakamura, 1952; Whelan and Goldich, 1961; Kohyama and Sudo, 1975). Although common as a near-surface weathering product of pyrrhotite in massive Ni-sulphide deposits of Western Australia (Nickel et al., 1974; Nickel et al., 1977; Butt and Nickel, 1981), this type of alteration is less common in Canadian Archean VMS deposits, most likely because of the minimal weathering profile developed in granite-greenstone terranes of the Canadian Shield. The unusual abundance of this alteration at West Ansil appears to be related to the high pyrrhotite (>>pyrite) content of the ores and possibly the near-surface faulting that may have allowed penetration of groundwater into the deposit.

4.6 RECONSTRUCTION OF THE WEST ANSIL LENSES

Figure 4.6 shows the possible reconstruction of the West Ansil deposit after the removal of the diorite sill and late faulting. The Lower lens and stockwork zone are interpreted to have been detached from the Main ore lens by a synvolcanic fault and the intrusion of the diorite. When the fault and sill are removed, the Main lens and Lower lens and stockwork zone are part of one single deposit and stringer zone. The alteration zonation (silicification of the hanging wall and the chloritization of the footwall) is also consistent with a single ore lens. However, the Upper lens and stockwork appear to have formed as part of a stacked system, perched above the Main ore lens along the Rusty Ridge basalt and Amulet dacite horizon.

The positions of the ore lenses suggest that additional mineralization could be located within the Rusty Ridge formation, (i) at the RRA-RRB contact along strike from the Main lens, (ii) at the RRB-Lower Amulet dacite contact along strike from the Upper lens, or (iii) at depth below the Main lens on the inferred synvolcanic structure hosting the Lower lens and stockwork zone. These represent potentially important untested exploration targets in the lower Mine Sequence stratigraphy of the Noranda Main Camp.

Table 4.1 Summary Characteristics of Noranda Deposits

Deep in the Mine Sequence: (e.g., Corbet, Ansil, West Ansil)	High in the Mine Sequence: (e.g., Amulet, Millenbach, Delbridge)
Po>Py	Py>Po
Abundant magnetite	Little or no magnetite
Chl>Ser	Ser=Chl
Cu>Zn	Zn>Cu
Cu-Au association	Zn-Au association
High temperature	Lower temperature
Deep (or deeply buried)	Shallow (?)

References: Corbet (Knuckey and Watkins, 1982), Ansil (Galley et al., 1995), West Ansil (this study), Amulet (Spence and de Rosen-Spence, 1975), Millenbach (Knuckey et al., 1982) and Delbridge (Barrett et al., 1993b)

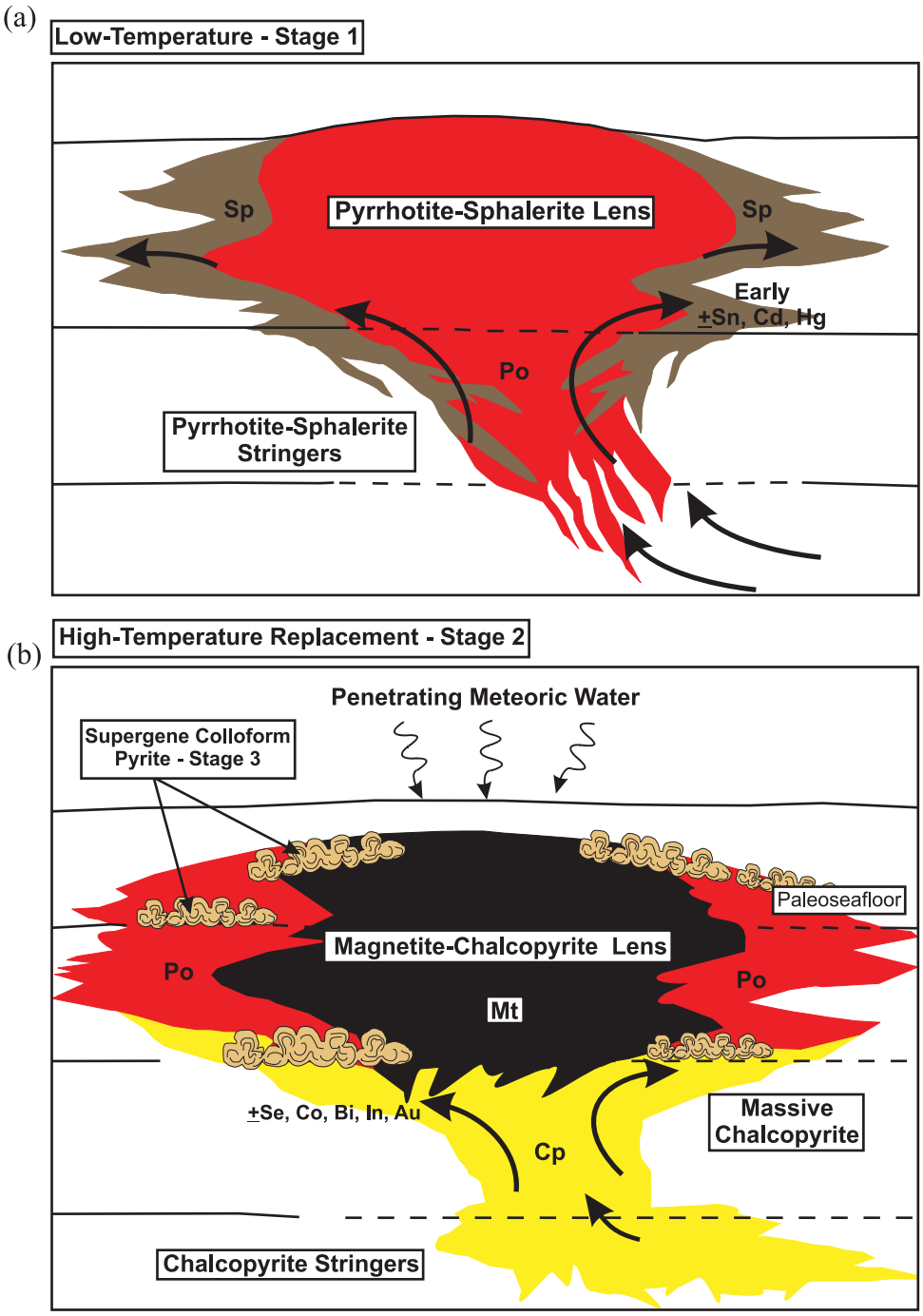

Figure 4.1 Schematic representation of the development of the West Ansil hydrothermal system. a) Mineralization commenced with a low-temperature stage dominated by early silicification of the footwall Rusty Ridge andesite, sphalerite stringer mineralization and the emplacement of massive sphalerite and pyrrhotite. b) Progressive sealing of the Rusty Ridge andesite by hanging-wall basalt increased temperatures in the vent complex, developed chlorite stringers in the footwall, formed chalcopyrite stringer mineralization and allowed the emplacement of massive chalcopyrite along a high-temperature replacement front. Higher temperatures caused by thermal insulation enriched the West Ansil ore lens in Cu, Se, Co, Bi, In and Au resulting in a strong Cu-Au association. Further replacement of pyrrhotite by magnetite occured at the highest temperatures. Finally supergene alteration of pyrrhotite occured along sheared contacts and late fractures and forming colloform pyrite and marcasite.

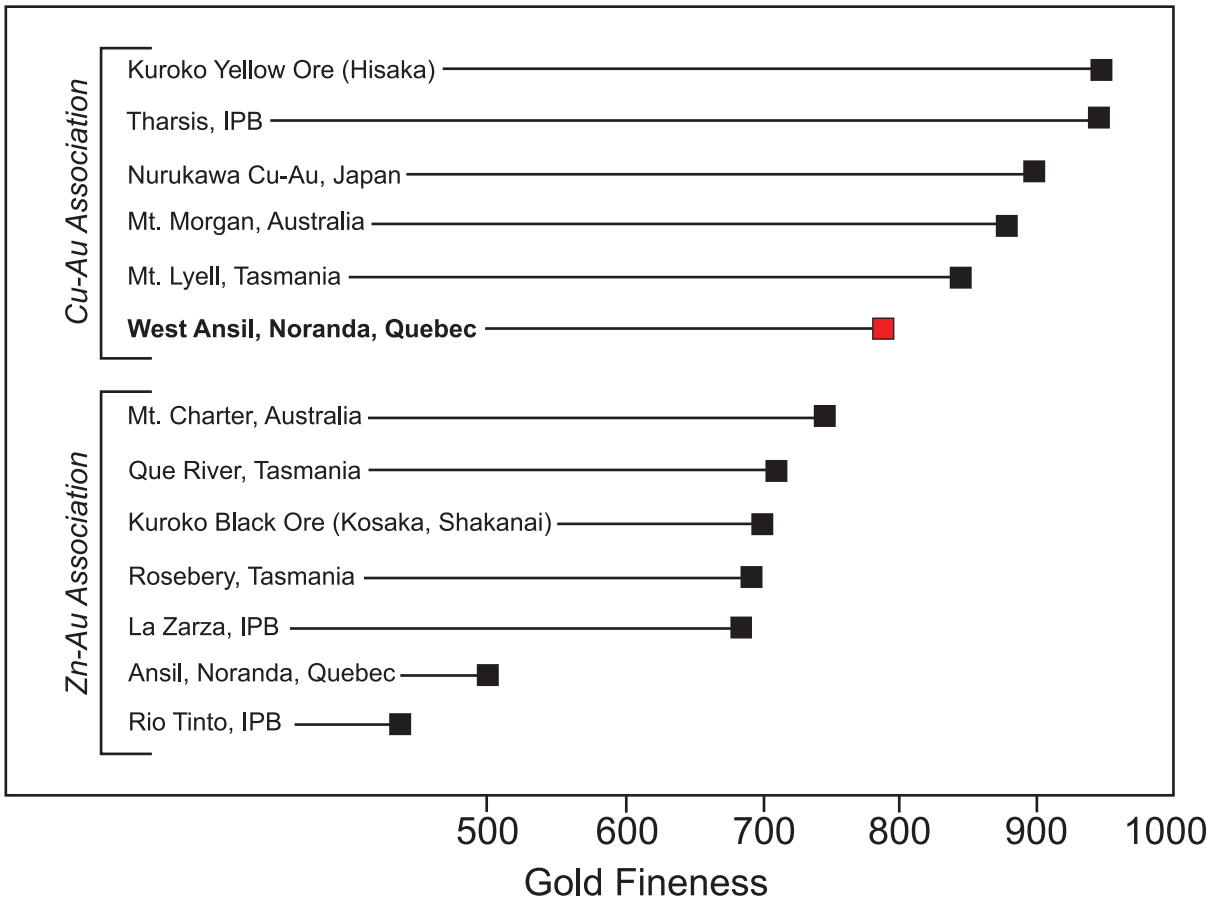

Figure 4.2 Comparison of the compositions of gold and electrum in Archean and Phanerozoic Cu-Zn deposits. The data plotted are average values of gold fineness from Shimazaki (1974), Huston et al. (1992), Westendorp (1992) and Leistel et al. (1998). High gold fineness appears to be strongly influenced by a strong Cu-Au association rather than a Zn-Au association, and therefore suggests a dependance on higher temperature versus lower temperature. (IPB, Iberian Pyrite Belt.

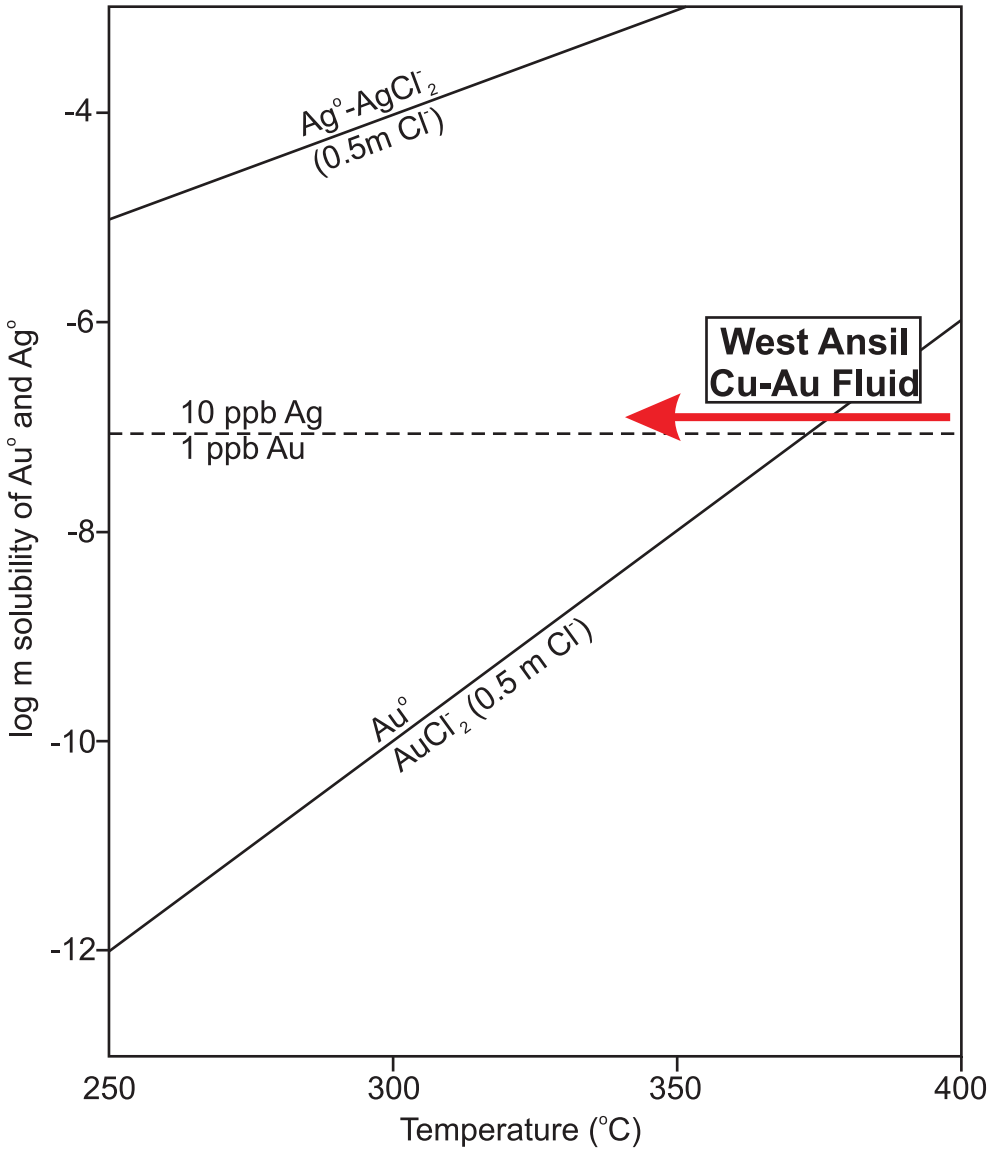

Figure 4.3 The relative solubilities of gold and silver as chloride complexes for a hypothetical West Ansil Cu-Au fluid containing 1 ppb Au and 10 ppb Ag in solution modified after Hannington et al. (1995). The strong Cu-Au association at West Ansil reflects the precipitation of gold at high temperatures while Ag remains in solution down to low temperatures.

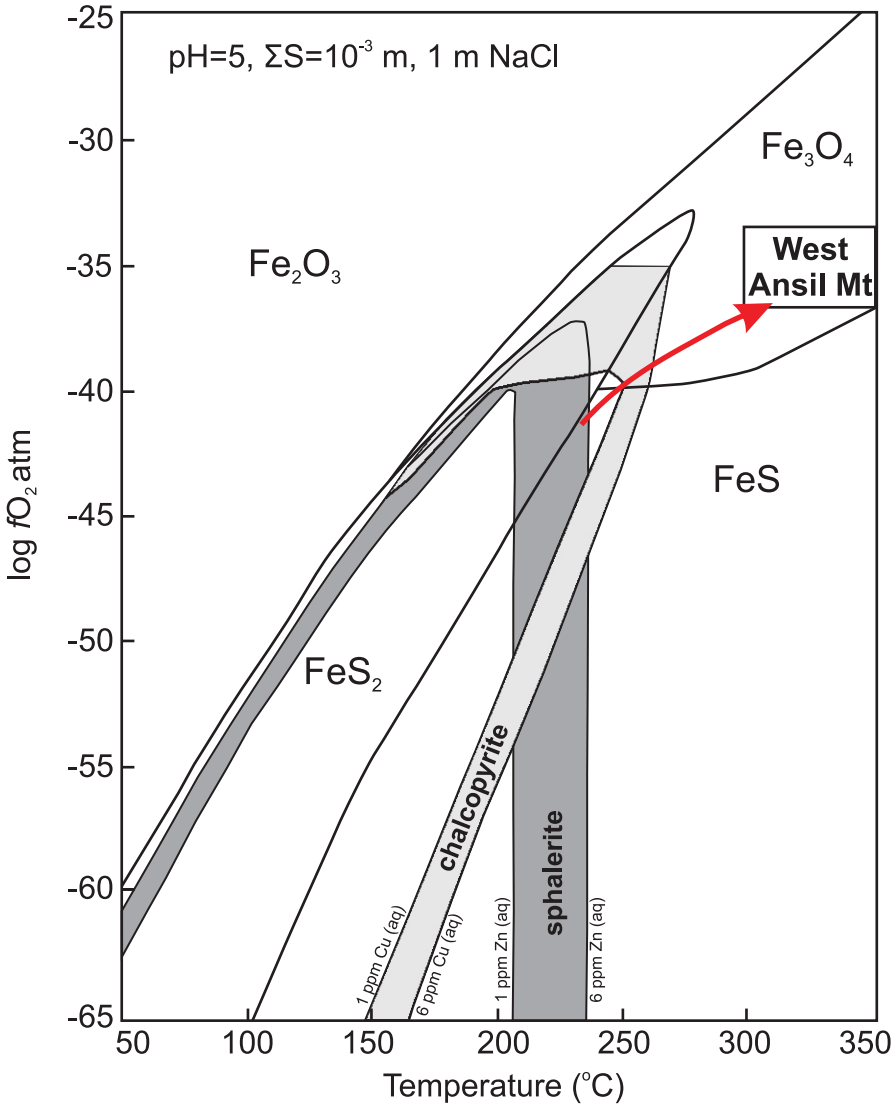

Figure 4.4 Temperature versus fo_2 diagram modified from Large (1977) showing the stability fields of py-po-mt in the Fe-S-O system and possible conditions of formation of magnetite in the West Ansil deposit (box). Note that the temperature must increase in order to dissolve chalcopyrite, so it is unlikely that replacement of pyrrhotite by magnetite is only a function of increasing fo_2.

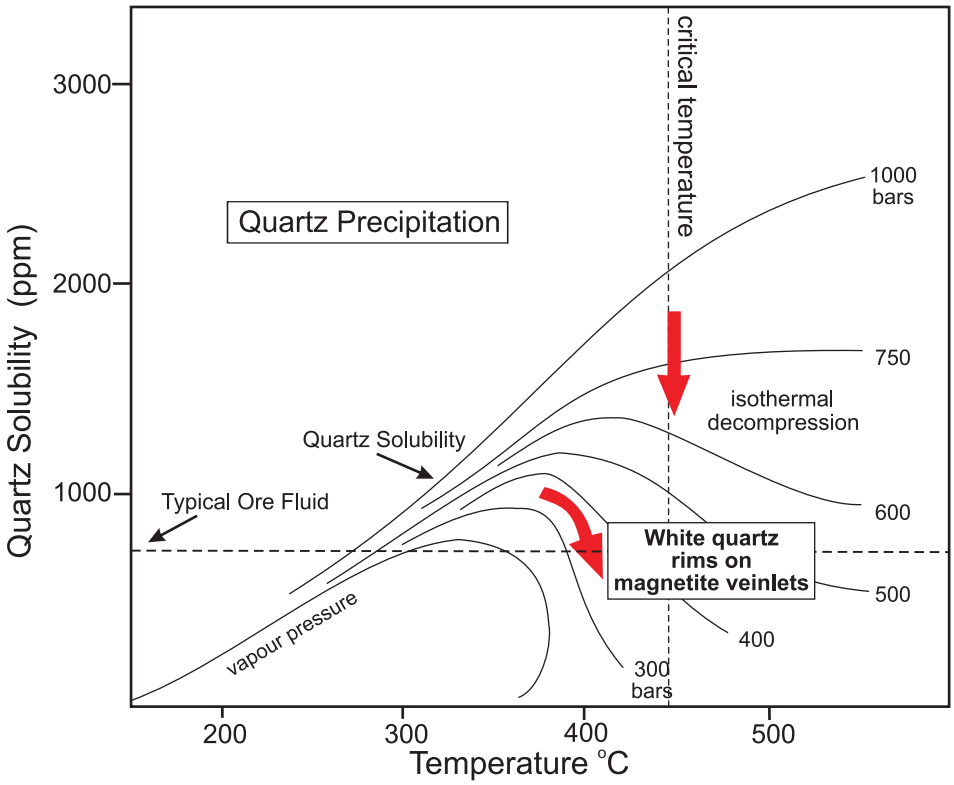

Figure 4.5 Quartz solubility diagram modified from Fournier (1985) showing the possible dumping of silica as the fluids exceeded the solubility maximum of quartz at about 400°C explaining the white quartz rims on magnetite veinlets.

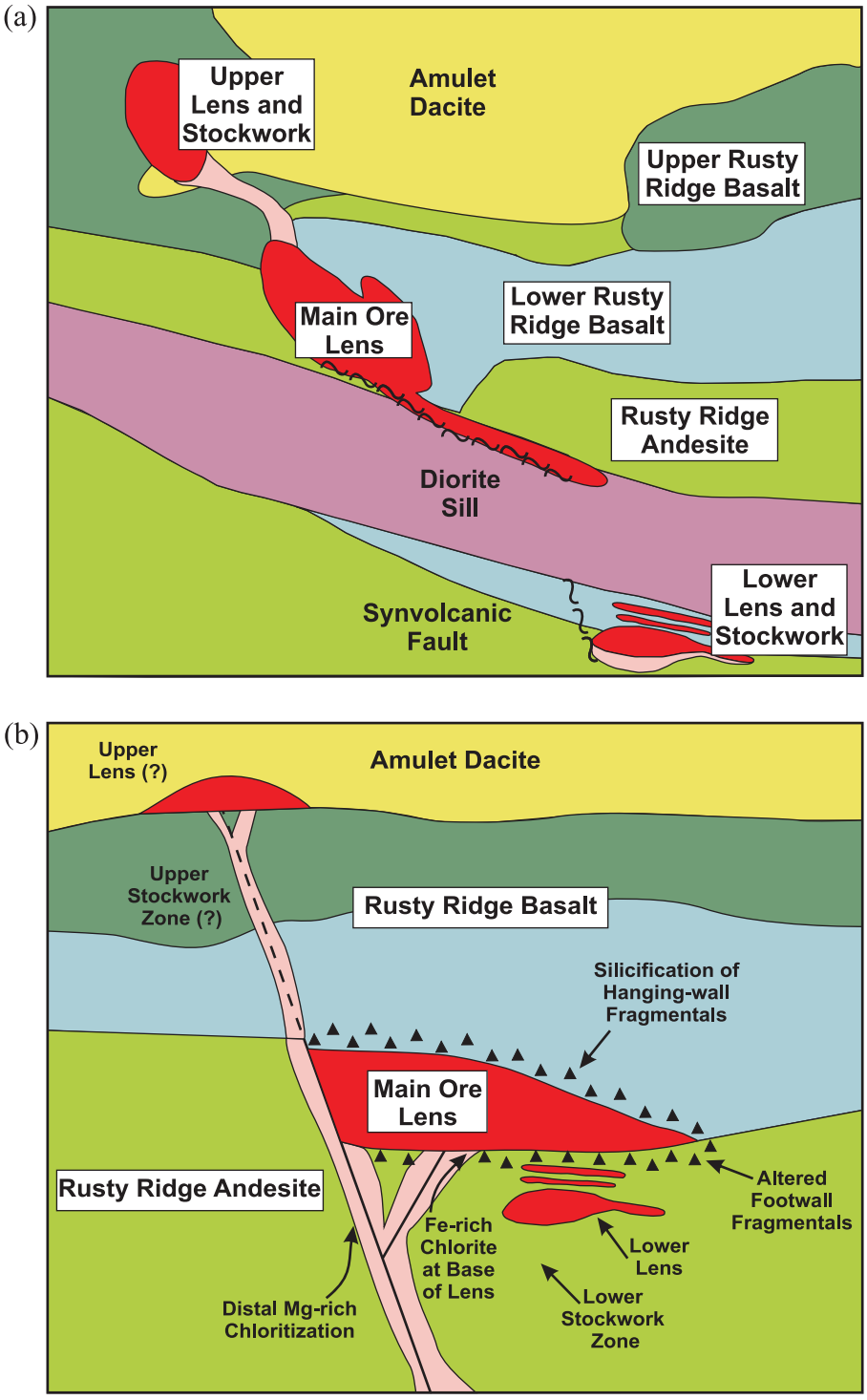

Figure 4.6 Possible reconstruction of the West Ansil deposit after the removal of the diorite and late faulting. a) The Lower lens and stockwork zone are detached and separated b) The Lower lens and stockwork zone are interpreted to be part of one single ore lens and stringer zone. The silicification in the hanging wall and the chloritization in the footwall are also consistent with a Main ore lens. The Upper lens and stockwork zone may have formed as part of a stacked system perched above the Main ore lens along the Rusty Ridge basalt and Amulet dacite horizon.

REFERENCES:

Baragar, W.R.A. 1968. Major-element geochemistry of the Noranda volcanic belt. Quebec-Ontario. *Canadian Journal of Earth Sciences*, **5:** 773-790.

Barrett, T.J., Cattalani, S., and MacLean, W.H. 1991. Massive sulphide deposits of the Noranda area, Quebec. III. The Ansil mine. *Canadian Journal of Earth Sciences,* **28:** 1699-1730.

Barrett, T.J., Cattalani, S., and MacLean, W.H. 1993a. Massive sulfide deposits of the Noranda area, Quebec. V. The Corbet mine. *Canadian Journal of Earth Sciences,* **30:** 1934-1954.

Barrett, T.J., Cattalani, S., and MacLean, W.H. 1993b. Volcanic lithogeochemistry and alteration at the Delbridge massive sulphide deposit, Noranda, Quebec. *Journal of Geochemical Exploration,* **48**: 135-173.

Barton, P.B. Jr. and Bethke, P.M., 1987. Chalcopyrite disease in sphalerite: Pathology and epidemiology. *American Mineralogist*, **72**: 451-467.

Butt, C.R.M. and Nickel, E.H., 1981. Mineralogy and Geochemistry of the Weathering of the Disseminated Nickel Sulphide Deposit at Mt. Keith, Western Australia. *Economic Geology*, **76**: 1736-1751.

Cattalani, S., Barrett, T. J., and MacLean,W. H., 1990. Géologie et géochimie du gisement d'Ansil, district de Noranda, Quebec: Ministère de l'Énergie et des Ressources du Québec, Rapport MB 90-26, 160 p.

Cattalani, S., Barrett, T.J., MacLean, W.H., and Hoy, L., 1993. Géologie et géochimie de la mine Ansil, Rouyn-Noranda. Ministère de l'Énergie et des Ressources du Québec, Rapport ET 91-03, 121 p.

Ciobanu, C.L., Cook, N.J., Damian, F., and Damian, G., 2006. Gold scavenged by bismuth melts: an example from Alpine shear-remobilizates in the Highis Massif, Romania. *Mineralogy and Petrology*, **87**: 351-384.

Craig, J.R. and Vaughan, D.J., 1981. Ore Microscopy and Ore Petrography, John Wiley and Sons, Inc., 406 p.

Crerar, D.A., Susak, N.J., Borcsik, M., and Schwartz, S., 1978. Solubility of the buffer assemblage pyrite+pyrrhotite+magnetite in NaCl solutions from 200 to 300°C. *Geochimica et Cosmochimica Acta,* **42**: 1427-1437.

de Caritat, P., Hutcheon, I., and Walshe, J.L., 1993. Chlorite geothermometry: A review – Clays. *Clay Minerals*, **41**: 219-239.

de Rosen-Spence, A.F. 1976. Stratigraphy, development and petrogenesis of the Central Noranda volcanic pile, Noranda, Quebec: Ph.D. Dissertation, Toronto, Ontario, Canada, University of Toronto, 166 p.

Dimroth, E., Imreh, L., Rocheleau, M. and Goulet, N. 1982. Evolution of the south-central part of the Archean Abitibi Belt, Quebec. Part I: Stratigraphy and paleogeographic model. *Canadian Journal of Earth Sciences,* **19:** 1729-1758.

Dubé, B., Mercier-Langevin, P., Hannington, M., Lafrance, B., Gosselin, G. and Gosselin, P. 2007. The LaRonde Penna world-class Au-rich volcanogenic massive sulfide deposit, Abitibi, Québec: mineralogy and geochemistry of alteration and implications for genesis and exploration. *Economic Geology*, **102:** 633-666.

Dugdale, A., Wilson, C.J.L., and Squire, R.J., 2006. Hydrothermal alteration at the Magdala gold deposit, western Victoria, Australia. *Journal of Earth Sciences*, **53**: 733-757.

Elmer, F.L., Dugdale, A.L. and Wilson, C.J.L., 2008. Application of mineral equilibria modeling to constrain T and XCO_2 conditions during the evolution of the Magdala gold deposit, Stawell, Western Australia. *Minerallium Deposita*, **43**: 759-776.

Fleet, M.E., 1978. The Pyrrhotite-Marcasite Transformation. *Canadian Mineralogist*, **16**: 31-35.

Floyd, P.A., and Winchester, J.A., 1978. Identification and discrimination of altered and metamorphosed volcanic rocks using immobile elements. *Chemical Geology*, **21**: 291-306.

Fournier, R.O., 1985. Silica minerals as indicators of conditions during gold deposition. In: E.W. Tooker, Editor, *Geologic Characteristics of the Sediment- and Volcanic-hosted Types of Gold Deposits – Search for an occurrence model:* U.S. Geological Survey, Bulletin 1646, p. 15-26.

Franklin, J.M., Lydon, J.W., and Sangster, D.F., 1981. Volcanic-associated massive sulfide deposits: *Economic Geology 75th Anniversary Volume,* p. 485-627.

Galley, A.G., 1994. The Geology of the Ansil Cu-Zn Massive Sulphide Deposit, Rouyn-Noranda, Quebec: Ph.D. Dissertation, Ottawa, Ontario, Canada, Carleton University, 377 p.

Galley, A.G., Watkinson, D.H., Jonasson, I.R. and Riverin, G., 1995. The Subseafloor Formation of Volcanic-Hosted Massive Sulphides: Evidence from the Ansil Deposit, Rouyn-Noranda, Canada. *Economic Geology*, **90**: 2006-2017.

Galley, A.G., Jonasson, I.R. and Watkinson, D.H., 2000. Magnetite-rich Calc-Silicate Alteration in Relation to Synvolcanic Intrusion at the Ansil Volcanogenic Massive Sulphide Deposit, Rouyn-Noranda, Quebec, Canada. *Mineralium Deposita*, **35**: 619-637.

Gélinas, L. and Ludden, J.N. 1984. Rhyolitic volcanism and the geochemical evolution of the Archean central ring complex: the Blake River Groups volcanics of the southern Abitibi Belt, Superior Province. *Physics of the Earth and Planetary Interiors,* **35:** 77-88.

Gélinas, L., Trudel, P. and Hubert, C. 1984. Chemostratigraphic division of the Blake River Group, Rouyn-Noranda area, Abitibi, Quebec. *Canadian Journal of Earth Sciences,* **21:** 220-231.

Gibson, H.L., 1990. The Mine Sequence of the Central Noranda Volcanic Complex: Geology, alteration, massive sulphide deposits and volcanological reconstruction. PhD. Thesis, Carleton University, Ottawa, Ontario, 715 p.

Gibson, H.L. and Watkinson, D.H. 1990. Volcanogenic massive sulphide deposits of the Noranda cauldron and shield volcano, Quebec. *In* The northwestern Quebec polymetallic belt. *Edited by* M. Rive, P. Verpaelst, V. Gagnon, J.M. Lulin, G. Riverin, and A. Simard. Canadian *Institute of Mining Metallurgy*, Special Volume **43**, pp. 119-132.

Gibson, H., and Galley, A., 2007. Volcanogenic massive sulphide deposits of the Archean, Noranda District, Quebec, *in* Goodfellow, W. D., ed., Mineral Deposits of Canada: A Synthesis of Major Deposit-types, District Metallogeny, the Evolution of Geological Provinces, and Exploration Methods, Special Publication No. 5, Mineral Deposits Division, Geological Association of Canada, p. 533-552.

Gifkins, C., Herrmann, W., and Large, R., 2005. Altered Volcanic Rocks: A guide to description and interpretation, Centre for Ore Deposit Research, University of Tasmania, 275 p.

Goldie, R. 1978. Magma mixing in the Flavrion pluton, Noranda area, Quebec. *Canadian Journal of Earth Sciences,* **15:** 132-144.

Goutier, J., McNicoll, V., Dion, C., Lafrance, B., Legault, M., Ross, P.-S., Mercier-Langevin, P., Cheng, L.-Z., de Kemp, E., and Ayer, J. 2009a. L'impact du Plan Cuivre et de L'ICG-3 sur la géologie de l'Abitibi et du Groupe de Blake River. Congrès Abitibi 2009 – Abitibi Cuivre, Rouyn-Noranda, September 28th, 2009, Proceedings Volume p. 9-13.

Goutier, J., McNicoll, V., Dion, C., Ross, P.-S., and Mercier-Langevin, P. 2009b. Portrait des grandes unites du Groupe de Blake River et leur relation avec les sulfures massifs volcanogènes. Congrès Abitibi 2009 – Abitibi Cuivre, Rouyn-Noranda, September 28th, 2009, Excursion Guidebook, p. 9-28.

Hannington, M.D. and Scott, S.D., 1989. Sulfidation equilibria as guides to gold mineralization in Volcanogenic Massive Sulfides: Evidence from sulphide mineralogy and the composition of sphalerite. *Economic Geology*, **84**: 1978-1995.

Hannington, M.D., Tivey, M.K., Larocque, A.C.L., Petersen, S., and Rona, P.A., 1995. The occurrence of gold in sulfide deposits of the TAG hydrothermal field, Mid-Atlantic Ridge. *Canadian Mineralogist,* **33**: 1285-1310.

Hannington, M.D., Bleeker, W., and Kjarsgaard, I., 1999. Sulfide mineralogy, geochemistry, and ore genesis of the Kidd Creek Deposit: Part I. North, Central , and South orebodies. *Economic Geology Monograph 10*, p. 163-244.

Hannington, M.D., Santaguida, F., Kjarsgaard, I.M., and Cathles, L.M., 2003. Regional greenschist facies hydrothermal alteration in the central Blake River Group, western Abitibi subprovince, Canada. *Mineralium Deposita*, **38**: 393-422.

Helgeson, H.C., 1969. Thermodynamics of hydrothermal systems at elevated temperatures and pressures. *American Journal of Science,* **267**: 729-804.

Hey, M.H., 1954. A new review of the chlorite. *Mineralogical Magazine*, **30**: 277-292.

Hoy, L.D., 1993. Regional evolution of hydrothermal fluids inthe Noranda district, Quebec: Evidence from $\Delta^{18}O$ values from volcanogenic massive sulfide deposits: *Economic Geology*, **88**: 1526–1541.

Huston, D.L., Bottrilll, R.S., Creelman, R.A., Zaw, K., Ramsden, T.R., Rand, S.W., Gemmell, B.J., Jablonski, W., Sie, S.H., and Large, R.R., 1992. Geological and geochemical controls on the mineralogy and grain size of gold-bearing phases, Eastern Australian volcanic-hosted massive sulphide deposits. *Economic Geology,* **87:** 542-563.

Ikingura, J.R., Bell, K., and Watkinson, D.H., 1989. Hydrothermal alteration and oxygen and hydrogen isotope geochemistry of the D-68 zone Cu-Zn massive sulphide deposit, Noranda, Quebec, Canada. *Mineralogy and Petrology*, **40**: 155-172.

Kalogeropoulos, S.I., and Scott, S.D., 1989. Mineralogy and geochemistry of an Archean tuffaceous exhalite: the main contact tuff, Millenbach mine area, Noranda, Quebec. *Canadian Journal of Earth Sciences*, **26**: 88-105.

Kerr, D.J., and Gibson, H.L., 1993. Comparison of the Horne Volcanogenic Massive Sulfide Deposit and Intracauldron Deposits of the Mine Sequence, Noranda, Quebec. *Economic Geology*, **88**: 1419-1442.

Knuckey, M.J. and Watkins, J.J., 1982. The geology of the Corbet massive sulfide deposit, Noranda, Quebec, Canada: Geological Association of Canada Special Paper 25, p. 297-318

Knuckey, M.J., Comba, C.D.A. and Riverin, G., 1982. Structure, metal zoning, and alteration at the Millenbach deposit, Noranda, Quebec, Canada: Geological Association of Canada Special Paper 25, p. 255-296.

Kohyama, N., and Sudo, T., 1975. Hisingerite occurring as a weathering product of iron-rich saponite. *Clays and Clay Minerals*, **23**: 215-218.

Kojima, S., 1992. The nature of chalcopyrite inclusions in sphalerite; exsolution, coprecipitation, or "disease"?; discussion. *Economic Geology*, **87**: 1191-1192.

Lambert, I.B. and Sato, T., 1974. The Kuroko and associated ore deposits of Japan. *Economic Geology*, **69**: 1215-1236.

Large, R.R., 1977. Chemical Evolution and Zonation of Massive Sulfide Deposits in Volcanic Terrains. *Economic Geology*, **72**: 549-572.

Large, R.R., Huston, D.L., McGoldrick, P. J., and Ruxton, P.A., 1989. Gold distribution and genesis in Australian volcanogenic massive sulfide deposits and their significance for gold transport models. *Economic Geology Monograph 6,* p. 520-536.

Larson, J.E., 1983. Geology, Geochemistry and Wallrock Alteration at the Magusi and New Insco Massive Sulfide Deposits, Hebecourt Township, Northwestern Quebec. Unpublished M.Sc. Thesis, University of Western Ontario, 173 p.

Leistel, J.M, Marcoux, E., Deschamps, Y., and Joubert, M., 1998. Antithetic behavior of gold in volcanogenic massive sulphide deposits of the Iberian pyrite belt. *Minerallium Deposita*, **33**: 82-97.

MacLean , W.H., and Kranidiotis, P., 1987. Immobile elements as monitors of mass transfer in hydrothermal alteration: Phelps Dodge massive sulphide deposit, Matagami, Quebec. *Economic Geology,* **82**: 951-962.

MacLean, W.H., and Hoy, L.D., 1991. Geochemistry of hydrothermally altered rocks at the Horne mine, Noranda, Quebec. *Economic Geology*, **86**: 506-528.

MacLean, W.H., and Barrett, T.J., 1993. Lithogeochemical techniques using immobile elements. *Journal of Geochemical Exploration,* **48**: 109-133.

Marcoux, E., Moelo, Y., and Leistel, J.M., 1996. Bismuth and cobalt minerals as indicators of stringer zones to massive sulphide deposits, Iberian pyrite belt. *Minerallium Deposita*, **31**: 1-26.

McDonough, W.F., and Sun, S.-s. 1995. The composition of the earth. *Chemical Geology*, **120**: 223-254.

McNicoll, V., Goutier, J., Dubé, B., Mercier-Langevin, P., David, J., Ross, P.-S., Dion, C., Monecke, T., Thurston, P., Pilote, P, Bédard, J., Bécu, V., Leclerc, F., Percival, J., Legault, M., Gibson., and Ayer, J., 2009. New U-Pb ages from the TGI-3 Abitibi project/Copper plan: Implications for geological interpretation and base metal exploration; in Québec Exploration

2009. Abstract of oral presentation and posters, Ministère des Ressources Naturelles et de la Faune (Québec), Report DV 2009-06, p.35.

Mercier-Langevin, P., Dubé, B., Hannington, M.D., Richer-Laflèche, M., and Gosselin, G., 2007. The LaRonde Penna Au-Rich Volcanogenic Massive Sulfide Deposit, Abitibi Greenstone Belt, Quebec: Part II. Lithogeochemistry and Paleotectonic Setting. *Economic Geology*, **102**: 611 - 631.

Miyano, T., and Klein, C., 1989. Phase equilibria in the system K2O-FeO-MgO-Al2O3-SiO2-H2O-CO2 and the stability limit of stilpnomelane in metamorphosed Precambrian iron formations. *Contributions to Mineralogy and Petrology*, **102**: 478-491.

Morrison, G.W., Rose, W.J., and Jarieth, S., 1991. Geological and geochemical controls on the silver content(fineness) of gold in gold-silver deposits. *Ore Geology Reviews,* **2**: 333-364.

Mortensen, J.K. 1987. Preliminary U-Pb zircon ages for volcanic and plutonic rocks of the Noranda-Lac Abitibi area, Abitibi Subprovince, Quebec, In current research, Part A, Geological Survey of Canada, Paper 87-1A, p. 581-590.

Murowchick, J.B., 1992. Marcasite Inversion and the Petrographic Determination of Pyrite Ancestry. *Economic Geology,* **87:** 1141-1152.

Nickel, E.H., Ross, J.R., and Thornber, M.R., 1974. The supergene alteration of pyrrhotite-pentlandite ore at Kambalda, Western Australia. *Economic Geology*, **69**: 93-107.

Nickel, E.H., Allchurch, P.D., Mason, M.G. and Wilmshurst, J.R., 1977. Supergene alteration at the Perseverance Nickel deposit, Agnew, Western Australia. *Economic Geology*, **72**: 184-203.

Nishiyama, T., 1974. Minor elements in some sulphide minerals from the kuroko deposits of the Shakanai mine. Mining Geology Special Issue 6, p. 371-376.

Ohmoto, H., 2003. Non-redox transformation of magnetite–hematite in hydrothermal systems, *Economic Geology*, **98**: 157-161.

Plimer, I.R., Finlow-Bates, T., 1978. Relationship between primary iron sulphide species, sulfur source, depth of formation and age of submarine exhalite sulphide deposits. *Mineralium Deposita*, **13**: 399-410.

Renders, P.J. and Seward, T.M., 1989. The stability hydrosulphido- and sulphido-complexes of Au(I) and Ag(I) at 25°C. *Geochimica et Cosmochimica Acta,* **53**: 245-253.

Riverin, G. and Hodgson, C.J. 1980. Wallrock alteration at the Millenbach Cu-Zn mine, Noranda, Quebec. *Economic Geology,* **75:** 424-444.

Riverin, G., LaBrie, M., Salmon, B., Cazavant, A., Asselin, R., and Gagnon, M. 1990. The geology of the Ansil deposit, Rouyn-Noranda, Quebec. *In The* Northwestern Quebec polymetallic belt. *Edited by* M. Rive, P. Verpaelst, Y. Gagnon, J.M. Lulin, G. Riverin, and A. Simard. Canadian Institute of Mining Metallurgy, Special Volume 43, pp. 143-151.

Seward, T.M., 1976. The stability of chloride complexes of silver in hydrothermal solutions up to 350°C. *Geochimica et Cosmochimica Acta,* **40**: 1329-1341.

Seward, T.M. and Barnes, H.L., 1997. Metal transport by hydrothermal ore fluids. In: H.L. Barnes, Editor, *Geochemistry of Hydrothermal Ore Deposits* (3rd ed.), Wiley, NY, New York, p. 435–486.

Sharpe, R. and Gemmell, B., 2002. The Archean Cu-Zn magnetite-rich Gossan Hill volcanic-hosted massive sulfide deposit, Western Australia: Genesis of a multistage hydrothermal system. *Economic Geology*, **97**: 517-539.

Shenberge, D.M. and Barnes, H.L., 1989. Solubility of gold in aqueous sulphide solutions from 150 to 350°C. *Geochimica et Cosmochimica Acta,* **53**: 269-278.

Shimazaki, Y., 1974. Ore minerals of the Kuroko-type deposits. *Society of Mining Geologists of Japan,* Special Issue **6:** 311-322.

Skirrow, R.G., and Franklin, J.M., 1994. Silicification and metal leaching in semi-conformable alteration beneath the Chisel Lake massive sulfide deposit, Snow Lake, Manitoba. *Economic Geology,* **89**: 31-50.

Smith, R.N., and Huston, D.L., 1992. Distribution and association of selected trace elements at the Rosebery deposit, Tasmania. *Economic Geology*, **87**: 706-719.

Spence, C.D., 1975. Volcanic features of theVauze sulfide deposit, Noranda, Quebec. *Economic Geology*, **70**: 102-114.

Spence, C.D., and de Rosen-Spence, A.F., 1975. The place of sulfide mineralization in the volcanic sequence at Noranda, Quebec. *Economic Geology*, **70**: 90-101.

Stumpfl, E.F. and Clark, A.M., 1964. A natural occurrence of Co_9S_8, identified by X-ray microanalyses. *Neues Jahrbuch für Mineralogie Monatshefte*, 240-245.

Sudo, T., and Nakamura, T., 1952. Hisingerite from Japan. *American Mineralogist*, **37**: 618-621.

Tanimura, S., Date, J., Takahashi, T., and Ohmoto, H., 1983. Geologic setting of the kuroko deposits, Japan. Part II. Stratigraphy and structureof the Hokuro district. *Economic Geology Monograph 5*, p. 24-38.

Taylor, S.R., Kaye, M., White, A.J.R., Duncan, A.R., and Ewart, A., 1969. Genetic significance of Co, Cr, Ni, Sc and V content of andesites. *Geochimica et Cosmochimica Acta*, **33**: 275-286.

Tooth, B., Brugger, J., Ciobanu, C.L., and Liu, W., 2008. Modelling of gold scavenging by bismuth melts coexisting with hydrothermal fluids. *Geology*, **36**: 815-818.

Weierhauser, L., 2005. Fluids associated with an Archean regional hydrothermal system, Abitibi Subprovince, Canada; Fluid inclusion characteristics and hot cathode cathodoluminescence characteristics of host minerals – Implications for Archean seawater chemistry and magmatic hydrothermal processes. PhD Thesis, University of Toronto, Canada, 127 p.

Westendorp, R.W., Watkinson, D.H., and Jonasson, I.R. 1991. Silicon-bearing zoned magnetite crystals and the evolution of hydrothermal fluid at the Ansil Cu-Zn Mine, Rouyn-Noranda, Quebec. *Economic Geology,* **86:** 1110-1114.

Westendorp, R.W., 1992, Magnetite Zones at the Ansil Cu-Zn Deposit, Rouyn-Noranda, Quebec: M.Sc. Dissertation, Ottawa, Ontario, Canada, Carleton University, 46 p.

Whelan, J.A., and Goldich, S.S., 1961. New data for hisingerite and neotocite. *American Mineralogist*, **46**: 1412-1423.

Xstrata Copper Canada Ltd, 2005, West Ansil Resourse Estimate 43-101F1 Technical Report, 50 p.

LIST OF APPENDICES

Appendix I. Drill-hole lithological profile and Cu-Zn-Au-Ag-Pb concentrations for AN-05-02.

Appendix II. Drill-hole lithological profile and Cu-Zn-Au-Ag-Pb concentrations for AN-05-03.

Appendix III. Drill-hole lithological profile and Cu-Zn-Au-Ag-Pb concentrations for AN- 05-04.

Appendix IV. Drill-hole lithological profile and Cu-Zn-Au-Ag-Pb concentrations for WAN-05-01.

Appendix V. Drill-hole lithological profile and Cu-Zn-Au-Ag-Pb concentrations for WAN-05-02.

Appendix VI. Drill-hole lithological profile and Cu-Zn-Au-Ag-Pb concentrations for WAN-05-04.

Appendix VII. Drill-hole lithological profile and Cu-Zn-Au-Ag-Pb concentrations for WAN-05-05.

Appendix VIII. Drill-hole lithological profile and Cu-Zn-Au-Ag-Pb concentrations for WAN-05-06.

Appendix IX. Drill-hole lithological profile and Cu-Zn-Au-Ag-Pb concentrations for WAN-05-07.

Appendix X. Drill-hole lithological profile and Cu-Zn-Au-Ag-Pb concentrations for WAN-05-09.

Appendix XI. Drill-hole lithological profile and Cu-Zn-Au-Ag-Pb concentrations for WAN-05-10.

Appendix XII. Drill-hole lithological profile and Cu-Zn-Au-Ag-Pb concentrations for WAN-05-12.

Appendix XIII. Drill-hole lithological profile and Cu-Zn-Au-Ag-Pb concentrations for WAN-05-15.

Appendix XIV. Drill-hole lithological profile and Cu-Zn-Au-Ag-Pb concentrations for WAN-05-18.

Appendix XV. Drill-hole lithological profile and Cu-Zn-Au-Ag-Pb concentrations for WAN-05-19.

Appendix XVI. Drill-hole lithological profile and Cu-Zn-Au-Ag-Pb concentrations for WAN-05-20W.

Appendix XVII. Location of samples in the Upper lens of the West Ansil deposit.

Appendix XVIII. Location of samples in the Middle lens of the West Ansil deposit.

Appendix XIX. Location of samples in the Lower lens of the West Ansil deposit.

Appendix XX. Ore geochemistry of all samples collected at West Ansil.

Appendix XXI. Analytical methods for ore types and whole-rock geochemistry.

Appendix XXII. Boucher, S.M., Hannington, M.D., Dubé, B., 2010. Primary and secondary ore textures in the West Ansil volcanic-hosted massive sulphide deposit, Noranda Mining Camp, Rouyn-Noranda, Québec, *Geological Survey of Canada*, Current Research 2010-10, 16 p.

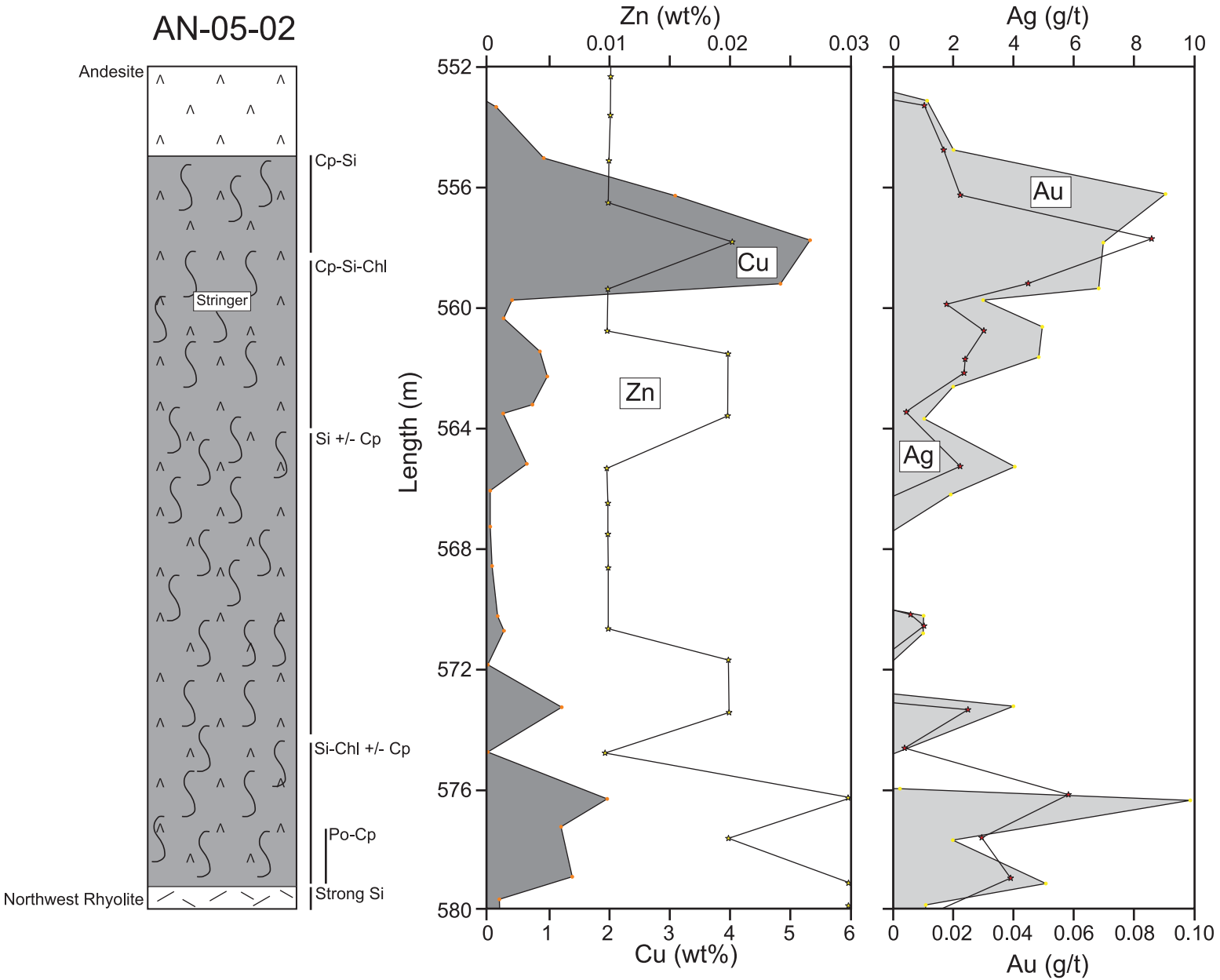

Appendix I. Drill-hole lithological profile and Cu-Zn-Au-Ag-Pb concentrations for hole AN-05-02 from the Lower stockwork zone. Data from Xstrata Copper Canada, Ltd. Si, silica; Chl, chlorite; Po, pyrrhotite; Cp, chalcopyrite; Py, pyrite.

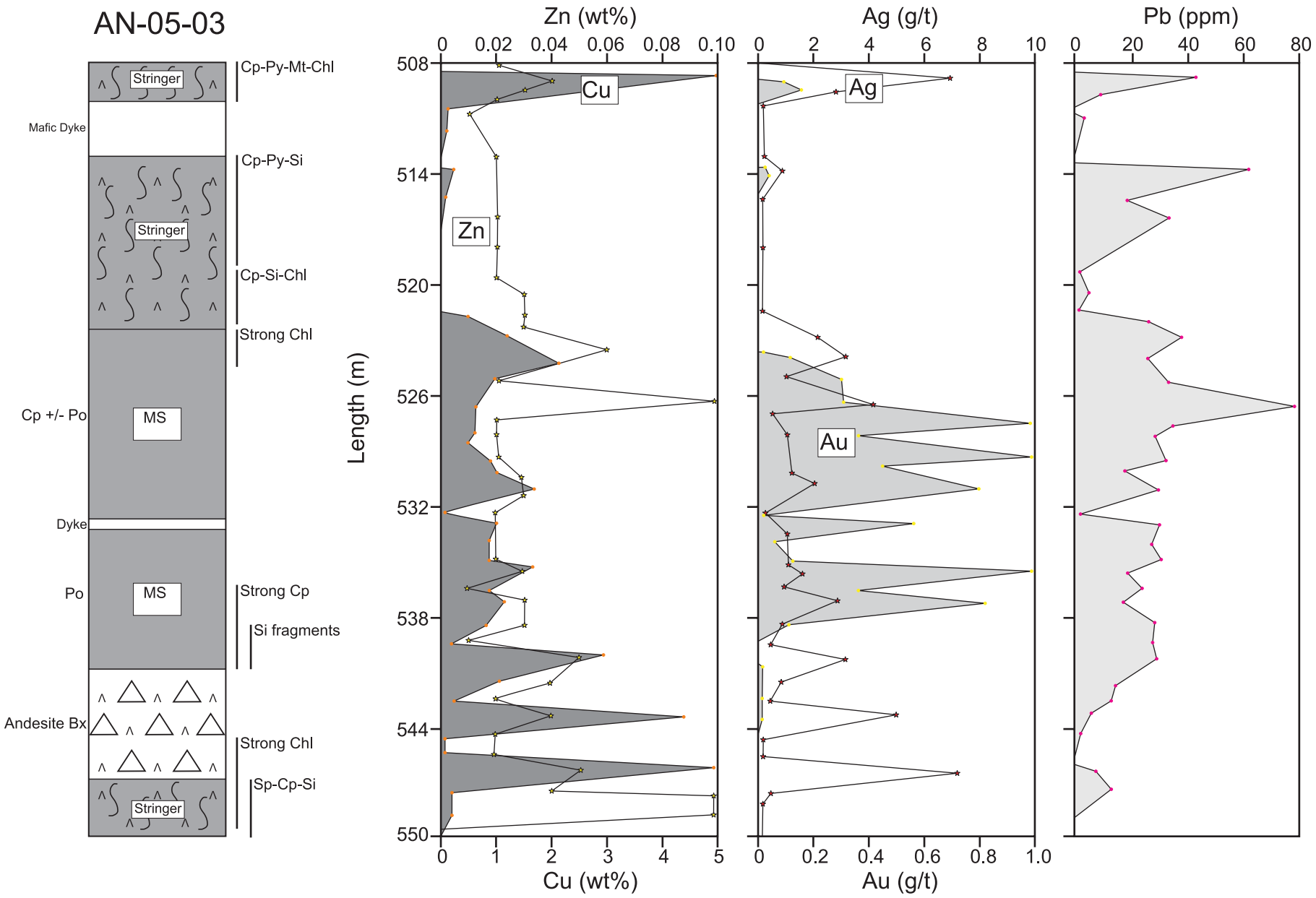

Appendix II. Drill-hole lithological profile and Cu-Zn-Au-Ag-Pb concentrations for hole AN-05-03 from the Lower Lens. Data from Xstrata Copper Canada, Ltd. Si, silica; Chl, chlorite; Po, pyrrhotite; Cp, chalcopyrite; Mt, magnetite; Sp, sphalerite; Py, pyrite.

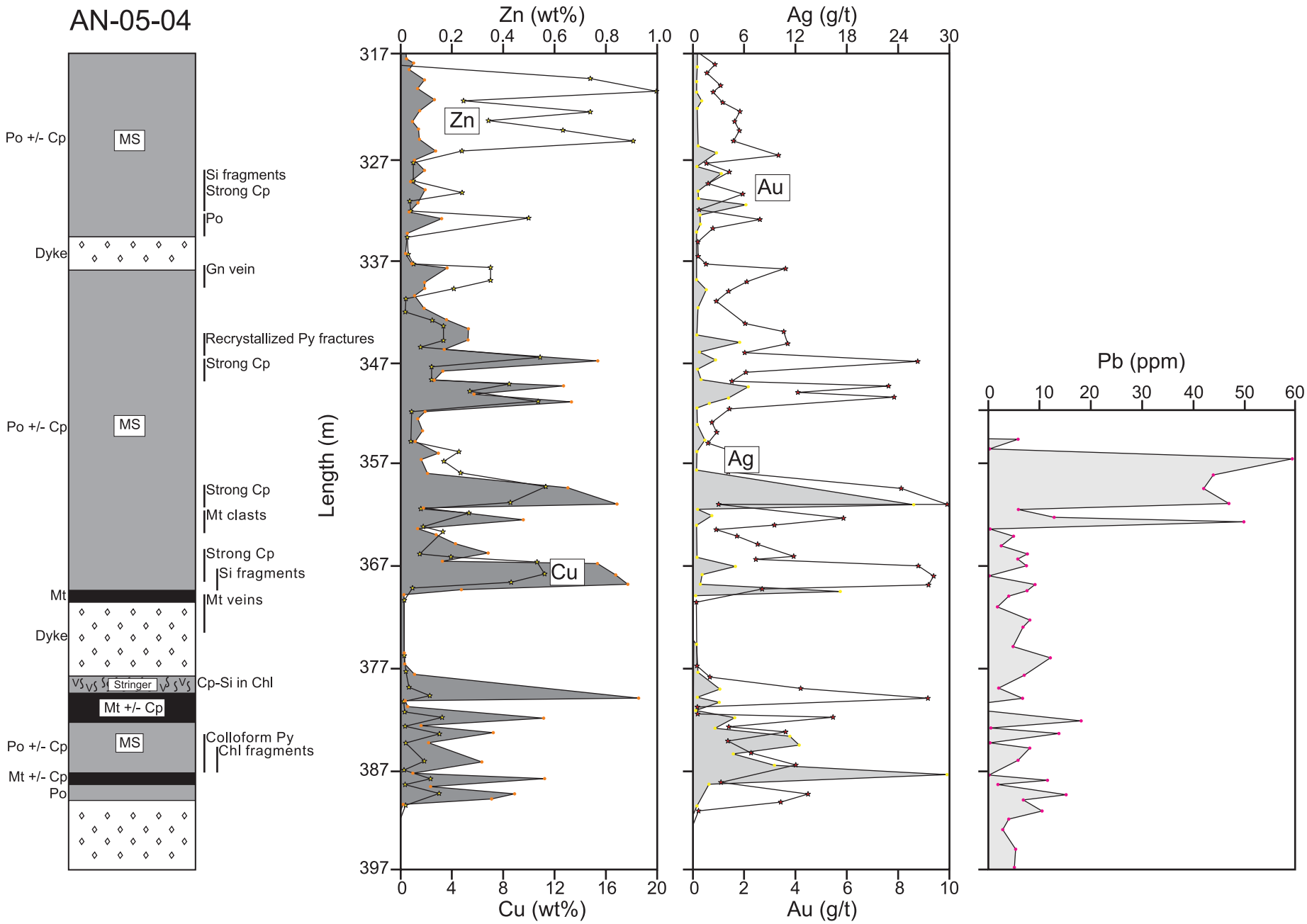

Appendix III. Drill-hole lithological profile and Cu-Zn-Au-Ag-Pb concentrations for hole AN-05-04 from the Middle lens. Data from Xstrata Copper Canada, Ltd. Si, silica; Chl, chlorite; Po, pyrrhotite; Cp, chalcopyrite; Mt, magnetite; Sp, sphalerite; Py, pyrite.

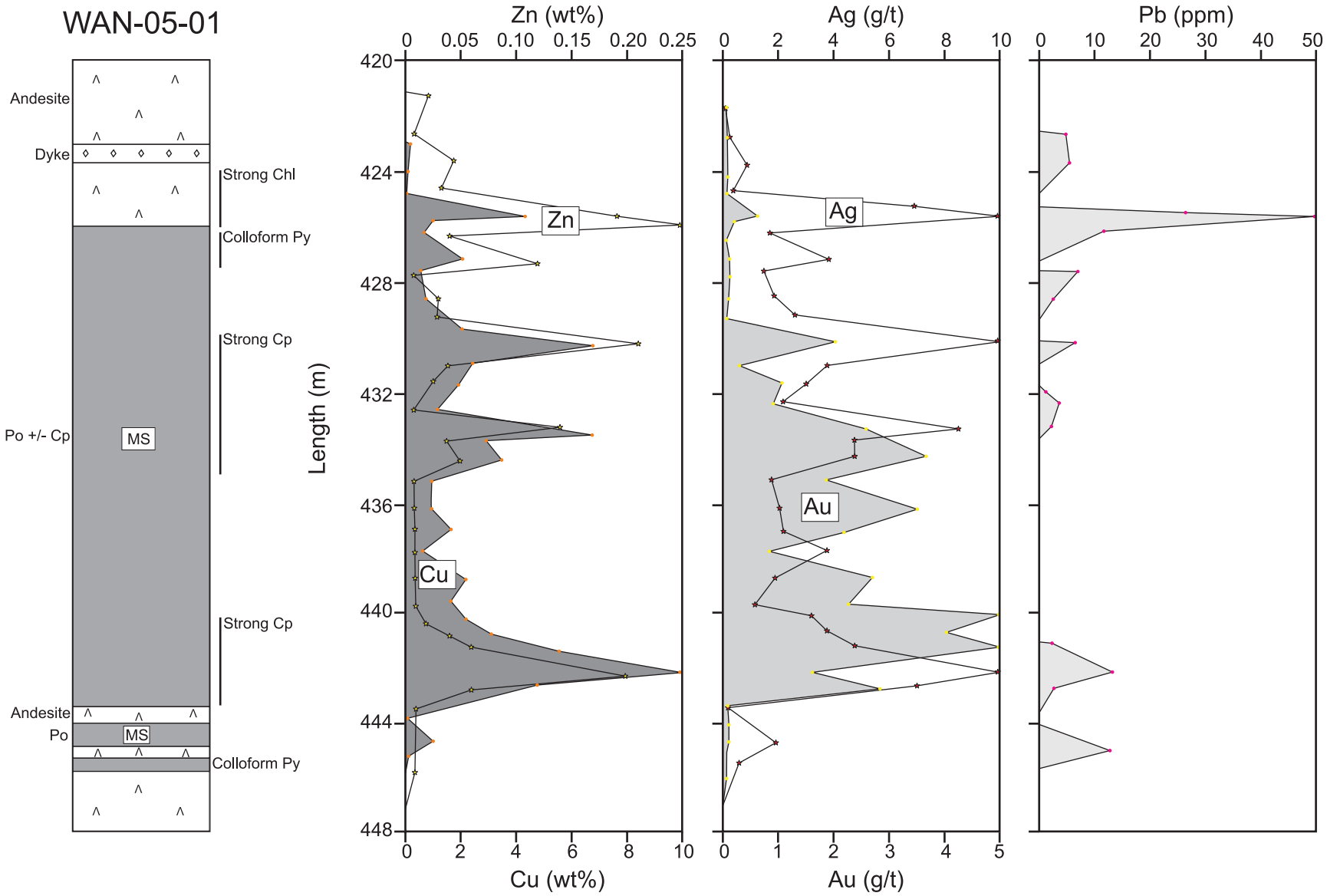

Appendix IV. Drill-hole lithological profile and Cu-Zn-Au-Ag-Pb concentrations for hole WAN-05-01 from the Middle lens. Data from Xstrata Copper Canada, Ltd. Si, silica; Chl, chlorite; Po, pyrrhotite; Cp, chalcopyrite; Py, pyrite.

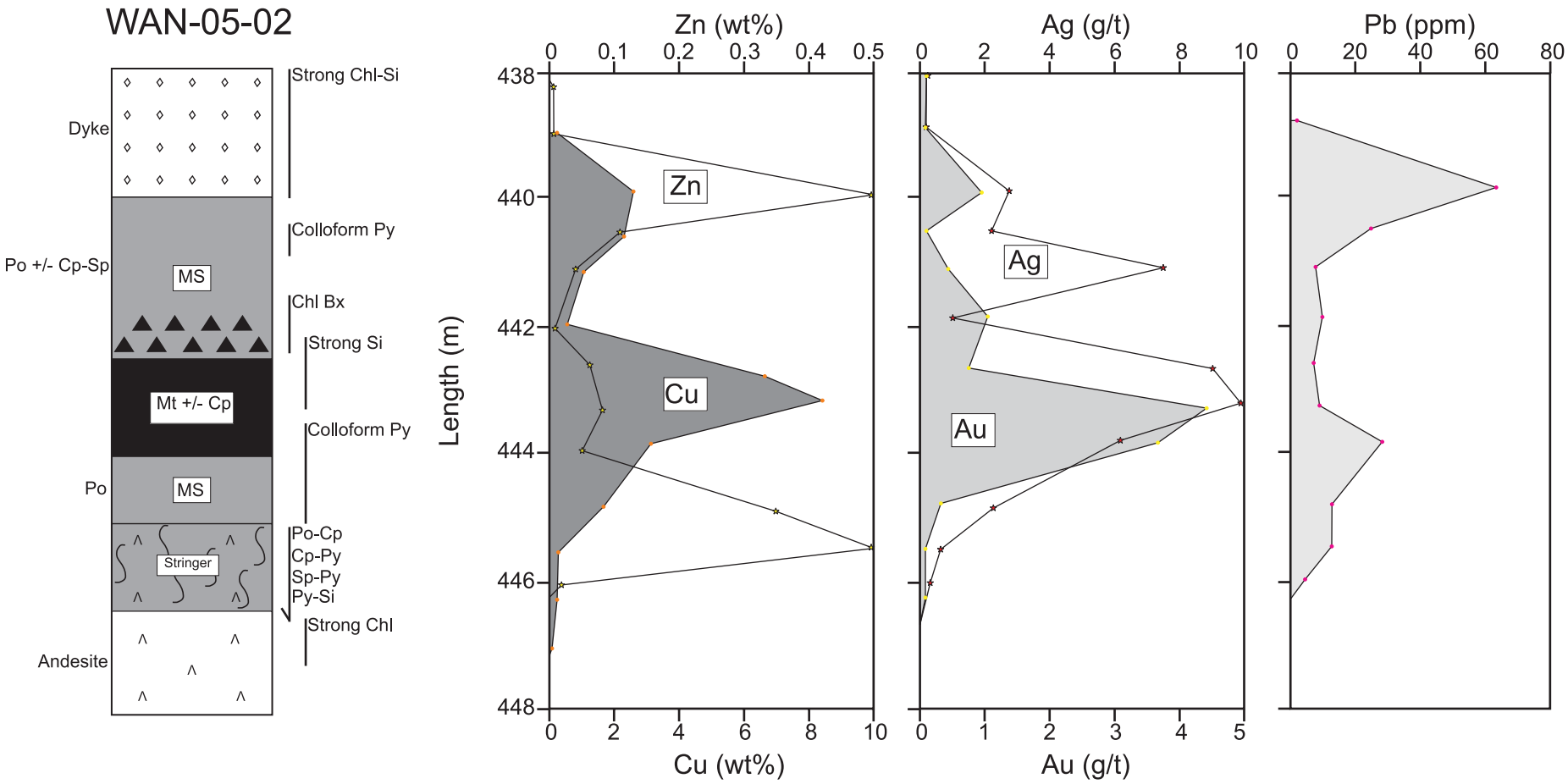

Appendix V. Drill-hole lithological profile and Cu-Zn-Au-Ag-Pb concentrations for hole WAN-05-02. Data from Xstrata Copper Canada, Ltd. Si, silica; Chl, chlorite; Po, pyrrhotite; Cp, chalcopyrite; Mt, magnetite; Sp, sphalerite; Py, pyrite.

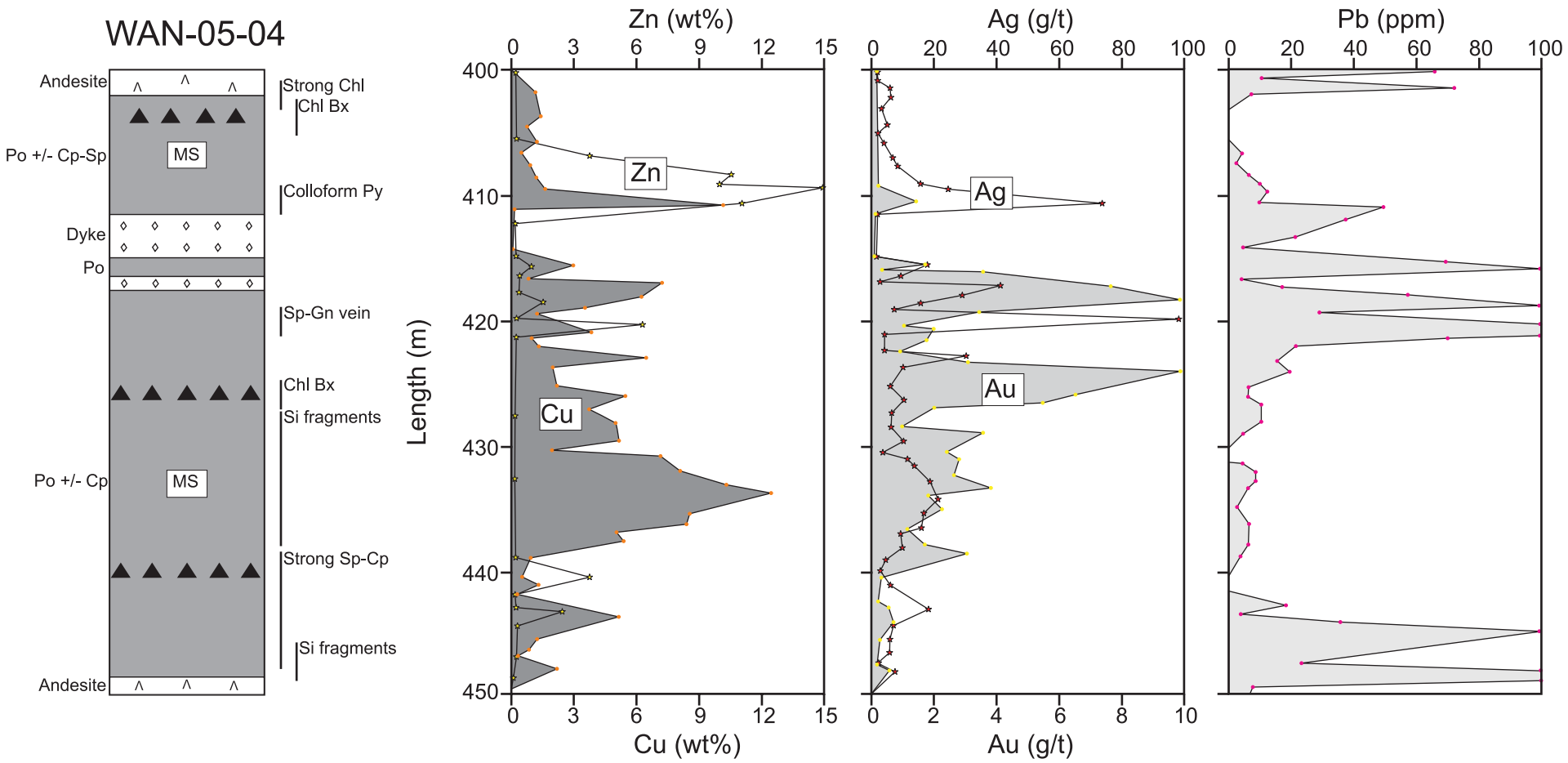

Appendix VI. Drill-hole lithological profile and Cu-Zn-Au-Ag-Pb concentrations for hole WAN-05-04 from the Middle lens. Data from Xstrata Copper Canada, Ltd. Si, silica; Chl, chlorite; Po, pyrrhotite; Cp, chalcopyrite; Sp, sphalerite; Py, pyrite; Gn, galena.

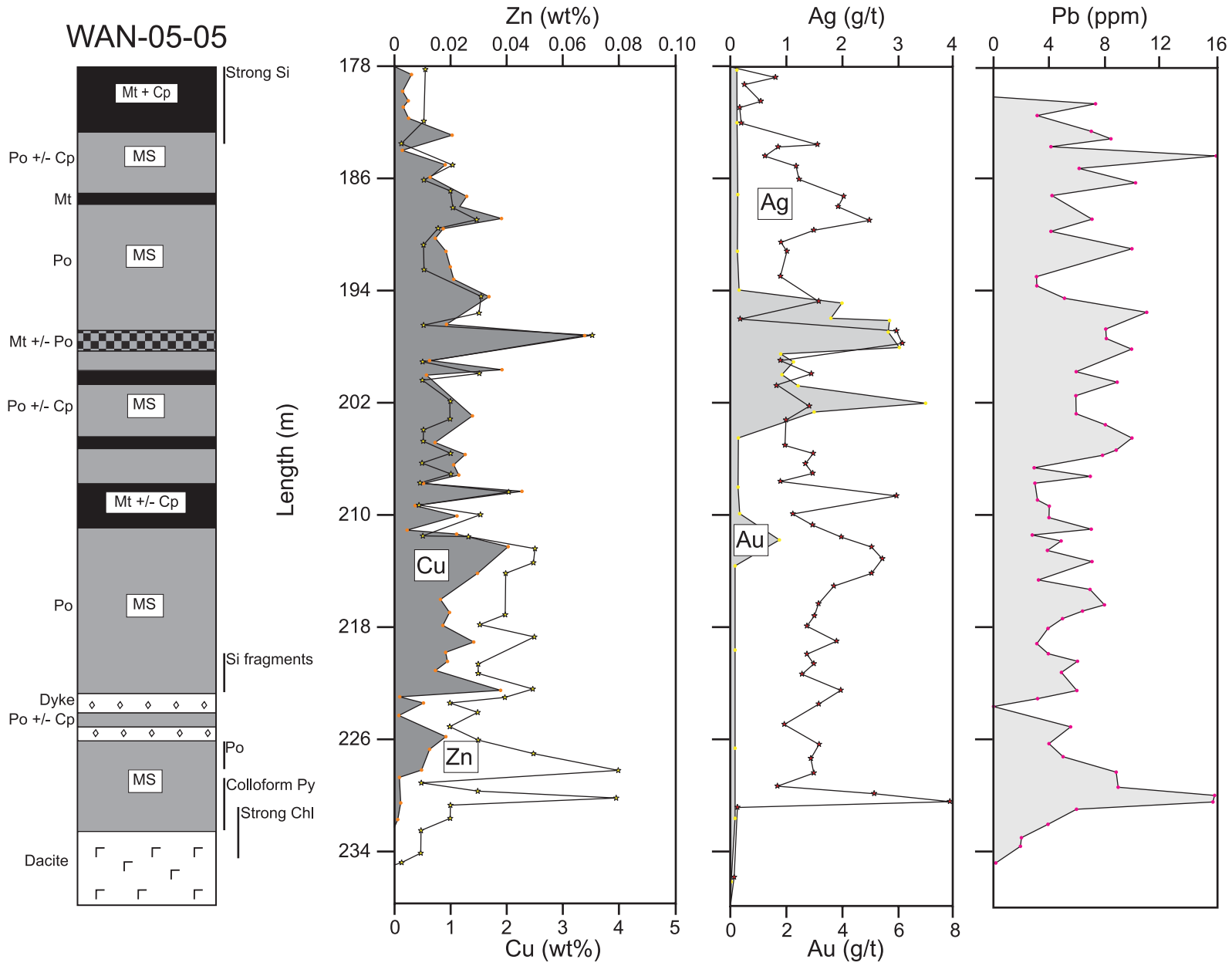

Appendix VII. Drill-hole lithological profile and Cu-Zn-Au-Ag-Pb concentrations for hole WAN-05-05 from the Upper lens. Data from Xstrata Copper Canada, Ltd. Si, silica; Chl, chlorite; Po, pyrrhotite; Cp, chalcopyrite; Mt, magnetite; Py, pyrite.

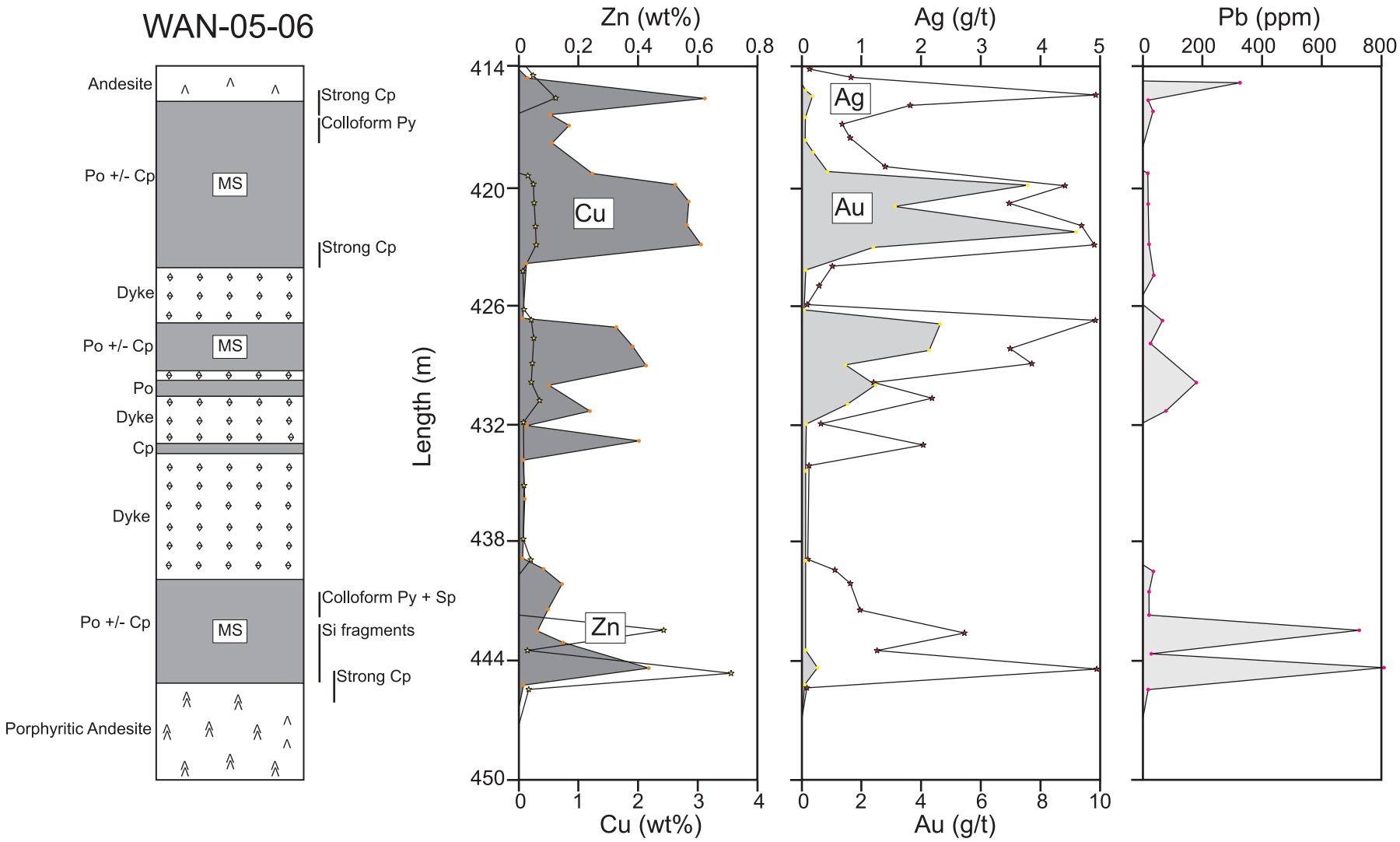

Appendix VIII. Drill-hole lithological profile and Cu-Zn-Au-Ag-Pb concentrations for hole WAN-05-06 from the Middle lens. Data from Xstrata Copper Canada, Ltd. Si, silica; Chl, chlorite; Po, pyrrhotite; Cp, chalcopyrite; Sp, sphalerite; Py, pyrite.

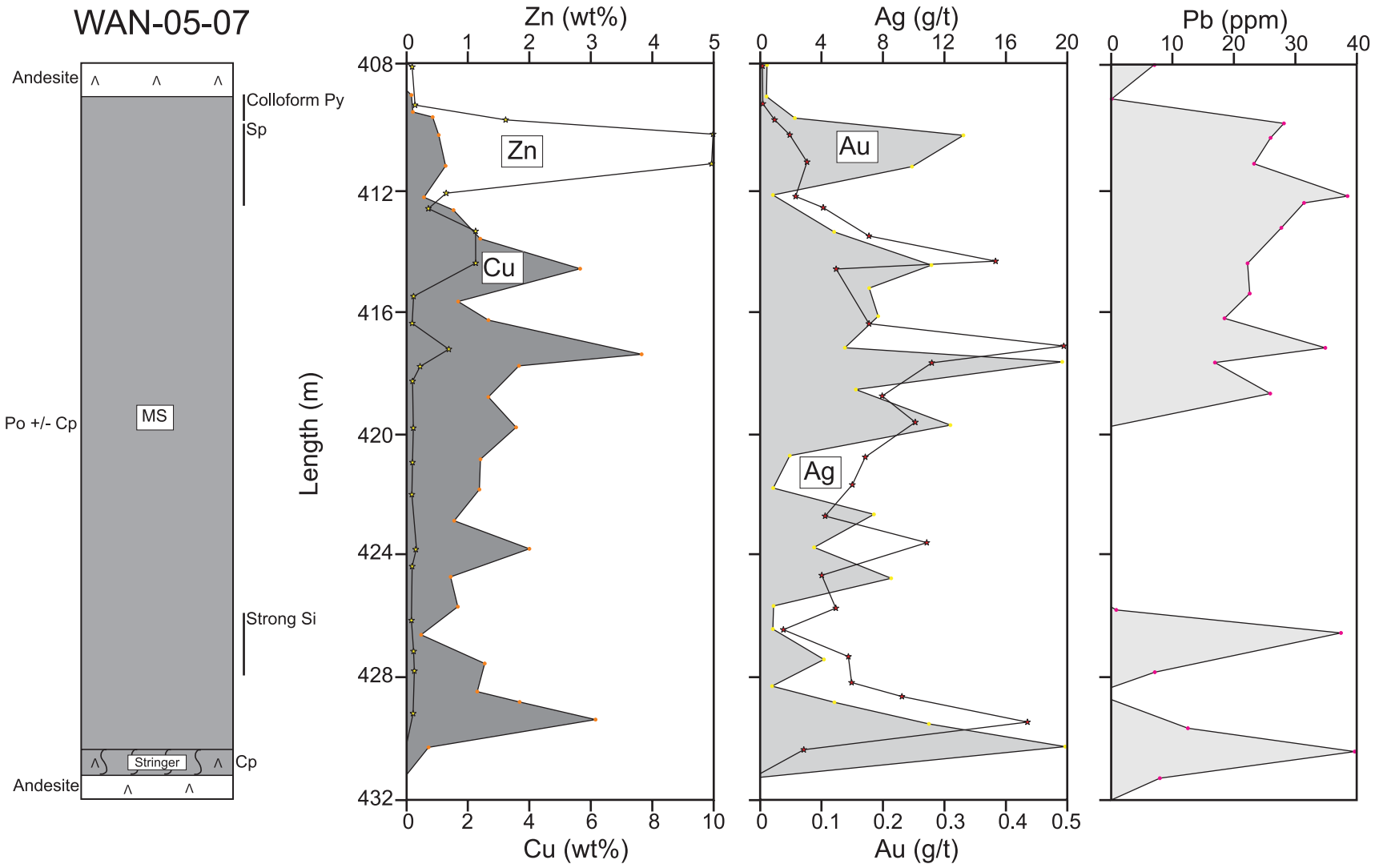

Appendix IX. Drill-hole lithological profile and Cu-Zn-Au-Ag-Pb concentrations for hole WAN-05-07 from the Middle lens. Data from Xstrata Copper Canada, Ltd. Si, silica; Chl, chlorite; Po, pyrrhotite; Cp, chalcopyrite; Sp, sphalerite; Py, pyrite.

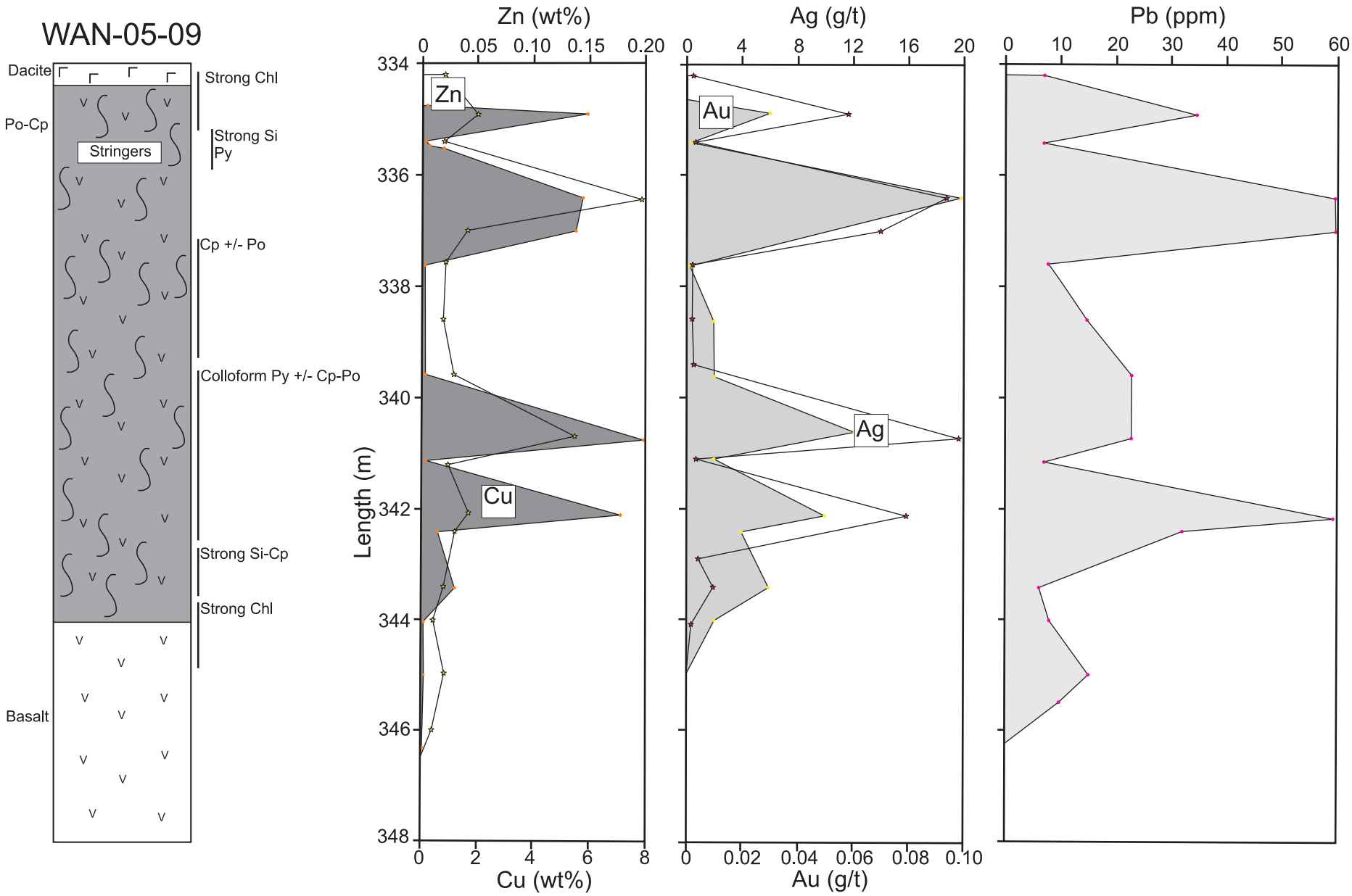

Appendix X. Drill-hole lithological profile and Cu-Zn-Au-Ag-Pb concentrations for hole WAN-05-09 from the Upper stockwork zone. Data from Xstrata Copper Canada, Ltd. Si, silica; Chl, chlorite; Po, pyrrhotite; Cp, chalcopyrite; Py, pyrite.

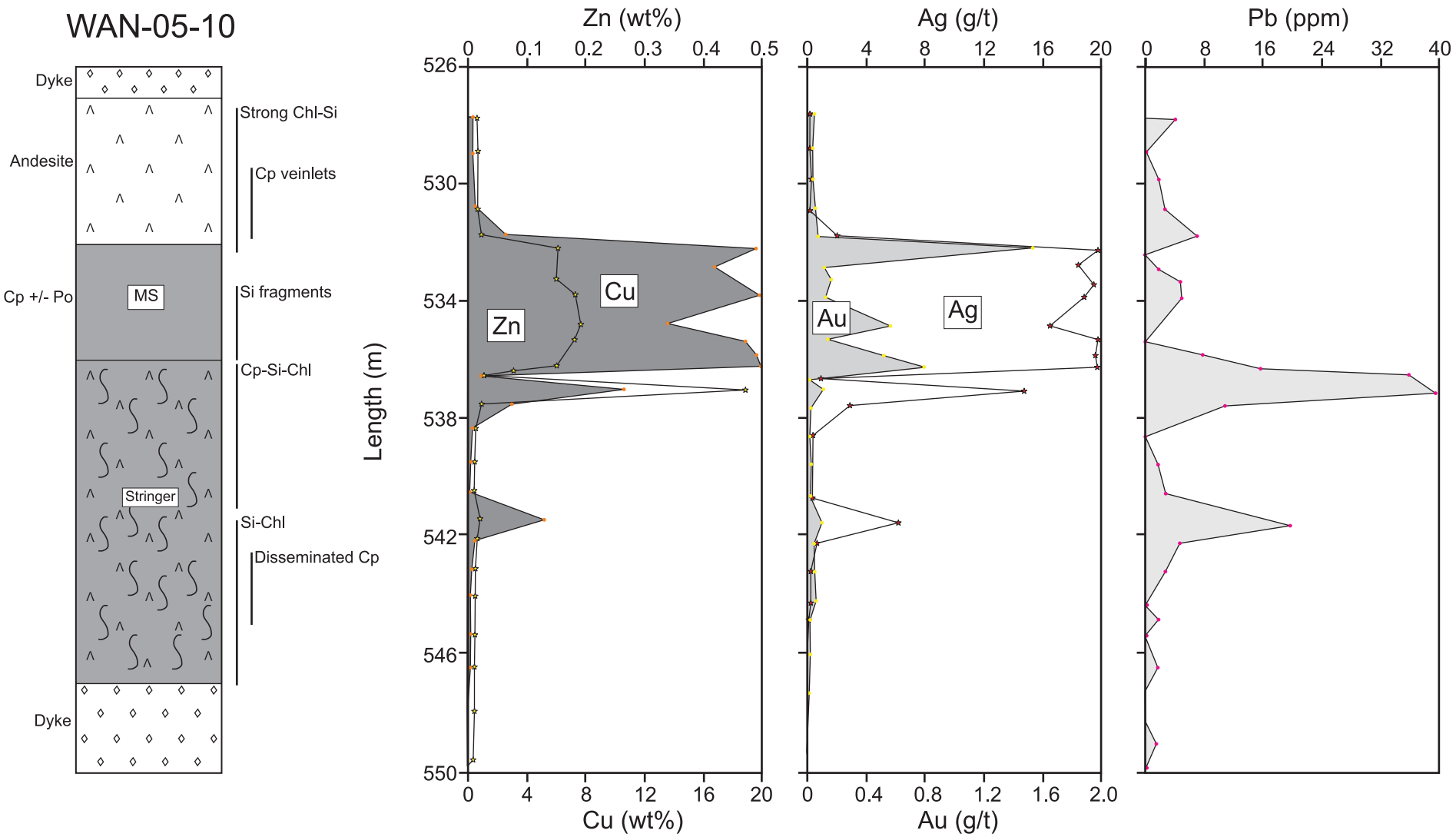

Appendix XI. Drill-hole lithological profile and Cu-Zn-Au-Ag-Pb concentrations for hole WAN-05-10 from the Lower lens. Data from Xstrata Copper Canada, Ltd. Si, silica; Chl, chlorite; Po, pyrrhotite; Cp, chalcopyrite.

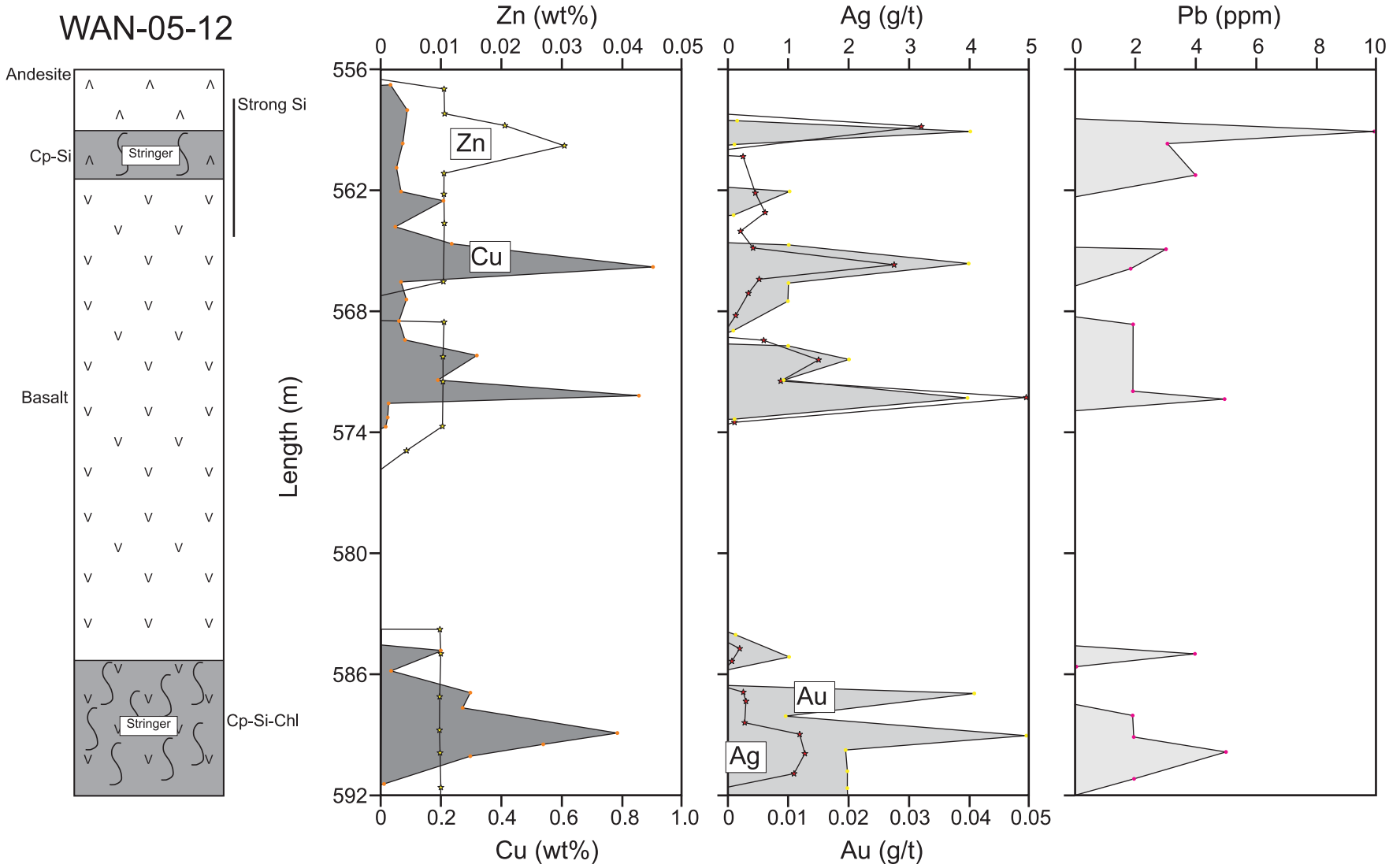

Appendix XII. Drill-hole lithological profile and Cu-Zn-Au-Ag-Pb concentrations for hole WAN-05-12 from the Lower stockwork zone. Data from Xstrata Copper Canada, Ltd. Si, silica; Chl, chlorite; Cp, chalcopyrite.

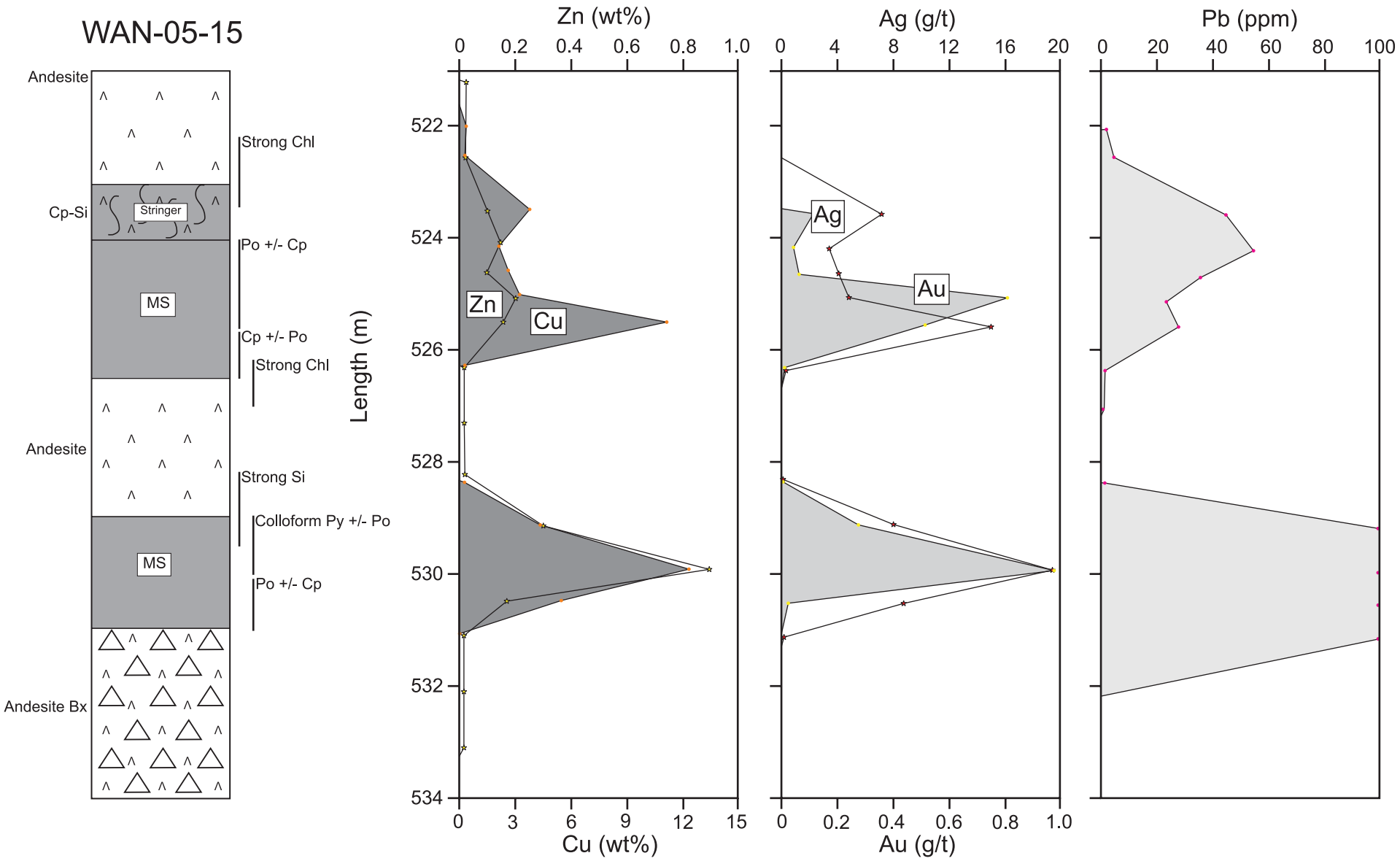

Appendix XIII. Drill-hole lithological profile and Cu-Zn-Au-Ag-Pb concentrations for hole WAN-05-15 from the Lower lens. Data from Xstrata Copper Canada, Ltd. Si, silica; Chl, chlorite; Po, pyrrhotite; Cp, chalcopyrite; Py, pyrite.

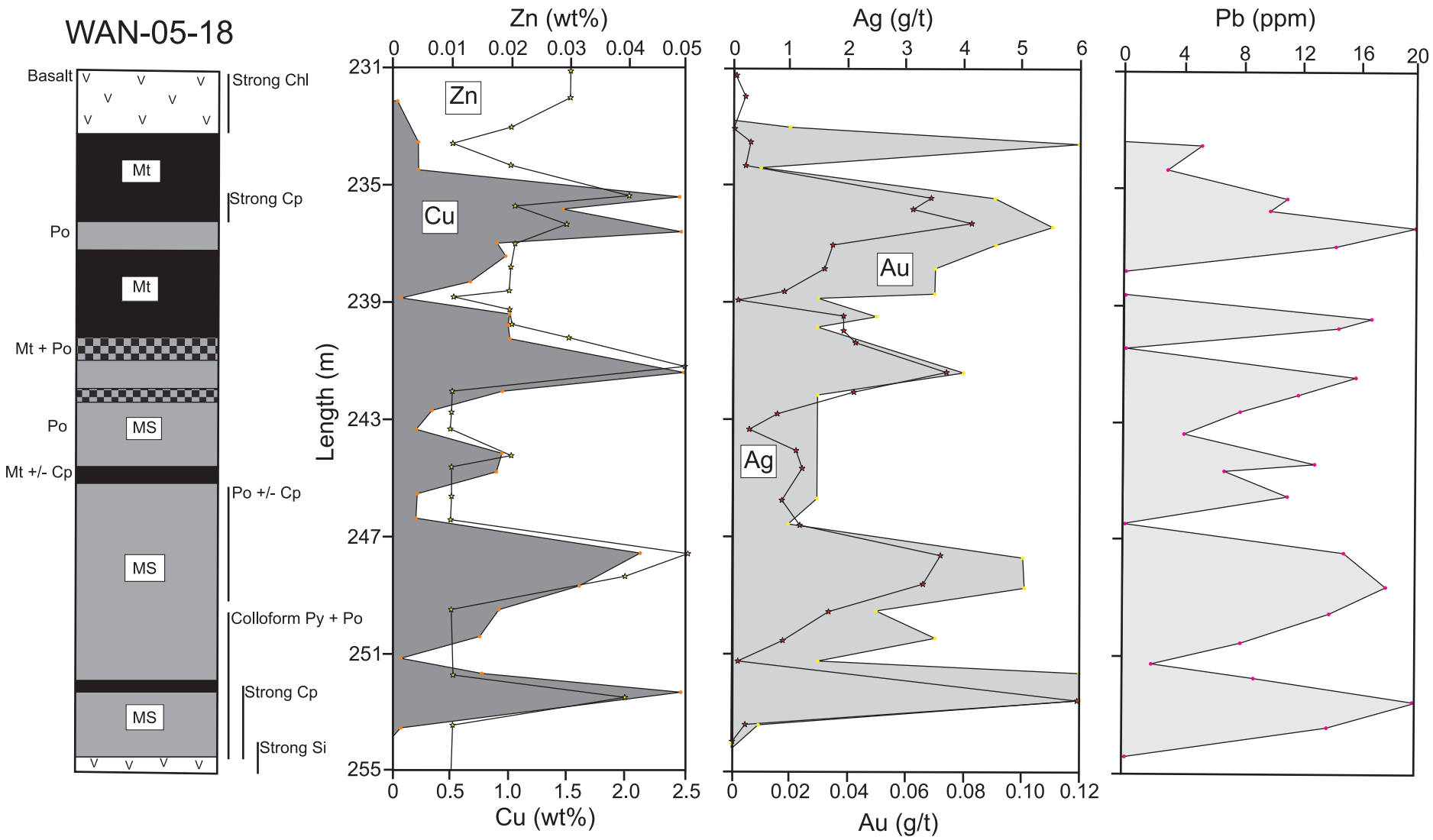

Appendix XIV. Drill-hole lithological profile and Cu-Zn-Au-Ag-Pb concentrations for hole WAN-05-18 from the Upper lens. Data from Xstrata Copper Canada, Ltd. Si, silica; Chl, chlorite; Po, pyrrhotite; Cp, chalcopyrite; Mt, magnetite; Py, pyrite.

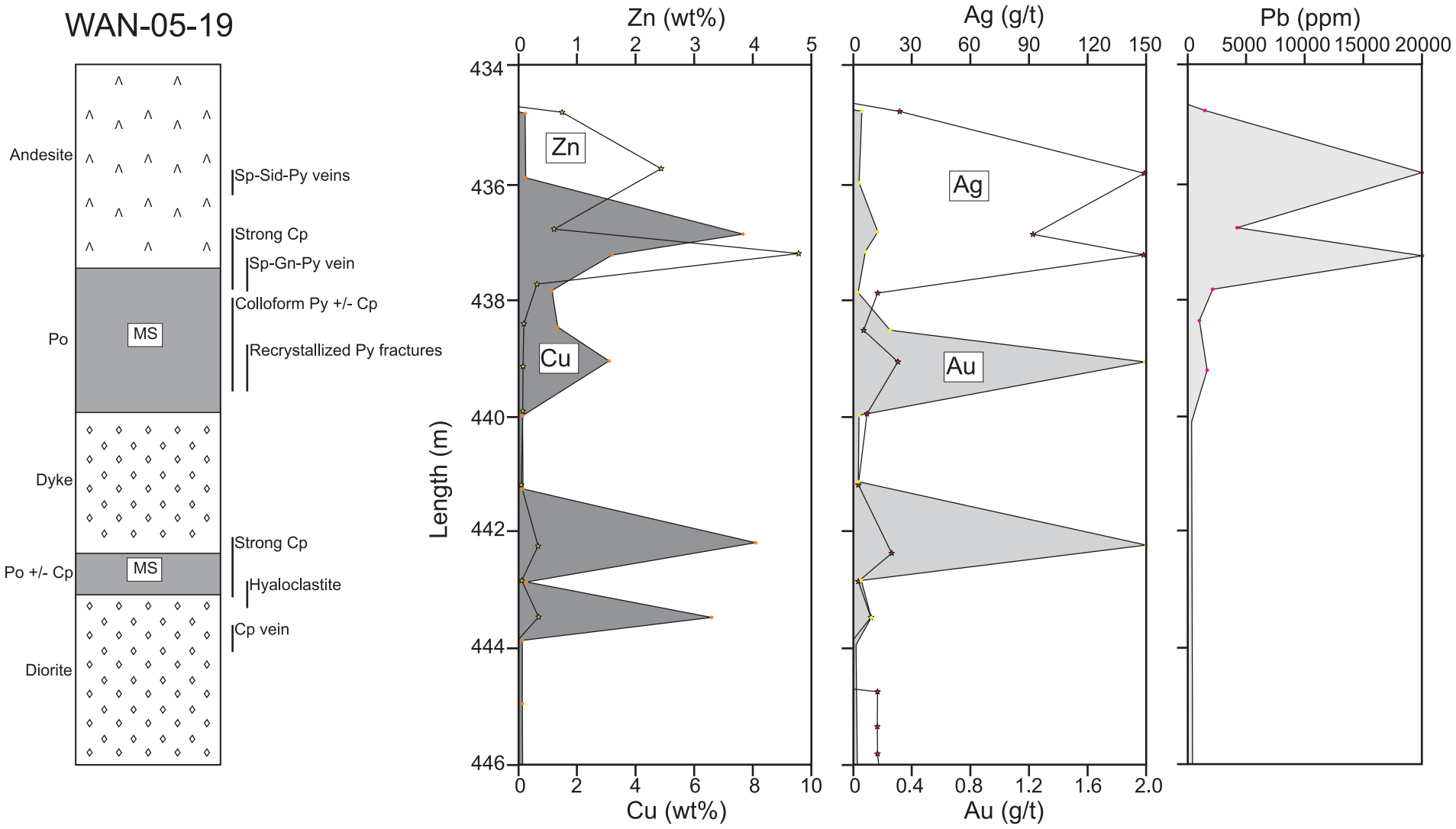

Appendix XV. Drill-hole lithological profile and Cu-Zn-Au-Ag-Pb concentrations for hole WAN-05-19 from the Middle lens. Data from Xstrata Copper Canada, Ltd. Si, silica; Chl, chlorite; Sid, siderite; Po, pyrrhotite; Cp, chalcopyrite; Sp, sphalerite; Py, pyrite; Gn, galena.

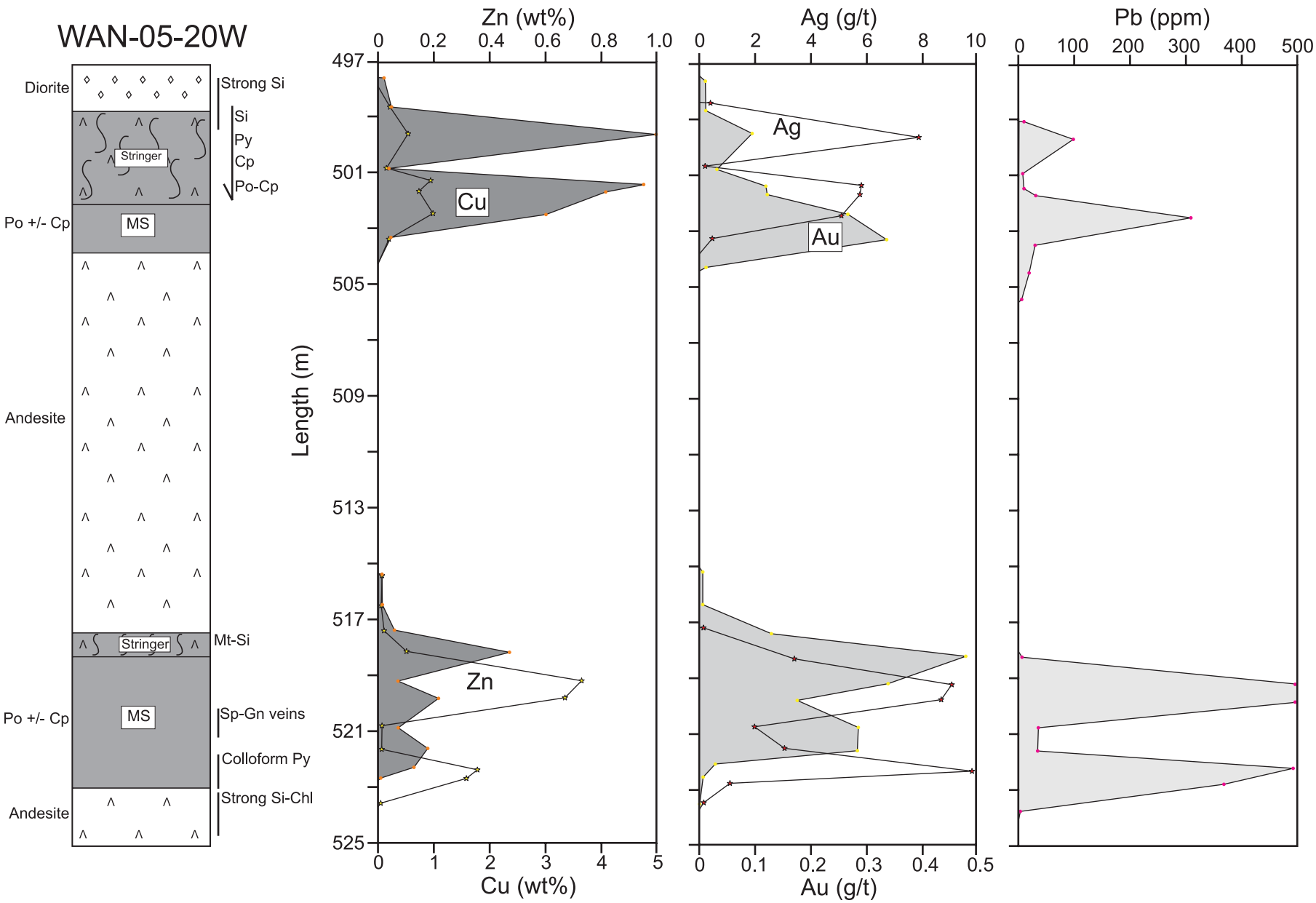

Appendix XVI. Drill-hole lithological profile and Cu-Zn-Au-Ag-Pb concentrations for hole WAN-05-20W from the Lower lens. Data from Xstrata Copper Canada, Ltd. Si, silica; Chl, chlorite; Po, pyrrhotite; Cp, chalcopyrite; Mt, magnetite; Sp, sphalerite; Py, pyrite; Gn, galena.

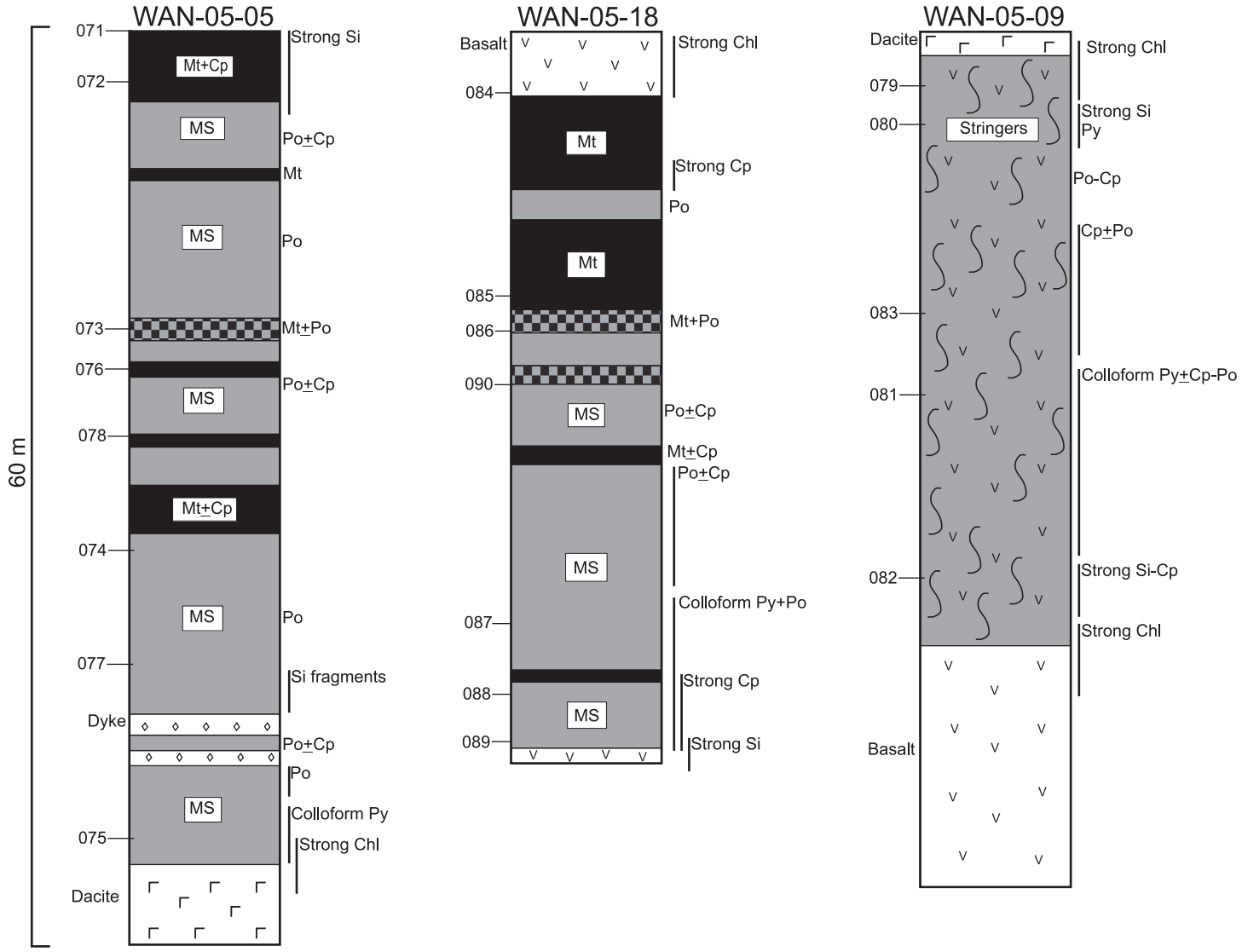

Appendix XVII. Lithological sections from drill holes of the Upper lens and stockwork zone with sample locations and massive sulphide intersections.

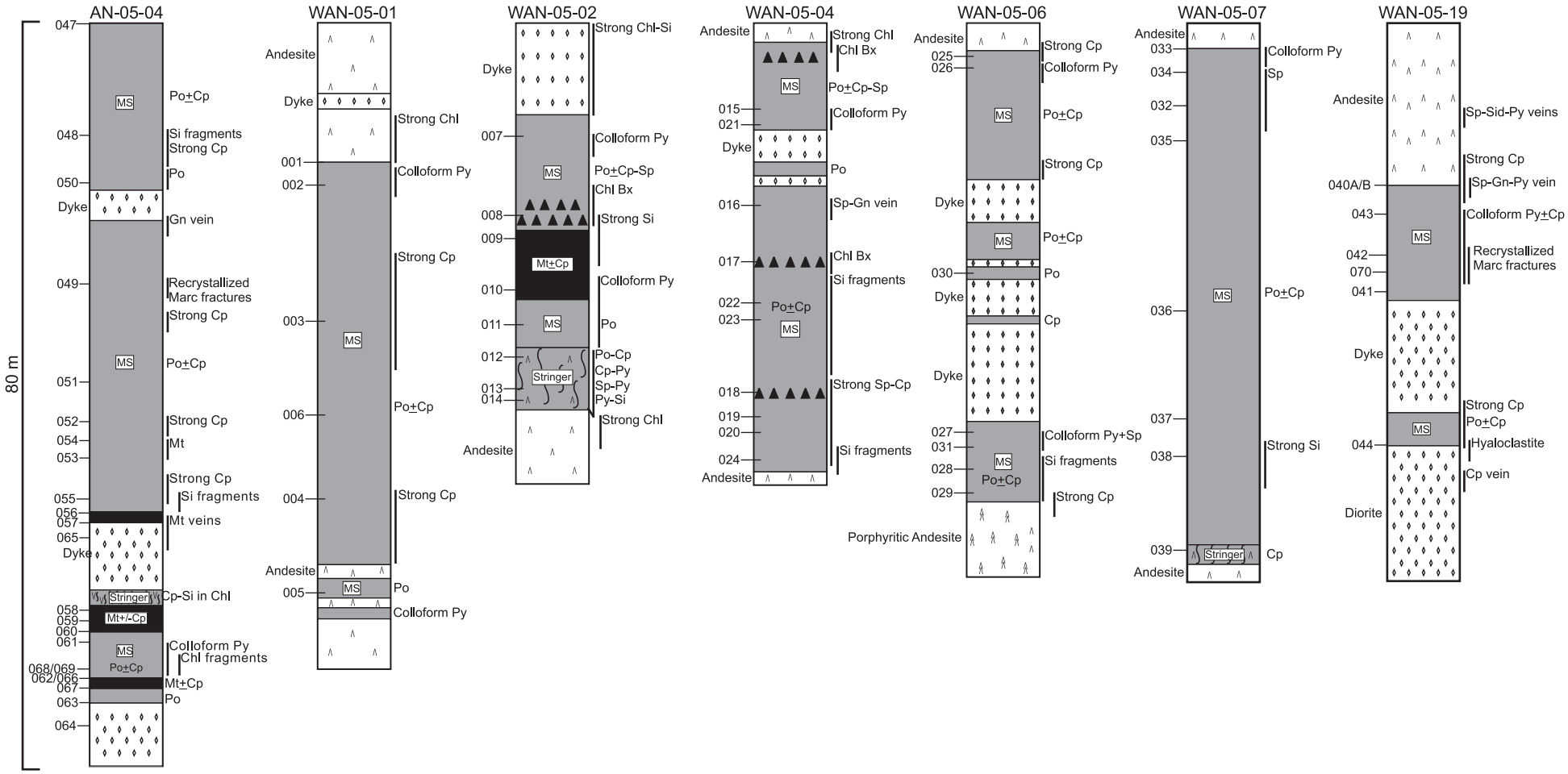

Appendix XVIII. Lithological sections from drill holes of the Middle lens with sample locations and massive sulphide intersections.

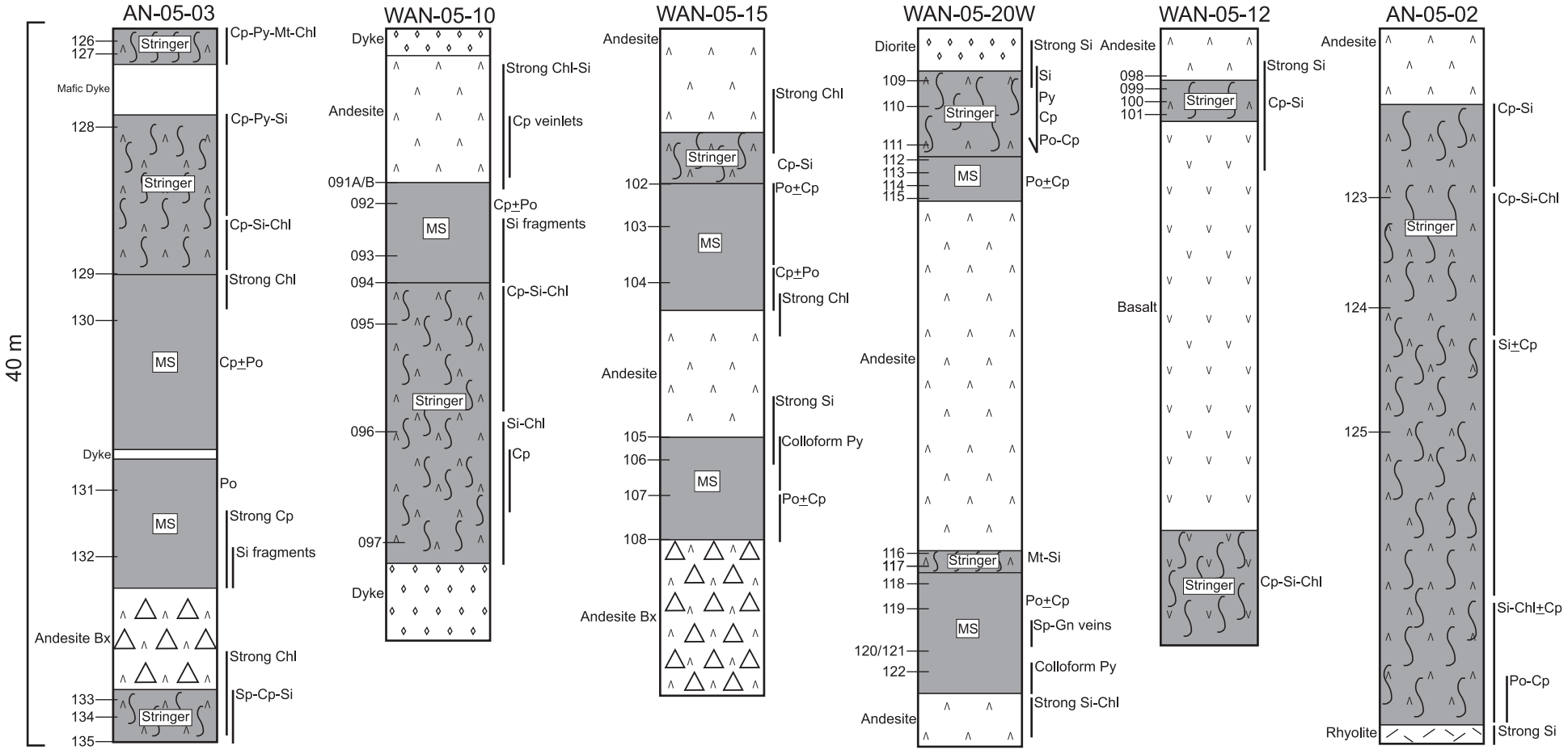

Appendix XIX. Lithological sections from drill holes of the Lower lens and stockwork zone with sample locations and massive sulphide intersections.

Appendix XX. Chemical Compositions of Representative Ore Samples from the West Ansil Deposit

Ore Type	Sample	Lens	Fe (wt%)	Cu (wt%)	Zn (wt%)	S (wt%)	Pb ppm	Sn ppm	Cd ppm	Ag ppm	Hg ppb	Ni ppm	Tl ppm	As ppm	Sb ppm	Au ppb	In ppm	Co ppm	Se ppm	Bi ppm
Massive Sphalerite	WAN015	Middle	32.7	8.9	20.0	34.4	7.6	232.0	399	49	37	5.0	0.1	47.9	1.1	1440	10.2	440	23	7.0
	WAN020		46.9	11.2	5.7	38.1	13.6	62.0	124	34	8.0	5.0	0.1	0.3	0.1	258	20.3	741	200	5.0
	WAN021		31.8	1.2	20.0	34.0	6.0	354.0	574	2.5	29	5.0	0.1	12.1	1.4	396	12.1	572	0.4	10
	WAN032		31.4	0.6	9.3	24.7	1.2	1.4	271	2.5	2.5	5.0	0.1	0.3	0.1	595	39.5	544	36	6.0
Sphalerite Stringers	WAN013	Middle	17.4	0.2	12.1	13.2	12.9	3.4	179	2.5	411	30	0.1	14.8	2.5	173	0.3	105	18	9.0
	WAN018		31.9	0.1	18.7	23.7	3.7	0.9	407	2.5	209	5.0	0.1	0.3	0.1	163	29.7	826	3	10
	WAN133	Lower	18.3	1.1	11.9	7.2	10.5	0.3	725	2.5	260	5.0	0.1	0.3	0.1	314	1.9	358	121	6.0
Massive Pyrrhotite	WAN077	Upper	58.2	0.7	0.0	38.8	1.5	0.3	1.0	2.5	2.5	5.0	0.1	0.3	0.1	43	0.2	718	143	1.0
	WAN090		57.5	0.9	0.0	36.4	2.3	0.3	1.0	2.5	2.5	5.0	0.1	0.3	0.1	41	0.4	814	107	1.0
	WAN074		51.8	1.3	0.0	32.2	1.6	0.3	1.0	2.5	2.5	5.0	0.1	0.3	0.1	36	0.1	714	67	1.0
	WAN075		33.2	16.8	0.1	27.4	55.8	0.3	4.0	27	20	5.0	1.9	8.0	1.0	121	1.1	355	138	3.0
	WAN001	Middle	52.9	5.0	0.1	35.9	7.7	0.7	3.0	2.5	6.0	5.0	0.1	0.3	0.1	69	1.1	1240	215	10
	WAN002		57.2	0.5	0.0	39.6	49.3	0.7	1.0	2.5	2.5	5.0	0.3	0.3	0.1	1.0	0.8	1300	172	28
	WAN006		56.5	1.9	0.0	38.3	2.0	1.7	1.0	2.5	2.5	5.0	0.1	0.3	0.1	13600	3.7	1080	176	125
	WAN022		49.5	2.1	0.1	33.7	12.9	0.9	3.0	2.5	2.5	5.0	0.1	0.3	0.1	54	1.8	721	159	4.0
	WAN030		58.3	1.4	0.0	39.9	1.9	1.3	1.0	2.5	2.5	30	0.1	0.3	0.1	30	4.8	1180	144	10
	WAN035		44.1	0.6	2.0	30.0	2.1	2.0	56	2.5	15	5.0	0.1	0.3	0.1	166	6.4	749	54	4.0
	WAN050		58.0	0.9	0.0	38.8	4.6	1.1	1.0	2.5	2.5	5.0	0.1	0.3	0.1	24	2.6	1390	298	7.0
	WAN017		51.6	2.1	0.1	32.7	8.9	2.2	3.0	2.5	2.5	5.0	0.1	0.3	0.3	588	5.4	647	81	20
	WAN048		38.2	2.6	0.0	25.9	64.8	1.7	1.0	2.5	2.5	5.0	0.1	0.3	0.1	692	0.3	546	159	13
	WAN102	Lower	38.9	3.1	0.2	21.8	115	6.0	7.0	2.5	2.5	5.0	0.1	0.3	0.1	238	2.9	905	133	14
	WAN103		57.5	2.2	0.1	36.4	19.8	20.0	3.0	2.5	2.5	10	0.1	8.7	0.1	847	6.1	1710	212	8.0
	WAN118		35.1	2.2	0.0	23.7	23	0.3	1.0	2.5	2.5	5.0	0.1	0.3	0.1	44	0.5	623	201	23
	WAN119		52.0	1.4	0.1	32.7	16.2	0.3	1.0	2.5	2.5	10	0.2	0.3	0.1	148	0.5	1000	182	11
	WAN121		52.3	2.0	3.4	37.3	11000	0.3	204	30	2.5	20	0.1	0.3	0.1	2040	1.8	1040	144	24
	WAN132		45.4	3.9	0.0	30.4	11.5	0.3	1.0	2.5	9.0	5.0	0.1	0.3	0.1	41	2.4	827	342	16
Massive Chalcopyrite	WAN004	Middle	43.6	18.9	0.3	36.4	48.6	29.3	9.0	18	2.5	5.0	0.1	104	0.9	359	76.3	571	1230	3070
	WAN009		11.9	7.1	0.1	9.3	5.8	3.6	1.0	2.5	10	5.0	0.1	16.8	0.1	638	6.4	179	84	18
	WAN036		29.1	8.9	0.2	22.4	14.1	17.4	7.0	21	2.5	50	0.1	36.3	0.6	152	26.2	404	254	6.0
	WAN052		39.8	22.9	0.5	35.3	68.1	41.0	19	34	15	5.0	0.1	14.5	0.1	24100	66.4	588	1460	84
	WAN061		48.5	11.1	0.1	37.0	8.9	3.4	2.0	2.5	15	5.0	0.1	0.3	0.1	3580	8.0	1020	442	41
	WAN092	Lower	41.3	15.1	0.2	32.2	9.4	22.4	5.0	2.5	17	10	0.1	0.3	0.1	635	48.9	2270	892	14
	WAN093		39.0	18.4	0.2	31.2	6.1	7.0	5.0	2.5	15	20	0.2	0.3	0.1	195	14.2	1850	448	8.0
	WAN130		54.5	3.0	0.1	36.7	13.9	1.6	1.0	2.5	13	5.0	0.1	205	0.1	419	5.5	1180	316	24
Chalcopyrite Stringers	WAN079	Upper	34.9	11.3	0.1	25.2	66.8	0.3	7.0	16	11	5.0	0.1	3.1	0.7	70	4.0	623	218	6.0
	WAN083		25.5	3.5	0.0	3.6	11.1	1.8	1.0	2.5	5.0	20	0.1	0.3	0.4	1.0	2.3	124	60	1.0
	WAN081		41.7	10.4	0.1	28.1	12.5	1.1	5.0	19	9.0	150	0.2	0.3	0.1	73	4.0	1180	288	11
	WAN080		21.4	20.0	0.1	23.7	106	1.7	12.0	45	30	130	0.9	8.3	0.3	99	11.7	432	442	35
	WAN095	Lower	21.1	10.9	0.8	10.7	94.9	1.1	65	19	6.0	5.0	0.3	2.8	0.5	108	13.0	239	323	13
	WAN099		22.1	13.6	0.0	14.3	4.7	5.6	1.0	2.5	2.5	20	0.1	8.6	0.1	1.0	24.3	341	537	1.0
	WAN101		26.2	26.1	0.0	26.7	2.0	18.5	1.0	10	5.0	5.0	0.1	45.6	0.6	24	47.4	158	637	1.0
	WAN125		17.7	15.7	0.0	16.4	9.3	1.3	1.0	17	2.5	20	0.1	4.1	0.1	147	3.0	42	353	6.0
	WAN111		38.8	4.8	0.0	20.0	19.1	0.3	1.0	2.5	2.5	5.0	0.1	0.3	0.1	33	0.1	847	68	1.0

Appendix XX. Chemical Compositions of Representative Ore Samples from the West Ansil Deposit

Ore Type	Sample	Lens	Fe (wt%)	Cu (wt%)	Zn (wt%)	S (wt%)	Pb ppm	Sn ppm	Cd ppm	Ag ppm	Hg ppb	Ni ppm	Tl ppm	As ppm	Sb ppm	Au ppb	In ppm	Co ppm	Se ppm	Bi ppm
Massive Magnetite	WAN071	Upper	44.3	0.1	0.0	0.1	0.4	0.5	1.0	2.5	2.5	10	0.1	0.3	0.1	1.0	0.5	44	0	1.0
	WAN072		45.5	1.6	0.0	42.8	90.8	3.5	1.0	2.5	18	5.0	0.8	0.3	0.7	61	2.9	1900	226	10
	WAN073		51.8	2.1	0.0	13.3	1.7	2.1	1.0	2.5	2.5	5.0	0.1	0.3	0.4	41	0.6	310	64	12
	WAN076		66.0	0.5	0.0	0.8	0.4	1.5	1.0	2.5	2.5	5.0	0.1	0.3	0.1	40	0.2	27	3	1.0
	WAN078		57.6	4.0	0.0	18.6	3.0	1.8	1.0	2.5	2.5	5.0	0.1	0.3	0.1	2690	4.0	313	135	21
	WAN084		37.6	0.0	0.0	0.1	0.4	0.5	1.0	2.5	2.5	50	0.1	0.3	0.1	1.0	0.1	81	0.4	1.0
	WAN085		61.5	0.4	0.0	10.2	1.1	3.3	1.0	2.5	2.5	5.0	0.1	0.3	0.1	55	0.7	243	47	1.0
	WAN086		57.8	0.1	0.0	18.2	3.0	1.0	1.0	2.5	2.5	5.0	0.1	0.3	0.1	10	0.1	432	71	3.0
	WAN054	Middle	54.7	2.5	0.1	34.8	8.3	6.3	4.0	2.5	2.5	5.0	0.1	11.2	0.4	1660	10.9	1430	477	4.0
	WAN056		33.5	6.0	0.1	7.2	8.0	10.1	1.0	2.5	7.0	5.0	0.1	10.8	0.1	216	14.4	141	188	25
	WAN058		42.3	16.3	0.1	16.5	15.5	21.3	3.0	21	12	5.0	0.1	7.5	0.1	902	7.3	223	269	19
	WAN060		65.6	0.2	0.0	0.3	1.5	1.5	1.0	2.5	2.5	5.0	0.1	0.3	0.5	36	0.2	16	4	1.0
	WAN062		48.8	13.4	0.1	21.9	5.7	4.3	3.0	25	27	5.0	0.1	0.3	0.1	27600	16.0	346	319	89
	WAN066		45.9	0.4	0.0	8.4	3.1	0.3	1.0	2.5	2.5	20	0.1	0.3	0.1	21	0.5	299	63	3.0
Colloform Pyrite-Marcasite	WAN087	Upper	49.5	1.0	0.0	37.8	20.5	0.3	1.0	2.5	2.5	5.0	0.6	0.3	0.1	36	0.5	848	236	3.0
	WAN088		42.1	2.6	0.0	41.6	147	1.7	3.0	22	18	5.0	8.8	0.3	0.1	45	1.4	1010	304	6.0
	WAN089		35.7	12.7	0.1	29.7	24	4.8	6.0	2.5	9.0	5.0	0.6	0.3	0.1	210	15.3	361	287	5.0
	WAN007	Middle	48.1	8.7	0.6	40.1	95	2.0	17	2.5	42	5.0	0.5	0.3	0.1	118	3.3	1600	441	14
	WAN010		45.4	4.4	0.0	25.8	80.8	6.0	1.0	2.5	33	5.0	0.9	0.3	0.7	2030	18.3	1310	379	44
	WAN016		48.1	1.7	0.6	39.1	1700	3.6	29	2.5	2.5	40	1.8	0.3	0.9	247	7.4	441	102	6.0
	WAN026		46.6	1.8	0.0	31.9	5.3	2.2	1.0	2.5	2.5	5.0	0.1	3.4	0.1	44	2.6	789	149	23
	WAN029		35.2	12.6	0.1	25.9	231	2.4	10	15	7.0	5.0	0.3	0.3	0.4	111	6.8	437	203	21
	WAN033		41.2	0.4	0.4	26.9	21.4	1.0	9.0	2.5	2.5	5.0	0.1	0.3	0.1	42	2.0	618	106	18
	WAN041		43.5	0.2	0.0	46.0	1250	1.3	1.0	49	45	5.0	9.3	0.3	0.6	64	3.0	2450	544	17
	WAN043		53.8	5.6	0.2	37.9	146	16.7	6.0	2.5	38	5.0	0.1	0.3	0.5	35	68.7	1310	956	589
	WAN069		34.7	0.8	0.0	25.0	10.2	1.2	1.0	2.5	2.5	170	0.1	4.3	0.1	52	1.0	1780	126	2.0
	WAN070		43.3	0.0	0.0	0.1	0.4	0.6	1.0	2.5	6.0	5.0	0.1	0.3	0.1	1.0	0.1	18	2	1.0
	WAN122	Lower	40.9	0.9	0.0	39.5	766	0.3	1.0	2.5	2.5	20	9.8	0.3	0.9	1.0	0.9	1220	244	12

Samples were analyzed by a combination of ICP-MS and INAA at Activation Laboratories, Ancaster, Ontario; Hg analyzed by FIMS, CO2 by infrared absorption.

Appendix XX. Chemical Compositions of Representative Ore Samples from the West Ansil Deposit

Ore Type	Sample	Lens	Mo	Te	W	V	U	Ga	Ge	SiO_2	Al_2O_3	Na_2O	K_2O	MgO	CaO	P_2O_5	TiO_2	CO_2	Mn	B
			ppm	ppm	ppm	ppm	ppm	ppm	ppm	(wt%)	(wt%)	(wt%)	(wt%)	(wt%)	(wt%)	(wt%)	(wt%)	(wt%)	ppm	ppm
Massive Sphalerite	WAN015	Middle	0.5	3.0	1.2	2.5	0.1	76.6	24.2	3.14	0.04	0.01	0.06	1.18	0.056	0.07	0.01	0.08	336	5.0
	WAN020		0.5	3.0	0.4	2.5	0.1	23.1	1.2	0.43	0.08	0.01	0.06	0.03	0.056	0.08	0.01	0.01	61	5.0
	WAN021		0.5	3.0	0.4	2.5	0.1	74.4	18.5	4.92	0.04	0.01	0.06	1.76	0.070	0.03	0.01	0.03	318	5.0
	WAN032		0.5	3.0	2.6	2.5	0.1	36.1	2.5	32.95	0.06	0.01	0.06	0.01	0.007	0.01	0.01	0.03	59	5.0
Sphalerite Stringers	WAN013	Middle	23	3.0	20.1	37	0.1	7.9	1.0	22.03	4.02	0.01	0.06	6.70	5.288	0.11	0.30	13.20	3790	5.0
	WAN018		0.5	3.0	2.7	72	0.1	42.0	5.9	9.18	6.48	0.01	0.06	4.05	0.168	0.11	0.50	0.01	839	5.0
	WAN133	Lower	2.0	3.0	1.1	184	0.1	33.5	1.2	30.16	10.18	0.01	0.06	5.39	0.588	0.11	0.67	0.04	1500	5.0
Massive Pyrrhotite	WAN077	Upper	0.5	3.0	0.4	2.5	0.1	0.1	0.4	3.44	0.01	0.01	0.06	0.08	0.007	0.03	0.01	0.01	50	5.0
	WAN090		1.0	3.0	0.4	2.5	0.1	0.5	0.4	3.02	0.08	0.01	0.06	0.46	0.210	0.04	0.01	0.01	448	5.0
	WAN074		5.0	3.0	0.4	2.5	0.1	1.2	1.6	11.25	0.21	0.04	0.06	1.74	1.231	0.05	0.01	0.01	1210	5.0
	WAN075		35	3.0	0.4	14	0.1	3.4	0.4	14.68	1.19	0.18	0.24	1.49	0.098	0.29	0.05	0.01	909	30
	WAN001	Middle	7.0	3.0	0.4	2.5	0.1	1.5	0.4	3.36	0.28	0.01	0.06	0.43	0.014	0.05	0.01	0.01	44	5.0
	WAN002		0.5	3.0	8.2	2.5	0.1	0.2	0.4	0.86	0.01	0.01	0.06	0.12	0.056	0.01	0.01	0.01	71	5.0
	WAN006		24	3.0	0.4	2.5	0.1	1.3	0.4	1.20	0.04	0.03	0.06	0.27	0.336	0.03	0.01	0.07	120	5.0
	WAN022		0.5	3.0	0.4	2.5	0.1	0.6	0.4	12.71	0.04	0.01	0.06	0.27	0.098	0.02	0.01	0.04	50	5.0
	WAN030		1.0	3.0	0.4	2.5	0.1	0.1	0.4	0.32	0.01	0.01	0.06	0.02	0.014	0.02	0.01	0.01	11	5.0
	WAN035		0.5	3.0	1.3	2.5	0.1	11.9	3.0	21.61	0.01	0.01	0.06	0.01	0.007	0.00	0.01	0.01	23	5.0
	WAN050		0.5	3.0	0.4	2.5	0.1	0.4	0.4	0.15	0.01	0.01	0.06	0.02	0.028	0.02	0.01	0.11	14	5.0
	WAN017		3.0	3.0	1.0	29	0.1	39.5	0.7	3.94	2.97	0.01	0.06	1.31	0.028	0.03	0.28	0.02	578	5.0
	WAN048		0.5	3.0	1.3	2.5	0.1	0.9	0.4	31.23	0.04	0.01	0.06	0.02	0.007	0.03	0.01	0.01	24	5.0
	WAN102	Lower	6.0	3.0	4.8	117	0.1	34.6	0.9	18.98	5.55	0.01	0.06	4.00	0.238	0.05	0.57	0.01	576	5.0
	WAN103		0.5	3.0	0.8	2.5	0.1	3.8	0.4	1.24	0.17	0.01	0.06	0.13	0.007	0.04	0.01	0.03	129	5.0
	WAN118		0.5	3.0	4.0	2.5	0.1	0.5	1.1	39.79	0.08	0.01	0.06	0.20	0.007	0.03	0.01	0.01	26	5.0
	WAN119		0.5	3.0	1.0	2.5	0.1	1.6	0.4	11.70	0.30	0.01	0.06	0.50	0.007	0.03	0.03	0.01	57	5.0
	WAN121		0.5	3.0	0.4	2.5	0.1	1.1	1.8	3.57	0.02	0.01	0.06	0.15	0.070	0.02	0.01	0.55	64	5.0
	WAN132		0.5	3.0	0.4	2.5	0.1	0.5	0.4	17.69	0.09	0.01	0.06	0.13	0.126	0.04	0.01	0.01	58	5.0
Massive Chalcopyrite	WAN004	Middle	1.0	8.0	0.4	2.5	0.1	5.3	0.4	1.58	0.01	0.01	0.06	0.22	0.028	0.14	0.01	0.02	112	5.0
	WAN009		1.0	3.0	0.4	2.5	0.1	1.7	0.9	68.46	0.06	0.01	0.06	0.12	0.042	0.05	0.01	0.17	165	5.0
	WAN036		2.0	3.0	10.9	2.5	0.1	5.3	0.4	37.22	0.08	0.01	0.06	0.01	0.007	0.07	0.01	0.01	41	5.0
	WAN052		0.5	3.0	0.4	2.5	0.1	6.4	0.4	0.86	0.01	0.01	0.06	0.03	0.007	0.18	0.01	0.01	92	5.0
	WAN061		5.0	3.0	0.4	2.5	0.1	1.5	0.4	1.18	0.13	0.01	0.06	0.27	0.007	0.09	0.01	0.01	72	5.0
	WAN092	Lower	1.0	3.0	2.4	2.5	0.1	4.2	0.4	10.59	0.09	0.01	0.06	0.15	0.007	0.13	0.01	0.01	64	5.0
	WAN093		0.5	3.0	0.4	7.0	0.1	8.7	0.4	6.59	0.60	0.01	0.06	0.36	0.056	0.12	0.07	0.10	158	5.0
	WAN130		0.5	3.0	0.4	2.5	0.1	0.6	0.4	0.43	0.02	0.01	0.06	0.12	0.007	0.03	0.01	0.05	10	5.0
Chalcopyrite Stringers	WAN079	Upper	2.0	7.0	0.9	59	0.1	17.7	0.8	19.04	3.19	0.03	0.06	2.01	0.070	0.11	0.32	0.01	407	10
	WAN083		0.5	3.0	1.2	287	0.2	79.2	1.6	27.17	14.04	0.01	0.06	8.34	0.700	0.05	1.45	0.01	1780	5.0
	WAN081		8.0	3.0	0.4	70	0.1	23.3	0.4	7.62	4.80	0.01	0.06	2.64	0.070	0.12	0.18	0.01	562	5.0
	WAN080		0.5	23	1.7	6.0	0.1	1.4	0.4	35.30	0.26	0.01	0.06	0.15	0.007	0.18	0.01	0.01	49	5.0
	WAN095	Lower	0.5	6.0	5.2	76	0.1	49.9	1.6	36.58	6.38	0.05	0.24	4.56	0.336	0.12	0.50	0.08	728	5.0
	WAN099		2.0	3.0	8.5	92	0.1	26.8	0.7	31.02	6.71	0.01	0.06	4.01	0.112	0.13	0.43	0.01	912	5.0
	WAN101		3.0	3.0	18	9.0	0.1	17.5	0.4	16.62	1.40	0.01	0.06	0.81	0.056	0.22	0.01	0.13	206	5.0
	WAN125		0.5	17	1.5	49	0.1	12.5	0.4	29.95	2.93	0.16	0.06	3.76	5.260	0.13	0.20	5.86	895	5.0
	WAN111		0.5	3.0	0.4	91	0.1	17.3	0.4	15.08	8.20	0.01	0.06	4.21	0.378	0.23	0.77	0.01	1030	5.0

Appendix XX. Chemical Compositions of Representative Ore Samples from the West Ansil Deposit

Ore Type	Sample	Lens	Mo ppm	Te ppm	W ppm	V ppm	U ppm	Ga ppm	Ge ppm	SiO_2 (wt%)	Al_2O_3 (wt%)	Na_2O (wt%)	K_2O (wt%)	MgO (wt%)	CaO (wt%)	P_2O_5 (wt%)	TiO_2 (wt%)	CO_2 (wt%)	Mn ppm	B ppm
Massive Magnetite	WAN071	Upper	12	3.0	3.6	179	0.1	68.4	2.7	17.86	7.88	0.08	0.24	4.66	0.007	0.05	1.05	0.02	1660	5.0
	WAN072		0.5	3.0	0.4	2.5	0.1	3.0	0.4	1.73	0.08	0.01	0.06	0.27	0.867	0.03	0.01	0.61	106	60
	WAN073		13	3.0	64.1	2.5	0.3	12.1	3.6	13.18	0.21	0.04	0.06	1.96	0.574	0.04	0.01	0.01	1660	5.0
	WAN076		1.0	3.0	5.1	2.5	0.1	13.0	3.4	7.70	0.06	0.03	0.06	0.50	0.007	0.03	0.01	0.01	781	5.0
	WAN078		27	3.0	2.6	2.5	0.7	5.6	1.8	6.91	0.06	0.01	0.06	0.80	0.007	0.04	0.01	0.01	802	5.0
	WAN084		5.0	3.0	2.1	258	0.5	54.5	2.5	22.68	11.52	0.07	0.12	6.53	0.007	0.05	1.43	0.01	2920	5.0
	WAN085		3.0	3.0	8.3	2.5	0.1	16.0	3.2	8.09	0.09	0.01	0.06	1.13	0.434	0.02	0.01	0.01	1280	5.0
	WAN086		80	3.0	3.3	2.5	0.1	12.9	8.0	9.84	0.06	0.01	0.06	1.36	0.168	0.03	0.01	0.02	938	5.0
	WAN054	Middle	0.5	3.0	0.4	2.5	0.1	6.2	1.3	2.78	0.08	0.01	0.06	0.60	0.364	0.03	0.01	0.01	204	5.0
	WAN056		8.0	8.0	2.3	2.5	0.1	19.1	4.5	37.22	1.42	0.09	0.06	0.90	0.238	0.28	0.02	0.03	444	5.0
	WAN058		0.5	3.0	1.6	2.5	0.1	18.5	3.6	6.16	0.66	0.09	0.06	1.31	1.567	0.13	0.05	2.50	569	5.0
	WAN060		22	3.0	0.4	2.5	0.1	43.1	8.5	4.60	0.25	0.05	0.06	0.30	0.007	0.00	0.01	0.16	245	5.0
	WAN062		654	3.0	0.4	2.5	0.1	18.6	3.4	3.21	0.17	0.03	0.06	0.23	0.007	0.13	0.01	0.02	158	5.0
	WAN066		2.0	3.0	0.4	44	0.1	28.0	5.8	21.37	2.59	0.22	0.36	2.64	1.091	0.02	0.17	0.01	1490	5.0
Colloform Pyrite-Marcasite	WAN087	Upper	108	3.0	1.5	2.5	0.1	0.9	1.1	7.98	0.09	0.01	0.06	2.34	0.168	0.02	0.01	0.22	359	10
	WAN088		178	3.0	2.4	13	0.1	1.1	0.8	4.88	0.08	0.01	0.06	0.71	0.126	0.04	0.01	0.02	118	5.0
	WAN089		138	3.0	3.2	7.0	0.1	1.7	0.4	19.53	0.47	0.04	0.06	0.46	0.098	0.12	0.01	0.03	240	5.0
	WAN007	Middle	1.0	3.0	0.4	2.5	0.1	0.7	0.4	1.01	0.13	0.01	0.06	0.20	0.056	0.07	0.01	0.06	28	5.0
	WAN010		2.0	3.0	0.4	2.5	0.1	5.5	2.7	11.68	0.06	0.03	0.06	0.30	2.210	0.04	0.01	1.60	209	5.0
	WAN016		2.0	3.0	1.2	2.5	0.1	2.3	1.2	1.54	0.30	0.01	0.06	0.41	0.406	0.02	0.01	2.53	459	10
	WAN026		1.0	3.0	0.8	2.5	0.1	1.4	0.4	17.33	0.08	0.01	0.06	0.22	0.056	0.03	0.01	0.01	42	5.0
	WAN029		0.5	10	1.4	26	0.1	18.2	0.4	20.79	2.00	0.03	0.06	1.08	0.056	0.10	0.22	0.02	282	5.0
	WAN033		4.0	3.0	1.9	41	0.1	51.5	1.0	20.75	1.91	0.04	0.06	1.61	0.007	0.02	0.20	0.01	406	5.0
	WAN041		9.0	3.0	0.4	2.5	0.1	3.5	0.7	2.97	0.08	0.01	0.06	0.40	0.014	0.02	0.01	0.28	110	110
	WAN043		0.5	3.0	0.4	2.5	0.1	12.0	0.8	0.83	0.01	0.01	0.06	0.10	0.007	0.05	0.01	0.01	26	5.0
	WAN069		0.5	3.0	0.4	2.5	0.1	2.1	0.4	34.23	0.74	0.03	0.06	0.35	0.007	0.03	0.03	0.07	154	5.0
	WAN070		3.0	3.0	9.6	2.5	0.1	23.8	2.8	37.44	0.09	0.01	0.06	0.80	0.007	0.01	0.01	0.01	629	5.0
	WAN122	Lower	0.5	3.0	0.4	2.5	0.1	2.4	0.4	13.95	0.19	0.01	0.06	1.29	0.406	0.02	0.01	0.58	99	5.0

Appendix XX. Chemical Compositions of Representative Ore Samples from the West Ansil Deposit

Ore Type	Sample	Lens	Th ppm	Rb ppm	Sr ppm	Cs ppm	Ba ppm	Br ppm	Hf ppm	Ir ppb	Sc ppm	Li ppm	Be ppm	Y ppm	Nb ppm	Ta ppm	La ppm	Ce ppm	Pr ppm	Nd ppm	Sm ppm
Massive Sphalerite	WAN015	Middle	0.1	0.2	1.5	0.1	1.5	0.25	0.5	2.5	0.05	1.5	1.5	0.05	1.2	0.1	0.2	0.4	0.05	0.2	0.05
	WAN020		0.1	0.2	5.0	0.1	1.5	0.25	0.5	2.5	0.40	1.5	1.5	0.30	1.2	0.1	0.2	0.4	0.05	0.2	0.05
	WAN021		0.1	0.2	1.5	0.1	1.5	0.25	0.5	2.5	0.05	1.5	1.5	0.05	1.2	0.1	0.2	0.4	0.05	0.2	0.05
	WAN032		0.1	0.2	1.5	0.1	1.5	0.25	0.5	2.5	0.05	1.5	1.5	0.05	1.2	0.1	0.2	0.4	0.05	0.2	0.05
Sphalerite Stringers	WAN013	Middle	0.1	0.2	71	0.1	1.5	0.25	0.5	2.5	6.80	4.0	1.5	11.2	1.2	0.1	3.7	6.8	1.2	4.9	1.4
	WAN018		0.6	1.1	6.0	0.4	1.5	0.25	0.5	2.5	9.90	1.5	1.5	9.4	2.8	0.1	6.7	16.0	2.3	10.0	2.3
	WAN133	Lower	0.7	3.0	6.0	1.1	1.5	0.25	2.0	2.5	18.9	1.5	1.5	20.8	3.5	0.3	6.3	15.4	2.2	9.7	2.8
Massive Pyrrhotite	WAN077	Upper	0.4	0.2	4.0	0.1	1.5	0.25	0.5	2.5	0.30	1.5	1.5	0.30	1.2	0.1	0.7	0.9	0.05	0.7	0.05
	WAN090		0.1	1.2	4.0	1.0	1.5	0.25	0.5	2.5	0.60	1.5	1.5	4.40	1.2	0.1	1.4	2.9	0.4	1.6	0.5
	WAN074		0.1	0.2	7.0	0.1	1.5	0.25	0.5	2.5	0.20	1.5	1.5	5.10	1.2	0.1	1.0	2.7	0.4	1.7	0.6
	WAN075		0.1	9.2	58	1.2	5.0	3.10	0.5	2.5	2.90	1.5	1.5	9.70	1.2	0.1	8.3	17.7	2.1	7.2	1.6
	WAN001	Middle	0.1	0.2	1.5	0.1	1.5	0.25	0.5	2.5	0.60	1.5	1.5	1.30	1.2	0.1	0.2	0.4	0.05	0.2	0.05
	WAN002		0.1	0.2	4.0	0.1	1.5	0.25	0.5	2.5	0.20	1.5	1.5	0.05	1.2	0.1	0.2	0.4	0.05	0.2	0.05
	WAN006		0.1	0.2	4.0	0.1	1.5	0.25	0.5	2.5	0.05	1.5	1.5	0.05	1.2	0.1	0.2	0.4	0.05	0.2	0.05
	WAN022		0.1	0.2	1.5	0.1	1.5	0.25	0.5	2.5	0.20	1.5	1.5	0.05	1.2	0.1	0.2	0.4	0.05	0.2	0.05
	WAN030		0.1	0.2	1.5	0.1	1.5	0.25	0.5	2.5	0.30	1.5	1.5	0.05	1.2	0.1	0.2	0.4	0.05	0.2	0.05
	WAN035		0.1	0.2	1.5	0.1	1.5	0.25	0.5	2.5	0.20	1.5	1.5	0.30	1.2	0.1	0.2	0.4	0.05	0.2	0.05
	WAN050		0.4	0.2	1.5	0.1	1.5	0.25	0.5	2.5	0.20	1.5	1.5	0.20	1.2	0.1	1.3	2.3	0.2	1.7	0.2
	WAN017		0.1	0.8	1.5	0.1	1.5	0.25	0.5	2.5	4.50	1.5	1.5	6.10	1.2	0.1	4.5	7.4	1.1	4.6	1.3
	WAN048		0.1	0.2	1.5	0.1	1.5	0.25	0.5	2.5	0.20	1.5	1.5	0.40	1.2	0.1	1.3	2.3	0.3	1.3	0.2
	WAN102	Lower	0.8	1.4	7.0	0.1	1.5	0.25	1.0	2.5	13.2	1.5	1.5	22.7	1.2	0.1	10.0	21.0	2.8	12.1	3.2
	WAN103		0.3	0.2	4.0	0.1	1.5	0.25	0.5	2.5	0.05	1.5	1.5	1.50	1.2	0.1	2.7	5.2	0.7	2.8	0.5
	WAN118		0.1	0.2	1.5	0.1	1.5	0.25	0.5	2.5	0.05	1.5	1.5	0.20	1.2	0.1	0.2	0.4	0.05	0.2	0.05
	WAN119		0.1	0.2	1.5	0.1	4.0	0.25	0.5	2.5	0.60	1.5	1.5	1.30	1.2	0.1	0.2	0.4	0.05	0.2	0.05
	WAN121		0.1	0.2	6.0	0.1	1.5	2.90	0.5	2.5	0.05	1.5	1.5	2.80	1.2	0.1	1.1	2.4	0.4	1.4	0.5
	WAN132		0.1	0.2	6.0	0.1	1.5	0.25	0.5	2.5	0.20	1.5	1.5	2.50	1.2	0.1	1.4	3.0	0.4	1.5	0.4
Massive Chalcopyrite	WAN004	Middle	0.1	0.2	1.5	0.1	1.5	1.70	0.5	2.5	0.05	1.5	1.5	0.10	1.2	0.1	0.2	0.4	0.05	0.2	0.05
	WAN009		0.1	0.2	3.0	0.1	1.5	0.25	0.5	2.5	0.20	1.5	1.5	0.05	1.2	0.1	0.2	0.4	0.05	0.2	0.05
	WAN036		0.9	0.2	1.5	0.1	1.5	0.25	0.5	2.5	0.05	1.5	1.5	0.40	1.2	0.1	1.0	3.4	0.3	1.9	0.4
	WAN052		0.3	0.2	1.5	0.1	1.5	0.25	0.5	2.5	0.20	1.5	1.5	0.60	1.2	0.1	0.9	2.4	0.3	1.6	0.3
	WAN061		0.1	0.2	1.5	0.1	1.5	0.25	0.5	2.5	0.05	1.5	1.5	0.50	1.2	0.1	0.2	0.4	0.05	0.2	0.05
	WAN092	Lower	0.1	0.6	3.0	0.1	1.5	0.25	0.5	2.5	0.05	1.5	1.5	0.80	1.2	0.1	2.6	6.2	0.9	3.4	0.8
	WAN093		0.1	0.8	1.5	0.1	1.5	0.25	0.5	2.5	1.30	1.5	1.5	2.10	1.2	0.1	5.5	12.7	1.7	7.4	1.7
	WAN130		0.1	0.2	1.5	0.1	1.5	2.30	0.5	2.5	0.05	1.5	1.5	0.60	1.2	0.1	2.4	5.0	0.7	2.8	0.7
Chalcopyrite Stringers	WAN079	Upper	0.4	0.8	10	0.1	1.5	0.25	0.5	2.5	6.90	1.5	1.5	22.2	1.2	0.1	20.0	41.5	5.4	22.7	5.1
	WAN083		1.2	0.9	7.0	0.4	1.5	0.25	4.0	2.5	29.8	1.5	1.5	32.1	5.0	0.1	10.9	22.6	3.1	13.3	3.8
	WAN081		0.2	0.2	6.0	0.1	1.5	0.25	0.5	2.5	7.50	1.5	1.5	17.1	1.2	0.1	34.4	71.6	9.4	37.7	8.8
	WAN080		0.2	0.2	4.0	0.1	1.5	0.25	0.5	2.5	0.80	1.5	1.5	14.6	1.2	0.1	7.9	15.0	2.0	8.0	2.0
	WAN095	Lower	0.7	18.5	9.0	0.9	29	0.25	3.0	2.5	14	1.5	1.5	15.2	2.9	0.1	4.1	9.6	1.4	6.4	2.1
	WAN099		0.4	1.6	6.0	0.1	3.0	0.25	1.0	2.5	13.2	3.0	1.5	12.2	1.2	0.1	5.5	12.6	1.7	7.4	1.7
	WAN101		0.1	0.2	6.0	0.1	1.5	0.25	0.5	2.5	0.80	1.5	1.5	5.60	1.2	0.1	8.0	18.4	2.6	11.2	2.8
	WAN125		0.1	0.9	15	0.1	3.0	3.80	0.5	2.5	5.60	1.5	1.5	14.4	1.2	0.1	13.6	29.4	3.8	15.9	3.5
	WAN111		0.7	1.2	1.5	0.1	1.5	0.25	3.0	2.5	16.4	1.5	1.5	23.3	3.1	0.1	5.6	13.7	2.1	9.4	2.8

Appendix XX. Chemical Compositions of Representative Ore Samples from the West Ansil Deposit

Ore Type	Sample	Lens	Th ppm	Rb ppm	Sr ppm	Cs ppm	Ba ppm	Br ppm	Hf ppm	Ir ppb	Sc ppm	Li ppm	Be ppm	Y ppm	Nb ppm	Ta ppm	La ppm	Ce ppm	Pr ppm	Nd ppm	Sm ppm
Massive Magnetite	WAN071	Upper	1.1	12.7	6.0	1.3	10	0.25	2.0	2.5	21	1.5	1.5	17.3	3.9	0.1	13.9	28.2	3.6	14.6	3.4
	WAN072		0.1	0.2	1.5	0.1	1.5	7.40	0.5	2.5	0.30	1.5	1.5	4.20	1.2	0.1	2.5	5.1	0.6	3.0	0.7
	WAN073		0.9	0.7	1.5	0.1	1.5	0.25	0.5	2.5	0.30	1.5	1.5	5.70	1.2	0.1	3.6	9.3	1.0	5.0	1.0
	WAN076		0.1	0.2	4.0	0.1	1.5	0.25	0.5	2.5	0.20	1.5	1.5	1.80	1.2	0.1	0.2	0.4	0.05	0.2	0.1
	WAN078		0.1	0.2	8.0	0.1	1.5	0.25	0.5	2.5	0.20	1.5	1.5	1.20	1.2	0.1	1.2	2.6	0.3	1.1	0.3
	WAN084		1.6	13	9.0	1.4	12	0.25	3.0	2.5	25.6	1.5	1.5	13.7	4.0	0.1	31.8	57.9	6.6	24.2	4.3
	WAN085		0.3	0.7	5.0	0.1	1.5	0.25	0.5	2.5	0.40	1.5	1.5	3.10	1.2	0.1	1.0	1.6	0.2	1.1	0.3
	WAN086		0.1	0.6	6.0	0.1	1.5	0.25	0.5	2.5	0.10	1.5	1.5	5.80	1.2	0.1	1.0	2.5	0.4	1.7	0.6
	WAN054	Middle	0.1	0.2	1.5	0.1	1.5	0.25	0.5	2.5	0.05	1.5	1.5	1.60	1.2	0.1	1.0	1.4	0.3	1.0	0.2
	WAN056		0.4	5.5	13	0.4	5.0	0.25	0.5	2.5	2.30	1.5	1.5	14.5	1.2	0.1	5.3	11.7	1.6	7.4	2.1
	WAN058		0.1	2.3	22	0.1	1.5	0.25	0.5	2.5	1.40	1.5	1.5	7.50	1.2	0.1	7.4	14.4	1.9	8.1	1.9
	WAN060		0.1	0.6	6.0	0.1	1.5	0.25	0.5	2.5	0.50	1.5	1.5	2.80	1.2	0.1	0.8	1.4	0.2	1.0	0.2
	WAN062		0.2	0.2	1.5	0.1	1.5	0.25	0.5	2.5	1.50	1.5	1.5	11.6	1.2	0.1	7.7	18.4	2.6	11.2	2.8
	WAN066		0.3	9.7	5.0	0.8	5.0	0.25	0.5	2.5	4.70	1.5	1.5	13.0	1.2	0.1	3.5	7.7	1.1	4.8	1.3
Colloform Pyrite-Marcasite	WAN087	Upper	0.1	0.2	9.0	0.1	1.5	0.25	0.5	2.5	0.40	13	1.5	6.30	1.2	0.1	3.2	6.8	0.8	3.0	0.6
	WAN088		0.1	0.2	10	0.2	1.5	4.10	0.5	2.5	0.30	1.5	1.5	16.2	1.2	0.1	5.2	12.0	1.5	6.4	1.8
	WAN089		0.1	1.8	22	0.3	1.5	0.25	0.5	2.5	1.70	1.5	1.5	16.9	1.2	0.1	4.1	8.4	1.1	4.1	1.2
	WAN007	Middle	0.1	0.2	6.0	0.1	1.5	0.25	0.5	2.5	0.20	1.5	1.5	0.05	1.2	0.1	0.2	0.4	0.05	0.2	0.05
	WAN010		0.1	0.8	12.0	0.2	5.0	0.25	0.5	2.5	0.20	1.5	1.5	2.00	1.2	0.1	4.1	6.0	0.9	4.4	1.1
	WAN016		0.1	0.2	6	0.1	1.5	0.25	0.5	2.5	0.30	1.5	1.5	4.80	1.2	0.1	2.1	2.4	0.5	1.9	0.7
	WAN026		0.1	0.2	1.5	0.1	1.5	0.25	0.5	2.5	0.20	1.5	1.5	4.50	1.2	0.1	3.5	5.6	0.9	3.5	1.2
	WAN029		0.1	1.9	5.0	0.2	5.0	0.25	0.5	2.5	4.20	1.5	1.5	4.60	1.2	0.1	4.6	7.3	1.1	4.1	1.0
	WAN033		0.4	4.0	9.0	0.1	6.0	0.25	0.5	2.5	3.40	1.5	1.5	12.3	1.2	0.1	11.0	20.5	2.5	10.9	2.4
	WAN041		0.2	0.2	1.5	0.1	1.5	8.70	0.5	2.5	0.20	1.5	1.5	3.00	1.2	0.1	1.6	2.7	0.3	1.9	0.4
	WAN043		0.1	0.2	1.5	0.1	1.5	0.25	0.5	2.5	0.05	1.5	1.5	0.60	1.2	0.1	0.4	0.4	0.05	0.4	0.05
	WAN069		0.1	0.2	1.5	0.1	6.0	0.25	0.5	2.5	1.50	1.5	1.5	5.40	1.2	0.1	2.8	6.0	0.8	3.6	0.8
	WAN070		0.1	0.2	1.5	0.1	1.5	0.25	0.5	2.5	0.20	1.5	1.5	2.80	1.2	0.1	0.2	0.4	0.05	0.4	0.05
	WAN122	Lower	0.1	0.2	11	0.1	1.5	3.80	0.5	2.5	0.50	6.0	1.5	6.30	1.2	0.1	3.1	8.2	1.2	4.9	1.3

Appendix XX. Chemical Compositions of Representative Ore Samples from the West Ansil Deposit

Ore Type	Sample	Lens	Eu ppm	Gd ppm	Tb ppm	Dy ppm	Ho ppm	Er ppm	Tm ppm	Yb ppm	Lu ppm
Massive Sphalerite	WAN015	Middle	0.05	0.05	0.05	0.2	0.1	0.05	0.05	0.05	0.12
	WAN020		0.05	0.05	0.05	0.2	0.1	0.05	0.05	0.05	0.03
	WAN021		0.05	0.05	0.05	0.2	0.1	0.05	0.05	0.05	0.03
	WAN032		0.05	0.05	0.05	0.2	0.1	0.05	0.05	0.05	0.03
Sphalerite Stringers	WAN013	Middle	0.9	1.9	0.3	2.1	0.4	1.1	0.2	1.0	0.21
	WAN018		0.5	2.2	0.3	1.9	0.4	1.0	0.1	0.9	0.03
	WAN133	Lower	0.5	3.1	0.6	3.7	0.8	2.1	0.3	2.2	0.43
Massive Pyrrhotite	WAN077	Upper	0.05	0.05	0.05	0.2	0.1	0.05	0.05	0.05	0.09
	WAN090		0.05	0.6	0.1	0.8	0.1	0.5	0.05	0.5	0.13
	WAN074		0.05	0.8	0.2	1.0	0.2	0.6	0.05	0.5	0.14
	WAN075		0.2	1.6	0.3	1.8	0.4	1.1	0.1	0.9	0.20
	WAN001	Middle	0.05	0.2	0.05	0.2	0.1	0.1	0.05	0.05	0.03
	WAN002		0.05	0.05	0.05	0.2	0.1	0.05	0.05	0.05	0.03
	WAN006		0.05	0.05	0.05	0.2	0.1	0.05	0.05	0.05	0.03
	WAN022		0.05	0.05	0.05	0.2	0.1	0.05	0.05	0.05	0.08
	WAN030		0.05	0.05	0.05	0.2	0.1	0.05	0.05	0.05	0.03
	WAN035		0.05	0.05	0.05	0.2	0.1	0.05	0.05	0.05	0.03
	WAN050		0.05	0.05	0.05	0.2	0.1	0.05	0.05	0.05	0.03
	WAN017		0.05	1.4	0.2	1.4	0.3	0.7	0.05	0.6	0.14
	WAN048		0.05	0.2	0.05	0.2	0.1	0.05	0.05	0.05	0.03
	WAN102	Lower	0.2	3.7	0.7	4.1	0.8	2.2	0.3	2.0	0.32
	WAN103		0.05	0.5	0.05	0.3	0.1	0.1	0.05	0.1	0.03
	WAN118		0.05	0.05	0.05	0.2	0.1	0.05	0.05	0.05	0.03
	WAN119		0.05	0.1	0.05	0.2	0.1	0.2	0.05	0.2	0.03
	WAN121		0.05	0.5	0.05	0.5	0.1	0.3	0.05	0.2	0.03
	WAN132		0.05	0.5	0.05	0.5	0.1	0.3	0.05	0.2	0.03
Massive Chalcopyrite	WAN004	Middle	0.05	0.05	0.05	0.2	0.1	0.05	0.05	0.05	0.03
	WAN009		0.05	0.05	0.05	0.2	0.1	0.05	0.05	0.05	0.03
	WAN036		0.05	0.2	0.05	0.2	0.1	0.05	0.05	0.05	0.03
	WAN052		0.05	0.2	0.05	0.2	0.1	0.05	0.05	0.05	0.03
	WAN061		0.05	0.05	0.05	0.2	0.1	0.05	0.05	0.05	0.03
	WAN092	Lower	0.05	0.6	0.05	0.2	0.1	0.05	0.05	0.05	0.03
	WAN093		0.1	1.3	0.2	0.6	0.1	0.2	0.05	0.2	0.08
	WAN130		0.05	0.5	0.05	0.2	0.1	0.05	0.05	0.1	0.03
Chalcopyrite Stringers	WAN079	Upper	0.3	4.6	0.7	4.0	0.8	2.3	0.3	1.8	0.38
	WAN083		0.2	4.3	0.8	5.4	1.2	3.6	0.6	3.9	0.68
	WAN081		0.3	7.6	1.0	4.5	0.8	1.9	0.2	1.5	0.24
	WAN080		0.05	2.2	0.4	2.8	0.7	1.9	0.3	1.5	0.40
	WAN095	Lower	0.3	2.2	0.5	2.9	0.6	1.8	0.3	1.7	0.26
	WAN099		0.1	1.9	0.3	2.2	0.4	1.3	0.2	1.2	0.27
	WAN101		0.1	2.2	0.3	1.5	0.2	0.6	0.05	0.3	0.12
	WAN125		0.4	3.1	0.5	2.5	0.5	1.3	0.2	1.1	0.18
	WAN111		0.9	3.1	0.6	4.0	0.9	2.6	0.4	2.6	0.40

Appendix XX. Chemical Compositions of Representative Ore Samples from the West Ansil Deposit

Ore Type	Sample	Lens	Eu ppm	Gd ppm	Tb ppm	Dy ppm	Ho ppm	Er ppm	Tm ppm	Yb ppm	Lu ppm
Massive Magnetite	WAN071	Upper	0.3	3.0	0.5	3.3	0.7	2.1	0.3	2.2	0.41
	WAN072		0.3	0.7	0.1	0.9	0.1	0.5	0.05	0.4	0.03
	WAN073		0.05	1.0	0.2	1.1	0.2	0.6	0.05	0.5	0.03
	WAN076		0.05	0.2	0.05	0.3	0.1	0.3	0.05	0.3	0.07
	WAN078		0.05	0.2	0.05	0.2	0.1	0.2	0.05	0.1	0.03
	WAN084		0.5	3.7	0.5	2.8	0.6	1.8	0.3	1.9	0.31
	WAN085		0.05	0.3	0.05	0.5	0.1	0.4	0.05	0.6	0.06
	WAN086		0.05	0.8	0.2	1.1	0.2	0.7	0.05	0.6	0.08
	WAN054	Middle	0.1	0.2	0.2	0.2	0.1	0.2	0.05	0.3	0.03
	WAN056		0.3	2.5	0.5	2.8	0.6	1.6	0.2	1.2	0.18
	WAN058		0.2	1.8	0.3	1.3	0.3	0.7	0.05	0.4	0.15
	WAN060		0.05	0.3	0.05	0.5	0.1	0.4	0.05	0.5	0.03
	WAN062		0.05	2.7	0.5	2.6	0.5	1.2	0.2	0.9	0.25
	WAN066		0.2	1.5	0.3	2.4	0.6	1.7	0.3	1.8	0.43
Colloform Pyrite-Marcasite	WAN087	Upper	0.05	0.8	0.2	1.3	0.3	0.8	0.1	0.7	0.10
	WAN088		0.2	2.3	0.5	3.2	0.7	2.0	0.3	2.0	0.31
	WAN089		0.1	1.7	0.4	3.1	0.7	2.2	0.3	2.4	0.32
	WAN007	Middle	0.05	0.05	0.05	0.2	0.1	0.05	0.05	0.1	0.03
	WAN010		0.05	0.9	0.1	0.5	0.1	0.2	0.05	0.1	0.03
	WAN016		0.05	0.9	0.1	0.8	0.1	0.3	0.05	0.3	0.08
	WAN026		0.1	1.2	0.2	1.0	0.1	0.4	0.05	0.2	0.03
	WAN029		0.05	1.1	0.1	0.9	0.1	0.5	0.05	0.5	0.15
	WAN033		0.2	2.4	0.4	2.6	0.5	1.3	0.2	1.2	0.26
	WAN041		0.05	0.4	0.05	0.6	0.1	0.3	0.05	0.3	0.07
	WAN043		0.05	0.1	0.05	0.2	0.1	0.05	0.05	0.1	0.18
	WAN069		0.1	0.9	0.2	0.9	0.1	0.5	0.05	0.4	0.03
	WAN070		0.05	0.2	0.05	0.4	0.1	0.4	0.05	0.5	0.09
	WAN122	Lower	0.2	1.3	0.2	1.2	0.3	0.7	0.05	0.5	0.03

Appendix XXI. Analytical Methods

Geochemistry of Ore Types

Minor and trace elements were analyzed a combination of INAA (instrumental neutron activation analysis) and ICP-MS (inductively coupled plasma – mass spectrometry) at Activation Laboratories, Ancaster, Ontario. All elements except Na and Hg were analyzed by ICP-MS. Fe, Zn, Sn, Ag, Ni, As, Sb, Au, Co, Se, Mo, W, U, Na, Ca, Th, Rb, Sr, Cs, Ba, Br, Hf, Ir, Sc, Ta, La, Ce, Nd, Sm, Eu, Tb, Yb and Lu were analyzed by INAA. The data were chosen based on the lowest detection limit. For INAA, a 30 g aliquot was encapsulated in a polyethylene vial and irradiated with an internal standard at a thermal neutron flux of 7 x 10^{12} n cm-2 s-1. After a 7-day delay to allow Na-24 to decay, the samples are counted on a high purity Ge detector with resolution of better than 1.7 KeV for the 1332 KeV Co-60 photopeak. The decay-corrected activities are compared to a calibration developed from multiple certified international reference materials. For ICP-MS, a combination of sodium peroxide fusion followed by multi-acid digestion was used to dissolve the metals. A minimum of 10 certified reference materials were used for the required analytes, all prepared by sodium peroxide fusion. Samples were analyzed using a Varian 735ES ICP or a Thermo 6500 ICAP and Perkin Elmer Sciex ELAN 6000, 6100 or 9000 ICP/MS. Mercury was analyzed by a cold vapour technique in which 0.5 g of sample is digested with aqua regia and Hg (II) is reduced to mercury vapour using stannous chloride. Argon is bubbled through the solution in a closed reaction system to liberate and transport the Hg atoms into an absorption cell where it is determined in a Perkins Elmer FIMS (Flow Injection Mercury System) 100 via the absorption of light at 253.7 nm. Infrared absorption analysis was used to determine CO_2, where 0.2 g sample is thermally decomposed in a resistance furnace in a pure nitrogen environment at 1000 $^{\circ}$C, directly releasing CO_2. Water is removed in a moisture

trap prior to the detection of carbon dioxide in the IR cell; the carbon dioxide absorbs IR energy at a precise wavelength within the IR spectrum. All other IR energy is prevented from reaching the IR detector by a narrow bandpass filter.

Whole-rock Geochemistry

Major element oxide data were obtained by X-ray fluorescence (XRF) analysis of samples that were first combusted to determine loss-on-ignition. LOI was determine by first heating to 100^{o}C under nitrogen atmosphere, then 1000^{o}C under oxygen atmosphere until constant wt % was reached. The sample was then fused with a borate flux to produce a glass bead which was dissolved using a closed vessel multi-acid digestion (hydrofluoric, hydrochloric, nitric, and perchloric acids), which is preferred for total dissolution of rare earth elements (REE), high-field strength elements (HFSE), and large ion lithophile elements (LILE). Minor and trace elemental analyses of the solutions were conducted by ICP-MS (inductively coupled plasma – mass spectrometry). Analyses were calibrated using a combination of synthetic multi-element solutions and certified reference materials. CO_2 and total S were analyzed by infrared absorption of oxidized samples previously combusted in an oxygen-rich environment.

Natural Resources Canada
Ressources naturelles Canada

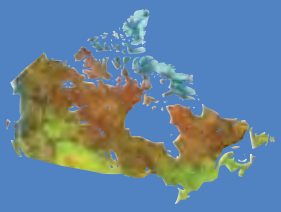

Primary and secondary ore textures in the West Ansil volcanic-hosted massive-sulphide deposit, Noranda mining camp, Rouyn-Noranda, Quebec

S.M. Boucher, M.D. Hannington, and B. Dubé

Geological Survey of Canada

Current Research 2010-10

2010

Canada

Geological Survey of Canada
Current Research 2010-10

Primary and secondary ore textures in the West Ansil volcanic-hosted massive-sulphide deposit, Noranda mining camp, Rouyn-Noranda, Quebec

S.M. Boucher, M.D. Hannington, and B. Dubé

2010

ISSN 1701-4387
Catalogue No. M44-2010/10E-PDF
ISBN 978-1-100-16614-8
DOI 10.4095/286047

A copy of this publication is also available for reference in depository libraries across Canada through access to the Depository Services Program's Web site at http://dsp-psd.pwgsc.gc.ca

A free digital download of this publication is available from GeoPub: http://geopub.nrcan.gc.ca/index_e.php

Toll-free (Canada and U.S.A.): 1-888-252-4301

Recommended citation

Boucher, S.M., Hannington, M.D., and Dubé, B., 2010. Primary and secondary ore textures in the West Ansil volcanic-hosted massive-sulphide deposit, Noranda mining camp, Rouyn-Noranda, Quebec; Geological Survey of Canada, Current Research 2010-10, 16 p.

Critical review
P. Mercier-Langevin

Correction date:

Primary and secondary ore textures in the West Ansil volcanic-hosted massive-sulphide deposit, Noranda mining camp, Rouyn-Noranda, Quebec

S.M. Boucher, M.D. Hannington, and B. Dubé

Boucher, S.M., Hannington, M.D., and Dubé, B., 2010. Primary and secondary ore textures in the West Ansil volcanic-hosted massive-sulphide deposit, Noranda mining camp, Rouyn-Noranda, Quebec; Geological Survey of Canada, Current Research 2010-10, 16 p.

Abstract: The West Ansil deposit is the first copper discovery in 25 years in the Noranda central camp. It has a combined indicated and inferred resource of about 1.2 Mt. Grades for the indicated resource are 3.4% Cu, 0.4% Zn, 1.4 g/t Au, and 9.2 g/t Ag. Locally, gold grades are up to 10 ppm within massive chalcopyrite ore, which is significantly higher than other central camp deposits (e.g. Corbet). The bulk of the resource is located in three massive-sulphide lenses (upper, middle, and lower) that are hosted in the Rusty Ridge unit above the Lewis exhalite. The Lewis exhalite is a key marker that is also related to the nearby Ansil mine (1.58 Mt, 8.03% Cu, 0.09% Zn) about 1.8 km northeast of the West Ansil deposit. The overall distribution of massive-sulphide ore and stringer zones at the West Ansil deposit suggests either stacking of separate lenses or dissection of a single deposit by late-stage faulting and dyke formation. The mineralization in all three ore lenses consists of massive pyrrhotite+chalcopyrite±magnetite. Semimassive sphalerite is restricted to the upper and lower parts of the middle lens. Massive magnetite occurs in the upper and middle lenses, where it replaces massive pyrrhotite. A striking feature of the West Ansil deposit is the presence of abundant colloform and nodular pyrite (±marcasite) in the massive-sulphide deposits, especially at the top and bottom of the main massive-sulphide lens. The colloform pyrite is interpreted to be a product of supergene alteration of pyrrhotite. This alteration may be related to shearing at the contacts of the lenses that allowed penetration of groundwater into the massive-sulphide deposits.

Résumé : Le gisement de West Ansil représente la première découverte de cuivre des 25 dernières années dans le camp central de Noranda. Il renferme des ressources indiquées et présumées totalisant environ 1,2 Mt. La teneur des ressources indiquées est de 3,4 % Cu, 0,4 % Zn, 1,4 g/t Au et 9,2 g/t Ag. Par endroits, les teneurs en or atteignent 10 ppm dans du minerai de chalcopyrite massive, une teneur considérablement plus élevée que celle d'autres gisements du camp central (p. ex. Corbet). La majeure partie de la ressource se trouve dans trois lentilles de sulfures massifs (lentilles supérieure, médiane et inférieure) encaissées dans l'unité de Rusty Ridge, sus-jacente à l'exhalite de Lewis. L'exhalite de Lewis est un repère clé qui est également lié à la mine Ansil (1,58 Mt, 8,03 % Cu, 0,09 % Zn) située à proximité, à environ 1,8 km au nord-est du gisement de West Ansil. La répartition générale du minerai et des faisceaux de filonnets de sulfures massifs dans le gisement de West Ansil laisse supposer soit un empilement de lentilles distinctes, soit la dissection d'un seul gisement par la formation de failles et de dykes de phase tardive. Dans les trois lentilles de minerai, la minéralisation se compose principalement de pyrrhotite+chalcopyrite ±magnétite massives. La sphalérite semi-massive se limite aux parties supérieure et inférieure de la lentille médiane. La magnétite massive est présente dans les lentilles supérieure et médiane, où elle remplace la pyrrhotite massive. Une caractéristique marquante du gisement de West Ansil est la présence abondante de pyrite (±marcasite) colloforme et nodulaire dans les sulfures massifs, particulièrement au sommet et à la base de la principale lentille de sulfures massifs. Selon notre interprétation, la pyrite colloforme serait le produit d'une altération supergène de la pyrrhotite. Cette altération pourrait être liée au cisaillement aux contacts des lentilles, qui aurait permis la pénétration des eaux souterraines dans les sulfures massifs.

INTRODUCTION

The West Ansil deposit is hosted by volcanic rocks of the Blake River Group, one of several Archean volcanic complexes that form the Abitibi greenstone belt of the southern Superior Province (Baragar, 1968; Dimroth et al., 1982; Gélinas et al., 1984). The deposit lies conformably in volcanic stratigraphy in the central part of the central camp, 6 km north of Rouyn-Noranda (Fig. 1). The orebody was discovered in 2005 by Xstrata Copper Canada Ltd. and is the first significant new base-metal discovery in the central camp in 25 years. The deposit occurs at the basalt-andesite contact within the Rusty Ridge unit in the Noranda camp and is the only known massive sulphide at this stratigraphic level (Fig. 2). The original drill targets were characterized by the presence of a significant alteration zone near the intersection of two recognized synvolcanic faults within the Rusty Ridge formation. Historical drillholes that intersected the alteration did not reach the Lewis contact, the deep horizon at which the nearby Ansil deposit was found, or the stratigraphic position of the Corbet deposit next to the Flavrian intrusion (Xstrata Copper Canada Ltd., 2005); however, several off-hole geophysical anomalies (borehole electromagnetic) were found stratigraphically above the interpreted position of the Lewis contact. These were subsequently targeted for drilling in 2005, and significant Cu-rich stringer mineralization and massive-sulphide deposits were intersected in three separate zones. The combined upper, middle, and lower lenses of the West Ansil deposit have indicated and inferred resources of about 1.2 Mt with grades for the indicated resource of 3.4% Cu, 0.4% Zn, 1.4 g/t Au, and 9.2 g/t Ag (Xstrata Copper Canada Ltd., 2005).

Like the Ansil deposit, the West Ansil deposit differs from the other massive-sulphide deposits of the central camp (e.g. Riverin and Hodgson, 1980; Riverin et al., 1990; Cattalani et al., 1993) in the following ways: 1) the bulk of the orebody is Cu-rich and Zn-poor and dominated by chalcopyrite and pyrrhotite; 2) massive magnetite forms a significant portion of the deposit; 3) there is a lack of conspicuous alteration around the middle lens; and 4) abundant late-stage colloform pyrite±marcasite overprints the massive pyrrhotite. This paper documents the main ore types of the West Ansil deposit, as well as metal zonation and the overall paragenesis, and discusses possible explanations for the high Cu/Cu+Zn ratios, the abundant magnetite, and the unusual late-stage pyrite and marcasite.

GEOLOGICAL SETTING OF THE WEST ANSIL DEPOSIT

Regional geology

The Blake River Group in the Noranda area is 12–15 km thick and composed of bimodal mafic and felsic volcanic rocks with rapid facies changes and a marked variation in the thicknesses of individual units (de Rosen-Spence, 1976; Gibson and Watkinson, 1990; Riverin et al., 1990). The Noranda volcanic complex is approximately 2.7 Ga and measures 35 km in diameter and 7.5–9 km in thickness. It is dominated by the Noranda cauldron and shield volcano (Gibson and Watkinson, 1990), which consists of rhyolitic, andesitic, and basaltic flows and minor pyroclastic rocks (Mortensen, 1987; Gibson and Watkinson, 1990). The volcanic rocks have been metamorphosed to the greenschist facies, although some areas include higher or lower grade rocks. The volcanic rocks of the Noranda volcanic complex have been divided into five cycles, each consisting of an andesitic to basaltic basal unit and mixed rhyolite and andesite upper unit (Gibson and Watkinson, 1990). Cycle 3, also referred to as the mine sequence, is host to most of the massive-sulphide deposits of the Noranda central camp and consists of a bimodal succession of tholeiitic basalt to rhyolite, interpreted to have erupted during periods of cauldron subsidence within the upper central part of the Noranda shield volcano (Gibson and Watkinson, 1990). The overall stratigraphic setting of the Blake River Group has recently been revised by Goutier et al. (2009) based on detailed U-Pb geochronology (e.g. McNicoll et al., (2009). The mine sequence is now considered to be part of the ca. 2702–2696.7 Ma Noranda rocks (*see* Goutier et al., 2009; McNicoll et al., 2009). The Corbet, Ansil, and West Ansil deposits are the lowest in the mine sequence stratigraphy (Barrett et al., 1991, 1993; Galley, 1994) (Fig. 2). Average grades indicate a generally higher Cu/Cu+Zn ratio (>0.5) for Corbet, Ansil, and West Ansil than for deposits located higher in the stratigraphy (Barrett et al., 1991, 1993)

Local geology

The West Ansil deposit is located within the Rusty Ridge formation, at an andesite-basalt contact, stratigraphically above the Ansil deposit (Fig. 2). The long axis of the deposit trends north and has a strike length of 200 m, with a thickness of approximately 50 m (Fig. 3). The stratigraphy in the immediate vicinity of the deposit includes the Northwest rhyolite, the Rusty Ridge andesite, the Amulet dacite, and the Amulet rhyolite (Fig. 4). These units generally dip toward the east-northeast at approximately 30° to 45°. All of the volcanic units have a dominantly tholeiitic affinity (Barrett et al., 1991). The top of the Northwest rhyolite corresponds to the position of the Lewis exhalite, but this horizon has not been observed at West Ansil. The Rusty Ridge formation, which comprises andesite overlain by basalt, is intruded by the Amulet dacite and rhyolite. The extrusive sequence is underlain by the Flavrian pluton, a composite body of mainly trondhjemitic composition (Goldie, 1978; Gibson and Galley, 2007).

The Rusty Ridge andesite is a dark green, massive, pillowed unit, with chloritized and brecciated flow margins. The pillows are metre-sized and locally contain centimetre-scale quartz- and chlorite-filled amygdales, fracture-filling

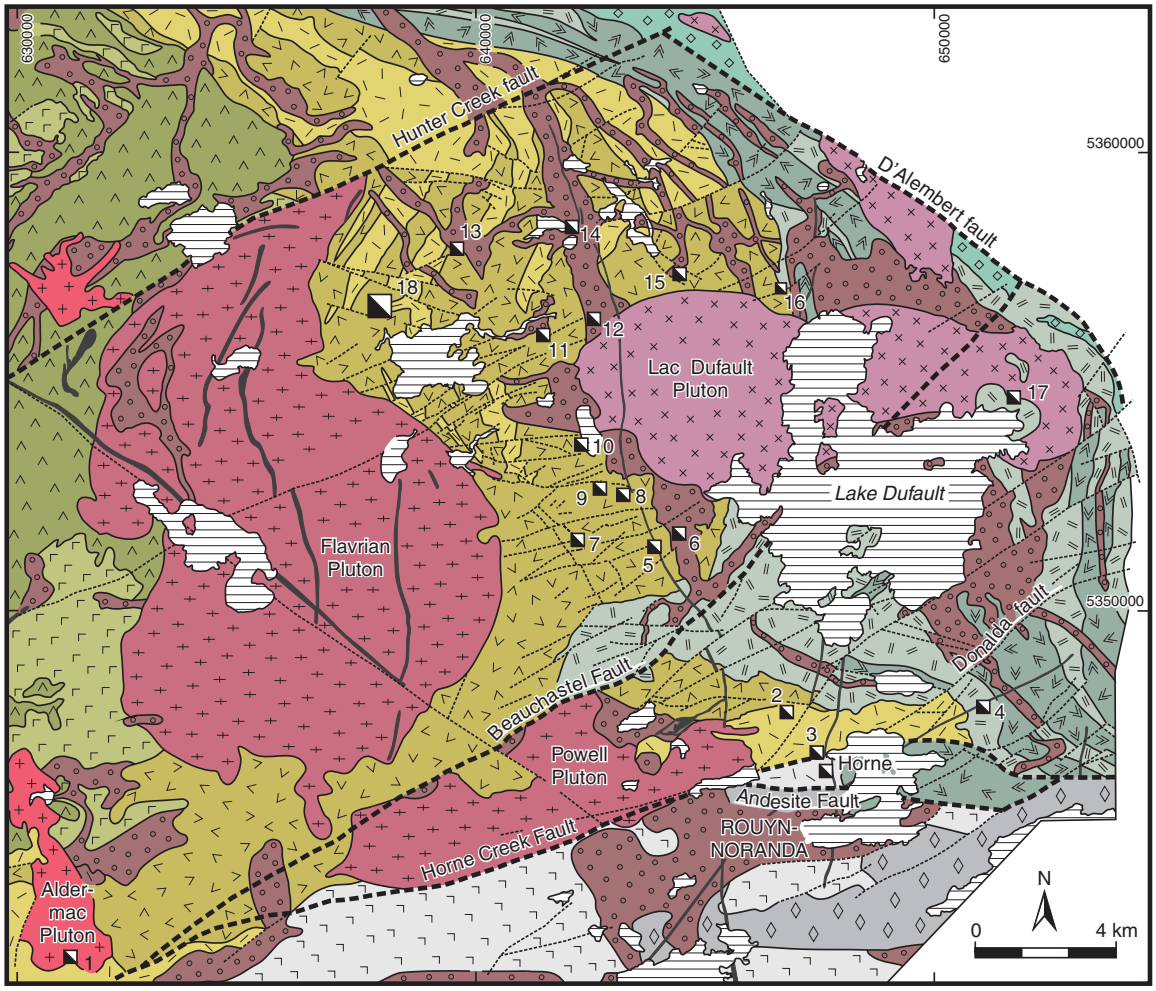

Deposits: 1 = Aldermac, 2 = Joliet, 3 = Quemont, 4 = Delbridge, 5 = D68, 6 = Millenbach, 7 = Corbet, 8 = Amulet A, 9 = Amulet C, 10 = Amulet F, 11 = Old Waite, 12 = East Waite, 13 = Ansil, 14 = Vauze, 15 = Norbec, 16 = Newbec, 17 = Gallen, and 18 = West Ansil

ARCHEAN EXTRUSIVE ROCKS
Undifferentiated
Rhyolite
Basalt and/or andesite
Cycle 1+2
Rhyolite
Basalt and/or andesite
Cycle 3
Rhyolite
Basalt and/or andesite
Cycle 4
Rhyolite
Basalt and/or andesite
Cycle 5
Basalt and/or andesite

ARCHEAN INTRUSIVE ROCKS
Syenite
Granodiorite
Trondhjemite, tonalite
Gabbro, quartz diorite

PROTEROZOIC INTRUSIVE ROCKS
Diabase

Major fault
Minor fault
Deposit

Figure 1. Generalized geological map of the Noranda camp, showing the regional geology, major structural elements, as well as the distribution of extrusive and intrusive rocks. West Ansil and other volcanic-hosted massive-sulphide deposits of the mine sequence are also shown (*after* Monecke et al., 2008).

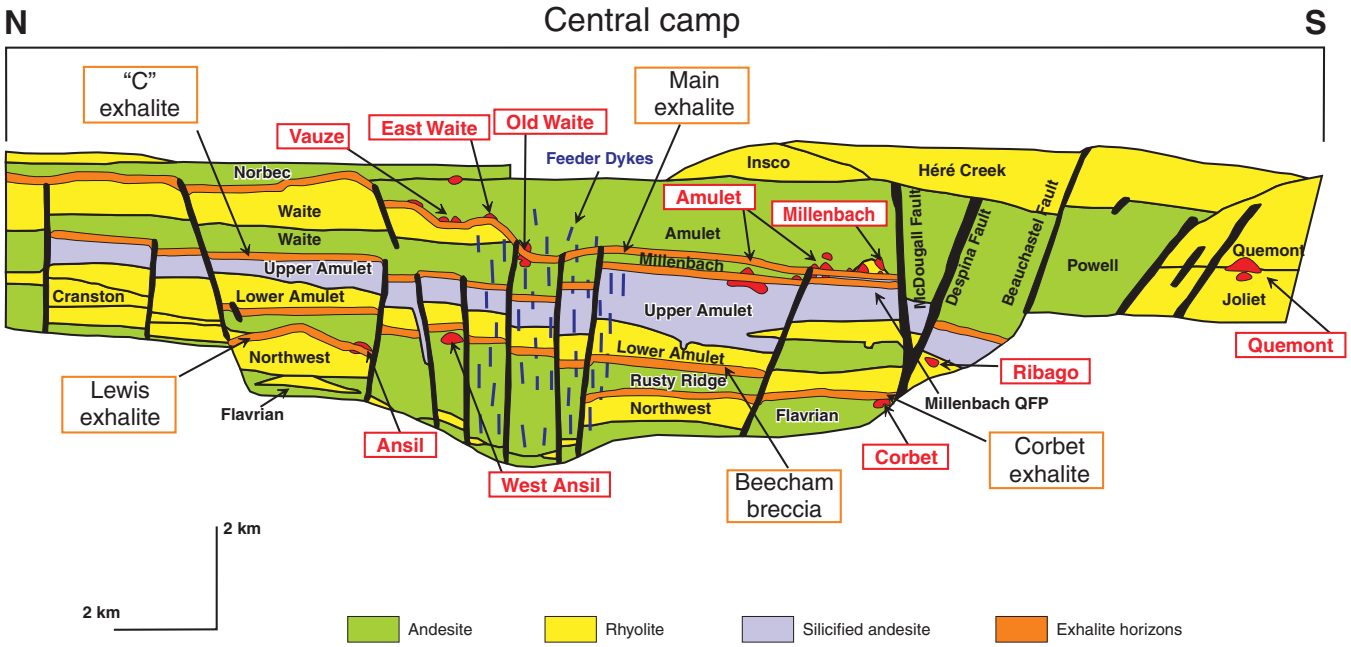

Figure 2. Stratigraphic position of the West Ansil deposit within the reconstructed Noranda cauldron showing the main exhalite horizons, synvolcanic structures, and the significant volcanic-hosted massive-sulphide deposits of the mine sequence (*after* Gibson and Galley, 2007).

chlorite, and disseminated pyrite and chalcopyrite. The flow-breccia units have a distinctly chloritized matrix. The Rusty Ridge basalt is also dark green, with massive to brecciated portions; its upper and lower parts can only be distinguished on the basis of lithogeochemistry (Xstrata Copper Canada Ltd., 2005). The brecciated portion is generally located at the top of the unit. The fragments range from 0.2 cm to 2 cm, with 2–5 volume per cent chlorite-filled amygdales, and the matrix is chloritized and silicified. The massive portion is generally fine grained, and contains 1–2 volume per cent chlorite-filled amygdales ranging from 1–2 mm. The Amulet dacite is pale to medium grey and is characterized by a massive aphanitic texture with rare quartz-filled amygdales and local disseminated pyrrhotite, pyrite, and chalcopyrite. It intrudes the Rusty Ridge formation and generally has brecciated contacts. At West Ansil, the lower contact of the dacite with the Rusty Ridge basalt is discordant, confirming its intrusive nature. Above the Rusty Ridge basalt, the lower Amulet rhyolite is present where the contact is not cut by the dacite. It is aphyric to granular, pale to medium grey, generally massive, with flow breccia, and contains 2–10 volume per cent quartz- and chlorite-filled amygdales. The brecciated facies is composed of clasts from 0.5 cm to 3 cm in a chlorite matrix.

The upper lens and stockwork zone of the West Ansil deposit are located within the upper Rusty Ridge basalt near the contact with the Amulet dacite. The middle lens occurs between the lower Rusty Ridge basalt and andesite. The lower lens and stockwork zone are located at the contact between the lower Rusty Ridge basalt and andesite (Fig. 4). A large, 60 m thick diorite sill separates the middle lens from the lower lens at the approximate location of the basalt-andesite contact. Other smaller diorite sills cut through the West Ansil deposit as well as most of the stratigraphy. A second set of subvertical feldspar porphyritic diorite dykes cut the middle lens and the Rusty Ridge andesite and basalt. They are associated with local recrystallization of sulphide minerals and quartz-carbonate veining (*see* 'West Ansil orebody' section, below).

WEST ANSIL OREBODY

The upper lens of the West Ansil deposit is an ovoid body located at a vertical depth of approximately 160 m with a dip extent of roughly 60 m, a maximum thickness of 30 m, and a width of 25 m (Fig. 3, 4). The dominant sulphide mineral is massive pyrrhotite with minor disseminated chalcopyrite and local chalcopyrite veins. Discontinuous lenses of massive magnetite are present throughout the upper lens, but are more abundant at the top where the thickest intersection of magnetite occurs (Fig. 5). Bands of colloform pyrite and marcasite, up to 30 cm thick, occur along the upper and lower contacts of the lens. A narrow stringer zone extending below the upper lens has a dip extent of about 80 m, a width of 5–10 m, and a length of 25 m. The stringer mineralization consists of chalcopyrite veins and veinlets with minor magnetite in a strongly chloritized black basalt-andesite breccia.

The middle lens represents the bulk of the West Ansil orebody and is located at a vertical depth of 285 m with a dip extent of 160 m, a width of about 50 m, and a thickness of 45 m at its centre and 5–8 m at its outer edge (Fig. 4). The lens consists mainly of massive pyrrhotite with minor disseminated chalcopyrite that surrounds a chalcopyrite-rich

core. Semimassive sphalerite also occurs within massive pyrrhotite in the upper western part of the lens. Minor massive magnetite is restricted to the lower part. A conspicuous feature of the massive-sulphide mineralization of the middle lens is the presence of abundant, partially replaced siliceous and chloritic wall-rock fragments (pseudobreccia). These are interpreted to represent relict clasts of basalt or andesite, possibly along flow contacts, that were infiltrated by the massive sulphide (*see* 'Principal ore types' section). Late-stage, colloform pyrite-marcasite nodules and bands up to 30 cm thick are present along the upper and lower contacts of the lens. Minor stringer-like mineralization occurs along the lower contact of the massive-sulphide minerals, but any obvious pipe-like stockwork zone appears to have been cut out by the diorite sill or it was never developed (Fig. 5). The middle lens also lacks conspicuous footwall or hanging-wall alteration along most of its lower and upper contacts. A reactivated synvolcanic fault parallel to the lower contact and diorite sill may have removed any footwall alteration from below the main massive-sulphide lens. This fault also appears to offset the lower lens from the middle lens.

Two small satellite bodies occur directly below the main diorite sill above the lower lens. These bodies are subhorizontal and relatively small, with a combined thickness of only 10 m and a width of approximately 25 m. The larger lower lens is about 20 m thick and 25 m wide and is located at a vertical depth of 485 m. It is relatively flat with a shallow plunge toward the west (Fig. 4). Massive chalcopyrite mineralization is dominant toward the bottom of this lens and grades into more pyrrhotite-rich massive sulphide with disseminated chalcopyrite at the top. Minor colloform pyrite-marcasite nodules and bands occur along the upper and lower contacts, as in the other lenses.

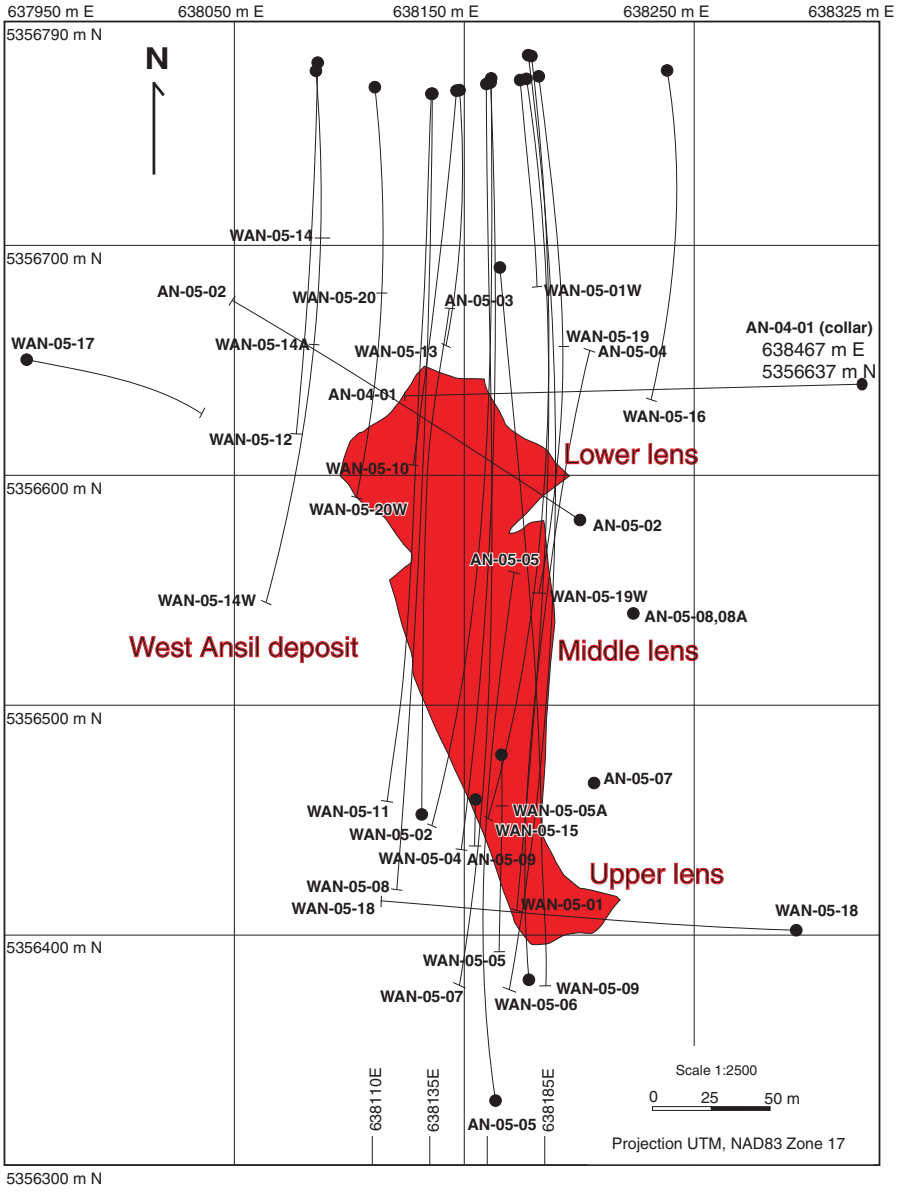

Figure 3. Surface orebody projection of the West Ansil deposit showing the location of drillholes as well as the position of north-south cross-sections in Figure 3b (*modified from* Xstrata Copper Canada Ltd., 2005).

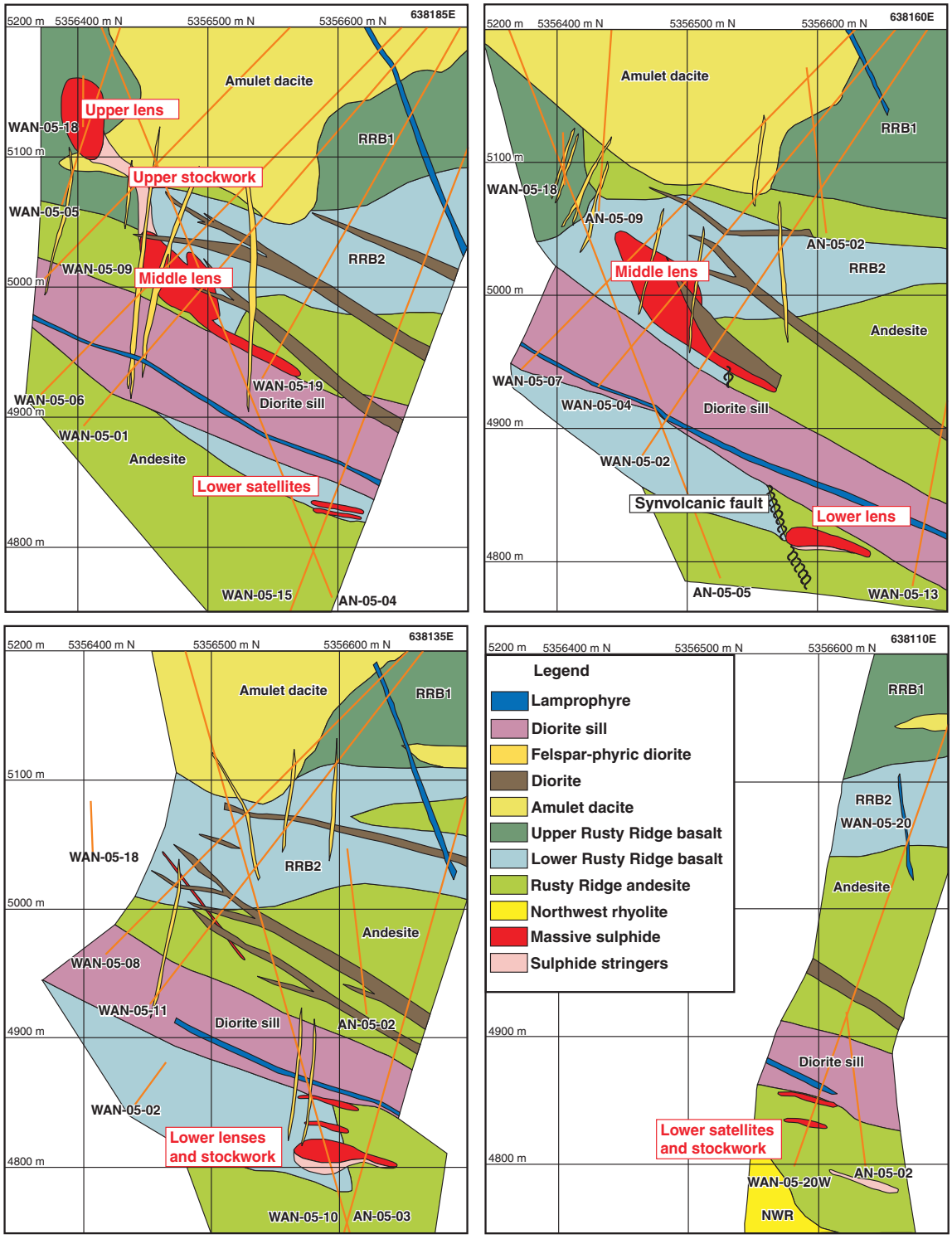

Figure 4. North-south cross-sections (facing west) through the West Ansil deposit showing the position of the upper, middle, and lower lenses. Local stratigraphic units including the Rusty Ridge basalt and andesite, Amulet dacite, as well as diorite sills and subvertical dykes are shown. Logged and sampled drillholes are indicated (*modified from* Xstrata Copper Canada Ltd., 2005).

The lower stockwork zone is located directly below the lower massive-sulphide lens and has an approximate thickness of 20 m and a width of 25 m. The stockwork consists of massive centimetre-scale chalcopyrite veins as well as network-like veinlets within strongly chloritized and silicified fragmental rocks, including hyaloclastite (Fig. 5). Sphalerite stringers occur toward the top of the stockwork zone and are overprinted by chalcopyrite veins and veinlets.

Principal ore types

Representative photographs and illustrations of the different ore types are shown in Figure 6 and Figure 7.

Massive pyrrhotite-chalcopyrite ore

Massive pyrrhotite-chalcopyrite ore is the most common ore type in all three sulphide lenses. The massive ore contains up to 90 olume per cent fine-grained pyrrhotite with 1–5 volume per cent fine-grained disseminated chalcopyrite (Fig. 6a, b). Chalcopyrite also occurs as wispy, planar to contorted discontinuous bands up to several centimetres wide (Fig. 7a). Contacts between alternating bands of chalcopyrite and pyrrhotite are sharp and smooth to serrate. Rounded millimetre-scale siliceous grains are abundant within the chalcopyrite-rich bands and wisps. Pseudobreccia zones are present throughout the massive-sulphide lenses and along footwall and hanging-wall contacts. They consist of angular fragments or clasts of chloritic or siliceous material (partially replaced wall rock) in a matrix of pyrrhotite and chalcopyrite (Fig. 6c 7b, c). The less well defined siliceous clasts, with intense pyrrhotite replacement, locally grade into more angular centimetre-scale chloritized fragments within a more or less continuous fine-grained chalcopyrite±sulphide matrix (Fig. 7b, c). These fragments commonly have alteration rims with projections of pyrrhotite or chalcopyrite into the fragments. Massive chalcopyrite is also locally concentrated at the upper and lower contacts of the massive-sulphide lenses separating the massive pyrrhotite from the strongly

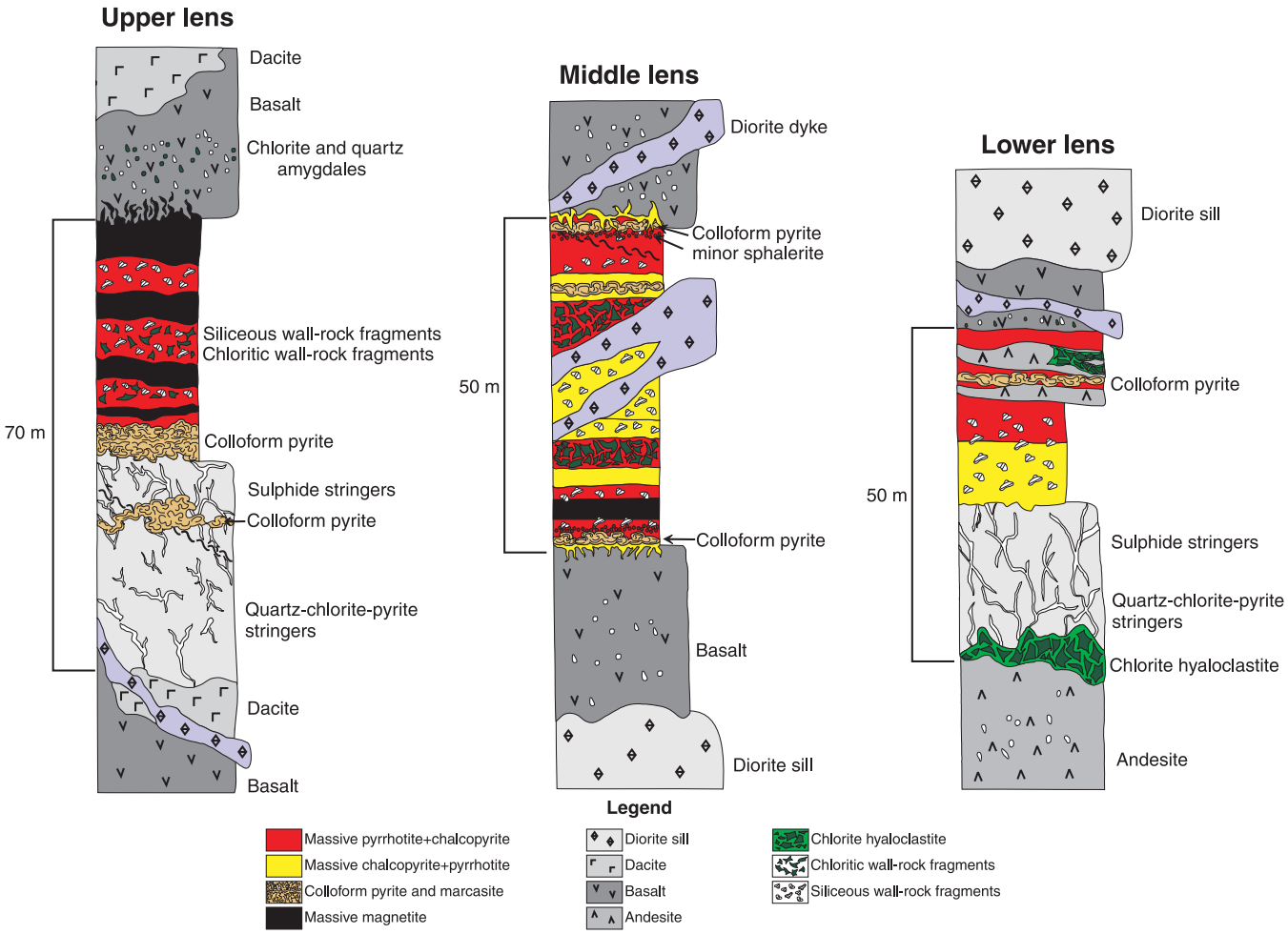

Figure 5. Composite graphic logs of the upper, middle, and lower lenses of the West Ansil deposit showing the dominant massive-sulphide ores and stockwork zones, contact relationships, the main mafic volcanic units, and major mafic dykes intruding the lenses. Note that the scale is intended to show the thickness of each lens, but not of the units in the lenses.

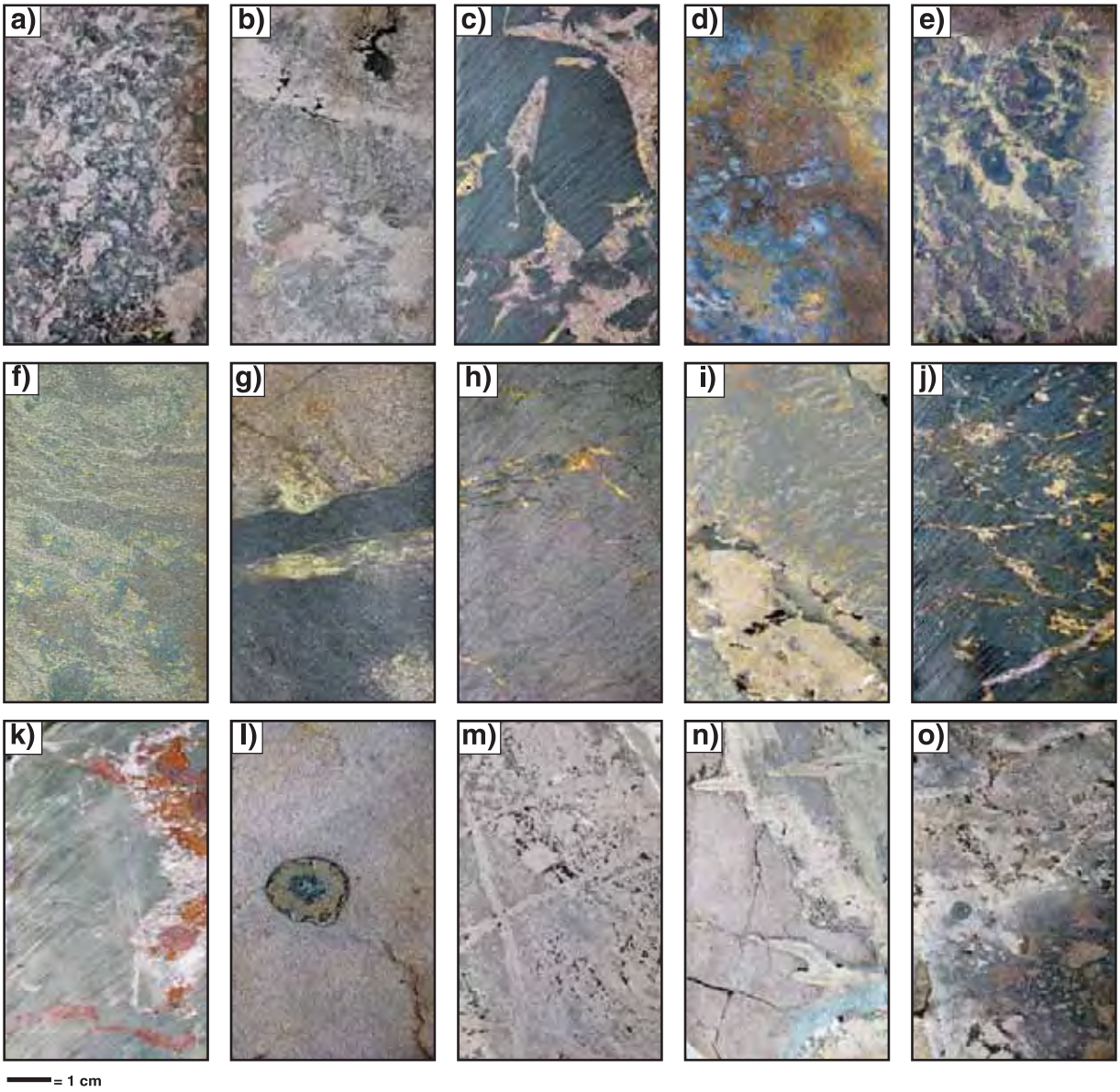

Figure 6. Representative photographs of drill-core samples showing sulphide ore textures in the West Ansil lenses. **a)** Partially pyrrhotite-replaced silicified and chloritized basalt pseudobreccia from the upper lens. 2010-190. **b)** Silicified-chloritized basalt pseudobreccia, almost completely replaced by massive pyrrhotite±chalcopyrite from the lower lens. 2010-189. **c)** Strongly chloritized basalt breccia in a pyrrhotite-rich matrix from the middle lens. 2010-193. **d)** Massive chalcopyrite±pyrrhotite ore with partially replaced siliceous fragments from the lower lens. 2010-186. **e)** Partially replaced siliceous fragments in a chalcopyrite±pyrrhotite matrix from the middle lens. 2010-192. **f)** Massive pyrrhotite±sphalerite with chalcopyrite in the middle lens showing millimetre- to centimetre-scale semicontinuous sphalerite-rich bands. Rounded microcrystalline quartz fragments are also present and appear to be the product of strong silicification. 2010-194. **g)** Magnetite bands in massive pyrrhotite±chalcopyrite from the upper lens. 2010-187. **h)** Massive magnetite with remobilized chalcopyrite veinlets from the upper lens. 2010-191. **i)** Massive magnetite in pyrrhotite±chalcopyrite with colloform pyrite-marcasite replacing pyrrhotite adjacent to the magnetite. Chalcopyrite has been remobilized into late fractures developed in the brittle magnetite. 2010-200. **j)** Chalcopyrite stringer in silicified-chloritized basalt from the lower stockwork zone. 2010-188. **k)** Sphalerite-pyrrhotite stringer in chloritized basalt from the bottom of the middle lens. 2010-196. **l)** Isolated secondary pyrite-marcasite nodule in massive pyrrhotite from the upper lens. 2010-199. **m)** Porous massive colloform pyrite-marcasite from the middle lens. 2010-198. **n)** Fracture-controlled recrystallized pyrite in colloform pyrite replacing massive pyrrhotite from the middle lens. 2010-195. **o)** Colloform pyrite-marcasite replacing the pyrrhotite-rich matrix of silicified basalt pseudobreccia from the middle lens. 2010-197. All photographs by S. Boucher.

chloritized basalt and andesite. Centimetre-scale colloform pyrite-marcasite nodules selectively replace the pyrrhotite where late fractures penetrate the massive-sulphide lenses (Fig. 7d, e, f).

Massive chalcopyrite-pyrrhotite ore

Massive chalcopyrite-rich ore occurs in the central part of the middle lens and dominates the lower lens. The massive ore contains up to 70 volume per cent fine-grained anhedral chalcopyrite with 20 volume per cent disseminated pyrrhotite (Fig. 6d). Chalcopyrite is present as large centimetre-scale continuous to discontinuous bands alternating with millimetre-scale bands of pyrrhotite (Fig. 7g). Locally, chalcopyrite, pyrrhotite, and sphalerite are intergrown, with about 50 volume per cent chalcopyrite, 30 volume per cent pyrrhotite, and 20 volume per cent sphalerite in some parts of the middle lens; however, pyrrhotite inclusions in chalcopyrite-rich bands suggest that the chalcopyrite may have replaced earlier massive pyrrhotite. As in the pyrrhotite-rich ore, the chalcopyrite appears to have replaced brecciated basalt, with unreplaced silicified and chloritized remnants of basalt locally preserved in the massive chalcopyrite and pyrrhotite (Fig. 6e).

Massive pyrrhotite-sphalerite ore

Sphalerite-rich ores are most common in the upper western part of the middle lens in association with massive pyrrhotite. The sphalerite occurs as millimetre- to centimetre-scale discontinuous to contorted bands in the massive pyrrhotite. Minor chalcopyrite is also present within the sphalerite bands, replacing both pyrrhotite and sphalerite (Fig. 6f). Contacts between sphalerite and pyrrhotite bands appear gradational, whereas contacts between chalcopyrite and pyrrhotite are sharp (Fig. 7h). Sphalerite is also present with pyrrhotite in the matrix of pseudobreccia zones, cementing partially replaced siliceous and chloritic wall-rock fragments. Minor remobilized chalcopyrite locally replaces the pyrrhotite-sphalerite-rich matrix along the contacts with the siliceous fragments.

Massive magnetite

Massive magnetite occurs at the top of the upper lens and as a 5 m thick pod near the bottom of the middle lens. At the top of the upper lens the massive magnetite is characterized by re-entrant cusps and centimetre-scale projections of magnetite into the strongly chloritized hanging-wall basalt progressing into disseminated magnetite that extends 15 cm into the basalt above the massive magnetite contact (Fig. 7i). Quartz-carbonate-chlorite veins and veinlets also extend into the hanging wall, which appear to be co-precipitating with magnetite (Fig. 5, 7i). In the main sulphide bodies the massive magnetite is fine grained and occurs in centimetre- to metre-scale bands of 60–90 volume per cent magnetite alternating with pyrrhotite (Fig. 6g). Quartz, chlorite, and actinolite are the dominant gangue minerals associated with the massive magnetite zones. Locally, siliceous and chloritic fragments occur as fine breccia in a matrix of magnetite (Fig. 6h, 7j). Inclusions of pyrrhotite are common in the magnetite and suggest that the magnetite replaced the pre-existing pyrrhotite (Fig. 7k). Chalcopyrite is abundant as disseminated grains in massive magnetite and especially as millimetre-scale veinlets; the latter appears to have been structurally remobilized into brittle fractures in the massive magnetite and along magnetite-pyrrhotite contacts (Fig. 6i, 7l). Colloform pyrite and marcasite are also commonly present replacing pyrrhotite along the contacts of the massive magnetite (Fig. 7m).

Chalcopyrite stringer mineralization

The chalcopyrite stringer mineralization below the upper and lower lenses occurs in two distinct styles: network-like stringers and massive chalcopyrite±pyrrhotite veins within strongly chloritized hyaloclastite and basalt-andesite breccia. The fine, network-like stringers occupy an extensive zone of microfractures within the chloritic basalt-andesite beneath each of the sulphide lenses, as well as beneath the massive chalcopyrite-pyrrhotite vein stockwork zones and extends a few metres above the middle and lower sulphide lenses (Fig. 5, 6j). Larger chalcopyrite±pyrrhotite veins predominate in the centre of the upper and lower stockwork zones, where individual veins can be up to 20 cm wide, often with cores or rims of pyrrhotite (Fig. 7n). The more pyrrhotite-rich stringers typically occur in the upper stockwork zone (below the upper lens). Both fine network-like stringers and larger veins contain chlorite and quartz which increase in abundance laterally and horizontally away from the core of the main chalcopyrite stockwork zones (Fig. 7o). Minor chalcopyrite stringers are also present directly below the middle sulphide lens, but a stockwork zone appears to be missing at this location (Fig. 5).

Sphalerite stringer mineralization

A network of millimetre- to centimetre-scale sphalerite stringers occurs mostly in the lower stockwork zone (below the lower lens) and locally in the immediate footwall of the middle lens where it is not cut by diorite. Individual veins of sphalerite are up to several centimetres wide within strongly chloritized hyaloclastite and basalt or andesite breccia. Minor pyrrhotite is also present in the sphalerite stringers and appears to have replaced sphalerite (Fig. 7p). Some sphalerite stringers contain euhedral millimetre-sized pyrite grains. In the lower stockwork zone, sphalerite stringers occur outside the chalcopyrite-rich core of the stockwork mineralization, but are cut by chalcopyrite-pyrrhotite veinlets (Fig. 6k).

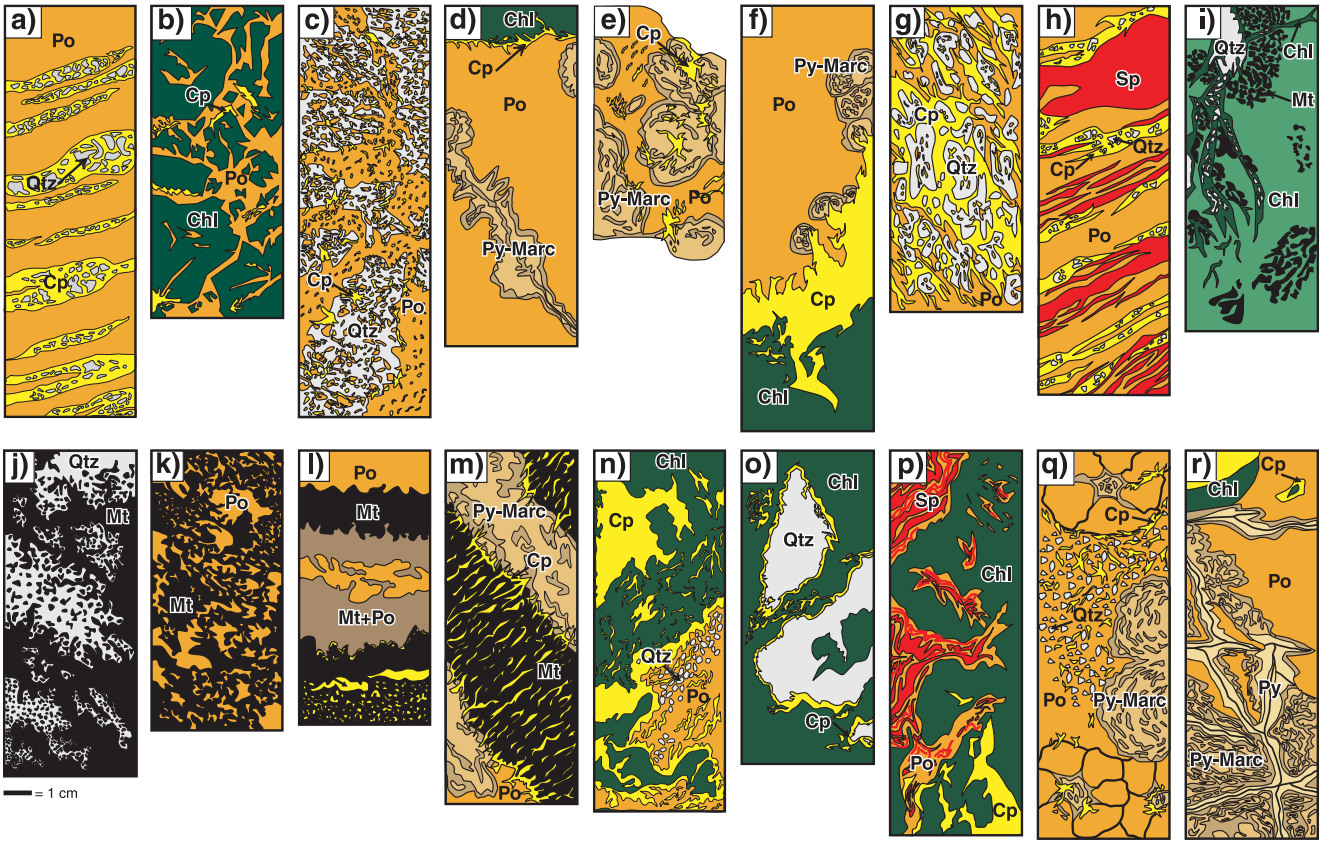

Colloform pyrite-marcasite

Bands or lenses of nodular and colloform pyrite and marcasite occur mostly at the top and bottom of all three sulphide lenses. The bands consist of fine-grained pyrite-marcasite intergrowths that form centimetre-sized spheroidal bodies (Fig. 6l) or clots and locally coalesce to form 5–40 cm thick porous layers that replace massive pyrrhotite (Fig. 6m, 7q). The initial stages of replacement appear to be characterized by clover-leaf shapes formed by the coalescence of small neighbouring clots of pyrite and marcasite; these acted as nuclei for larger nodular growths (Fig. 7q). Typically, the pyrite-marcasite growths are centred on fractures in the pyrrhotite, and colloform bands or layers develop parallel to the fractures (Fig. 6n, 7r). Contacts between the pyrite-marcasite and massive pyrrhotite are characterized by the presence of 'skrinkage cracks' indicating volume loss, where dark brown siliceous material separates both sulphide minerals. The dark brown material is interpreted to be hisingerite, which is an amorphous iron-silicate mineral commonly formed as a secondary product of weathering of pyrrhotite-rich ore (Murowchick, 1992; *see* 'Evolution of the massive sulphide lenses' section). It occurs locally as centimetre-scale bands around the pyrite-marcasite nodules and also contains desiccation cracks. Recrystallized pyrite is present within late fractures in some colloform bands, possibly indicating late-stage fluid circulation. Locally, the pyrite and marcasite nodules are surrounded by a carbonate- and quartz-rich matrix (Fig. 6o). At the top of the middle lens, remobilized sphalerite and galena fill late open spaces within and between the nodular pyrite-marcasite crusts. Minor remobilized chalcopyrite also occurs between nodules or colloform bands and along pyrite-marcasite and pyrrhotite contacts (Fig. 7q, r).

Metal zonation

Ore assays from 1 m long core splits were used to construct metal zonation profiles of the upper, middle, and lower lenses. The Cu, Zn, Au, Ag, and Pb concentrations in 16 drillholes from all three lenses were plotted on composite sections in Figure 8. Metal contents in the West Ansil deposit do not show a consistent stratigraphic zonation of a Cu-rich base to a Zn-rich top, except in the upper part of the middle lens. The upper lens has an ambiguous zonation apparently caused by the late-stage emplacement of massive magnetite.

The upper lens has a Cu-rich core (3–6 weight per cent Cu), with up to 8 weight per cent Cu in the stockwork zone. High Au (up to 8 ppm) and Ag (up to 15 ppm) also occur in the Cu-rich core, consistent with a strong positive correlation between Cu, Au, and Ag throughout the deposit. Higher concentrations of Ag (up to 20 ppm) were also found in the Cu-rich stockwork zone. The Zn (<0.2 weight per cent) and Pb (<0.01 weight per cent) grades are very low throughout the upper lens; however, Zn values up to 1 weight per cent are present in the stockwork zone. Neither Au nor Ag shows any correlation with Zn. The massive magnetite zone is barren (Fig. 8a).

Figure 7. Schematic illustrations of ore textures in the West Ansil deposit. **a)** Banded pyrrhotite-chalcopyrite (Po-Cp) ore showing discontinuous centimetre-scale chalcopyrite-rich bands containing rounded, partly replaced siliceous wall-rock fragments (Qtz = quartz). Contacts between pyrrhotite and chalcopyrite are sharp and smooth to serrate. The pyrrhotite also contains fine-grained disseminated chalcopyrite and sphalerite. **b)** Chlorite-rich (Chl) basalt breccia from the middle lens with abundant pyrrhotite (Po) in the matrix between angular and partially replaced fragments of black chloritized basalt. The pyrrhotite matrix also contains minor disseminated chalcopyrite (Cp) and remobilized chalcopyrite along the boundaries of chlorite fragments. **c)** Intensely silicified basalt and andesite pseudobreccia from the middle lens with abundant pyrrhotite (Po) and lesser chalcopyrite (Cp) in the matrix between large centimetre-scale angular and almost completely replaced siliceous clasts (Qtz). The quartz-rich fragments appear to be the product of very strong silicification of basalt. Both pyrrhotite and chalcopyrite invade the fragments; however, late chalcopyrite also replaces pyrrhotite. **d)** Massive sulphide at the top of the middle lens with remobilized chalcopyrite (Cp) separating the chloritized (Chl) hanging-wall basalt from the massive pyrrhotite (Po). Remobilized chalcopyrite-rich stringers extend into both the pyrrhotite and the wall rock. The massive pyrrhotite is also partly replaced by centimetre-scale colloform pyrite-marcasite (Py-Marc) nodules and veins centred on late fractures. **e)** Colloform pyrite-marcasite (Py-Marc) in massive pyrrhotite from the middle lens. The large centimetre-scale pyrite-marcarite nodules contain unreplaced pyrrhotite (Po) and late-stage remobilized chalcopyrite (Cp) in shrinkage cracks. **f)** Massive sulphide at the bottom of the middle lens with remobilized chalcopyrite (Cp) separating the chloritized (Chl) footwall basalt from the massive pyrrhotite (Po). Remobilized chalcopyrite-rich stringers extend into both the pyrrhotite and wall rock. Colloform centimetre-scale pyrite-marcasite (Py-Marc) nodules selectively replace the fine-grained pyrrhotite at the lower sulphide contact. **g)** Discontinuous chalcopyrite-rich (Cp) bands from the lower lens alternating with bands of pyrrhotite (Po). Partly replaced siliceous (Qtz) material is present within the bands and is interpreted to represent unreplaced fragments of silicified wall rock. Pyrrhotite inclusions within the chalcopyrite bands suggest that the pyrrhotite was replaced by chalcopyrite, although the present banding is likely tectonic. **h)** Banded pyrrhotite-chalcopyrite±sphalerite (Po-Cp±Sp) ore showing discontinuous millimetre- to centimetre-scale chalcopyrite- and sphalerite-rich bands. Rounded siliceous (Qtz) fragments are present only in the chalcopyrite bands. Contacts between pyrrhotite and chalcopyrite are sharp, whereas contacts between pyrrhotite and sphalerite are more gradational. The pyrrhotite also contains fine-grained disseminated chalcopyrite and sphalerite. **i)** Disseminated magnetite±actinolite grains and clusters within strongly chloritized (Chl) basalt at the top of the upper lens, 10 cm from the massive magnetite (Mt) contact. A quartz-calcite-chlorite (Qtz = quartz) vein appears to cuts the disseminated magnetite and is therefore late. **j)** Massive magnetite (Mt) from the upper lens replacing strongly silicified (Qtz) basalt fragments and forming a continuous matrix in the pseudobreccia. Minor chlorite and actinolite are also overprinted by magnetite. **k)** Massive magnetite (Mt) replacing pyrrhotite (Po) from the upper lens. The massive magnetite contains abundant pyrrhotite inclusions that suggest later introduction of magnetite. **l)** Massive magnetite (Mt) and pyrrhotite (Po) from the upper lens. Massive magnetite generally forms re-entrant cusps into the pyrrhotite. Alternating centimetre-scale bands of pyrrhotite show evidence of extensive remobilization. The magnetite also contains an abundance of disseminated and veinlet chalcopyrite introduced during late remobilization of sulphide minerals into fractures developed in the more brittle magnetite. A chalcopyrite-rich rim occurs at the contact between magnetite and pyrrhotite. **m)** Massive magnetite (Mt) band from the middle lens. The magnetite band appears to crosscut the more massive pyrrhotite. Remobilized chalcopyrite (Cp) veinlets are present throughout the magnetite in late brittle fractures and along the contact with pyrrhotite. Colloform pyrite-marcasite (Py-Marc) along the pyrrhotite-magnetite contact locally replaces pyrrhotite, but not magnetite. **n)** Chalcopyrite-pyrrhotite (Cp-Po) stringer mineralization from the upper stockwork zone. Large centimetre-scale chalcopyrite network-like veins occur within a strongly chloritized (Chl) basalt and appear to have replaced pyrrhotite. Smaller millimetre-scale chalcopyrite veinlets have been locally remobilized into late fractures. Qtz = quartz. **o)** Chlorite (Chl) and minor chalcopyrite (Cp) stringer mineralization in the upper stockwork zone. Centimetre-scale chlorite-actinolite network-like veins occur within a strongly silicified (Qtz) and chloritized basalt breccia. Chalcopyrite rims the siliceous fragments and occurs as microveinlets in the more massive chlorite-actinolite. **p)** Sphalerite (Sp) and pyrrhotite (Po) stringers at the base of the middle lens. The stringers have a rim of pyrrhotite, that may reflect the replacement of early sphalerite stringers by later pyrrhotite. Chl = chlorite, Cp = chalcopyrite. **q)** Colloform pyrite-marcasite (Py-Marc) replacing massive pyrrhotite (Po) in the middle lens. Fracture-controlled centimetre-scale pyrite-marcasite nodules and spheroids are centred on late fractures and invade the massive pyrrhotite. Remobilized chalcopyrite (Cp) also occurs in the late fractures. The radial pattern of some fractures reflects volume loss during replacement of pyrrhotite by pyrite and marcasite. **r)** Colloform pyrite-marcasite (Py-Marc) in massive pyrrhotite (Po) in the middle lens. Replacement of pyrrhotite by centimetre-scale spheroidal bodies of pyrite-marcasite occurs along and between late fractures. Recrystallized pyrite is present within the fractures and remobilized sphalerite fills. Chl = chlorite, Cp = chalcopyrite.

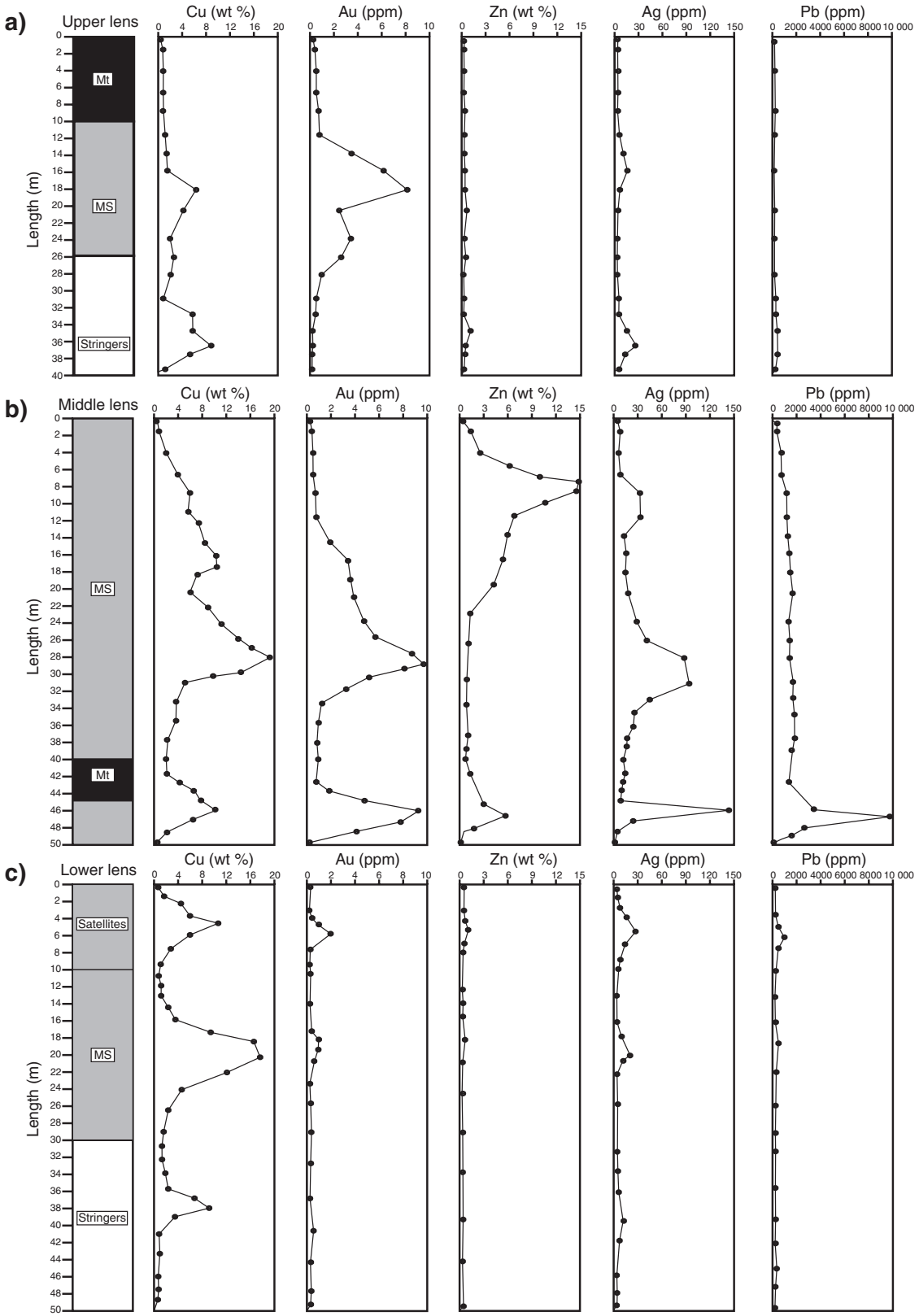
a)
Upper lens
Cu (wt %)
Au (ppm)
Zn (wt %)
Ag (ppm)
Pb (ppm)
Length (m)
Mt
MS
Stringers
b)
Middle lens
Cu (wt %)
Au (ppm)
Zn (wt %)
Ag (ppm)
Pb (ppm)
Length (m)
MS
Mt
c)
Lower lens
Cu (wt %)
Au (ppm)
Zn (wt %)
Ag (ppm)
Pb (ppm)
Length (m)
Satellites
MS
Stringers

The middle lens has a distinctive Zn-rich top (up to 15 weight per cent Zn), Cu-rich core (12–20 weight per cent Cu), and a moderately Cu-rich base and stockwork zone (8–12 weight per cent Cu). Minor Zn (3–6 weight per cent Zn) is also present in the network-like veins at the base of the lens; however, the bulk of the lens contains less than 2 weight per cent Zn. High Au (up to 10 ppm) and Ag (60–150 ppm) are also found in the Cu-rich core and base of the middle lens, supporting the overall Cu-Au-Ag correlation of the deposit. High Pb (~1 weight per cent) occurs at the bottom of the lens and can be explained by remobilized quartz-carbonate-sphalerite-galena veins; however, most of the lens contains less than 0.2 weight per cent Pb. The Au, Ag, and Pb are poorly correlated with Zn, as in the upper lens, and the massive magnetite in the middle lens is barren (Fig. 8b).

The lower lens and stockwork zone are notably Cu-rich, with up to 12 weight per cent Cu in the satellite bodies, 20 weight per cent Cu in the core, and 12 weight per cent Cu in the stringer zone. Gold (2–4 ppm) and silver (15–50 ppm) correlate with the high concentrations of copper. Zinc grades (<1 weight per cent) are very low throughout the lower lens, which could suggest that this was the high-temperature feeder zone of the hydrothermal system. Minor Au, Ag, Pb, and Cu in the satellite bodies can be explained by locally remobilized precious-metal-bearing galena and chalcopyrite (Fig. 8c).

Although the overall gold content of the West Ansil deposit is 1.4g/t, significantly higher grades are found in some parts of the middle lens. The association with high Cu grades is similar to that observed in other deposits of the Central camp such as Ansil and Corbet (Barrett et al., 1991, 1993).

EVOLUTION OF THE MASSIVE-SULPHIDE LENSES

The overall distribution of massive-sulphide ore and stringer zones at the West Ansil deposit suggests either stacking of separate lenses or dissection of a single deposit by late-stage faulting and dyke formation. The presence of a subvertical synvolcanic fault controlling high-temperature stockwork mineralization is suggested by displacement in the volcanic stratigraphy near the lower lens (Fig. 4); however, a stockwork zone beneath the larger middle lens appears to be missing and likely was removed by the massive diorite. The coherent Cu-to-Zn metal zonation in the middle lens suggests that it is intact except for the absence of the stockwork zone. The unusual metal zonation and lack of Zn or Pb enrichment in the upper lens suggests that it might also be out of place (e.g. a faulted portion of the main lens, rather than a stacked lens); however, the presence of the Amulet unit immediately beneath the upper lens is consistent with stacking of lenses. In some sections, there are no obvious subvertical feeders immediately below massive-sulphide parts of the lenses, but semiconformable zones of disseminated sulphide minerals and magnetite are present with semimassive sulphide infilling chlorite-altered hyaloclastite. This suggests that mineralizing fluids may have moved in part laterally through the Rusty Ridge unit, probably through zones of high porosity such as breccia and hyaloclastite (Barrett et al., 1991).

Two stages of mineralization are recognized at the West Ansil deposit: 1) an early stage of sphalerite-pyrrhotite±pyrite mineralization with associated chlorite-quartz alteration, and 2) a later stage of pyrrhotite-chalcopyrite mineralization with magnetite±actinolite replacement. The ore was later subjected to secondary processes that were responsible for colloform pyrite-marcasite replacing pyrrhotite (Fig. 9).

Remnants of the early-stage mineralization (massivebanded sphalerite-pyrrhotite and sphalerite-pyrrhotite-cemented pseudobreccia) occur at the western top of the middle lens. Remnants of sphalerite-pyrrrhotite-rich stringer mineralization within strongly chloritized and silicified andesite also occur locally below the middle lens and at the margins of the lower stockwork zone. Massive sphalerite only occurs at the top of the middle lens, where brecciated basalt is infilled and partly replaced by pyrrhotite and sphalerite. At the nearby Ansil deposit, Galley et al. (1995) interpreted this texture to represent basaltic flows on-lapping the andesite during early-stage hydrothermal activity.

Figure 8. a) Composite metal zonation of the upper lens based on assay data from WAN-05-05, WAN-05-09, and WAN-05-18. The Cu, Au, and Ag show a positive correlation in the centre of the lens and the stockwork zone. The Zn and Pb concentrations are uniformly low. **b)** Composite metal zonation profiles of the middle lens based on assay data from AN-05-04, WAN-05-01, WAN-05-02, WAN-05-04, WAN-05-06, WAN-05-07, and WAN-05-19W. The middle lens has a Zn-rich top and a Cu-rich core and stringer zone. Again, a positive correlation between Cu, Au, and Ag is apparent in the central part of the lens and stringer zone. The high Pb, Zn, Ag, and Au values at the bottom of the lens are due to remobilized galena veins at the basal contact. **c)** Composite metal zonation of the lower lens and stockwork zone based on assay data from AN-05-02, AN-05-03, WAN-05-10, WAN-05-12, WAN-05-15, and WAN-05-20W, including a satellite zone. The Zn and Pb values are low, and Cu, Au, and Ag are positively correlated. MS = massive sulphide, MT = magnetite.

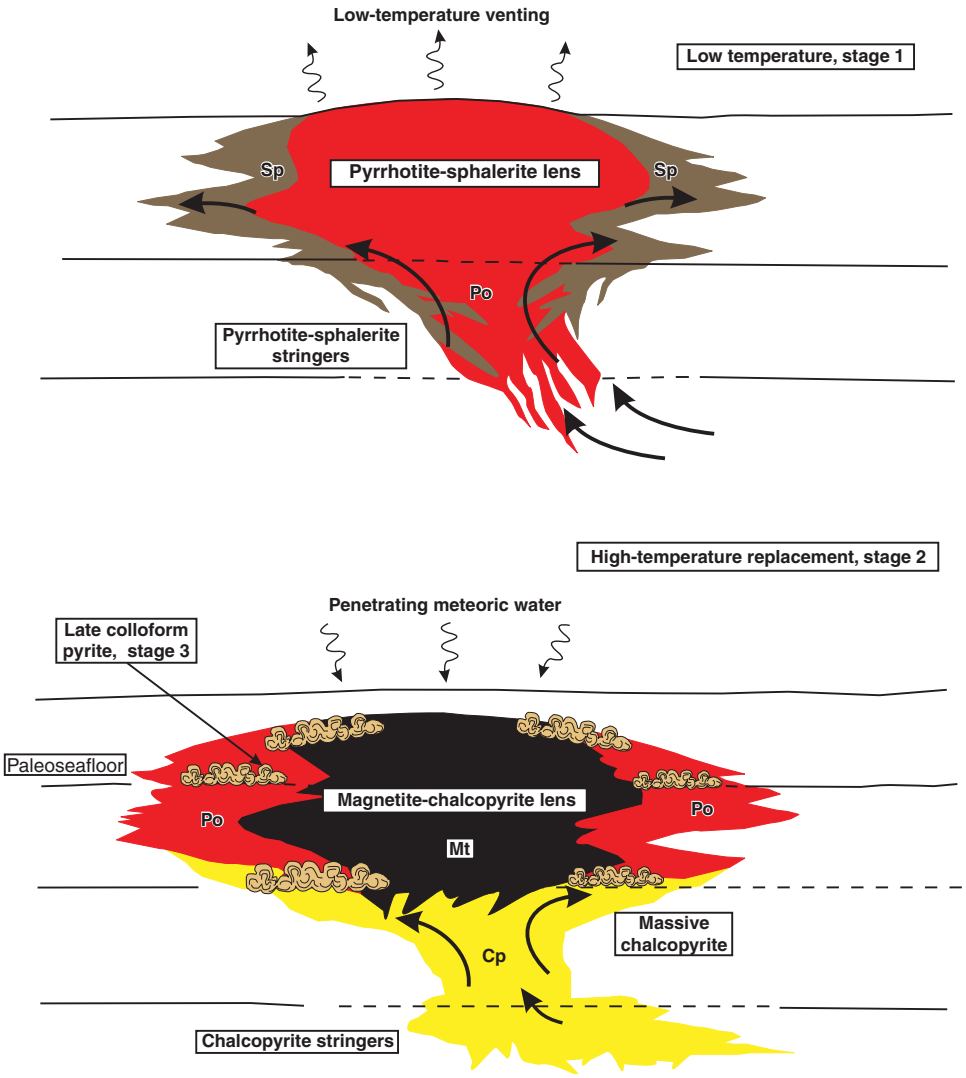

Figure 9. Schematic representation of the development of the West Ansil hydrothermal system. The main stages of mineralization include 1) contruction of a low-temperature sphalerite-pyrrhotite (Sp-Po) vent complex, above a sphalerite-pyrrhotite stockwork; 2) development of late chalcopyrite stringer networks; 3) emplacement of massive chalcopyrite (Cp) and magnetite along a higher temperature replacement front at the base of the sphalerite-pyrite-pyrrhotite lens; and 4) alteration of pyrrhotite along sheared contacts and late fractures and formation of colloform pyrite and marcasite.

The second stage of mineralization involved the development of a pyrrhotite-chalcopyrite vein system below the upper and lower lenses, where the most intense chloritization of the basalt and andesite occurs. The Cu-rich stockworks grade upward into pyrrhotite-chalcopyrite-rich massive sulphide. The middle lens lacks this conspicuous transition, which was most likely removed by the diorite sill that separates the middle lens from the lower lens. The middle and lower lenses both contain a chalcopyrite-rich core which likely formed at peak temperatures in the hydrothermal system (e.g. Barrett et al., 1991). Massive magnetite found in the upper and middle lenses appears to have formed as a replacement of pyrrhotite- and chalcopyrite-rich ore. Magnetite generally forms re-entrant cusps into the massive pyrrhotite and appears to have advanced into or replaced the massive-sulphide minerals, as observed at the Ansil deposit (Riverin et al., 1990; Westendorp et al., 1991; Westendorp, 1992); however, magnetite feeders have not been observed directly below the massive magnetite. Because of its brittle nature, the massive magnetite is commonly veined by remobilized chalcopyrite. At the Ansil deposit, Westendorp (Westendorp et al., 1991; Westendorp, 1992) and Galley et al. (1995, 2000) interpreted the magnetite replacement to have formed when rising hot (350°C) fluids were able to mix with cooler, less acidic, and more oxidized seawater along the footwall and hanging-wall contacts of the massive-sulphide lenses.

Late-stage replacement of massive pyrrhotite by colloform pyrite and marcasite, mostly along the upper and lower contacts of the lenses, appears to be a secondary feature caused by alteration of pyrrhotite along fractures in the ore. The observed nodular and spheroidal pyrite and marcasite closely resemble supergene alteration of massive pyrrhotite in pyrrhotite-rich NiS deposits in other Archean greenstone belts (e.g. Butt and Nickel, 1981). The replacement of massive pyrrhotite by pyrite and marcasite leads to a significant volume reduction, which likely accounts for conspicuous 'shrinkage cracks' associated with the replacement (Fleet, 1978). The amorphous iron oxide, hisingerite, present in these cracks is also a product of sulphide weathering (Murowchick, 1992). This feature is rare in other deposits of the Noranda central camp, but has been described at the New Insco deposit north of Noranda (Larson, 1983). Shearing

and faulting at the contacts of the massive-sulphide lenses at West Ansil may have allowed meteoric water to penetrate into the ore zone to cause pyrrhotite replacement.

Figure 9 illustrates the inferred stages of development of the West Ansil hydrothermal system: 1) construction of a 'low-temperature' sphalerite-pyrrhotite vent complex above a sphalerite-pyrrhotite stockwork, 2) development of higher temperature chalcopyrite stringer networks, 3) emplacement of massive chalcopyrite and magnetite along a replacement front at the base of the sphalerite-pyrrhotite, and 4) alteration of massive pyrrhotite by penetration of groundwater along sheared contacts and late fractures.

The origins of the unusual magnetite-rich zones and the late-stage colloform pyrite and marcasite are being investigated further with detailed chemistry and stable isotopes.

ACKNOWLEDGMENTS

The author would like to thank the personnel at Xstrata Copper Canada Ltd. and Alexis Minerals for providing the geological information such as drill core and Cu-Zn-Ag-Au geochemical data presented in this paper. The author is also grateful to the TGI3-Targeted Geoscience Initiative –3 Abitibi project of the Geological Survey of Canada for their financial support and knowledgeable geological information. Many thanks to M.D. Hannington and T. Monecke for leading the author in the right direction with their assistance in the field, as well as for their academic support.

REFERENCES

Baragar, W.R.A., 1968. Major-element geochemistry of the Noranda volcanic belt, Quebec-Ontario; Canadian Journal of Earth Sciences, v. 5, p. 773–790.

Barrett, T.J., MacLean, W.H., Cattalani, S., Hoy, L., and Riverin, G., 1991. Massive sulfide deposits of the Noranda area, Quebec. III. The Ansil mine; Canadian Journal of Earth Sciences, v. 28, p. 1699–1730.

Barrett, T.J., MacLean, W.H., Cattalani, S., and Hoy, L., 1993. Massive sulfide deposits of the Noranda area, Quebec. V. The Corbet mine; Canadian Journal of Earth Sciences, v. 30, p. 1934–1954.

Butt, C.R.M. and Nickel, E.H., 1981. Mineralogy and geochemistry of the weathering of the disseminated nickel sulfide deposit at Mt. Keith, Western Australia; Economic Geology and the Bulletin of the Society of Economic Geologists, v. 76, p. 1736–1751. doi:10.2113/gsecongeo.76.6.1736

Cattalani, S., Barrett, T.J., MacLean, W.H., Hoy, L., Hubert, C., and Fox, J.S., 1993. Métallogénèse des gisements Hornes et Quemont (region de Rouyn-Noranda); Ministère de l'Énergie et des Ressources du Québec, Rapport ET 90-07, 121 p

de Rosen-Spence, A.F., 1976. Stratigraphy, development and petrogenesis of the Central Noranda volcanic pile, Noranda, Quebec; Ph.D. thesis, University of Toronto, Toronto, Ontario, Canada, 166 p.

Dimroth, E., Imreh, L., Rocheleau, M., and Goulet, N., 1982. Evolution of the south-central part of the Archean Abitibi Belt, Quebec. Part I: stratigraphy and paleogeographic model; Canadian Journal of Earth Sciences, v. 19, p. 1729–1758.

Fleet, M.E., 1978. The pyrrhotite-marcasite transformation; Canadian Mineralogist, v. 16, p. 31–35.

Galley, A.G., 1994. The geology of the Ansil Cu-Zn massive sulphide deposit, Rouyn-Noranda, Quebec; Ph.D. thesis, Carleton University, Ottawa, Ontario, 377 p.

Galley, A.G., Watkinson, D.H., Jonasson, I.R., and Riverin, G., 1995. The subseafloor formation of volcanic-hosted massive sulphides: evidence from the Ansil deposit, Rouyn-Noranda, Canada; Economic Geology and the Bulletin of the Society of Economic Geologists, v. 90, p. 2006–2017. doi:10.2113/gsecongeo.90.7.2006

Galley, A.G., Jonasson, I.R., and Watkinson, D.H., 2000. Magnetite-rich calc-silicate alteration in relation to synvolcanic intrusion at the Ansil volcanogenic massive sulphide deposit, Rouyn-Noranda, Quebec, Canada; Mineralium Deposita, v. 35, p. 619–637. doi:10.1007/s001260050267

Gélinas, L., Trudel, P., and Hubert, C., 1984. Chemostratigraphic division of the Blake River Group, Rouyn-Noranda area, Abitibi, Quebec; Canadian Journal of Earth Sciences, v. 21, p. 220–231.

Gibson, H. and Galley, A., 2007. Volcanogenic massive sulphide deposits of the Archean, Noranda District, Quebec; *in* Mineral deposits of Canada: a synthesis of major deposit types, district metallogeny, the evolution of geological provinces and exploration methods, (ed.) W.D. Goodfellow; Geological Association of Canada, Mineral Deposits Division, Special Publication No. 5, p. 533–552.

Gibson, H.L. and Watkinson, D.H., 1990. Volcanogenic massive sulphide deposits of the Noranda cauldron and shield volcano, Quebec; *in* The northwestern Quebec polymetallic belt, (ed.) M. Rive, P. Verpaelst, Y. Gagnon, J.M. Lulin, G. Riverin, and A. Simard; Canadian Institute of Mining Metallurgy, Special Volume 43, p. 119–132.

Goldie, R., 1978. Magma mixing in the Flavrian pluton, Noranda area, Quebec; Canadian Journal of Earth Sciences, v. 15, p. 132–144.

Goutier, J., McNicoll, V., Dion, C., Lafrance, B., Legault, M., Ross, P.-S., Mercier-Langevin, P., Cheng, L.-Z., de Kemp, E., and Ayer, J., 2009. L'impact du Plan Cuivre et de L'ICG-3 sur la géologie de l'Abitibi et du Groupe de Blake River; *in* Proceedings Volume, Congrès Abitibi 2009 – Abitibi Cuivre, Rouyn-Noranda, September 28th, 2009, p. 9–13.

Larson, J.E., 1983. Geology, geochemistry and wall-rock alteration at the Magusi and New Insco massive sulfide deposits, Hebecourt Township, northwestern Quebec; M.Sc. thesis, University of Western Ontario, London, Ontario, 173 p.

McNicoll, V., Goutier, J., Dion, C., Ross, P.-S., and Mercier-Langevin, P., 2009. Portrait des grandes unites du Groupe de Blake River et leur relation avec les sulfures massifs volcanogènes; *in* Excursion Guidebook, Congrès Abitibi 2009 – Abitibi Cuivre, Rouyn-Noranda, September 28th, 2009, p. 9–28.

Monecke, T., Gibson, H., Dubé, B., Laurin, J., Hannington, M.D., and Martin, L., 2008. Geology and volcanic setting of the Horne deposit, Quebec: initial results of a new research project; Geological Survey of Canada, Current Research 2008-9, 16 p.

Mortensen, J.K., 1987. Preliminary U-Pb zircon ages for volcanic and plutonic rocks of the Noranda-Lac Abitibi area, Abitibi Subprovince, Quebec; *in* Current Research, Part A; Geological Survey of Canada, Paper 87–1A, p. 581–590.

Murowchick, J.B., 1992. Marcasite inversion and the petrographic determination of pyrite ancestry; Economic Geology and the Bulletin of the Society of Economic Geologists, v. 87, p. 1141–1152. doi:10.2113/gsecongeo.87.4.1141

Riverin, G. and Hodgson, C.J., 1980. Wallrock alteration at the Millenbach Cu-Zn mine, Noranda, Quebec; Economic Geology and the Bulletin of the Society of Economic Geologists, v. 75, p. 424–444. doi:10.2113/gsecongeo.75.3.424

Riverin, G., LaBrie, M., Salmon, B., Cazavant, A., Asselin, R., and Gagnon, M., 1990. The geology of the Ansil deposit, Rouyn-Noranda, Quebec; *in* The northwestern Quebec polymetallic belt, (ed.) M. Rive, P. Verpaelst, Y. Gagnon, J.M. Lulin, G. Riverin, and A. Simard; Canadian Institute of Mining Metallurgy, Special Volume 43, p. 143–151.

Westendorp, R.W., 1992. Magnetite zones at the Ansil Cu-Zn deposit, Rouyn-Noranda, Quebec: M.Sc. thesis, Carleton University, Ottawa, Ontario, 46 p.

Westendorp, R.W., Watkinson, D.H., and Jonasson, I.R., 1991. Silicon-bearing zoned magnetite crystals and the evolution of hydrothermal fluid at the Ansil Cu-Zn Mine, Rouyn-Noranda, Quebec; Economic Geology and the Bulletin of the Society of Economic Geologists, v. 86, p. 1110–1114. doi:10.2113/gsecongeo.86.5.1110

Xstrata Copper Canada Ltd., 2005. West Ansil resource estimate; 43-101F1 Technical Report, 50 p.

Geological Survey of Canada Project X91